Springer Theses
Recognizing Outstanding Ph.D. Research

Abdulrahman Shahul Hameed

Phosphate Based Cathodes and Reduced Graphene Oxide Composite Anodes for Energy Storage Applications

Springer

Springer Theses

Recognizing Outstanding Ph.D. Research

Aims and Scope

The series "Springer Theses" brings together a selection of the very best Ph.D. theses from around the world and across the physical sciences. Nominated and endorsed by two recognized specialists, each published volume has been selected for its scientific excellence and the high impact of its contents for the pertinent field of research. For greater accessibility to non-specialists, the published versions include an extended introduction, as well as a foreword by the student's supervisor explaining the special relevance of the work for the field. As a whole, the series will provide a valuable resource both for newcomers to the research fields described, and for other scientists seeking detailed background information on special questions. Finally, it provides an accredited documentation of the valuable contributions made by today's younger generation of scientists.

Theses are accepted into the series by invited nomination only and must fulfill all of the following criteria

- They must be written in good English.
- The topic should fall within the confines of Chemistry, Physics, Earth Sciences, Engineering and related interdisciplinary fields such as Materials, Nanoscience, Chemical Engineering, Complex Systems and Biophysics.
- The work reported in the thesis must represent a significant scientific advance.
- If the thesis includes previously published material, permission to reproduce this must be gained from the respective copyright holder.
- They must have been examined and passed during the 12 months prior to nomination.
- Each thesis should include a foreword by the supervisor outlining the significance of its content.
- The theses should have a clearly defined structure including an introduction accessible to scientists not expert in that particular field.

More information about this series at http://www.springer.com/series/8790

Abdulrahman Shahul Hameed

Phosphate Based Cathodes and Reduced Graphene Oxide Composite Anodes for Energy Storage Applications

Doctoral Thesis accepted by
National University of Singapore, Singapore

Springer

Author
Dr. Abdulrahman Shahul Hameed
Department of Chemistry and Earth Sciences
Qatar University
Doha
Qatar

Supervisor
Prof. J.J. Vittal
National University of Singapore
Singapore
Singapore

ISSN 2190-5053 ISSN 2190-5061 (electronic)
Springer Theses
ISBN 978-981-10-2301-9 ISBN 978-981-10-2302-6 (eBook)
DOI 10.1007/978-981-10-2302-6

Library of Congress Control Number: 2016947759

Printed on acid-free paper

This Springer imprint is published by Springer Nature
The registered company is Springer Science+Business Media Singapore Pte Ltd.

Supervisor's Foreword

It is a great pleasure to introduce the Ph.D. thesis work of Dr. Abdulrahman Shahul Hameed which won the Springer Thesis Award 2016 for outstanding original work and accepted for publication within Springer Theses. Shahul ranked second in his B.Sc. (2004–2007) from Calicut University, India. Later, he was admitted to Indian Institute of Technology—Delhi, one of the prestigious institutes in India through a highly competitive national-level Joint Admission Test to do M.Sc. (2008–2010) before joining National University of Singapore for his Ph.D. degree. Shahul completed Ph.D. doctoral work under my supervision in the Department of Chemistry during the period August 2010–August 2014, defended his Ph.D. thesis, and received his Ph.D. degree in January 2015.

Shahul's thesis work deals with developing novel cathode and anode materials for lithium-ion battery applications. This includes synthesizing novel nanomaterials, characterizing the as-synthesized materials and fabrication of the electrodes, and assembling the lithium-ion battery in glove box. Shahul had carried out his research independently.

Shahul received several awards for this work. He obtained travel grant to attend Asian Crystallography Association (AsCA) to attend AsCA'13 conference in Hong Kong in 2013. He was awarded "Rising Star Award" at the same conference for his presentation. He also won the Best Poster Award at the 8th Singapore International Chemistry Conference (SICC-8) in December 2014. Shahul also obtained travel grant from the department to attend the International School on "Materials for Renewable Energy" in Erice, Italy, in 2014.

Shahul published 8 international papers from his research work, one submitted for publication and one more to be written for publication. Li-ion batteries (LIBs) are considered as one of the best available technologies for the production of eco-friendly electric vehicles (EVs). High cost of LIBs is mainly responsible for commercialization of the LIBs in conventional vehicles. Shahul tried to address this to produce cheaper high-performance cathode materials for LIBs; an rGO/MOPOF (reduced graphene oxide/Metal Organophosphate Open Framework) nanocomposite with $\sim$4 V of operation has been developed by a cost-effective room

temperature synthesis that eliminates any expensive post-synthetic treatments at high temperature under Ar/Ar-H_2. Enhanced lithium cycling has been witnessed with rGO/MOPOF nanocomposite which exhibits minimal capacity fading thanks to increased electronic conductivity and enhanced Li diffusivity. This work has the potential for commercialization due to cheap and easy synthesis of the cathode materials (*Scientific Reports*, 2015). Shahul showed how to improve good reversible capacity and better capacity retention of $ZnFe_2O_4$ material by Mg(II) and Cu (II) doping using solgel-assisted combustion method. The reversible capacity of the samples was improved by annealing at higher temperature. However, there is still capacity fading during the initial few cycles which can be minimized with the help of carbon coating or by preparing graphene-$Mg_{0.2}Cu_{0.2}Zn_{0.62}Fe_{1.98}O_4$ composites (*ACS Applied Materials & Interfaces*, 2015). Newer synthetic methods are also very important in material synthesis as the performance depends on the synthetic methods and easy access to large amount of materials in pure phase. Shahul discovered a new method of synthesizing $Li_3V_2(PO_4)_3$ by thermal decomposition of another cathode material $Li_2(VO)_2(HPO_4)_2(C_2O_4)\cdot 6H_2O$. Carbon coating of $Li_3V_2(PO_4)_3$ has also achieved by mixing the precursor with sucrose and subsequent decomposition in argon atmosphere to improve its performance (*Electrochimica Acta*, 2014).

Shahul synthesized a new lithium containing hybrid inorganic-organic open framework material, $Li_2(VO)_2(HPO_4)_2(C_2O_4)\cdot 6H_2O$, which was difficult to achieve before in our laboratory. The presence of extractable lithium ions in the inter-layer space together with the feasibility of $V^{4+/5+}$ redox couple make this compound suitable for cathode applications in 4-V Li-ion batteries. The material exhibits excellent reversible lithium insertion/extraction during cycling (*J. Mater. Chem.*, 2013). The higher redox potential ($\sim$4 V) of $LiVOPO_4$ blended with its good theoretical capacity of 166 mA h g^{-1} makes its energy density higher than $LiFePO_4$ and projects to be a potential high-voltage cathode material for LIBs. So far, research has mainly been focused on studying the performance of two well-known phases of $LiVOPO_4$, namely the triclinic α-$LiVOPO_4$ and the orthorhombic β-$LiVOPO_4$. In addition to these phases, a new phase α_I-$LiVOPO_4$ was observed during lithium insertion of α_I- and α_{II}-$VOPO_4$. Theoretical studies on this phase has shown the possibility of a 2D lithium ion migration and expected to exhibit a better lithium storage performance than α and β phases. However, a detailed electrochemical study of this phase is still lacking. Shahul discovered a convenient method to synthesize $LiVOPO_4\cdot 2H_2O$ in bulk. He was able to achieve a direct chemical synthesis of the tetragonal α_I-$LiVOPO_4$ by an easier and a cost-effective route. Electrochemical studies reveal that α_I-$LiVOPO_4$ exhibits highly reversible lithium insertion and extraction with a negligible capacity fading during cycling (*J. Mater. Chem.*, 2012). Overall, Shahul focussed on the vanadium phosphates, a battery material in his Ph.D. thesis. His Ph.D. work generated lots of attention and interest among the battery community which you may realize while reading his thesis.

Singapore
June 2016

Prof. J.J. Vittal

Parts of this thesis have been published in the following journal articles:

A. Shahul Hameed, M. V. Reddy, Jeremiah L. T. Chen, B. V. R. Chowdari and Jagadese J. Vittal, *"RGO/Stibnite Nanocomposite as a Dual Anode for Lithium and Sodium Ion Batteries"*, ACS Sustainable Chem. Eng., 2016, 4, 2479–2486.

A. Shahul Hameed, M. V. Reddy, M. Nagarathinam, Tomče Runčevski, Robert E Dinnebier, Stefan Adams, B. V. R. Chowdari and Jagadese J. Vittal, *"Room temperature large-scale synthesis of layered frameworks as low-cost 4 V cathode materials for lithium ion batteries"*, Sci. Rep., 2015, 5, 16270.

A. Shahul Hameed, M. V. Reddy, B. V. R. Chowdari and Jagadese J. Vittal, *"Preparation of rGO-wrapped magnetite nanocomposites and their energy storage properties",* RSC Adv., 2014, 4, 64142–64150.

A. Shahul Hameed, M. V. Reddy, B. V. R. Chowdari and Jagadese J. Vittal, *"Carbon coated $Li_3V_2(PO_4)_3$ from the single-source precursor, $Li_2(VO)_2(HPO_4)_2(C_2O_4)\cdot 6H_2O$ as cathode and anode materials for Lithium ion batteries",* Electrochim. Acta, 2014, 128, 184–191.

A. Shahul Hameed, M. Nagarathinam, Martin Schreyer, M. V. Reddy, B. V. R. Chowdari and Jagadese J. Vittal, *"A layered oxalatophosphate framework as a cathode material for Li-ion batteries"*, J. Mater. Chem. A, 2013, 1, 5721–5726.

A. Shahul Hameed, M. Nagarathinam, M. V. Reddy, B. V. R. Chowdari and Jagadese J. Vittal, *"Synthesis and electrochemical studies of layer-structured metastable α_I-$LiVOPO_4$"*, J. Mater. Chem., 2012, **22**, 7206–7213.

Contents

Chapter 1
Introduction to Li-ion Batteries

Abstract This chapter highlights the importance and principle of Lithium ion batteries (LIBs) along with a concise literature survey highlighting the research trend on the different components of LIBs namely, cathode, anode and electrolyte. The aims of the present study and the thesis outline are given at the end of the chapter.

1.1 Introduction

Ever-growing population, modernization and the betterment of human lifestyle has culminated in burgeoning usage of fossil fuels like coal, petroleum and natural gas to meet the high energy demands. This has resulted in the depletion of the fossil fuel deposits coupled with alarming increase in the levels of green-house gases leading to global warming. In addition to tackling the problems of global warming, every country is looking forward to improve their energy security. Owing to these reasons, the focus of energy research has shifted from conventional fossil fuel technology to renewable energy (clean energy) technology such as solar, wind, tidal, biomass and geothermal energy. Though the energy available from these sources are enormous and sustainable, it cannot be harnessed continuously. For non-intermittent and proper utilization of these sources, we need energy storage devices such as batteries and supercapacitors. Therefore the research and development in the conversion of renewable energy and the energy storage should go hand in hand for a fruitful future.

Among the various available energy storage systems, LIBs have been proved to be the best owing to their compactness, light weight, long cycle life, environment friendliness, flexibility in design and high operating voltages ($\sim$4 V) with high energy densities up to 250 Wh/kg [1]. LIBs are currently used in a variety of portable electronic devices such as mobile phones, tablets, laptops, digital cameras, etc. In addition, LIBs have been looked at attentively as the potential candidate to harness the various renewable energy for utilization in the transportation sector such as Hybrid Electric Vehicles (HEVs), Plug-in Hybrid Electric Vehicles (PHEVs) [2]. In addition, low cost batteries are needed for large scale energy storage in electric grids.

A.S. Hameed, *Phosphate Based Cathodes and Reduced Graphene Oxide Composite Anodes for Energy Storage Applications*,
Springer Theses, DOI 10.1007/978-981-10-2302-6_1

Despite the commercial success of LIBs over the past two decades, they are still the subject of intense research. Commercial LIBs mainly use $LiCoO_2$ as the cathode material and graphite as the anode material. The high cost, toxicity and low structural stability of $LiCoO_2$ during lithium cycling, demands the need for alternate cathode materials. The commercial anode, graphite has many advantages like abundance, low cost, longer cycle life and environmental friendliness. However, it has low specific capacity of 372 mAh g^{-1}. In addition, it poses safety concerns, as the Li metal deposition on the graphite during charging of batteries gives rise to dendrite formation which can penetrate the microporous separator resulting in short-circuiting of the battery. Owing to these reasons, alternate safer anode materials are being investigated which also possess better theoretical capacity compared to graphite.

For large scale utilization of LIBs for grid storage and transportation, various improvements in the technology are obligatory which encompass the identification and optimization of novel electrode materials which are safer and cheaper with good cycle life. In this perspective, this thesis aims at the synthesis and investigation of electrochemical properties of some vanadium containing phosphate based materials such as $LiVOPO_4$, $A_2(VO)_2(HPO_4)_2(C_2O_4)$ (where A = Li and K) and $Li_3V_2(PO_4)_3$ for potential application as 4 V cathodes in LIBs. In addition, rGO composites of Fe_3O_4 and Sb_2S_3 have been investigated for anode application in LIBs. The following sections of this chapter deal with a brief introduction to LIB concepts with a concise literature review on various cathode, anode and electrolyte materials.

1.2 Definition and Classification of Batteries

An electrical battery is a device that converts chemical energy contained in its chemical component directly into electrical energy. A battery is a pile of one or more electrochemical cells that are connected in parallel or series to deliver the required voltage and power. Each cell consists of three main components, namely, cathode, anode and electrolyte. The working principle of a battery relies on the redox (oxidation-reduction) reaction occurring in the active material. The electrons generated during the redox reactions are utilized to do external work.

During the usage of a battery, the negative electrode or the anode, witnesses the oxidation of its active material giving away electrons. These electrons pass from the anode through the external circuit to the cathode or positive electrode where its active material gets reduced. The electrolyte shuttles the charge carriers between the cathode and anode during the redox reaction. It should be an electronic insulator to prevent the direct shuttling of electrons between the cathode and the anode. In some cases, the redox reaction occurring in the two electrodes can be reversible by supplying external energy and thus the active materials return to original state which enables the reaction to occur repeatedly. Depending on whether the redox reactions are reversible or not, the batteries are classified in two types namely, primary (disposable) and secondary (rechargeable) batteries [3].

1.2.1 Primary Batteries

Primary batteries are a class of batteries in which the electrochemical reactions of the active materials are not reversible and hence they are designed to use for a single discharge and discarded. These batteries are usually cheap and easy to handle. They are commonly used for low-power drain applications such as watches, alarms, calculators, torch lights, etc. They are also called as disposable batteries as the active materials are less toxic and are easily disposable. The well-known commercially available primary batteries include zinc-carbon batteries and alkaline (e.g. Zn/MnO_2) batteries.

1.2.2 Secondary Batteries

Secondary batteries or rechargeable batteries are those in which the active materials can be renewed to its original form after the first discharge and hence available for further use. The redox reactions can be repeated several times and hence they are advantageous over the primary batteries. These rechargeable batteries are used in a wide range of applications in our daily life mainly due to their high specific energy, longer cycle life, low cost, lesser impact on environment. The rechargeable batteries, also called as accumulators or storage batteries come in different shapes and sizes. The common rechargeable batteries available in the market include Lead-Acid, Nickel-Cadmium (Ni-Cd), Nickel-Metal hydride (Ni-MH) and Lithium ion batteries (LIBs).

1.2.3 Comparison of Secondary Batteries

Lead-acid battery is the oldest rechargeable battery technology, dated back to 1859. The low cost and high surge current of the lead-acid batteries make them suitable for motor vehicles for providing high current required by automobile starter motors. Though they have low energy density and limited cycle life, they are still used to provide continuous power supply in other important applications such as cell phone towers, hospital equipment and in marine applications. Ni-Cd batteries have relatively better energy density and low internal resistance than the lead-acid batteries. They were popular for use in small devices like cordless and wireless telephones, emergency lighting, aircraft batteries, etc. However, they suffered from many problems like memory effect and the use of toxic cadmium metal which resulted in the loss of market to Ni-MH batteries and LIBs. Ni-MH batteries are similar to Ni-Cd batteries in operation. However, increase in the capacity by 2–3 times and the non-usage of toxic metals like cadmium helped them to replace Ni-Cd batteries. They are used for many applications, notably as small rechargeable batteries (AA type).

Though LIBs emerged almost the same time as Ni-MH batteries, they outperformed the latter owing to various advantages. Some of the salient features of LIBs include:

- Higher energy density (Light-weight and Compactness)
- Design flexibility
- No memory effect
- Longer cycle life
- Negligible self-discharge
- Less toxicity
- Low maintenance cost.

Figure 1.1 compares the energy densities of different secondary batteries such as Lead-Acid, Nickel-Cadmium, Nickel-Metal hydride and Lithium ion batteries. The smallest size and low atomic weight of Li enables the highest volumetric and gravimetric energy densities of LIBs [1]. Due to the various advantages of LIBs, they occupy about 70 % market share in secondary batteries.

1.3 Principle of Operation of LIBs

Like any type of battery, LIBs have three main components; cathode, anode and electrolyte. The basic principle of operation of LIBs is presented in Fig. 1.2. The cathode material in commercial LIBs is a layered oxide, $LiCoO_2$ while graphite is the widely used anode material. The Li^+ ions present in the cathode material are to be removed first from $LiCoO_2$ and transferred to the anode by applying energy to initiate the electrochemical process. This is called as initial charging of the battery. During this charge cycle, Li^+ ions are de-intercalated from $LiCoO_2$ which travels to the graphite anode through the electrolyte. The electrons released from the oxidation of transition metal (Co^{3+} to Co^{4+}) migrate to the anode through an external circuit. The anode receives the Li^+ ions and electrons, resulting in the intercalation

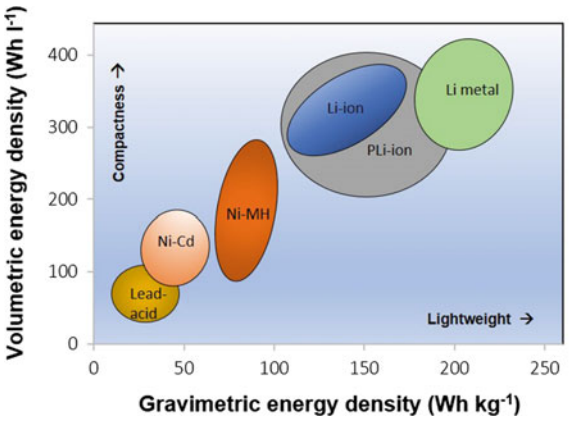

Fig. 1.1 Comparison of gravimetric and volumetric energy densities of various secondary batteries

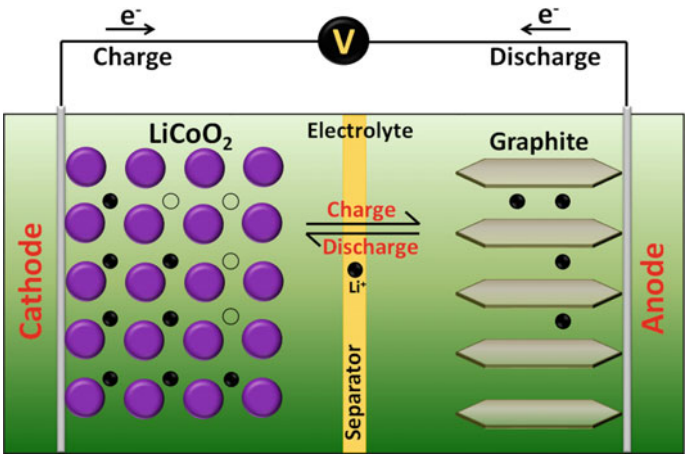

Fig. 1.2 Principle of operation of Lithium ion batteries. *Full black circles* and *hollow circles* represent the Li^+ ions and vacant Li sites respectively

of graphite (LiC_6). In this way, electric energy can be stored as chemical energy in the battery. The reactions involved during the charge cycle are depicted in Eqs. 1.1–1.3.

$$\text{Cathode:} \quad LiCoO_2 \rightarrow Li_{1-x}CoO_2 + xLi^+ + xe^- \tag{1.1}$$

$$\text{Anode:} \quad C_6 + xLi^+ + xe^- \rightarrow Li_xC_6 \tag{1.2}$$

$$\text{Overall:} \quad LiCoO_2 + C_6 \rightarrow Li_{1-x}CoO_2 + Li_xC_6 \tag{1.3}$$

During the discharge cycle, de-intercalation of the lithiated graphite (LiC_6) initiates the transfer of Li^+ ions from anode to cathode. The electrons flowing through the external circuit performs the work. The reactions involved during the discharge cycle are shown in Eqs. 1.4–1.6. As these reactions happening in the cathode and anode are reversible, LIBs can be used for a large number of cycles.

$$\text{Cathode:} \quad Li_{1-x}CoO_2 + xLi^+ + xe^- \rightarrow LiCoO_2 \tag{1.4}$$

$$\text{Anode:} \quad Li_xC_6 \rightarrow xLi^+ + xe^- + C_6 \tag{1.5}$$

$$\text{Overall:} \quad Li_{1-x}CoO_2 + Li_xC_6 \rightarrow LiCoO_2 + C_6 \tag{1.6}$$

The free energy change accompanying an electrochemical reaction in a cell is given by Eq. 1.7.

$$\Delta G^0 = -nFE^0 \tag{1.7}$$

where F is the Faraday constant (96,496 C/mol), n is number of electrons involved in the reaction, and E^0 is the standard potential of the cell. The overall potential of the cell E^0_{cell} is determined by the electrode potentials of the individual electrodes, the cathode $\left(E^0_{pos}\right)$ and the anode $\left(E^0_{neg}\right)$ as shown in Eq. 1.8.

$$E^0_{cell} = E^0_{pos} - E^0_{neg} \tag{1.8}$$

The measurable potential of the cell is given by the actual potential difference between the cathode and the anode and is related to the standard potential by Nernst equation (Eq. 1.9).

$$\Delta E = \Delta E^0 - \frac{RT}{nF} \ln \frac{a_i(A)}{a_i(C)} \tag{1.9}$$

where R is the gas constant, T is the absolute temperature and $a_i(C)$, $a_i(A)$ are the activity of the cathode and anode materials respectively.

1.4 Applications of LIBs: State of the Art and Future

LIBs are extensively used in portable electronic devices such as mobile phones, notebooks, tablets, digital cameras and camcorders. They are also used in medical applications like pace makers, defibrillators, etc. Owing to the various advantages of LIBs, they are considered as the best candidate for powering electric vehicles (EV), hybrid electric vehicles (HEV) and plug-in hybrid vehicles (PHEV), in which they either replace or complement the internal combustion (IC) engines. The electric vehicles can help in the reduction of CO_2 emission compared to normal vehicles. Hence, LIBs are subject of intense research for large scale utilization in EVs in the near future. The commercial LIBs for portable devices come in different sizes and shapes like coin cells, cylindrical, prismatic and thin type batteries. Figure 1.3 shows the illustration of a cylindrical LIB assembly in which large number of cells are connected together [4].

1.5 Research Trend on LIB Materials

The performance of a LIB mainly depends on the properties of the individual components and the way of their assembly. Thus, the materials constituting the cathode, anode and electrolyte are subject of high value. In this section, the research trend and evolution of different electrode and electrolyte materials are discussed.

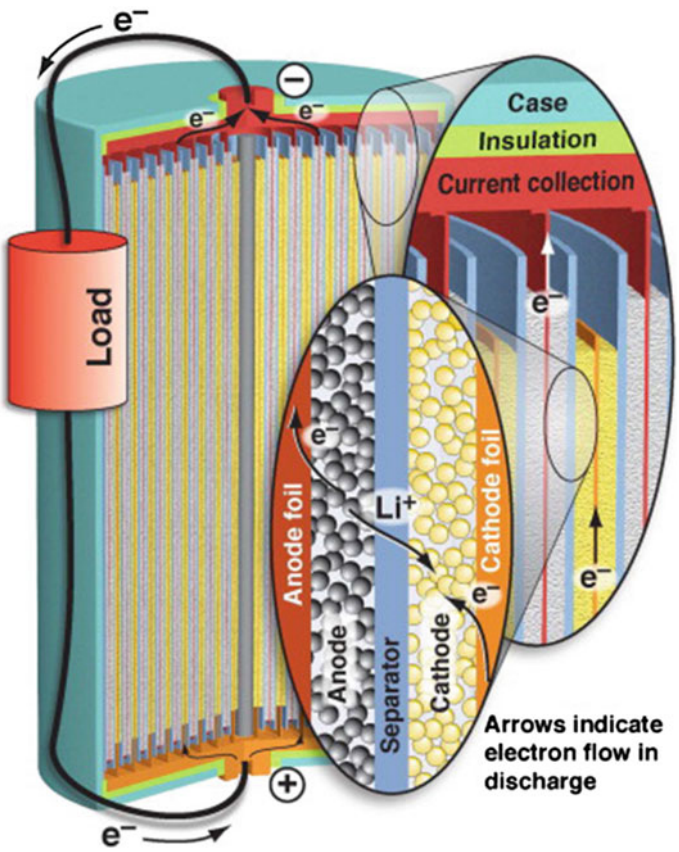

Fig. 1.3 Schematic of a cylindrical LIB assembly containing large number of electrochemical cells. Reproduced from Ref. [4] with permission of Elsevier

1.5.1 Cathode Materials

Cathode is the most important component of LIBs. The energy density of a Lithium ion cell is mainly determined by the voltage of the cathode material and hence it is of great interest to develop a good cathode material with high voltage. In addition, ~40 % of the cost of a Lithium ion cell is due to the cathode material (Fig. 1.4) and hence it highly influences the total cost of the battery [5]. Therefore, various materials have been investigated for cathode application [6].

A good cathode material should satisfy the following conditions.

- Easy and reversible reduction/oxidation of transition metal ion present in the cathode material.
- High oxidation state of the metal for maximizing the cell voltage and hence energy density.

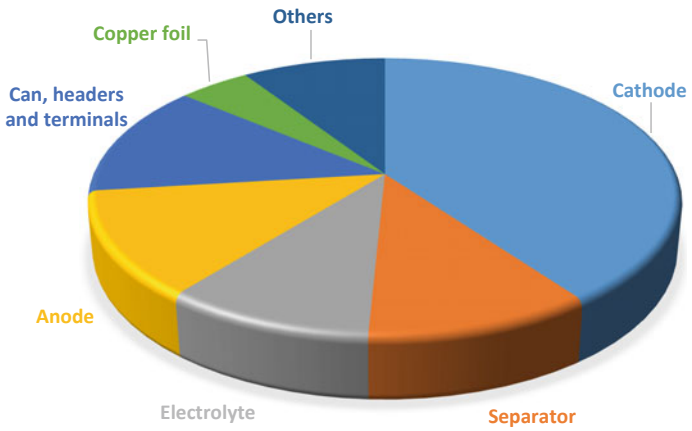

Fig. 1.4 Cost distribution of Lithium ion cells

- High structural stability of the cathode material to enhance cycle life.
- Higher lithium content per formula unit.
- Low molecular mass to achieve high theoretical specific capacity.
- Stable in the operating voltage window and should be inert with the electrolyte.
- Good ionic and electronic conductivities (mixed conductor).
- Low cost and Environmental friendliness.

The following sections review some of the important family of cathodes like the chalcogenides, layered oxides, spinel oxides and polyanion based materials.

1.5.1.1 Chalcogenides

The active research on rechargeable LIBs started with the layered chalcogenides developed for cathode applications. These chalcogenides have drawn considerable interest because of their layered structure which enables high Li^+ ion diffusivity [7]. Among the various chalcogenides, titanium disulfide (TiS_2) was found to possess then best structural stability during reversible lithium intercalation/de-intercalation [8]. It was the lightest semimetal and the cheapest electrode material available that time. In addition, existence of solid solution over the entire composition, as Li_xTiS_2 ($0 \leq x \leq 1$) eliminates the additional energy required for nucleation of the lithiated phase. Thus the single phase reaction and the absence of structural rearrangement during the reaction, helps in a reversible and efficient way of the lithium diffusion in this material. Figure 1.5 demonstrates the reversible lithiation of TiS_2 at a current density of 10 mA cm^{-2}. The sloping plateau indicate the single phase reaction during lithium intercalation in the material [9]. TiS_2 was demonstrated to exhibit good cycle life of >1000 cycles with minimal capacity fading. This material was later marketed by Exxon in the form of button cells for small devices such as

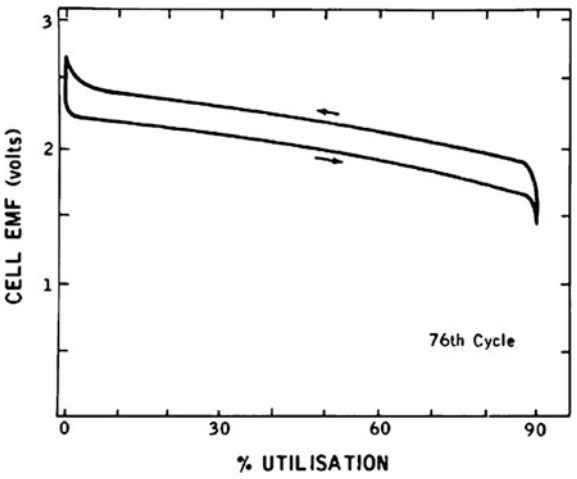

Fig. 1.5 Discharge-charge curves of Li/TiS_2 cell at 10 mA cm^{-2}. Reproduced from Ref. [9] with permission of Elsevier

watches in 1977–1979. However, the relatively low voltage of ~2 V made it less preferable as a cathode with the advent of oxide cathodes which exhibits higher voltage and hence higher energy density.

Another successful lithium intercalation host from the family of chalcogenides was vanadium diselenide (VSe_2) which can take up to two Li^+ ions per formula unit, forming Li_2VSe_2 via two bi-phasic reactions. The two-phase behaviour of VSe_2 were found to have less effect on the reversibility of lithium intercalation as the resulting intercalated phases does not differ much from the structure of VSe_2 [10]. Various other di and trichalcogenides exhibiting a similar single-phase lithium insertion like TiS_2 were investigated by Whittingham [11, 12]. However, the practical applications of these materials as cathodes are generally limited by their low output voltages.

1.5.1.2 Layered Oxides, $LiMO_2$

Lithium cobalt oxide, $LiCoO_2$, was introduced in 1980 as another lithium intercalation cathode from the group of Goodenough [13]. The compound is the most successful cathode material as it is still serving as the cathode material in most of the commercial LIBs. This layered oxide has a rhombohedral structure with Li^+ ions present in the octahedral sites of a distorted cubic-close-packed (ccp) oxygen ion lattice (Fig. 1.6) [14, 15]. The layered framework facilitates a two dimensional Li^+ ion diffusion. Removal of the entire lithium from the material to CoO_2 can result in a theoretical capacity of about 274 mAh g^{-1}. However, the structural instability of the de-lithiated phase, Li_xCoO_2 (at $x < 0.5$) leads to serious capacity fading [16]. However, when only ~0.5 mol of lithium is extracted, very stable capacity of 120–140 mAh g^{-1} can be achieved with negligible capacity fading. Sony announced the first successful commercialization of $LiCoO_2$ using carbon as

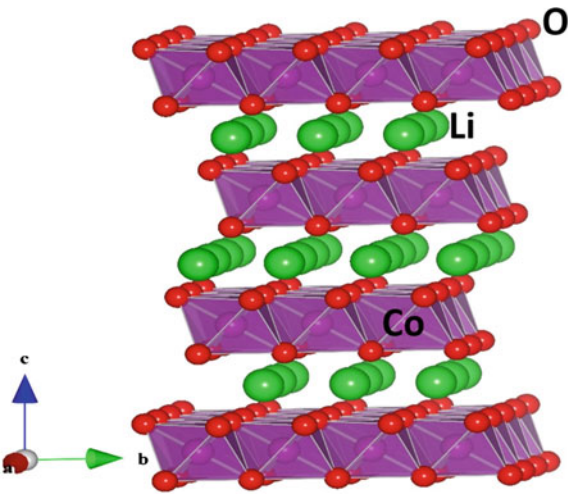

Fig. 1.6 Crystal structure of a layered cathode material, $LiCoO_2$

anode [17]. This material has an advantage of high Li diffusion coefficient (5×10^{-9} cm^2 s^{-1}), thanks to the layered structure. This helps the material to cycle at high current density of 10 mA cm^{-2} and voltage of 4 V [9]. On the other hand, the electronic conductivity varies with its lithium content. At x = 1.1, it behaves as a semiconductor while at x = 0.6, it exhibits metallic behaviour, thus acting as a mixed conductor. Improvement in capacity of the material can be achieved only by stabilization of the structure at low Li content in Li_xCoO_2. Therefore, various attempts such as surface coating of $LiCoO_2$ with different materials like SnO_2 [18], Al_2O_3 [19, 20], MgO [21] and metal phosphates [22, 23] have been adopted to achieve better structural stability. Alumina coated samples exhibits excellent capacity retention owing to the formation of $LiCo_{1-x}Al_xO_2$ which improved the structural stability of $LiCoO_2$ during lithium cycling [24–26]. In addition to the surface coating of $LiCoO_2$ particles, doping of the Co site with other transition metals like Mn, Ni or Al were taken up to improve the cycling stability.

The nickel containing layered oxide, $LiNiO_2$ has a layered structure similar to $LiCoO_2$. Its theoretical capacity of 274 mAh g^{-1} is same as the cobalt counterpart. It has various advantages of being less expensive, less toxic and abundant compared to $LiCoO_2$ [27–29]. However, usage of pure $LiNiO_2$ as a cathode material is hindered by various reasons. Firstly, the stoichiometric excess of nickel ($Li_{1-y}Ni_{1+y}O_2$), is observed in most of the reports. The excess Ni^{2+} ions present in between the NiO_2 layers, hold the layers together and hinders the flow of Li^+ ions, which in turn reduces the electrochemical properties of the material. Secondly, the charged state, $Li_{1-x}NiO_2$ has less thermal stability in contact with the organic solvents and can be dangerous [30]. In addition, the working potential of $LiNiO_2$ is slightly lower ($\sim$3.8 V) than $LiCoO_2$. However, the higher diffusion coefficient of the Li^+ ions (6×10^{-6} cm^2 s^{-1}) than the $LiCoO_2$ is advantageous. Hence various doped compounds were studied for optimizing the properties. Of

these notable compositions are $Li(Ni_{1-x}Mn_x)O_2$, $Li(Ni_{1/3}Mn_{1/3}Co_{1/3})O_2$ called as NMC and $Li(Ni_{1-x-y}Co_xAl_y)O_2$ called as NCA cathodes [31–37]. The low cost, higher energy and power and improved safety of these doped compounds made them commercial success.

1.5.1.3 Spinel Oxide ($LiMn_2O_4$)

Spinel $LiMn_2O_4$ is one of the promising cathode materials for LIBs. Unlike cobalt and nickel which forms the layered oxides of type $LiMO_2$, manganese preferably crystallize in the spinel structured oxide, $LiMn_2O_4$ (Fig. 1.7). It is a three dimensional lithium host in which the Li^+ ions occupy the tetrahedral sites while the $Mn^{3+/4+}$ ions occupy the octahedral sites in a cubic close-packed (ccp) oxygen lattice [15]. Proposed by Thackeray et al., it is a good host for Li storage owing to the reversible extraction of the Li^+ ions without collapsing the three-dimensional M_2O_4 spinel framework [38]. It also has advantages of low cost, abundance, better thermal stability than the layered oxides and environmental friendliness. The ionic and electronic conductivities of $LiMn_2O_4$ is better, of the order of 10^{-6} and 10^{-4} S cm^{-1} [39]. It has a theoretical capacity of 148 mAh g^{-1} and a high voltage of operation, $\sim$4 V. However, practically only 100–130 mAh g^{-1} can be achieved. The lithium insertion/removal occurs in two steps via two bi-phasic reactions with the formation of a stable phase, $Li_{0.5}Mn_2O_4$ due to the ordering of the Li^+ ions at the tetrahedral sites. In addition, it undergoes another lithium intercalation reaction at $\sim$3 V. However, it is not reversible due to asymmetric lattice distortion during lithiation/delithiation. This is mainly caused by the Jahn-Teller distortions of Mn^{3+} ions which leads to phase transformation from cubic to tetragonal phase. Thus only one Li can be reversibly stored in the material.

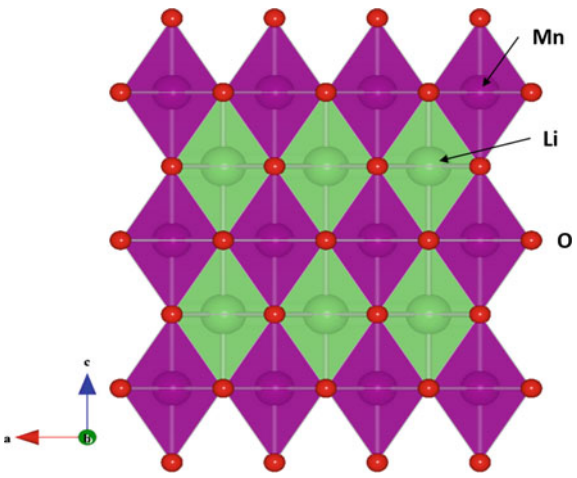

Fig. 1.7 Crystal structure of spinel cathode material, $LiMn_2O_4$

Despite of the above mentioned advantages of $LiMn_2O_4$, its wide-spread application in LIBs is limited, as capacity of $\sim$120 mAh g^{-1} can be practically achieved. In addition, severe capacity fading has been observed during lithium cycling, especially at elevated temperatures of >60 °C. Surface dissolution of manganese in the electrolyte has been demonstrated as the main reason for this capacity fading. The surface dissolution occurs via the disproportionation of Mn^{3+} ions ($2\ Mn^{3+} \rightarrow Mn^{2+} + Mn^{4+}$) and the resulting Mn^{2+} ions diffuse to the anode and get reduced to manganese metal. To achieve better cycling stability in this material, different approaches have been attempted to prevent the dissolution of Mn in the electrolyte. This include doping of Mn with other cations [22, 40, 41]. Even though, the specific capacity of the substituted spinels is slightly lesser than the virgin $LiMn_2O_4$, lithium cycling was found to be greatly enhanced by doping. Another effective way to achieve good stability is by preventing the surface contact of $LiMn_2O_4$ with electrolyte by coating the particles with inert materials such as Al_2O_3, $AlPO_4$, AlF_3, ZrO_2, and SiO_2 or by substitution of $LiPF_6$ by other electrolytes [42–45]. Though the coating of these materials act as a protective layer, resistance may increase when thickness of the coating is too large, resulting in the deterioration of electrochemical performance. Hence coating with electrically conducting compounds have also been reported with better performance [46]. With the enhancement in the capacity and prevention of Mn dissolution large scale commercialization of $LiMn_2O_4$ has been possible.

1.5.1.4 Polyanion Based Cathodes

As described earlier, the commercial cathode material, $LiCoO_2$ suffers from serious problems such as high toxicity, high cost and structural instability when over-charged. To address these drawbacks, Manthiram and Goodenough introduced the concept of lithium intercalation in polyanion based materials, $Fe_2(XO_4)_3$; where X = Mo and W. The covalently bonded polyanion hosts possess decreased redox energies because of inductive effect, which in turn increase the cell voltage compared to the respective oxides. In addition, the polyanion materials exhibit better structural stability which gained popularity for use as LIB cathodes. This motivated the introduction of various polyanion based cathodes like phosphates, silicates, borates and sulphates, etc. [47], which are described in the following sections.

1.5.1.5 Olivine Phosphates

Padhi et al. demonstrated the successful lithium storage in an olivine structured phosphate, $LiFePO_4$ [48]. In this material, the frameworks made of polyanion phosphate units provide a highly stable three dimensional network owing to strong covalent nature of P-O bonds [49]. This eliminates the possibility of oxygen liberation and hence improves the operational safety of batteries. In addition, $LiFePO_4$ has better theoretical capacity of 170 mAh g^{-1} and has other advantages like

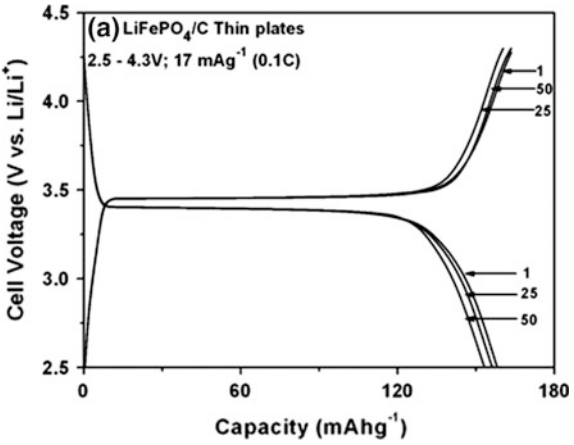

Fig. 1.8 Discharge-charge curves of $LiFePO_4$ nanoplates in the voltage range; 2.5–4.3 V. Reproduced from Ref. [57] with permission of the Royal Society of Chemistry

environmental friendliness, low cost, less toxicity and very flat potential. Despite the above mentioned advantages, $LiFePO_4$ has two serious problems such as poor electronic and ionic conductivities [50]. This limits the practical capacity and rate capability of the material. Therefore, various approaches have been made to improve the ionic conductivity [51, 52]. Synthesis of nano-sized $LiFePO_4$ particles resulted in the improvement of lithium diffusion due to shorter path length [53–56]. The time taken for lithium diffusion is given by $t = L^2/D$, where L is the diffusion length and D is the diffusion coefficient. Thus decrease in particle size leads to easier diffusion. As the lithium diffusion in $LiFePO_4$ occurs along the *b*-axis, nanoplates with shortest distance along *b*-axis can lead to tremendous improvement in lithium diffusion kinetics [57, 58]. In addition, the electronic conductivity of $LiFePO_4$ was found to improve by carbon coating [56, 59, 60]. Figure 1.8 shows the charge-discharge profile of $LiFePO_4$ hierarchical nanoplates prepared by solvothermal synthesis. The effect of particle size on the battery performance was found to be higher than carbon coating [61].

Though better electronic and ionic conductivities can be achieved as mentioned above, the material's low operating voltage of 3.4 V makes the overall energy density low (580 Wh kg^{-1}). This limits the large scale utilization of $LiFePO_4$ in commercial LIBs. Hence, other phosphates such as $LiMPO_4$; (M = Mn, Co and VO), $Li_3M_2(PO_4)_3$, (M = Mn, Fe and V) etc., have attracted researchers owing to higher voltage and hence higher energy density.

Another olivine phosphate, $LiMnPO_4$ is considered as an excellent candidate for stable and high energy density cathodes [62]. This material can provide higher operational voltage (4.1 V) than $LiFePO_4$ and exhibits a similar capacity. Hence it can provide a superior theoretical energy density of $\sim$700 Wh kg^{-1}. However, low ionic and electronic conductivities [63], Jahn-Teller distortion of the charged phase ($MnPO_4$), and huge volumetric change ($\sim$10 %) during Li intercalation/deintercalation make it unsuitable as a good cathode material. However, different approaches were followed to achieve tremendous improvement in the electrochemical properties of the material [62, 64–67].

$LiVOPO_4$

As mentioned in the previous section, $LiVOPO_4$ has a higher redox couple of $\sim$4 V along with a good theoretical capacity of 166 mAh g^{-1}, making its energy density ($\sim$650 Wh kg^{-1}) higher than that of $LiFePO_4$. Thus, it is considered as an alternate prospective cathode material for LIBs. It exists mainly as two crystal modifications, namely, α- and β-$LiVOPO_4$, depending on the spatial arrangement of VO_6 octahedra and PO_4 tetrahedra. The α-$LiVOPO_4$ was first synthesized by Lavrov et al. [68] which exhibits a monoclinic crystal structure ($P\,\overline{1}$ space group), while the β-$LiVOPO_4$ first synthesized by Lii et al. [69] exhibits a triclinic structure (Space group: *P*nma).

The first electrochemical study on $LiVOPO_4$ was due to Gaubicher et al. [70]. He demonstrated the lithiation in β-$VOPO_4$ phase and it was undergoing reversible phase transformation to β-$LiVOPO_4$ upon lithium intake. A reversible capacity of 90 mAh g^{-1} was observed at a current rate of 0.05 C. Later, Kerr et al. [71] showed the formation of α-$LiVOPO_4$ when ε-$VOPO_4$ was subjected to reversible lithiation. At a cycling rate of 0.1 C, specific capacity of over 100 mAh g^{-1} was observed that was stable for at least 100 cycles. Subsequent attempts were made to synthesize the lithiated phase directly as it could exhibit better storage performance than $VOPO_4$. Till now, $LiVOPO_4$ has been synthesized employing high temperature ceramic routes, hydrothermal/solvothermal method, sol-gel route, etc. [72–81]. However, the electrochemical properties of the material was found to be unimpressive owing to the poor lithium diffusion kinetics and low electronic conductivity. Recently, Tang et al. [82] prepared carbon coated α-$LiVOPO_4$ by sol-gel route which showed better capacity of 138 mAh g^{-1} due to carbon coating. However, it has still been a challenge to achieve the theoretical capacity and good rate performance for both the systems.

In addition to these phases, a metastable phase of $LiVOPO_4$ designated as α_I-$LiVOPO_4$ (tetragonal crystal structure) was observed by Dupre et al., during lithium insertion into α_I- α_{II}-polymorphs of $VOPO_4$ [83, 84]. It exhibits a layered structure with $VOPO_4$ layers made of VO_5 and PO_4 polyhedra and the Li^+ ions are present in the inter-layer space. The lithium storage in this phase by Dupre et al., was not satisfactory. However, the theoretical studies on this phase have shown the possibility of a 2D Li^+ ion migration owing to its layered structure [84]. Hence it is expected to exhibit a better lithium storage performance than the α- and β-phases due to improved lithium diffusion kinetics. However, a detailed electrochemical study of this phase is still lacking. More research is required to enhance the material's electrochemical performance.

$Li_3M_2(PO_4)_3$

$Li_3M_2(PO_4)_3$; where M = Fe, V is another attractive class of cathode materials having NASICON type framework. $Li_3Fe_2(PO_4)_3$ can reversibly cycle only two Li^+

ions which limits its theoretical capacity to 128 mAh g^{-1} [85–87]. However, the possibility of V^{3+} to V^{5+} redox couple in $Li_3V_2(PO_4)_3$ can result in the reversible utilization of 3 Li^+ ions, corresponding to a higher theoretical capacity of 197 mAh g^{-1}. This higher capacity and higher working potential of $Li_3V_2(PO_4)_3$ can lead to higher energy density than $LiFePO_4$. In addition, it has better structural stability and better ionic conductivity owing to the three dimensional Li^+ ion migration in the material [88]. Despite having such advantages, separated VO_6 octahedra in this compound make the electronic conductivity very low which affects the rate capability. Carbon coating has been found as the effective and cheaper way to achieve electronic conductivity [89, 90]. Better electrochemical properties can also be achieved by nanoparticle synthesis [91, 92] via suitable route or doping with other atoms [93–95]. In $Li_3V_2(PO_4)_3$ only two Li ions can be reversibly extracted when cycled in the voltage window of 3.0–4.3 V, which gives a theoretical capacity of 133 mAh g^{-1}, while the extraction of three Li ions completely when charged to 4.8 V gives a capacity of 197 mAh g^{-1}. In addition, high rate capability of the material can be achieved for the carbon coated nanomaterials for 2 Li^- utilization. However, the overall capacity is slightly lower than $LiFePO_4$. When all the three Li is extracted, it leads to capacity fading. Thus, if stability of the material can be improved for the third Li removal, its high capacity and high voltage can help to achieve better energy density than the olivine phosphate.

Silicates

Transition metal silicates are another interesting class of polyanion cathode materials for LIBs [96–98]. These silicates, Li_2MSiO_4; where M = Fe, Mn and Co has very good lithium diffusion properties as they fall in the family of LISICONs (LIthium Super Ionic CONductors) [99, 100]. Since the silicate has one negative charge more than the phosphate anion, they can intercalate reversibly more than one mole of lithium per transition metal and hence they can provide higher energy density. Among them, Li_2FeSiO_4 is the most investigated system owing to its abundance, low cost and environmentally friendliness. Considering the utilization of one Li per mole of the silicate, its theoretical capacity is calculated to 165 mAh g^{-1} which is similar to that of $LiFePO_4$ [101–104]. However, the lithium intercalation occurs at a relatively low voltage of 2.8 V resulting in low energy density of $\sim$460 Wh kg^{-1}.

Other silicates like Li_2MnSiO_4, Li_2CoSiO_4 can allow utilization of 2 Li ions per mole due to the possibility of oxidation of Mn^{2+} to Mn^{4+} and Co^{2+} to Co^{4+} [105, 106]. This results in high capacity of 330 mAh g^{-1} and hence high energy density. The existence of Mn^{4+} in the charge state was proved by Kuezma et al. from the in-situ XPS analysis indicating that 2 Li^+ ions can be extracted from the material [107]. However, the capacity fading was too high. Kokalj et al. demonstrated the deterioration of the crystal structure with the help of XRD, solid-state NMR and TEM, when all the Li are extracted [108]. Another major problem with these materials is their inferior conductivity ($<10^{-13}$ S cm^{-1}). Thus better lithium storage

Table 1.1 Comparison of different commercial cathode materials

Cathode material	Capacity (Ah kg^{-1})	Voltage (V)	Energy density (Wh kg^{-1})	Raw material cost	Safety	Life span (cycles)
$LiCoO_2$ (LCO)	~140	3.7	~520	High	Low	500–1000
$LiMn_2O_4$ (LMO)	130–140	3.8	500–520	Moderate	Moderate	500–1000
$Li(NiMnCo)O_2$ (NMC)	>200	3.8	~720	High	Moderate	1000–2000
$LiFePO_4$ (LFP)	~150	3.3	~500	Low	Excellent	1000–2000

in these materials can be achieved by improvement in the electronic conductivity and stabilization of Mn^{4+} state. The properties of various commercially viable cathode materials are shown in Table 1.1.

1.5.2 Anode Materials

Commercial LIBs mainly use graphite or mesocarbon microbeads (MCMB) as the anode material. Although they have several advantages and widely used in many portable electronic devices, lithium deposition on this material at high current rates leads to safety problem. The electric vehicle application needs an improved LIB technology, in terms of safety, cost and energy density. In this context, various prospective materials are being investigated to develop a better anode to replace graphite as commercial LIBs [22, 109–113]. Based on their mode of reactivity with lithium, they can be classified into the following types.

- Anodes based on intercalation/de-intercalation mechanism
- Anodes undergoing alloying/de-alloying reaction
- Conversion reaction based anodes
- Conversion and alloying reaction based anodes.

The important requirements for a good anode material are as follows:

- Low chemical potential (μ) to enhance the overall cell voltage and its energy density
- High specific capacity
- Low structural changes during lithium insertion/extraction
- Chemical stability and inertness with electrolyte
- Good electronic conductivity and lithium intercalation kinetics
- Small particle size to enhance the lithium transport properties
- Low cost and environmentally benign.

1.5.2.1 Intercalation Based Anodes

Anode materials working on this mechanism undergo reversible insertion and extraction of Li^+ ions into the host lattice without destroying crystal structure of the host material. The important criteria for the material to intercalate Li is the availability of empty sites in the host lattice in the form of one-dimensional (1D) channels or 2D inter-layer space. Graphite is one of the layered material which undergoes lithium storage by this mechanism. Various other materials undergoing this mechanism have been studied. The additional criteria which the host compound should fulfill for this mechanism is the presence of a transition metal or a rare earth metal which exhibits more than one stable oxidation states. This is because Li intercalation should be accompanied by reduction of transition metal to maintain electro-neutrality. Other than graphite, the most important anode materials based on this mechanism are TiO_2 and $Li_4Ti_5O_{12}$.

Graphite

Graphite is the most extensively studied anode material for LIBs. It provides a suitable layered structure for Li-intercalation to achieve reversible lithium storage [114, 115]. Proposed by Armand et al. [116] the lithium insertion between the carbon layers leads to the formation of Li intercalated graphite (LiC_6) at a very low voltage, which make it a suitable material for the negative electrode application [117–119]. Intercalation in graphite is referred as topotactic reaction which means that the insertion results in an increase in the inter-layer distance. However, the atomic arrangement in each layer remains intact [120]. Detailed studies were carried out to understand the mechanism of lithium intercalation [121, 122]. The Li ions were shown to sit between two adjacent graphene planes in a way to achieve the maximum composition, LiC_6. In addition, the lithium intercalation was found to occur through a staging mechanism where the intercalation occur completely into a specific layers before entering into the neighboring layers. The highly reversible lithium intercalation in graphite makes it a successful anode material used in most of the commercial LIBs.

TiO_2

Titanium dioxide (TiO_2) is an attractive anode for LIBs owing to its low cost, abundance and environment friendliness. TiO_2 exhibits 8 different polymorphs, namely, anatase, rutile, brookite, TiO_2-B (bronze), TiO_2-R (ramsdellite), TiO_2-H (hollandite), TiO_2-II (columbite) and TiO_2-III (baddeleyite), all of which contain TiO_6 octahedra. They have a good theoretical capacity of 335 mAh g^{-1} for 1 mol of Li insertion per TiO_2 (Eq. 1.10) and hence they have attracted great attention as a replacement for graphite. Among them, only rutile, anatase, brookite and TiO_2 (B) phases have been generally tested as anodes for LIBs [123–126]. It has been

demonstrated that the Li migration in bulk material is sluggish resulting in a very low capacity well below the theoretical limit. However, size reduction of the particles was found to improve the lithium storage properties than the bulk particles [126, 127]. Still, more efforts will be needed to improve the lithium storage to realize its commercialization.

$$TiO_2 + xLi^+ + xe^- \leftrightarrow Li_xTiO_2 \tag{1.10}$$

$Li_4Ti_5O_{12}$

Lithium Titanium Oxide, $Li_4Ti_5O_{12}$ (LTO) is one of the well-studied anode materials owing to its high stability, good lithium cyclability and high power [128–133]. The material can accommodate three Li per formula unit corresponding to a theoretical capacity of 175 mAh g^{-1} which is nearly half of that provided by graphite. Li insertion (discharge) of the material leads to phase separation between a new Li rich phase ($Li_7Ti_5O_{12}$) and a Li-poor phase ($Li_{4.02}Ti_5O_{12}$) and this equilibrium persists until lithiation is completed, yielding the pure Li-rich phase as per Eq. 1.11. This bi-phasic reaction results in a flat plateau with almost no hysteresis which is an advantage for the material. However, the high voltage of Li cycling at (1.5 V vs. Li/Li^+) lowers the overall output voltage of the cell, thus leading to a reduced energy density compared to graphitic anodes. Still they are pursued as anode materials because of improved safety features by the avoiding the formation of lithium dendrites at low voltage. In addition, the volume change accompanying the lithiation/delithiation was very low (0.2 %) which helps to achieve excellent cycling stability. Hence, it has been studied as anode material against different cathodes. The output voltage of cell with different cathode materials against $Li_4Ti_5O_{12}$ anode is shown in Fig. 1.9 [134]. However, development of high voltage cathodes may be coupled with this material to achieve better output voltage.

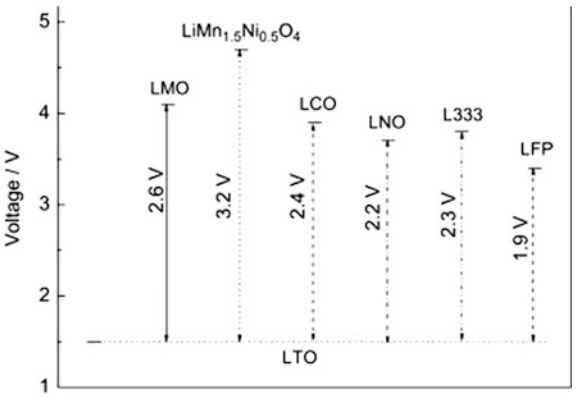

Fig. 1.9 Output voltage of LIBs with LTO anodes against different cathodes. L333 denotes $Li_{1.1}Ni_{0.3}Mn_{0.3}Co_{0.3}O_2$. Reproduced from Ref. [139] with permission of Elsevier

The intrinsic low electronic conductivity of $<10^{-13}$ S cm^{-1} is one of the major issues hindering its commercialization. Therefore, different strategies were implemented to overcome the problem which include synthesis of LTO in the form of nanoparticles, carbon coating and doping of Ti [135–138]. These improvements made LTO as the front-runner among different prospective anode materials.

$$Li_4Ti_5O_{12} + 3\,Li^+ + 3\,e^- \leftrightarrow Li_7Ti_5O_{12} \tag{1.11}$$

1.5.2.2 Alloying/De-alloying Anodes

Elements like Si, Sb, Sn, Al, and Cd can undergo reversible Li storage via alloying/de-alloying reactions at considerably low potentials of <1 V versus Li metal and hence they are considered as prospective anodes for LIBs [139]. In addition, they can provide very high capacities compared to graphite. However, huge volume change occur during lithiation/de-lithiation in these metals as shown in Fig. 1.10 which leads to capacity fading [140]. Oxides of these metals have been investigated as anodes as they are easier to handle compared to the metal itself. When these oxides are reduced by Li metal during the first discharge, metal particles are formed which are embedded in Li_2O matrix. Thus it can slightly decrease the effect of volume change. These metal particles then undergoes reversible alloying reaction with Li metal forming the respective alloy. Silicon, tin oxides like SnO and SnO_2 are the important anode materials which undergo lithium storage by this mechanism.

Tin Oxides

The tin oxides, SnO and SnO_2 are extensively studied as anode materials in the recent years [141–147]. The monoxide, SnO adopts a tetragonal structure made up of SnO_6 octahedra while the dioxide, SnO_2 adopts a tetragonal rutile structure. The

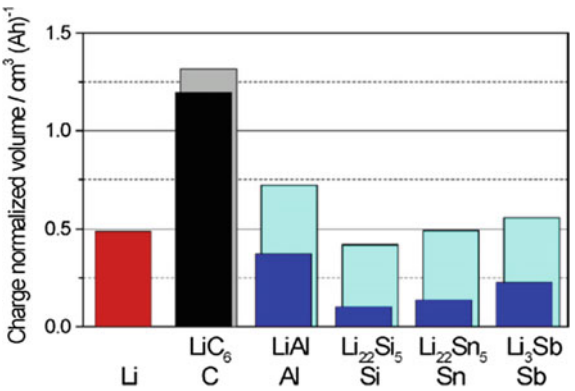

Fig. 1.10 Volume changes encountered in anode materials during lithiation. Reproduced from Ref. [140] with permission of Elsevier

theoretical capacities of SnO and SnO_2 are calculated as 875 and 782 mAh g^{-1}, respectively which are lesser than the Sn metal itself. They undergo reversible lithium insertion by alloying/de-alloying mechanism. During the initial discharge, both SnO and SnO_2 undergo lithiation in a similar fashion to form Sn metal and Li_2O as per Eqs. 1.12 and 1.13 respectively. The metallic Sn undergoes further intake of 4.4 lithium to form the alloy, $Li_{4.4}Sn$ (Eq. 1.14). During the first charge cycle and the subsequent charge/discharge cycles, the alloying/de-alloying mechanism manages the reversible lithium storage.

$$SnO + 2\,Li^+ + 2\,e^- \rightarrow Sn + Li_2O \tag{1.12}$$

$$SnO_2 + 4\,Li^+ + 4\,e^- \rightarrow Sn + 2\,Li_2O \tag{1.13}$$

$$Sn + 4.4\ Li^+ + 4.4\,e^- \leftrightarrow Li_{4.4}Sn \tag{1.14}$$

Though SnO and SnO_2 can provide better cycling than the Sn metal because of the presence of Li_2O matrix, they still suffer from large volume change during Li cycling up to 300 % which deteriorates its long-term cyclability. Research by various groups have found that the bulk SnO/SnO_2 particles can give high initial capacity, but the capacity fades drastically on long-term cycling due to the volume change. Therefore, different approaches were carried out to take care of the volume change in these materials during lithiation. One of the effective way is to prepare these oxides in the form of nanoparticles which give better performance.

1.5.2.3 Conversion Reaction Based Anodes

The principle underlying lithium storage in the conversion based anodes is the reversible redox (displacement) reaction of the material with Li as shown in Eq. 1.15.

$$M_aX_b + nb\ Li \leftrightarrow bLi_nX + aM \tag{1.15}$$

where X = O, N, F, S and P and M = transition metal like Mn, Fe, Co, Ni, Cu, etc. [148]. Thus, certain transition metal oxides, nitrides, fluorides, sulphides and phosphides undergo lithium storage by conversion mechanism.

In 2000, Poizot et al. reported the reversible lithium storage in transition metal oxides via conversion reaction mechanism [149]. The Li reactivity of these materials is based on the formation of metal nanoparticles during the first discharge, which enables the formation and decomposition of Li_2O during subsequent cycles. Increase in the ionic character of M–X bond will increase the output voltage of the reaction. Thus the voltage is expected to increase from the highly covalent metal nitrides and sulfides, to the oxides and to the highly ionic metal fluorides. Iron oxides such as FeO, Fe_2O_3 and Fe_3O_4 are important anodes which undergo lithium storage by this mechanism.

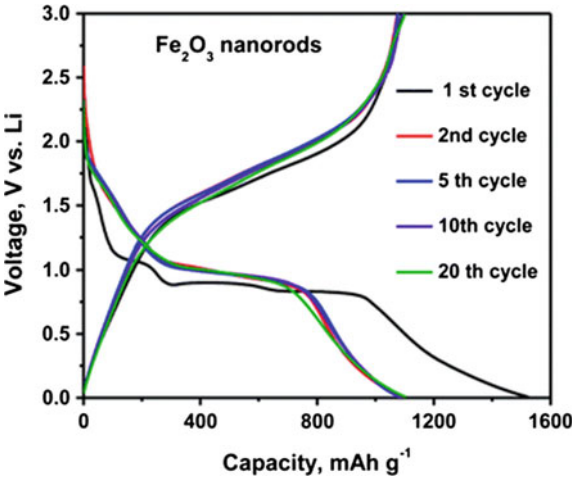

Fig. 1.11 Galvanostatic charge-discharge profiles of electrospun Fe_2O_3 nanorods. Reproduced from Ref. [156] with permission of the Royal Society of Chemistry

Iron Oxides

The α-Fe_2O_3 phase with corundum (Al_2O_3) structure is an attractive anode material for LIBs owing to its abundance, low cost and high theoretical capacity of 1005 mAh g^{-1} [150]. When cycled in the voltage range, 0.005–3.0 V versus Li, 8 mol of Li per mole of Fe_2O_3 can be reversibly utilized resulting in a very high capacity. During the first discharge, crystal structure destruction and formation of Fe^0 nanoparticles embedded in Li_2O matrix happen as per Eqs. 1.16–1.17. During the first charge and subsequent charge/discharge cycles, the Fe nanoparticles react reversibly with Li_2O resulting in the lithium storage as shown in Eq. 1.18. The charge-discharge profiles of the material prepared as nanorods are shown in Fig. 1.11.

$$Fe_2O_3 + xLi^+ + xe^- \rightarrow Li_xFe_2O_3 \tag{1.16}$$

$$Li_xFe_2O_3 + (6-x)Li^+ + (6-x)e^- \rightarrow 2Fe + 3Li_2O \tag{1.17}$$

$$2Fe + 3Li_2O \leftrightarrow Fe_2O_3 + 6Li^+ + 6e^- \tag{1.18}$$

Micron sized particles of Fe_2O_3 were found to undergo severe capacity fading [151]. However, nanosized Fe_2O_3 in the form of nanorods, nanowires and nanoparticles possess better cycling properties with reversible capacities of >1000 mAh g^{-1} and good cycling stability [152–155]. Electrospun Fe_2O_3 nanorods were shown to exhibit high and stable capacity by Cherian et al. [156]. In addition, improvement in lithium cycling were observed for carbon coating and compositing with CNT and graphene [157–161]. With the above mentioned improvements in the lithium storage of α-Fe_2O_3, it is seen as a prospective anode material for LIBs.

Fe_3O_4 is another important anode material which undergoes lithium storage by conversion mechanism, similar to Fe_2O_3 [162]. It adopts an inverse spinel structure and is abundant in nature as the mineral magnetite. It has low cost, high theoretical capacity of 926 mAh g^{-1} and is environmentally viable. There are many reports in the literature on the synthesis and anodic studies of Fe_3O_4 with capacities in the range 800–900 mAh g^{-1}. However, capacity fading were observed with many cases. Preparation of Fe_3O_4 composites with conducting carbon, CNT and graphene were found to improve the electrochemical properties with capacities of over 1000 mAh g^{-1} [163–167]. It can be concluded that carbon coating/conducting additives like graphene or CNT is essential for stable Li cycling in this material.

1.5.2.4 Anodes Based on Both Conversion and Alloying Mechanism

These materials undergo lithium storage via both conversion mechanism and alloying/de-alloying mechanism [139]. Oxides such as ZnM_2O_4 (M = Co, Fe), $CdFe_2O_4$ and tin containing oxides like M_2SnO_4, where M = Co, Mn, Mg, and Zn fall in this category. Many sulphides like Bi_2S_3, Sb_2S_3 and SnS_2 also undergo lithium storage by this mechanism. In this class of materials, the lithium storage mechanism is similar to that of the conversion based anodes. These oxides/sulphides undergo the conversion or redox reaction with lithium, forming metal nanoparticles embedded in Li_2O/Li_2S matrix. However, certain metals (Zn, Al, Sb, Sn, Bi, etc.) may undergo additional lithium consumption by alloying/de-alloying reaction providing extra capacity. For example, upon the first discharge reaction, $ZnFe_2O_4$ forms Zn and Fe nanoparticles embedded in Li_2O matrix. Of the two metals, Zn can form the alloy LiZn by reacting with Li. Thus additional capacity is obtained from the alloying mechanism. The lithium storage in the first discharge cycle of $ZnFe_2O_4$ is described by Eqs. 1.19–1.21 while the first charge and subsequent charge/discharge cycles are based on Eqs. 1.21–1.22.

$$ZnFe_2O_4 + xLi^+ + xe^- \rightarrow Li_xZnFe_2O_4 \tag{1.19}$$

$$Li_xZnFe_2O_4 + (8-x)Li^+ + (8-x)e^- \rightarrow Zn + 2Fe + 4Li_2O \tag{1.20}$$

$$Zn + Li^+ + e^- \leftrightarrow LiZn \tag{1.21}$$

$$Zn + 2Fe + 4Li_2O \leftrightarrow ZnO + Fe_2O_3 + 8Li^+ + 8e^- \tag{1.22}$$

1.5.3 Electrolyte Materials

Electrolyte is an essential component in all electrochemical devices including batteries. The electrolyte functions as a bridge between cathode and anode assisting in the transfer of charge carriers. In the case of LIBs, the electrolyte performs the

transfer of Li^+ ions between the two electrodes. Though the energy density of a LIB depends on the electrode materials, their lifetime are mainly governed by the side reactions at electrode–electrolyte interface. Breaking the SEI may also lead to lithium dendrite formation resulting in short-circuiting of the cell. In addition, the limited Li^+ mobility through the SEI and bulk electrolyte decreases the battery performance. Thus the electrochemical stability and ionic conductivity are the two main parameters for selection of a suitable electrolyte for LIBs. As electrochemical decomposition of H_2O occurs at 1.23 V versus H_2, LIBs usually employ non-aqueous electrolytes. Depending on the nature the electrolytes used in LIBs, they may be classified into the following categories.

- Liquid electrolytes
- Polymer electrolytes
- Solid electrolytes.

Irrespective of its nature, a good electrolyte for LIB should meet the following requirements.

(1) Good ionic conductivity ($\sigma_{Li} > 10^{-4}$ S cm^{-1}) to transfer Li^+ ions between the working electrodes.
(2) Good insulator to electrons ($\sigma_e < 10^{-10}$ S cm^{-1}) to reduce the internal cell resistance and resistive heating of the battery.
(3) High chemical stability of the components of the electrolyte.
(4) Good electrochemical stability in a large voltage window to accommodate high voltage cathodes and low voltage anodes.
(5) Low melting point of the electrolyte is preferred to maintain sufficient conductivity at very low temperatures and also to avoid solidification and phase separation.
(6) The boiling point of the electrolyte should be high which can avoid its evaporation when working at high temperatures. I can also prevent the pressure building up in the cell.
(7) Preferably environmentally benign and low cost.

The liquid electrolyte for LIBs normally consists of an inorganic salt dissolved in organic solvents. The commonly used lithium salts include $LiPF_6$, $LiClO_4$, and $LiBF_4$. Organic carbonates were found to be the best solvents, owing to their high dielectric constant, aprotic and polar nature. Propylene carbonate (PC) and ethylene carbonate (EC) along with co-solvents such as DMC (Dimethyl carbonate), DEC (Diethyl carbonate) and EMC (Ethylmethyl carbonate) have been studied as the solvents to carry the Li^+ ions. PC is not compatible with graphite anode owing to the intercalation of Li^+ ions along with the PC into the graphite layers which created interest in other solvents. EC in DEC (1:1 v/v %), EC in DMC and EC in DMC and DEC (1:1:1) are generally used which have good stability. Among the inorganic salts, $LiPF_6$ exhibits several advantages such as less toxicity, excellent passivation of current collector and high thermal stability compared to other salts. The electrolyte solution made of 1 M $LiPF_6$ in 1:1 mixture (by volume) of ethylene

carbonate (EC) and diethyl carbonate (DEC) has high Li^+ ion conductivity of $\sim 10^{-2}$ S cm^{-1} and stable over satisfactorily broad range of potential and temperature. Hence it is widely used for LIBs. However, liquid electrolytes possess significant disadvantages like non-flexibility of design, leakage when not sealed properly and pressure accumulation in the LIB when operated at high temperatures. Hence various solid electrolytes are being studied for LIB applications.

1.6 Aims of the Present Study

Based on the above review, it is clear that the common commercial cathode material, $LiCoO_2$ is expensive, toxic and unsafe. In addition, the commercial anode material graphite has low energy density and poses safety issues. Therefore, research on the existing materials to improve the performance and the identification of novel materials with better properties are of commercial and scientific importance. Moreover, the large scale utilization of LIBs in large scale for electric vehicle applications needs various advancement in the LIB technology. Other than enhanced energy density, improved safety features and low cost are the important criteria to achieve better LIBs.

Extensive research has been devoted in the past two decades to develop olivine structured cathode materials $LiMPO_4$ (M = Fe, Mn, Co and Ni), particularly $LiFePO_4$, in order to replace $LiCoO_2$. $LiFePO_4$ is a prospective polyanion cathode material due to its various advantages like low cost, structural stability, good cycle life and flat potential. However, its low voltage of 3.4 V results in a low energy density which hinders its wide scale application. Hence, many polyanion hosts have been investigated to find a better Li intercalation cathode. Motivated by the extensive research on the polyanion hosts, I have carried out the investigation of some vanadium based phosphates for cathode applications owing to their high potentials and high energy density.

In addition, the low capacity of graphite coupled with safety reasons, have led to extensive reach on various alternate anodes, especially in the form of nanoparticles. As the rGO/CNT composites can enhance the electrochemical properties of electrode materials, the composites of anode materials with the carbon additives have also been extensively investigated.

In summary, the aims of the present study were

- To synthesize and investigate vanadium containing phosphate, $LiVOPO_4$ for cathode application.
- To develop the novel class of cathode materials, Metal Organophosphate Open Framework (MOPOF) like $Li_2(VO)_2(HPO_4)_2(C_2O_4)$ and rGO/$K_2(VO)_2(HPO_4)_2(C_2O_4)$ for cathode applications.

- To synthesize of $Li_3V_2(PO_4)_3$ utilizing the MOPOF material, $Li_2(VO)_2(HPO_4)_2(C_2O_4)$ as a single source precursor.
- To develop simple strategies for the synthesis of reduced graphene oxide based composite anodes, namely, rGO/Sb_2S_3 and rGO/Fe_3O_4.

1.7 Thesis Outline

- In this chapter discusses the principle of Lithium ion batteries along with a brief literature survey on different cathode, anode and electrolyte materials.
- Chapter 2 discusses in detail, the principle of synthetic methods used in the preparation of different electrode materials. Structural, morphological and electrochemical characterization of the synthesized compounds are also discussed.
- Chapter 3 deals with the synthesis of a novel Metal Organophosphate Open Framework (MOPOF) material, $Li_2(VO)_2(HPO_4)_2(C_2O_4)$ for cathode application in LIBs.
- Chapter 4 deals with room temperature synthesis of another MOPOF material, $K_2(VO)_2(HPO_4)_2(C_2O_4)\cdot 4.5H_2O$ and its rGO composites. The dehydrated phases were studied as cathode materials for LIBs. Detailed information on the synthesis and electrochemical characterization are discussed in this chapter.
- Chapter 5 discusses the synthesis of carbon coated $Li_3V_2(PO_4)_3$-V_2O_3 composites from a single source precursor, $Li_2(VO)_2(HPO_4)_2(C_2O_4)\cdot 6H_2O$. Details of the electrochemical characterization of the composite as anode and cathode are discussed in this chapter.
- Chapter 6 deals with synthesis of a metastable α_I-$LiVOPO_4$ phase from a hydrated phosphate, $LiVOPO_4\cdot 2H_2O$. Structural transformation mechanism accompanying the dehydration reaction and the electrochemical studies of the material are discussed in detail.
- Chapter 7 discusses the synthesis of rGO/Sb_2S composites from a single source precursor, $Sb(SCOPh)_3$ by solid state decomposition. Anodic studies of the material is also described.
- Chapter 8 deals with synthesis and electrochemical studies of rGO/Fe_3O_4 composites obtained by a simple precipitation reaction followed by annealing.

References

1. J.M. Tarascon, M. Armand, Nature **414**, 359–367 (2001)
2. O.K. Park, Y. Cho, S. Lee, H.-C. Yoo, H.-K. Song, J. Cho, Energy Environ. Sci. **4**, 1621–1633 (2011)
3. D. Linden, T.B.R. McGraw-Hill., Handbook of Batteries, 3rd edn. (McGraw-Hill, 2002)
4. A.M. Colclasure, R.J. Kee, Electrochim. Acta **55**, 8960–8973 (2010)
5. R.J. Brodd, C. Helou, J. Power Sources **231**, 293–300 (2013)

6. M.S. Whittingham, Chem. Rev. **104**, 4271–4302 (2004)
7. J. Broadhead, F.A. Trumbore, in *9th International Power Sources Symposium Committee* (1974)
8. M.S. Whittingham, Science **192**, 1126–1127 (1976)
9. M.S. Whittingham, Prog. Solid State Chem. **12**, 41–99 (1978)
10. M.S. Whittingham, Mater. Res. Bull. **13**, 959–965 (1978)
11. M.S. Whittingham, Prog. Solid State Chem. **12**, 41–99 (1978)
12. M.S. Whittingham, F.R. Gamble Jr., Mater. Res. Bull. **10**, 363–371 (1975)
13. K. Mizushima, P.C. Jones, P.J. Wiseman, J.B. Goodenough, Mater. Res. Bull. **15**, 783–789 (1980)
14. J.N. Reimers, J.R. Dahn, J. Electrochem. Soc. **139**, 2091–2097 (1992)
15. A. Manthiram, T. Muraliganth, *Handbook of Battery Materials*, Wiley-VCH Verlag GmbH & Co. KGaA, Editon edn. (2011)
16. C. Delmas, Mat. Sci. Eng. B **3**, 97–101 (1989)
17. Y. Nishi, Chem. Rec. **1**, 406–413 (2001)
18. J. Cho, C.S. Kim, S.I. Yoo, Electrochem. Solid State Lett. **3**, 362–365 (2000)
19. S. Oh, J.K. Lee, D. Byun, W.I. Cho, B.W. Cho, J. Power Sources **132**, 249–255 (2004)
20. J. Cho, Y.J. Kim, B. Park, Chem. Mater. **12**, 3788–3791 (2000)
21. Z. Wang, C. Wu, L. Liu, F. Wu, L. Chen, X. Huang, J. Electrochem. Soc. **149**, A466–A471 (2002)
22. H. Li, Z. Wang, L. Chen, X. Huang, Adv. Mater. **21**, 4593–4607 (2009)
23. J. Cho, Y.-W. Kim, B. Kim, J.-G. Lee, B. Park, Angew. Chem. Int. Ed. **42**, 1618–1621 (2003)
24. Y. Bai, Y. Yin, N. Liu, B. Guo, H. Shi, J. Liu, Z. Wang, L. Chen, J. Power Sources **174**, 328–334 (2007)
25. G.T.K. Fey, H.M. Kao, P. Muralidharan, T.P. Kumar, Y.D. Cho, J. Power Sources **163**, 135–143 (2006)
26. N. Kosova, E. Devyatkina, A. Slobodyuk, V. Kaichev, Solid State Ionics **179**, 1745–1749 (2008)
27. T. Ohzuku, A. Ueda, M. Nagayama, J. Electrochem. Soc. **140**, 1862–1870 (1993)
28. J.R. Dahn, U. Von Sacken, M.W. Juzkow, H. Al-Janaby, J. Electrochem. Soc. **138**, 2207–2211 (1991)
29. R. Alcantara, P. Lavela, J. Tirado, R. Stoyanova, E. Kuzmanova, E. Zhecheva, Chem. Mater. **9**, 2145–2155 (1997)
30. J. Morales, C. Pérez-Vicente, J.L. Tirado, Mater. Res. Bull. **25**, 623–630 (1990)
31. Y. Bentaleb, I. Saadoune, K. Maher, L. Saadi, K. Fujimoto, S. Ito, J. Power Sources **195**, 1510–1515 (2010)
32. D. Bhuvaneswari, Gangulibabu, N. Kalaiselvi, J. Solid State Electrochem. **16**, 3667–3674 (2012)
33. S.K. Martha, E. Markevich, V. Burgel, G. Salitra, E. Zinigrad, B. Markovsky, H. Sclar, Z. Pramovich, O. Heik, D. Aurbach, I. Exnar, H. Buqa, T. Drezen, G. Semrau, M. Schmidt, D. Kovacheva, N. Saliyski, J. Power Sources **189**, 288–296 (2009)
34. S.K. Martha, H. Sclar, Z. Szmuk Framowitz, D. Kovacheva, N. Saliyski, Y. Gofer, P. Sharon, E. Golik, B. Markovsky, D. Aurbach, *J. Power Sources* **189**, 248–255 (2009)
35. J.K. Ngala, N.A. Chernova, M. Ma, M. Mamak, P.Y. Zavalij, M.S. Whittingham, J. Mater. Chem. **14**, 214–220 (2004)
36. M. Guilmard, C. Pouillerie, L. Croguennec, C. Delmas, Solid State Ionics **160**, 39–50 (2003)
37. T. Ohzuku, Y. Makimura, Chem. Lett. **30**, 642–643 (2001)
38. M.M. Thackeray, W.I.F. David, P.G. Bruce, J.B. Goodenough, Mater. Res. Bull. **18**, 461–472 (1983)
39. J. Guan, M. Liu, Solid State Ionics **110**, 21–28 (1998)
40. P. Arora, B.N. Popov, R.E. White, J. Electrochem. Soc. **145**, 807–815 (1998)
41. S.-T. Myung, S. Komaba, N. Kumagai, J. Electrochem. Soc. **148**, A482–A489 (2001)

42. C. Li, H.P. Zhang, L.J. Fu, H. Liu, Y.P. Wu, E. Rahm, R. Holze, H.Q. Wu, Electrochim. Acta **51**, 3872–3883 (2006)
43. J.S. Kim, C.S. Johnson, J.T. Vaughey, S.A. Hackney, K.A. Walz, W.A. Zeltner, M.A. Anderson, M.M. Thackeray, J. Electrochem. Soc. **151**, A1755–A1761 (2004)
44. J.S. Gnanaraj, V.G. Pol, A. Gedanken, D. Aurbach, Electrochem. Commun. **5**, 940–945 (2003)
45. S. Lim, J. Cho, Electrochem. Commun. **10**, 1478–1481 (2008)
46. X. Yi, X. Wang, B. Ju, H. Shu, W. Wen, R. Yu, D. Wang, X. Yang, Electrochim. Acta **134**, 143–149 (2014)
47. C. Masquelier, L. Croguennec, Chem. Rev. **113**, 6552–6591 (2013)
48. A.K. Padhi, K.S. Nanjundaswamy, J.B. Goodenough, J. Electrochem. Soc. **144**, 1188–1194 (1997)
49. A.K. Padhi, K.S. Nanjundaswamy, C. Masquelier, S. Okada, J.B. Goodenough, J. Electrochem. Soc. **144**, 1609–1613 (1997)
50. M. Park, X. Zhang, M. Chung, G.B. Less, A.M. Sastry, J. Power Sources **195**, 7904–7929 (2010)
51. S.-Y. Chung, J.T. Bloking, Y.-M. Chiang, Nat. Mater. **1**, 123–128 (2002)
52. H. Huang, S.C. Yin, L.F. Nazar, Electrochem. Solid-State Lett. **4**, A170–A172 (2001)
53. C. Delmas, M. Maccario, L. Croguennec, F. Le Cras, F. Weill, Nat. Mater. **7**, 665–671 (2008)
54. J.-P. Jegal, K.-C. Kim, M.S. Kim, K.-B. Kim, J. Mater. Chem. A **2**, 9594–9599 (2014)
55. T. Liu, L. Zhao, D. Wang, J. Zhu, B. Wang, C. Guo, RSC Adv. **4**, 10067–10075 (2014)
56. Y. Wang, Y. Wang, E. Hosono, K. Wang, H. Zhou, Angew. Chem. Int. Ed. **47**, 7461–7465 (2008)
57. K. Saravanan, M.V. Reddy, P. Balaya, H. Gong, B.V.R. Chowdari, J.J. Vittal, J. Mater. Chem. **19**, 605–610 (2009)
58. C. Zhang, X. He, Q. Kong, H. Li, H. Hu, H. Wang, L. Gu, L. Wang, G. Cui, L. Chen, CrystEngComm **14**, 4344–4349 (2012)
59. P.S. Herle, B. Ellis, N. Coombs, L.F. Nazar, Nat. Mater. **3**, 147–152 (2004)
60. X.-L. Wu, L.-Y. Jiang, F.-F. Cao, Y.-G. Guo, L.-J. Wan, Adv. Mater. **21**, 2710–2714 (2009)
61. M. Gaberscek, R. Dominko, J. Jamnik, Electrochem. Commun. **9**, 2778–2783 (2007)
62. V. Aravindan, J. Gnanaraj, Y.-S. Lee, S. Madhavi, J. Mater. Chem. A **1**, 3518–3539 (2013)
63. C. Delacourt, L. Laffont, R. Bouchet, C. Wurm, J.B. Leriche, M. Morcrette, J.M. Tarascon, C. Masquelier, J. Electrochem. Soc. **152**, A913–A921 (2005)
64. H. Guo, C. Wu, J. Xie, S. Zhang, G. Cao, X. Zhao, J. Mater. Chem. A **2**, 10581–10588 (2014)
65. Y. Hong, Z. Tang, Z. Hong, Z. Zhang, J. Power Sources **248**, 655–659 (2014)
66. K. Su, F. Liu, J. Chen, J. Power Sources **232**, 234–239 (2013)
67. M. Zhao, Y. Fu, N. Xu, G. Li, M. Wu, X. Gao, *J. Mater. Chem. A* (2014) (Ahead of Print)
68. A.V. Lavrov, V.P. Nikolaev, G.G. Sadikov, M.A. Porai-Koshits, Dokl. Akad. Nauk SSSR **266**, 343–346 (1982)
69. K.H. Lii, C.H. Li, C.Y. Cheng, S.L. Wang, J. Solid State Chem. **95**, 352–359 (1991)
70. J. Gaubicher, T.L. Mercier, Y. Chabre, J. Angenault, M. Quarton, J. Electrochem. Soc. **146**, 4375–4379 (1999)
71. T.A. Kerr, J. Gaubicher, L.F. Nazar, Electrochem. Solid-State Lett. **3**, 460–462 (2000)
72. C.J. Allen, Q. Jia, C.N. Chinnasamy, S. Mukerjee, K.M. Abraham, J. Electrochem. Soc. **158**, A1250–A1259 (2011)
73. B.M. Azmi, H.S. Munirah, T. Ishihara, Y. Takita, Ionics **11**, 402–405 (2005)
74. J. Barker, M.Y. Saidi, J.L. Swoyer, J. Electrochem. Soc. **151**, A796–A800 (2004)
75. K.L. Harrison, C.A. Bridges, C.U. Segre, C.D. Varnado, D. Applestone, C.W. Bielawski, M.P. Paranthaman, A. Manthiram, Chem. Mater. **26**, 3849–3861 (2014)
76. M.M. Ren, Z. Zhou, X.P. Gao, J. Appl. Electrochem. **40**, 209–213 (2010)
77. M.M. Ren, Z. Zhou, X.P. Gao, L. Liu, W.X. Peng, J. Phys. Chem. C **112**, 13043–13046 (2008)

78. M.M. Ren, Z. Zhou, L.W. Su, X.P. Gao, J. Power Sources **189**, 786–789 (2009)
79. K. Saravanan, H.S. Lee, M. Kuezma, J.J. Vittal, P. Balaya, J. Mater. Chem. **21**, 10042–10050 (2011)
80. L. Wang, L. Yang, L. Gong, X. Jiang, K. Yuan, Z. Hu, Electrochim. Acta **56**, 6906–6911 (2011)
81. Y. Yang, H. Fang, J. Zheng, L. Li, G. Li, G. Yan, Solid State Sci. **10**, 1292–1298 (2008)
82. A. Tang, J. Shen, Y. Hu, G. Xu, D. He, Q. Yi, R. Peng, J. Electrochem. Soc. **161**, A10–A13 (2014)
83. N. Dupre, J. Gaubicher, J. Angenault, G. Wallez, M. Quarton, J. Power Sources **97–98**, 532–534 (2001)
84. N. Dupre, G. Wallez, J. Gaubicher, M. Quarton, J. Solid State Chem. **177**, 2896–2902 (2004)
85. M. Morcrette, C. Wurm, C. Masquelier, Solid State Sci. **4**, 239–246 (2002)
86. A.K. Padhi, K.S. Nanjundaswamy, C. Masquelier, S. Okada, J.B. Goodenough, J. Electrochem. Soc. **144**, 1609–1613 (1997)
87. S. Patoux, C. Wurm, M. Morcrette, G. Rousse, C. Masquelier, J. Power Sources **119–121**, 278–284 (2003)
88. X.H. Rui, N. Ding, J. Liu, C. Li, C.H. Chen, Electrochim. Acta **55**, 2384–2390 (2010)
89. Y. Li, Z. Zhou, X. Gao, J. Yan, Electrochim. Acta **52**, 4922–4926 (2007)
90. M.M. Ren, Z. Zhou, X.P. Gao, W.X. Peng, J.P. Wei, J. Phys. Chem. C **112**, 5689–5693 (2008)
91. H. Huang, S.-C. Yin, T. Kerr, N. Taylor, L.F. Nazar, Adv. Mater. **14**, 1525–1528 (2002)
92. A. Pan, J. Liu, J.-G. Zhang, W. Xu, G. Cao, Z. Nie, B.W. Arey, S. Liang, Electrochem. Commun. **12**, 1674–1677 (2010)
93. Y. Chen, Y. Zhao, X. An, J. Liu, Y. Dong, L. Chen, Electrochim. Acta **54**, 5844–5850 (2009)
94. Q. Kuang, Y. Zhao, X. An, J. Liu, Y. Dong, L. Chen, Electrochim. Acta **55**, 1575–1581 (2010)
95. M. Ren, Z. Zhou, Y. Li, X.P. Gao, J. Yan, J. Power Sources **162**, 1357–1362 (2006)
96. M.E. Arroyo-de Dompablo, M. Armand, J.M. Tarascon, U. Amador, *Electrochem. Commun.* **8**, 1292–1298 (2006)
97. R. Dominko, J. Power Sources **184**, 462–468 (2008)
98. M.S. Islam, R. Dominko, C. Masquelier, C. Sirisopanaporn, A.R. Armstrong, P.G. Bruce, J. Mater. Chem. **21**, 9811–9818 (2011)
99. S.-I. Nishimura, S. Hayase, R. Kanno, M. Yashima, N. Nakayama, A. Yamada, J. Am. Chem. Soc. **130**, 13212–13213 (2008)
100. C. Sirisopanaporn, C. Masquelier, P.G. Bruce, A.R. Armstrong, R. Dominko, J. Am. Chem. Soc. **133**, 1263–1265 (2011)
101. A.R. Armstrong, N. Kuganathan, M.S. Islam, P.G. Bruce, J. Am. Chem. Soc. **133**, 13031–13035 (2011)
102. T. Muraliganth, K.R. Stroukoff, A. Manthiram, Chem. Mater. **22**, 5754–5761 (2010)
103. A. Nyten, A. Abouimrane, M. Armand, T. Gustafsson, J.O. Thomas, Electrochem. Commun. **7**, 156–160 (2005)
104. A. Nyten, S. Kamali, L. Haeggstroem, T. Gustafsson, J.O. Thomas, J. Mater. Chem. **16**, 2266–2272 (2006)
105. D. Santamaria-Perez, U. Amador, J. Tortajada, R. Dominko, D.M.E. Arroyo-de, Inorg. Chem. **51**, 5779–5786 (2012)
106. M. Molenda, M. Swietoslawski, A. Rafalska-Lasocha, R. Dziembaj, Funct. Mater. Lett. **4**, 135–138 (2011)
107. M. Kuezma, S. Devaraj, P. Balaya, J. Mater. Chem. **22**, 21279–21284 (2012)
108. A. Kokalj, R. Dominko, G. Mali, A. Meden, M. Gaberscek, J. Jamnik, Chem. Mater. **19**, 3633–3640 (2007)
109. J. Cabana, L. Monconduit, D. Larcher, M.R. Palacin, Adv. Mater. **22**, E170–E192 (2010)
110. J.B. Goodenough, Y. Kim, Chem. Mater. **22**, 587–603 (2010)

111. S. Goriparti, E. Miele, F. De Angelis, E. Di Fabrizio, R. Proietti Zaccaria, C. Capiglia, J. Power Sources **257**, 421–443 (2014)
112. L. Ji, Z. Lin, M. Alcoutlabi, X. Zhang, Energy Environ. Sci. **4**, 2682–2699 (2011)
113. U. Kasavajjula, C. Wang, A.J. Appleby, J. Power Sources **163**, 1003–1039 (2007)
114. J.O. Besenhard, Carbon **14**, 111–115 (1976)
115. J.O. Besenhard, H.P. Fritz, J. Electroanal. Chem. Interfacial Electrochem. **53**, 329–333 (1974)
116. M. Armand, P. Touzain, Mat. Sci. Eng. **31**, 319–329 (1977)
117. J.R. Dahn, T. Zheng, Y. Liu, J.S. Xue, Science **270**, 590–593 (1995)
118. N.A. Kaskhedikar, J. Maier, Adv. Mater. **21**, 2664–2680 (2009)
119. Y.P. Wu, E. Rahm, R. Holze, J. Power Sources **114**, 228–236 (2003)
120. X.Y. Song, K. Kinoshita, T.D. Tran, J. Electrochem. Soc. **143**, L120–L123 (1996)
121. J.R. Dahn, Phy. Rev. B **44**, 9170–9177 (1991)
122. T. Ohzuku, Y. Iwakoshi, K. Sawai, J. Electrochem. Soc. **140**, 2490–2498 (1993)
123. A.R. Armstrong, G. Armstrong, J. Canales, P.G. Bruce, Angew. Chem. Int. Ed. **43**, 2286–2288 (2004)
124. A.R. Armstrong, G. Armstrong, J. Canales, R. Garcia, P.G. Bruce, Adv. Mater. **17**, 862–865 (2005)
125. M. Wagemaker, A.P.M. Kentgens, F.M. Mulder, Nature **418**, 397–399 (2002)
126. Y.-S. Hu, L. Kienle, Y.-G. Guo, J. Maier, Adv. Mater. **18**, 1421–1426 (2006)
127. J. Xu, C. Jia, B. Cao, W.F. Zhang, Electrochim. Acta **52**, 8044–8047 (2007)
128. L. Zhao, Y.-S. Hu, H. Li, Z. Wang, L. Chen, Adv. Mater. **23**, 1385–1388 (2011)
129. E.M. Sorensen, S.J. Barry, H.-K. Jung, J.R. Rondinelli, J.T. Vaughey, K.R. Poeppelmeier, Chem. Mater. **18**, 482–489 (2006)
130. L. Kavan, J. Prochazka, T.M. Spitler, M. Kalbac, M. Zukalova, T. Drezen, M. Gratzel, J. Electrochem. Soc. **150**, A1000–A1007 (2003)
131. E. Ferg, R.J. Gummow, A. de Kock, M.M. Thackeray, J. Electrochem. Soc. **141**, L147–L150 (1994)
132. K. Zaghib, M. Simoneau, M. Armand, M. Gauthier, J. Power Sources **81–82**, 300–305 (1999)
133. L. Kavan, M. Gratzel, Electrochem. Solid-State Lett. **5**, A39–A42 (2002)
134. T.-F. Yi, L.-J. Jiang, J. Shu, C.-B. Yue, R.-S. Zhu, H.-B. Qiao, J. Phys. Chem. Solids **71**, 1236–1242 (2010)
135. Y. Wang, H. Liu, K. Wang, H. Eiji, Y. Wang, H. Zhou, J. Mater. Chem. **19**, 6789–6795 (2009)
136. K. Amine, I. Belharouak, Z. Chen, T. Tran, H. Yumoto, N. Ota, S.-T. Myung, Y.-K. Sun, Adv. Mater. **22**, 3052–3057 (2010)
137. A.S. Prakash, P. Manikandan, K. Ramesha, M. Sathiya, J.M. Tarascon, A.K. Shukla, Chem. Mater. **22**, 2857–2863 (2010)
138. H.-G. Jung, S.-T. Myung, C.S. Yoon, S.-B. Son, K.H. Oh, K. Amine, B. Scrosati, Y.-K. Sun, Energy Environ. Sci. **4**, 1345–1351 (2011)
139. M.V. Reddy, G.V. Subba Rao, B.V.R. Chowdari, Chem. Rev. **113**, 5364–5457 (2013)
140. B. Scrosati, J. Garche, J. Power Sources **195**, 2419–2430 (2010)
141. I.A. Courtney, J.R. Dahn, J. Electrochem. Soc. **144**, 2045–2052 (1997)
142. X.W. Guo, X.P. Fang, Y. Sun, L.Y. Shen, Z.X. Wang, L.Q. Chen, J. Power Sources **226**, 75–81 (2013)
143. W. Liu, X. Huang, Z. Wang, H. Li, L. Chen, J. Electrochem. Soc. **145**, 59–62 (1998)
144. P. Meduri, C. Pendyala, V. Kumar, G.U. Sumanasekera, M.K. Sunkara, Nano Lett. **9**, 612–616 (2009)
145. S. Oro, K. Urita, I. Moriguchi, Chem. Commun. **50**, 7143–7146 (2014)
146. M.J. Osiak, E. Armstrong, T. Kennedy, C.M. Sotomayor Torres, K.M. Ryan, C. O'Dwyer, ACS Appl. Mater. Interfaces **5**, 8195–8202 (2013)
147. J. Wang, W. Li, F. Wang, Y. Xia, A.M. Asiri, D. Zhao, Nanoscale **6**, 3217–3222 (2014)
148. M. Armand, J.M. Tarascon, Nature **451**, 652–657 (2008)

149. P. Poizot, S. Laruelle, S. Grugeon, L. Dupont, J.M. Tarascon, Nature **407**, 496–499 (2000)
150. M.V. Reddy, T. Yu, C.-H. Sow, Z.X. Shen, C.T. Lim, G.V.S. Rao, B.V.R. Chowdari, Adv. Funct. Mater. **17**, 2792–2799 (2007)
151. D. Larcher, C. Masquelier, D. Bonnin, Y. Chabre, V. Masson, J.B. Leriche, J.M. Tarascon, J. Electrochem. Soc. **150**, A133–A139 (2003)
152. Y.-M. Lin, P.R. Abel, A. Heller, C.B. Mullins, J. Phys. Chem. Lett. **2**, 2885–2891 (2011)
153. H. Liu, G. Wang, J. Park, J. Wang, H. Liu, C. Zhang, Electrochim. Acta **54**, 1733–1736 (2009)
154. Z. Wang, D. Luan, S. Madhavi, C.M. Li, X.W. Lou, Chem. Commun. **47**, 8061–8063 (2011)
155. X.-L. Wu, Y.-G. Guo, L.-J. Wan, C.-W. Hu, J. Phys. Chem. C **112**, 16824–16829 (2008)
156. C.T. Cherian, J. Sundaramurthy, M. Kalaivani, P. Ragupathy, P.S. Kumar, V. Thavasi, M.V. Reddy, C.H. Sow, S.G. Mhaisalkar, S. Ramakrishna, B.V.R. Chowdari, J. Mater. Chem. **22**, 12198–12204 (2012)
157. X. Zhu, Y. Zhu, S. Murali, M.D. Stoller, R.S. Ruoff, ACS Nano **5**, 3333–3338 (2011)
158. H. Liu, G. Wang, J. Wang, D. Wexler, Electrochem. Commun. **10**, 1879–1882 (2008)
159. L. Tian, Q. Zhuang, J. Li, C. Wu, Y. Shi, S. Sun, Electrochim. Acta **65**, 153–158 (2012)
160. G. Wang, T. Liu, Y. Luo, Y. Zhao, Z. Ren, J. Bai, H. Wang, J. Alloy. Compd. **509**, L216–L220 (2011)
161. Z. Wang, D. Luan, S. Madhavi, Y. Hu, X.W. Lou, Energy Environ. Sci. **5**, 5252–5256 (2012)
162. P.L. Taberna, S. Mitra, P. Poizot, P. Simon, J.M. Tarascon, Nat. Mater. **5**, 567–573 (2006)
163. E. Kang, Y.S. Jung, A.S. Cavanagh, G.-H. Kim, S.M. George, A.C. Dillon, J.K. Kim, J. Lee, Adv. Funct. Mater. **21**, 2430–2438 (2011)
164. P. Lian, X. Zhu, H. Xiang, Z. Li, W. Yang, H. Wang, Electrochim. Acta **56**, 834–840 (2010)
165. J.-Z. Wang, C. Zhong, D. Wexler, N.H. Idris, Z.-X. Wang, L.-Q. Chen, H.-K. Liu, Chem. Eur. J. **17**, 661–667 (2011)
166. W.-M. Zhang, X.-L. Wu, J.-S. Hu, Y.-G. Guo, L.-J. Wan, Adv. Funct. Mater. **18**, 3941–3946 (2008)
167. G. Zhou, D.-W. Wang, F. Li, L. Zhang, N. Li, Z.-S. Wu, L. Wen, G.Q. Lu, H.-M. Cheng, Chem. Mater. **22**, 5306–5313 (2010)

Chapter 2
Physicochemical and Electrochemical Characterization

Abstract The different experimental procedures used in this study for the synthesis of various electrode materials and their principle involved are discussed in this chapter. In addition, methodology and principles of different techniques used in the physicochemical and electrochemical characterization of the materials are also discussed in this chapter.

2.1 Introduction

Various synthetic procedures such as hydrothermal, single source precursor approach, sonochemical route and room temperature mechanical stirring have been used in this study to prepare the different electrode materials. The details of these synthetic procedures and the principle involved are discussed in detail in Sect. 2.2. This chapter also provides the details of the different structural, morphological and electrochemical characterization techniques used for the investigation of the synthesized electrode materials. Single crystal X-Ray diffraction (SCXRD), Powder X-Ray Diffraction (PXRD), Temperature dependent (in-situ) X-Ray Diffraction, Quantitative Rietveld refinement of the XRD data, Brunauer-Emmett-Teller (BET) surface area, Raman Spectroscopy, Elemental Analysis (EA) and Thermogravimetric Analysis (TGA) have been utilized in this study for the structural characterization. The morphology of the synthesized materials were studied with the help of Scanning Electron Microscopy (SEM) and Transmission Electron Microscopy (TEM). Electrochemical investigation of the electrode materials were carried out using Galvanostatic cycling, Cyclic Voltammetry (CV) and Electrochemical Impedance Spectroscopy (EIS) studies.

A.S. Hameed, *Phosphate Based Cathodes and Reduced Graphene Oxide Composite Anodes for Energy Storage Applications*,
Springer Theses, DOI 10.1007/978-981-10-2302-6_2

2.2 Synthesis of Electrode Materials

In this study, hydrothermal method was used for the synthesis of cathode materials like $LiVOPO_4$ and $Li_2(VO)_2(HPO_4)_2(C_2O_4)$. $K_2(VO)_2(HPO_4)_2(C_2O_4)$ and its rGO composites were synthesized via three different synthetic routes, namely mechanical stirring at room temperature, grinding and sonochemical reaction. Single source precursor approach was employed for the preparation of $Li_3V_2(PO_4)_3$ and rGO/Sb_2S_3. Fe_3O_4 nanoparticles wrapped by rGO were obtained by a simple precipitation method followed by annealing at high temperature. The details of the important synthetic procedures such as hydrothermal, single source precursor route and sonochemical reaction are described in detail in the following sections.

2.2.1 Hydrothermal Synthesis

The hydrothermal method involves the synthesis of materials under high vapour pressure and usually at higher temperatures than the boiling point of water [1]. The term hydrothermal is of geologic origin as the conditions beneath the earth crust are similar which helps in the synthesis of different chemicals and crystals. In laboratories, the hydrothermal reactions are usually carried out in a Teflon container enclosed in a stainless autoclave. These conditions help in the synthesis of the desired material at a shorter time and at lower temperatures than the corresponding solid state reaction. In addition, nanoparticles of the desired material can also be obtained with definite particle size and a definite morphology by controlling the synthetic conditions. This technique is also useful for growing single crystals of many organic, inorganic and hybrid materials. If an organic solvent such as ethanol, ethylene glycol, etc., is used instead of water, it is termed as solvothermal synthesis. Ionothermal synthesis utilize ionic liquids as solvents in the synthesis.

In this work, phosphate based materials such as $LiVOPO_4{\cdot}2H_2O$, $Li_2(VO)_2(HPO_4)_2(C_2O_4){\cdot}6H_2O$ were prepared using hydrothermal route. An aqueous solution containing LiOH, oxalic acid, phosphoric acid and V_2O_5 was heated in an autoclave at a temperature of 120 °C. Single crystals were obtained for $LiVOPO_4{\cdot}2H_2O$ while $Li_2(VO)_2(HPO_4)_2(C_2O_4){\cdot}6H_2O$ was obtained as green powder by evaporation of the solution obtained after the hydrothermal reaction. These hydrated phases were subjected to dehydration to obtain the anhydrous phases for electrochemical characterization as LIB cathodes.

2.2.2 Single Source Precursor Approach

Single Source Precursor (SSP) approach is a synthetic method used to prepare different inorganic materials like metal oxides [2], metal sulphides [3–5], metal selenides [6, 8] etc. The desired product is obtained from a single molecule which is

used as the precursor, by a single-step decomposition. All the elements that are required in the target compound are incorporated in the precursor molecule. Usually, an organometallic compound or a metal complex is used as the precursor. Decomposition of the single source precursor either in solid state or solution phase yields the desired product in a single step through elimination of unwanted organic moieties [9]. The major advantages of the Single Source Precursor method over other synthetic procedures are:

- Precise stoichiometry of active elements in the desired product
- Synthesis of nanomaterials with good crystallinity and low concentration of impurity
- Lower defect concentrations
- Easier preparation of thin films by chemical vapour deposition (CVD)
- The precursors are often stable in air and less toxic which are easy to handle
- Decomposition at low temperatures compared to other synthetic routes
- Synthesis of the desired compound in a short time.

In this study, Sb_2S_3 and $Li_3V_2(PO_4)_3$ were prepared by the Single source precursor route. The anode material, Sb_2S_3 was prepared by solid state decomposition of $Sb(SCOPh)_3$ in Argon atmosphere at 400 °C. The cathode material, $Li_3V_2(PO_4)_3$ was made from a Metal Organophosphate Open Framework (MOPOF) material, $Li_2(VO)_2(HPO_4)(C_2O_4)\cdot 6H_2O$ by solid-state decomposition in Argon atmosphere at 800 °C.

2.2.3 Sonochemical Reaction

Sonochemical reaction deals with the synthesis of materials using ultrasonic waves. Sonochemistry arises from the formation, growth of bubbles in a liquid and their implosive collapse [10]. The ultrasonic waves help in the enhancement of the rate of a chemical reaction as many as million folds. These waves excites the atomic and molecular modes like vibrational, rotational, and translational modes thus behaving as a catalyst. Furthermore, the solid reactants used in the reaction are broken into smaller pieces due to the energy released by collapse of the bubbles created by cavitation. This increases the surface area of the reactants which helps the reaction to proceed at an increased rate. In this study, $K_2(VO)_2(HPO_4)_2(C_2O_4)$ was synthesized by sonochemical route using an ultrasonic bath.

2.3 Structural Characterization

2.3.1 Powder X-Ray Diffraction

Powder X-Ray diffraction (PXRD) is a rapid analytical technique primarily used for phase identification and quantification of crystalline solids and is a non-destructive

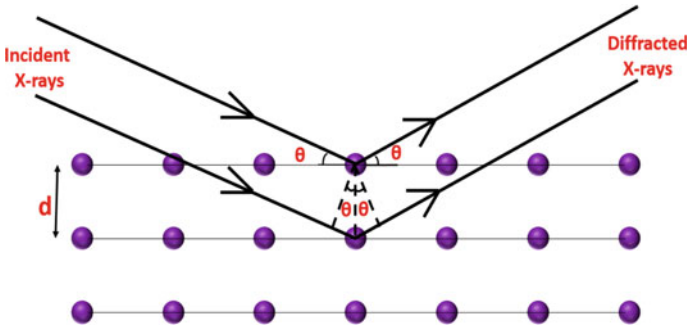

Fig. 2.1 Diffraction of X-rays from crystal lattice

method [11–13]. In addition, it can be used for determination of lattice parameters, space group, crystallite size, degree of crystallinity, residual stress, etc. The analyzed material is ground into a fine powder, homogenized, and the XRD patterns are recorded which determines the average bulk composition of the sample.

The technique relies on the wave-particle duality of X-rays. The wavelength of X-rays are similar to the inter-layer spacing (d-spacing) of the atomic layers in crystalline solids which enables the diffraction of X-rays by crystal lattices of the material under certain circumstances. These diffracted X-rays provide information about the arrangement of atoms in the crystal lattice. Interaction of monochromatic X-rays with a target material results in scattering of these X-rays (Fig. 2.1) which may undergo constructive and destructive interference. The diffraction of X-rays by crystals is determined by the Bragg's law (Eq. 2.1).

$$2\,d\sin\theta = n\,\lambda \tag{2.1}$$

where d is the interplanar spacing, θ is the angle between incident X-ray beam and the plane of atoms, λ is the wavelength of the incident X-rays, n is an integer known as order of reflectance. The scattered X-rays result in constructive interference when the Bragg's law is satisfied.

Directions of the possible diffractions be determined by the size and shape of unit cell of the material. Intensities of the diffracted waves of a particular plane are dependent on the arrangement of atoms and their atomic number. However, most solids are not available as single crystals, but contains numerous tiny crystallites which are randomly arranged. When a powder containing many randomly oriented crystallites is placed in an X-ray beam, the beam will meet all possible interatomic planes (Fig. 2.2) and for each set of planes, a certain number of crystals must be oriented at an angle to satisfy the Bragg's law. The peak positions and intensities of the diffracted beams are recorded by the detector. The resultant diffraction pattern is presented in the form of a plot of intensity of diffracted X-rays versus 2θ (degrees). A typical PXRD pattern contains the following information:

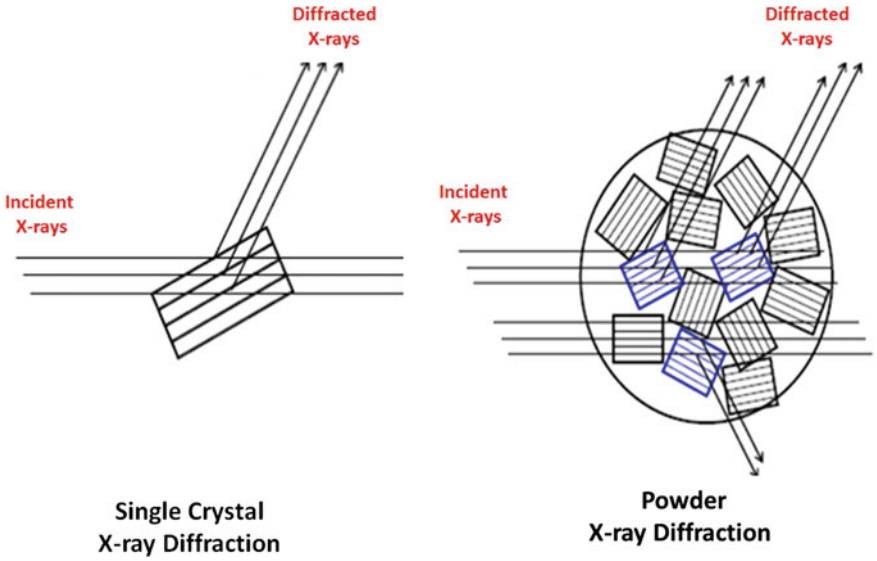

Fig. 2.2 Diffraction of X-rays from a single crystalline sample and a polycrystalline sample

- Peak Position: It gives information about the translational symmetry that is the size and shape of the unit cell.
- Peak Intensity: It gives information about the electron density inside the unit cell.
- Peak Shapes and peak widths give information about deviations from perfect crystal.

The inter-planar spacing, d can be calculated from the Bragg equation ($d = n\lambda/2 \sin\theta$). The International Centre for Diffraction Data (ICDD) offers the database of PXRD patterns of a large number of substances like inorganic, organic, polymer and minerals in the form of Joint Committee on Powder Diffraction Standards (JCPDS) files. As the PXRD pattern is the characteristic of a particular phase, the phase identification of an unknown sample can be primarily identified from the JCPDS files, even if the analyte is a mixture of different phases.

In this study, PXRD patterns of the synthesized compounds were recorded on a Siemens D5005 diffractometer with graphite monochromatised Cu-Ka radiation (λ = 1.54056 Å) or a high resolution Empyrean (Analytical) diffractometer.

2.3.2 In Situ X-Ray Diffraction

In-situ X-ray diffraction is a fast and accurate technique to investigate the structure, phases and crystallite sizes of a material during the course of a reaction. Often, the technique is used to record the PXRD patterns at different temperatures, called as

temperature dependent X-ray diffraction. In this technique, the powdered sample was kept in holder and PXRD patterns are recorded at specific intervals of temperature, while the heating or cooling is carried out at a specific rate. In this study, the dehydration of $LiVOPO_4 \cdot 2H_2O$, $Li_2(VO)_2(HPO_4)(C_2O_4) \cdot 6H_2O$ and $K_2(VO)_2(HPO_4)(C_2O_4) \cdot 4.5H_2O$ and were investigated using a Bruker D8 Advance diffractometer (Bruker-AXS GmbH, Karlsruhe, Germany) fitted with Anton Paar high temperature chamber (Model HTK 1200) and low temperature chamber (Model TTK450).

2.3.3 Rietveld Refinement

Rietveld refinement is a basic technique used for the characterization of crystalline materials introduced by Hugo Rietveld. This method is normally used for refinement of neutron and X-ray diffraction pattern of powder samples. The height, width and position of the reflections of a PXRD or neutron diffraction pattern can be used to determine many aspects of the materials structure. In the Rietveld method, a least squares approach is used to refine a theoretical line profile until it matches the experimental pattern. The Rietveld refinement of the XRD patterns were carried out in this study using TOPAS software (version 3.0). The main objective of the Rietveld refinement in this study is to show the phase purity of bulk samples used for the electrochemical studies.

2.3.4 Single Crystal X-Ray Diffraction

Single-crystal X-ray Diffraction is a non-destructive analytical technique which provides detailed information about the structure of crystalline substances. In this technique, a single crystal is mounted on a thin glass fiber and mounted on goniometer head and subjected to X-rays. The diffracted X-rays can be used for the structural solution and refinement. Some of the applications of single-crystal diffraction include:

- Identification, crystal structure solution and refinement of new compounds
- Determination of unit cell, bond-lengths, bond-angles and site-ordering
- Characterization of cation-anion coordination geometry.

In this study, crystal structure of $LiVOPO_4 \cdot 2H_2O$ was determined by single crystal X-ray diffraction. Single crystals suitable for the data collection were selected under an optical microscope, mounted on a glass fiber and the data were collected on a Bruker AXS SMART CCD diffractometer. Graphite-monochromatized Mo-K_α (λ = 0.71073 Å) radiation was used for data collection. Unit cell dimensions were obtained by least-squares refinements, and the structure was solved by direct methods. The program *SMART* [14] was used for collecting frames of data, indexing

reflections and determining lattice parameters and *SAINT* [14] for integration of intensity of reflections and scaling; *SADABS* [15] was used for empirical absorption correction and *SHELTL* [16] was used for space-group determination, structure solution and least-squares refinements on F^2.

2.3.5 Elemental Analysis (EA)

Elemental analysis is an important analytical technique used to investigate the composition of a material. The sample is examined for its elemental constituents qualitatively (presence of certain elements) and quantitatively (mass % of different elements). CHNS analysis is the most common application of elemental analysis which provides a means for rapid determination of the elements carbon, hydrogen, nitrogen and sulphur present in organic compounds, polymers and other types of materials. This method relies on the combustion of the sample under investigation at high temperatures ($\sim$1000 °C) in oxygen-rich environment. In this combustion process, carbon is converted to CO_2; hydrogen is converted to H_2O while nitrogen and sulphur are converted to the respective oxides. These combustion products are selectively adsorbed by different traps and the increase in mass of these traps are used to calculate the composition of the sample. In the present study, CHNS elemental analyzer (Elementar Vario MICRO CUBE) was used for the analysis of C, H and S content of the prepared samples.

Quantification of elements other than carbon, hydrogen, nitrogen and sulphur present in the samples can be made by inductively coupled plasma optical emission spectrometry (ICP-OES). This technique uses an inductively coupled plasma which excites the atoms and ions of the different elements present in the sample which emit electromagnetic radiation at certain wavelengths characteristic of that particular element [17]. The intensity of emission determines the concentration of the element within the sample. In this present work, ICP analysis was carried out to determine the quantity of different elements like V, P, Li, K, Fe and Sb. The sample preparation for ICP analysis involves the digestion of samples in certain acids by Milestone microwave laboratory system and the ICP analysis was done using Dual-view Optima 5300 DV ICP-OES system.

2.3.6 Thermogravimetric Analysis

Thermogravimetric analysis (TGA) is an analytical method used to understand the changes in physical and chemical properties of materials [18]. In this technique, a sample is heated at a constant rate and the weight change of the material is monitored as a function of temperature or time. Information on various physical phenomena such as absorption, adsorption, desorption, vaporization and sublimation can be obtained from this method. TGA can also be used to obtain useful

information about chemical phenomena like loss of water or other solvents (dehydration/desolvation), decomposition, oxidation or reduction of the sample. The results are usually represented by a plot of weight of the sample versus temperature and is called a thermogram. The choice of heating rate and the atmosphere such as air, inert gases (He, N_2, Ar, etc.) or vacuum play crucial role on the nature of the plot. The first derivative of the weight loss curve can also be plotted as a function of temperature and is called differential thermogravimetric or DTG curve. This curve can be used to find the precise temperature at which weight loss occurs. In the present work, TGA was used to find out the amount of solvents present in the sample from the corresponding weight losses and the temperature required for preparation of anhydrous phases from hydrated phases. TA Instruments (SDT-2960 Simultaneous DTA-TGA) was used for the analysis with samples weighing $\sim$10 mg in air or N_2 atmosphere.

2.4 Morphological Characterization

2.4.1 Scanning Electron Microscopy

Scanning electron microscopy (SEM) is a microscopic technique that uses electron beams instead of light for imaging an object. In SEM, a highly focused beam of high-energy electrons are used to generate a variety of signals at the surface of solid specimens. The signals derived the interaction between the electrons and the sample assist in obtaining information about the sample. Various information such as external morphology, chemical composition, and crystalline structure are obtained from SEM [19].

In this technique, an electron beam is produced by an electron gun at the top of the microscope, which makes a vertical path through the microscope which held within a vacuum. Focusing of the beam towards the sample are possible by electromagnetic fields. Upon the impingement of electron beam on the specimen, it interacts with atoms on the surface which gives rise to different types of radiation. They can provide the basis for surface imaging or analysis of elemental composition of the analyte. Investigation of the specimen mainly involves two types of signals namely, secondary electrons and backscattered electrons. These secondary and backscattered electrons are produced constantly from the surface of the specimen under the electron beam.

When a part of the primary electrons striking the specimen surface are deflected through large angles and re-emitted without energy loss (elastic scattering) from the surface, they are called as backscattered electrons. Since they arise from atomic nucleus interactions, the intensity of the backscattered image depends upon the atomic number of the elements present in specimen. Hence heavy elements are able to backscatter the electrons more strongly and appear brighter in the image while the lighter elements looks less bright. Secondary Electrons are low energy electrons (<50 eV) arising from electron-electron interactions (inelastic events) and are

emitted from the top 5–10 nm zone of excitation area. The amount of secondary electrons depend on the angle of the beam and surface. These secondary electrons are collected by a secondary electron detector (SED) and constitute the basis for the three dimensional imaging of a specimen surface with a scanning electron microscope. The secondary electrons are most valuable as they provide information about the morphology and topography of samples while the backscattered electrons used for illustrating contrasts especially in multiphase samples for phase discrimination.

While there are several other types of signals that are generated by the primary electrons, X-ray signal is typically the only other signal widely used in SEM. This technique called as energy dispersive X-ray spectroscopy (EDS or EDX) is used for the elemental analysis of a sample. X-rays are generated when the primary electrons undergo inelastic collisions with the sample resulting in the excitation of electrons in discrete orbitals. As these excited electrons return to lower energy states, they yield X-rays which exhibit characteristic wavelength and energy patterns of the elements present which leads to its elemental composition.

In the present study, SEM images were recorded with a JEOL JSM-6700F field emission scanning electron microscope (FESEM) operated at 5 kV and 10 μA. Since electronically-conducting materials are preferable for SEM investigation, samples were coated with a 100 nm thin platinum coating using DC sputtering.

2.4.2 Transmission Electron Microscopy

Transmission electron microscopy (TEM) is a microscopic technique in which a beam of high energy electrons (300 kV) is transmitted through an ultra-thin specimen which interacts with the specimen as it passes through. This interaction produces an image which is enlarged and focused onto an imaging device such as a fluorescent screen or a photographic film. It provides morphological, compositional and crystallographic information of the samples. TEM finds application in metallurgy, materials science, nanotechnology and various fields of biological sciences.

Transmission Electron Microscope produces a high-resolution image from the interaction between the specimen and energetic electrons in a vacuum chamber. The electrons then pass through a series of electromagnetic lenses down the column and make contact with the screen where the electrons are converted to light and form an image of the specimen. By varying the strength of these lenses, magnification of the image can be adjusted. In TEM, the image is acquired as a projection of the entire sample. However, due to electron absorption, only thin specimen sections are used to produce a 2D image on the viewing screen. The brightness of a specific area of the image is proportional to the quantity of electrons that pass through the specimen. Thus, the area of the sample where a large number of electrons can pass through look bright while the dense areas look darker. These provide information on the structure, texture, shape and size of the sample.

2.4.2.1 TEM Sample Preparation

The specimen must be extremely thin for the electrons to pass through, which provide the desired information of the specimen. In this study, the samples containing nanoparticles were dispersed in few mL of ethanol in a closed vial using an ultrasonic bath. The suspended nanoparticles were deposited on to a carbon coated TEM copper grid and dried under vacuum.

2.5 Coin Cell Fabrication

Electrochemical properties of the different electrode materials used in this study were investigated by preparing coin cells (type 2016; 20 mm diameter and 1.6 mm height). The coin cell fabrication involves mainly the following steps:

- Preparation of electrodes of the material under investigation in the form of thin films.
- Assembling the electrode into a coin cell.

The details of these processes are described in the following sections.

2.5.1 Electrode Fabrication

To fabricate the electrode, a slurry was prepared by mixing the active material with super P carbon black and Polyvinylidene difluoride binder (PVDF, Kynar 2801) in a weight ratio of 70:15:15. N-methyl pyrrolidinone (NMP) was used as the solvent in slurry preparation. The slurry was subjected to magnetic stirring for $\sim$12 h to ensure homogeneous mixing. Super P carbon is used to provide a continuous carbon network which help the electrons to hop on between the particles to the current collector resulting in enhanced electronic conductivity. The polymer binder PVDF helps in proper adherence of the material on the current collector. The slurry was then coated onto an etched current collector of $\sim$10 μm thickness. The choice of current collector depends on the material. Copper foil was used as the current collector for anode materials owing to its excellent electronic conductivity and non-tendency of alloy formation with Li at lower voltages. Aluminium foil is the preferred current collector for cathode materials as copper metal can oxidise at higher voltages. Aluminium forms alloy with lithium at lower voltages and hence it is not a good choice for anode materials.

The coated foil was then dried at 80 °C for $\sim$12 h for complete removal of the organic solvent, NMP. After proper drying, the composite electrodes of $\sim$20 μm thickness were pressed between twin rollers (Soei Singapore Scientific Quartz Co.)

at ~2 MPa pressure to ensure good contact between the particles and good adherence of the active material onto the current collector. The electrodes were then cut into circular discs of 16 mm diameter. Selected electrodes were weighed in a high precision balance to calculate the mass of active material in each electrode. The active material content in the electrodes was around 2–5 mg. The electrodes were then dried again in a vacuum oven at 80 °C for 12 h prior to cell fabrication.

2.5.2 Coin Cell Assembly

Coin cells were assembled in an Argon filled glove box (MBraun, Germany) with O_2 and H_2O level maintained below 1 ppm. Li metal (Kyokuto Metal Co., Japan) was mainly used as the counter electrode. Glass microfiber filter (GF/F, Cat No. 1825 055, Whatman Int. Ltd., Maidstone, England) or Celgard (2502) polypropylene microporous membrane was used as the separator. 1 M $LiPF_6$ in ethylene carbonate (EC), dimethyl carbonate (DMC) and diethyl carbonate (DEC) (1:1:1 v/v, Merck) was mainly used as the Li^+ ion conducting electrolyte.

The composite electrode was placed in the bottom cup of coin cell (stainless steel) with the active material facing upwards and the separator was placed above the electrode. Then ~50 μL of liquid electrolyte was added to wet the separator, followed by placing the lithium metal and top cap welded with a wave spring (stainless steel). Finally, the coin cells were assembled by crimp sealing in a mechanical hand press. A plastic O-ring was used to prevent the direct contact of cathode and anode which can result in short-circuiting of the cell. It also provides air tight sealing of the cell. A schematic diagram for the coin cell assembly is shown in Fig. 2.3. The fabricated coin cells were aged for 12 h for good percolation of electrolyte into the electrode materials before subjecting to electrochemical studies.

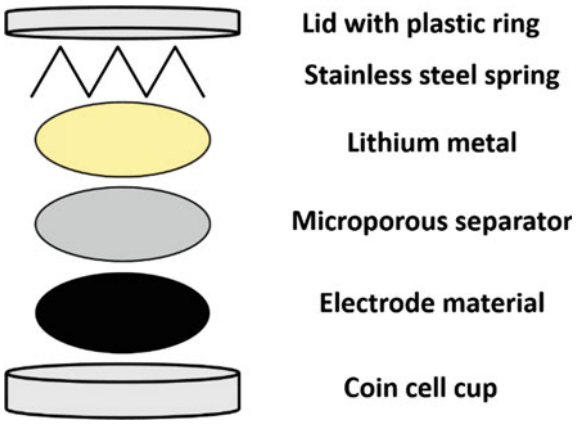

Fig. 2.3 Schematic of coin cell assembly

2.6 Electrochemical Characterization

2.6.1 Galvanostatic Cycling

Galvanostatic cycling or constant current cycling is an important technique for examining the Li storage and cycling behavior of an electrode material. In the current study, the galvanostatic cycling of the cathode materials, $LiVOPO_4$, $Li_2(VO)_2(HPO_4)_2(C_2O_4)$, $rGO/K_2(VO)_2(HPO_4)_2(C_2O_4)$ and $Li_3V_2(PO_4)_3$ and the anode materials rGO/Sb_2S_3 and rGO/Fe_3O_4 were carried out at room temperature (25 °C) using a computer controlled Bitrode multiple battery tester (model SCN, Bitrode, USA). Cycling stability of the materials were investigated by carrying out the lithium cycling for a fairly large number of charge-discharge cycles.

The voltage of an electrochemical cell depends on the state of charge or discharge of the electrode materials of the cell. During galvanostatic cycling, a constant current (I) is applied to the cell and the potential of the cell (V) was monitored as a function of time (t) or state of charge/discharge. The product of the applied current (in ampere) and the time taken (in hours) for complete lithium removal/insertion is the total charge (in mAh) stored by the material and is termed as capacity of the electrode material. The capacity obtained per unit mass of the active material is termed as specific capacity, defined by Eq. 2.2.

$$C = \frac{It}{m} \tag{2.2}$$

where C is the specific capacity in mAh g^{-1}; I is the current applied in mA; t is the time taken for complete discharge/charge in hours and m is the mass of active material in grams. The theoretical specific capacity of an electrode material is given by the following relation.

$$C_{th} = \frac{N\,F\,1000}{3600\,M} \tag{2.3}$$

where C_{th} is the theoretical specific capacity in mAh g^{-1}; F is the Faraday constant (96,496 coulombs per mole) obtained by the product of electronic charge (1.6×10^{-19} C) and Avagadro's number (6.022×10^{23} mol^{-1}); N is the number of moles of Li^+ ions/electrons involved in the electrochemical reaction per mole of the electrode material and M is the molar mass of the compound in g mol^{-1}. For example, the theoretical capacity of Fe_3O_4 is calculated to be $(96{,}500 \times 8 \times 1000)/(3600 \times 231.5) = 926$ mAh g^{-1} as 8 mol of Li^+ ions are involved in the lithium storage per mole of Fe_3O_4. Good reversibility in lithium cycling of an electrode material is often described by the capacity retention over a large number of cycles and is usually represented as a plot of capacity versus cycle number.

2.6.1.1 Rate Capability Studies

For certain applications, faster charging and discharging of a battery is highly desirable. Rate capability studies of an electrode material is a useful method to investigate the lithium storage performance of a material at different current rates. In this study, rate capability of various electrode materials were investigated by carrying out the galvanostatic cycling at different current rates. The following method is adopted to calculate the C rate. If x mAh g^{-1} is the theoretical capacity of the material, the applied current densities of 100, 500 and 1000 mA g^{-1} etc., correspond to the C-rates of 100/x, 500/x and 1000/x etc. For 1 C current rate, a current density of x mA g^{-1} is applied. For different electrode materials investigated in this study, the applied current densities were different, depending on their theoretical capacity and are discussed in individual chapters.

2.6.2 Cyclic Voltammetry

Cyclic voltammetry is an electrochemical technique in which the potential applied to the working electrode is swept at a constant rate and the resulting current is measured as a function of the potential. The current (I) at the working electrode is plotted against the applied voltage (V) to obtain the cyclic voltammogram of the analyte. This technique has found widespread application in understanding the mechanisms of redox reactions, reversibility of a reaction and electron transfer kinetics [20]. The oxidation and reduction potentials of the analyte and the diffusion coefficients of species taking part in the electrochemical reaction can also be found by this method. This method normally uses a three-electrode setup containing a working electrode, a reference electrode and a counter electrode. For a two electrode system such as a coin cell, the counter electrode and the reference electrode are the same.

In cyclic voltammetry, the potential is applied between the reference electrode and the working electrode is ramped between two specified voltage limit at a constant rate in the order of few mV s^{-1} to few V s^{-1}. The voltage is ramped both forward and backward for certain number of cycles and hence the name cyclic voltammetry. As the potential is swept back and forth, a current flows through the electrode that either oxidizes/reduces the analyte and the current (I) between the working electrode and the counter electrode is measured and plotted against the potential. The important parameters in a CV are the anodic and cathodic peak currents ($i_{p,c}$ and $i_{p,a}$) and the corresponding peak potentials $E_{p,c}$ and $E_{p,a}$. By IUPAC convention, the anodic current is positive and the cathodic current is negative. The expression for peak current is given by the Randles-Sevcik expression at 25 °C (Eq. 2.4).

$$I_p = \left(2.69 \times 10^5\right) n^{3/2} A\, C\, D^{1/2} \nu^{1/2} \tag{2.4}$$

where I_p is the peak current in A, n is the no. of electrons involved in the redox reaction, A is the area of electrode in cm^2, D is the diffusion coefficient in $cm^2\ s^{-1}$, C is the bulk concentration of the electroactive species in mol cm^{-3} and v is the scan rate in V s^{-1}. CVs of the cathode and anode materials prepared in the present study were recorded at room temperature at a scan rate of 0.058 mV s^{-1} employing a computer controlled Mac-pile system (Bio logic, France).

2.6.3 Electrochemical Impedance Spectroscopy (EIS)

EIS is a non-destructive electroanalytical tool used for the evaluation of mechanistic and kinetic information of a wide range of materials like batteries, fuel cells, corrosion inhibitors, etc [21]. In EIS studies of battery systems, the cell is held at equilibrium at a constant voltage and a small amplitude ac-signal is applied. The response of the system to this perturbation from equilibrium is measured in terms of the amplitude and phase of the resultant current. This provides information about the overall impedance of the cell. The frequency of the ac-signal is varied and the impedance of the cell is recorded as a function of frequency. The impedance is represented as a complex quantity z comprising of 'in phase' (Z_{re}) and 'out of phase' (Z_{im}) impedances. The plots of imaginary versus the real impedance at different frequencies are called Nyquist plots. EIS provides a means to understand the detailed kinetic and mechanistic information to monitor the battery properties under different conditions such as:

- Analysis of state of charge
- Investigation of reaction mechanisms
- Evaluation of electrode kinetics of each electrode
- Change of active surface during operation
- Evaluation of separators
- Passivating film behaviour
- Identification of possible electrode corrosion process.

The total impedance of a cell is the combination of different processes occurring during cycling, namely, diffusion, electron transfer kinetics, charge transfer impedance, bulk impedance, passivating layers, Warburg impedance and intercalation capacitance. The relative contributions of these different processes depends on frequency. The electron transfer kinetics dominates at high to intermediate frequency range (1 MHz–1 kHz). The diffusion process dominates in the low frequency range (1 kHz–3 MHz). Therefore, the EIS measurements were carried over wide frequency range of 180 kHz–0.001 Hz.

In this study, impedance spectroscopy measurements were carried out using Solartron 1260 A impedance analyzer. An ac-signal with amplitude of 5 mV is used to measure the impedance response over the frequency range of 180 kHz–0.001 Hz. The Nyquist plots were examined to determine the individual components constituting the overall impedance using Zview software by fitting an equivalent electrical

circuit to the Nyquist plots. These models (circuits) are designed using combination of constant phase elements (CPE) and resistors in parallel or series to match the observed Nyquist plots.

References

1. K. Byrappa, M. Yoshimura, *Handbook of Hydrothermal Technology* (Elsevier, 2001)
2. S. Daniele, R. Papiernik, L.G. Hubert-Pfalzgraf, S. Jagner, M. Håkansson, Inorg. Chem. **34**, 628–632 (1995)
3. J. Sun, W.E. Buhro, Angew. Chem. Int. Ed. **47**, 3215–3218 (2008)
4. S.L. Cumberland, K.M. Hanif, A. Javier, G.A. Khitrov, G.F. Strouse, S.M. Woessner, C.S. Yun, Chem. Mater. **14**, 1576–1584 (2002)
5. P.S. Nair, T. Radhakrishnan, N. Revaprasadu, G. Kolawole, P. O'Brien, J. Mater. Chem. **12**, 2722–2725 (2002)
6. J.J. Vittal, T.N. Meng, Acc. Chem. Res. **39**, 869–877 (2006)
7. M.A. Malik, P. O'Brien, N. Revaprasadu, Adv. Mater. **11**, 1441–1444 (1999)
8. S.L. Castro, S.G. Bailey, R.P. Raffaelle, K.K. Banger, A.F. Hepp, Chem. Mater. **15**, 3142–3147 (2003)
9. N.O. Boadi, M.A. Malik, P. O'Brien, J.A.M. Awudza, Dalton Trans. **41**, 10497–10506 (2012)
10. K.S. Suslick, Sci. Am. **260**, 80–86 (1989)
11. L.V. Azaroff, M.J. Buerger, *The Powder Method in X-Ray Crystallography* (McGraw Hill, New York, 1958)
12. H. Lipson, H. Steeple, *Interpretation of X-ray Powder Diffraction Patterns* (Macmillan-London, St Martin's Press-New York, 1970)
13. B.D. Cullity, S.R. Stock, *Elements of X-ray Diffraction*, 3rd edn. (Prentice Hall, New York, 2001)
14. *SMART and SAINT Software Reference Manuals Version 5.0, 2000* (Bruker Analytical X-ray Systems Inc., Madison, WI)
15. G.M. Sheldrick, *SADABS, A Software for Empirical Absorptions Correction, Version 2.03, 2001* (University of Göttingen, Göttingen, Germany)
16. *SHELXTL Reference Manual, Version 6.1, 2000* (Bruker Analytical X-ray Systems Inc., Madison, WI)
17. J.I. Goldstein, D.E. Newbury, P. Echlin, D.C. Joy, C.E. Lyman, E. Lifshin, L. Sawyer, J.R. Michael, *Scanning Electron Microscopy and X-Ray Microanalysis*, 3rd edn. (Kluwer Academic, New York, 1994)
18. P. Gabbott, *Principles and Applications Of Thermal Analysis*, 1st edn. (Blackwell, Ames, Iowa, 2008)
19. J. Nolte, *ICP Emission Spectrometry: a Practical Guide* (Wiley-VCH, Weinheim, 2003)
20. D.K. Gosser, *Cyclic Voltammetry: Simulation and Analysis of Reaction Mechanism* (Wiley-VCH, NY, 1993)
21. M.E. Orazem, BernardTribollet, *Electrochemical Impedance Spectroscopy* (John Wiley & Sons Inc., New Jersey, 2008)

Chapter 3
Synthesis and Electrochemical Studies of a Novel MOPOF Cathode Material, $[Li_2(VO)_2(C_2O_4)(HPO_4)_2]$

Abstract This chapter deals with the synthesis and ab initio structure determination of a novel lithium containing Metal Organophosphate Open Framework (MOPOF) material, $[Li_2(VO)_2(HPO_4)_2(C_2O_4)]\cdot 6H_2O$. It was synthesized by hydrothermal method at 120 °C and the crystal structure was solved and refined from its powder X-ray diffraction data. The anhydrous phase, $[Li_2(VO)_2(HPO_4)_2(C_2O_4)]$ obtained by dehydration of the hydrated phase at 200 °C was studied as a novel cathode material for Lithium ion batteries. The presence of extractable Li^+ ions in the inter-layer space together with the feasibility of V^{4+}/V^{5+} redox couple and a good theoretical capacity of 125 mAh g^{-1} make this compound suitable as a cathode material. Electrochemical properties of the material was investigated using cyclic voltammetry, galvanostatic charge-discharge cycling, electrochemical impedance spectroscopy (EIS) and ex situ XRD studies. The material exhibits reversible lithium insertion at ~4 V with a reversible capacity of 80 mAh g^{-1} at 0.1 C current rate.

3.1 Introduction

World-wide research has been carried out on the development of new electrode and electrolyte materials, aiming to achieve cheaper, greener and safer lithium ion battery technology. In this quest for new materials, past two decades have witnessed the development of various polyanion cathode materials such as $LiMPO_4$ [1–5], $Li^3M_2(PO_4)_3$ [6–8], Li_2MSiO_4 [9–11], $LiMSO_4F$ [12–14], $LiMBO_3$ [15, 16], $Li_2MP_2O_7$ [17, 18] and $LiMPO_4F$ [19, 20] (M = Fe, Mn, V, Co, etc.). Of these materials, the olivine structured $LiFePO_4$ stood out to be the most promising cathode material for the future LIBs. However, the low operating voltage (3.4 V) and high processing cost of $LiFePO_4$ hinder its large scale utilization. Therefore, the search for better electrode materials in terms of cost and safety is still of scientific and commercial importance.

Apart from the conventional inorganic materials, organic materials and metal–organic frameworks (MOFs) have also received attention in the area of LIBs [21]. Since MOFs have high porosity and robust structure, they have been investigated for

A.S. Hameed, *Phosphate Based Cathodes and Reduced Graphene Oxide Composite Anodes for Energy Storage Applications*,
Springer Theses, DOI 10.1007/978-981-10-2302-6_3

various applications such as gas storage, gas separation, gas purification, sensors, catalysis, drug delivery, etc. Few MOFs have also been investigated as electrode materials for LIBs. Li et al., demonstrated the lithium storage in a Zn based MOF, [Zn_4O(1,3,5-benzenetribenzoate)$_2$] (MOF-177) in the voltage range of 0.1–1.6 V. However, the results did not prove it to be a good electrode material due to its very low capacity [22]. Ferey et al., investigated a Fe based MOF, [$Fe^{III}(OH)_{0.8}F_{0.2}(O_2C–C_6H_4–CO_2)$] (MIL-53) as a cathode material for LIBs [23]. Though this material showed good cycling stability, it has rather poor capacity of $\sim$70 mAh g^{-1}. Efforts were made to enhance the electrochemical capacity of MIL-53 by introducing an electrochemically active guest molecule (1,4-benzoquinone) within its framework [24]. The benzoquinone trapped MIL-53 displayed better capacity than the bare framework. However, the extra capacity rapidly faded upon cycling due to the progressive exchange of the guest with DMC molecules from the electrolyte. Saravanan et al., reported good lithium cycling stability and rate capability in Zn and Co formate MOFs [25]. However, the development of MOFs as electrode materials for LIBs encounter major drawbacks like high molecular weight, low density and the difficulty in large scale synthesis which need to be addressed.

The quest for stable and low cost materials with considerably good energy density has motivated us to investigate the lithium storage in a new class of open framework materials called Metal Organophosphate Open Frameworks (MOPOFs). These MOPOFs are inorganic-organic hybrid open framework materials with multidimensional architectures and are constructed from metal phosphates cross-linked by organic linkers such as oxalate ligand [27–30]. These frameworks are generally stable and are known for their structural diversity and have been tested for different applications like redox reactions, catalysis, gas storage and luminescence. However, they were not investigated for energy storage properties.

Two MOPOF materials $K_{2.5}[(VO)_2(HPO_4)_{1.5}(PO_4)_{0.5}(C_2O_4)]$ and $Na_2[(VO)_2(HPO_4)_2(C_2O_4)]$ were investigated as cathode materials for the first time by our research group [26]. Insertion of an oxalate unit in the vanadium phosphate framework increases the molecular weight of the compound compared to $LiVOPO_4$ and hence slightly decreases the specific capacity. However, the synthetic simplicity of these MOPOFs with redox-active metal centers and the possible two-dimensional lithium migration in these compounds owing to their layered structure motivated the investigation of these MOPOFs as cathode materials. These materials showed reversible lithium insertion/extraction at $\sim$4 V and the results proved that oxalate bridged inorganic materials can be designed as one of the promising cathode materials.

However, the potassium containing framework may experience mixed Li/K intercalation during the first discharge and subsequent cycles. It is also anticipated that upon extraction of large K^+ ions from the oxalatophosphate framework, the small Li^+ ions may stick to one side of the large channelled framework which in turn may result in slower Li^+ diffusion compared to the K^+ ions. In order to clear these ambiguities, it is highly desirable to synthesize and investigate the electrochemical properties of the Li analogue. In addition, $[Li_2(VO)_2(HPO_4)_2(C_2O_4)]$ has a higher theoretical capacity of 125 mAh g^{-1}. Therefore, it is of great importance to investigate lithium insertion in this material.

Although a plethora of oxalate bridged open framework materials are available in the literature [27–30], it is still synthetically challenging to obtain the Li analogues of these complexes due to significantly smaller ionic radius of Li^+ compared to K^+ and the associated high hydration energy of Li^+. This reiterates the importance of synthesis and crystal structure determination of the Li analogues. In this chapter, the synthesis of a novel lithium containing MOPOF material, $[Li_2(VO)_2(HPO_4)_2(C_2O_4)]\cdot 6H_2O$ was carried out by a simple hydrothermal method and the structure was elucidated from ab initio calculations. The anhydrous phase, $[Li_2(VO)_2(HPO_4)_2(C_2O_4)]$ was obtained by dehydration and was investigated as a novel cathode material for Lithium ion batteries.

3.2 Experimental Section

All the chemicals and solvents used in this study are commercially available and used without further purification.

3.2.1 Synthesis of $[Li_2(VO)_2(HPO_4)_2(C_2O_4)]\cdot 6H_2O$

Synthesis of $[Li_2(VO)_2(HPO_4)_2(C_2O_4)]\cdot 6H_2O$ was carried out by a simple hydrothermal method. In a typical synthesis, an aqueous solution which contains vanadium pentoxide (Alfa Aesar, 98 %), oxalic acid dihydrate (Merck, 99.5 %), lithium hydroxide (Merck, 99 %) and phosphoric acid (85 wt%) in a molar ratio of 1:2:5:5 was prepared using deionised water. The solution was sonicated and sealed tightly in a 23 mL Teflon-lined stainless steel autoclave with a fill factor of ~40 %. The autoclave was heated under autogenous pressure at 120 °C for 24 h and cooled to room temperature, resulting in a blue solution. The solution was kept for evaporation at room temperature which yielded a bluish green precipitate of $[Li_2(VO)_2(HPO_4)_2(C_2O_4)]\cdot 6H_2O$ in an appreciable yield of ~60 % within 24 h. The precipitate was washed with minimum quantities of deionised water, dried under vacuum and used for structural characterization. Anal. Calcd. For $[Li_2(VO)_2(HPO_4)_2(C_2O_4)]\cdot 6H_2O$ (Mol wt. 535.12 g mol^{-1}): C, 4.48; H, 2.63; Li, 2.59; P, 11.56; V, 19.01. Found: C, 4.38; H, 2.52; Li, 2.37; P, 10.32; V, 18.31.

3.2.2 Synthesis of $[Li_2(VO)_2(HPO_4)_2(C_2O_4)]$

The anhydrous phase, $[Li_2(VO)_2(HPO_4)_2(C_2O_4)]$ was obtained by the removal of water from the as-prepared precursor at 200 °C for 2 h and was used for electrochemical characterization.

3.2.3 X-Ray Data Collection and Structure Determination

High quality powder X-ray diffraction (PXRD) data were collected for the structural solution in Bragg-Brentano geometry on a Bruker D8 Advance diffractometer (Bruker-AXS GmbH, Karlsruhe, Germany), equipped with a Cu-K_α source, over an angle range of 2–105° with a step size of 0.0167°. The powder was packed into a top-loading sample holder. Sample spinning was used to improve particle statistics. A variable counting time scheme [31] was employed to improve the counting statistics at high angles. The measurement was divided into 6 ranges; 2–11°, 11–20°, 20–29°, 29–47°, 47–65° and 65–105° which were measured with counting times of 0.25, 0.36, 0.63, 1.07, 2.64 and 5.21 s per step. Subsequently, all the ranges were normalized to 0.25 s per step and this combined dataset was used for solving the structure.

Ab initio structure determination of $[Li_2(VO)_2(HPO_4)_2(C_2O_4)]\cdot 6H_2O$ was carried out from its powder diffraction data. Peak search, peak fit and indexing [32] were performed using TOPAS software (version 4.2) which incorporates Fundamental Parameters [33, 34] even for position sensitive detectors. The structure model was geometrically optimized on density functional theory level using CASTEP as implemented in Materials Studio (version 5.5). The final structure was refined by Rietveld refinement using TOPAS software.

Details of other characterization techniques used to investigate the sample have been described previously in Chap. 2.

3.3 Results and Discussion

3.3.1 Controlled Synthesis of $[Li_2(VO)_2(HPO_4)_2(C_2O_4)]\cdot 6H_2O$

$[Li_2(VO)_2(HPO_4)_2(C_2O_4)]\cdot 6H_2O$ was synthesized by systematically varying different parameters such as molar ratio of reactants, reaction temperature and reaction time. However, isolation of the pure product could be achieved only when the reaction conditions mentioned in Sect. 3.2.1 were maintained. The effect of different parameters on the synthesis of the compound are described below in detail.

3.3.1.1 Effect of Molar Ratio of the Reactants

In this class of oxalatophosphates, the anionic frameworks are held together with the help of large organic amine cations or alkali metal cations. However, our study aimed at synthesis of a lithium containing oxalatophosphate framework for the first time. Because of the smaller size of Li^+ cation and its high hydration energy, the compound did not precipitate out easily at lower concentrations of LiOH even after long time of evaporation of the reaction mixture. Increase in the pH with increasing concentration of LiOH helped in the isolation of $[Li_2(VO)_2(HPO_4)_2(C_2O_4)]\cdot 6H_2O$.

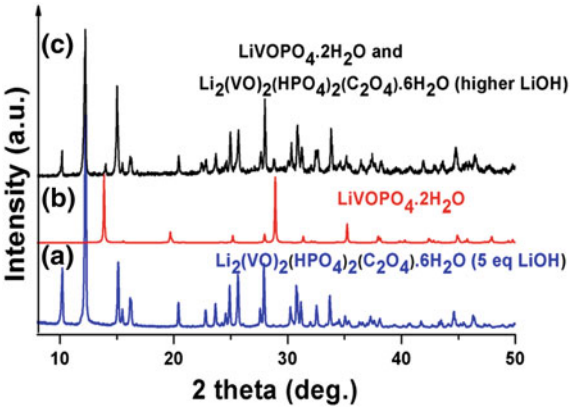

Fig. 3.1 PXRD patterns of **a** pure $[Li_2(VO)_2(HPO_4)_2(C_2O_4)]\cdot 6H_2O$, **b** $LiVOPO_4\cdot 2H_2O$ and **c** mixture of $[Li_2(VO)_2(HPO_4)_2(C_2O_4)]\cdot 6H_2O$ and $LiVOPO_4\cdot 2H_2O$

However, $LiVOPO_4\cdot 2H_2O$ was also formed as impurity at further high LiOH concentrations (Fig. 3.1). When the LiOH concentration was too high (10 mol ratio), $LiVOPO_4\cdot 2H_2O$ was formed as the exclusive product. Thus the pure phase of $[Li_2(VO)_2(HPO_4)_2(C_2O_4)]\cdot 6H_2O$ was only obtained when 5 mmol ratio of LiOH was used in the synthesis.

In addition, there was not any observable effect in the concentration of H_3PO_4 except at very high concentrations where the pH becomes too low and the formation of the desired product was not favoured.

3.3.1.2 Effect of Temperature

The reaction was carried out at different temperatures to obtain the compound in pure phase. At temperatures around 120 °C, pure phase was obtained when the molar ratio of V_2O_5, $H_2C_2O_4\cdot 2H_2O$, LiOH and H_3PO_4 was maintained at 1:2:5:5. At higher temperatures incorporation of organic moiety (oxalate) in the compound is unlikely.

3.3.2 TGA

TGA of $[Li_2(VO)_2(HPO_4)_2(C_2O_4)]\cdot 6H_2O$ (Fig. 3.2) shows three consecutive weight losses between 40 and 210 °C corresponding to the loss of six molecules of H_2O (Observed, 20.1 %, Calculated, 20.2 %). During each step, 2 water molecules are lost as inferred by equal weight loss during each step. This can be interpreted as formation of tetrahydrate, dihydrate and anhydrous phases respectively after the first, second and third weight loss steps. The weight loss between $\sim$300 and 550 °C corresponds to the loss of oxalate ligand and hydrogen atoms from HPO_4 units (Observed, 16.3 %, Calculated, 16.4 %). Therefore, the dehydration temperature

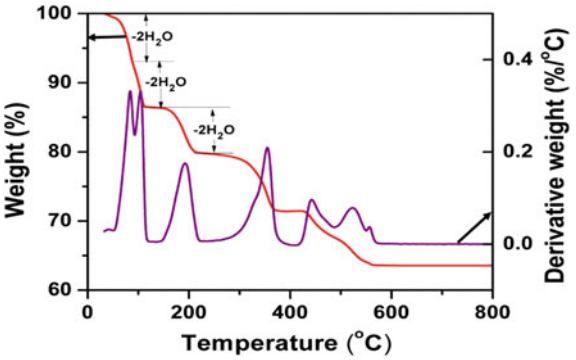

Fig. 3.2 TGA-DTG of $[Li_2(VO)_2(HPO_4)_2(C_2O_4)]\cdot 6H_2O$ in nitrogen flow at a heating rate of 5 °C min^{-1}

was chosen to be 200 °C to obtain $[Li_2(VO)_2(HPO_4)_2(C_2O_4)]$ for investigation of Li storage properties.

3.3.3 In Situ PXRD

In situ PXRD patterns of $[Li_2(VO)_2(HPO_4)_2(C_2O_4)]\cdot 6H_2O$ was recorded at intervals of 5 °C from RT to 250 °C in He atmosphere to study the dehydration mechanism. Figure 3.3 shows the in situ XRD patterns which indicate three structural

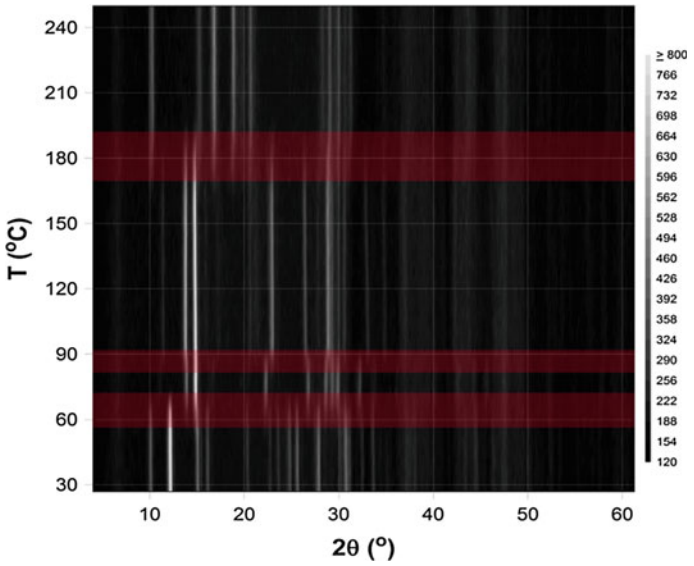

Fig. 3.3 Temperature dependant PXRD pattern of $[Li_2(VO)_2(HPO_4)_2(C_2O_4)]\cdot 6H_2O$ from RT to 250 °C at intervals of 5 °C recorded in helium atmosphere. Scale bar on the right denotes the intensity of the diffraction peaks

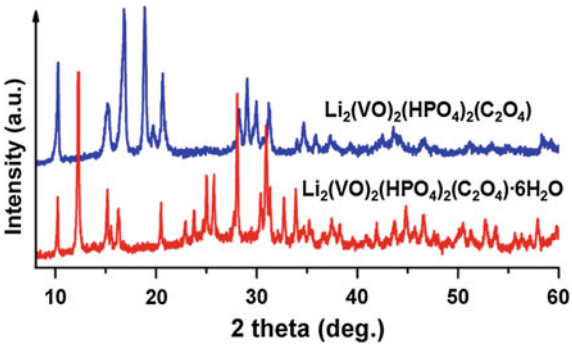

Fig. 3.4 PXRD patterns of $[Li_2(VO)_2(HPO_4)_2(C_2O_4)]\cdot 6H_2O$ and $[Li_2(VO)_2(HPO_4)_2(C_2O_4)]$

transformations occurring at ~70, 90 and 180 °C as shown by a red band in Fig. 3.3. This can be ascribed to the loss of six molecules of water from the hydrated phase in three steps which are congruent with the TGA results. Figure 3.4 shows the PXRD pattern of the hexahydrate and the anhydrous phases. The anhydrous compound was found to be hygroscopic and it undergoes hydration and dehydration in a completely reversible manner.

3.3.4 Ab Initio Structure Determination

Indexing of the PXRD data indicated a triclinic unit cell with $a = 6.41$ Å, $b = 9.22$ Å, $c = 14.62$ Å, $\alpha = 95.0°$, $\beta = 91.8°$ and $\gamma = 107.8°$ which is very similar to the unit cell for $[K_{2.5}(VO)_2(HPO_4)_2(C_2O_4)]\cdot 4.5H_2O$ [26]. Since the elemental analysis determined the new compound as $[Li_2(VO)_2(HPO_4)_2(C_2O_4)]\cdot 6H_2O$, the structure of the potassium analogue was therefore chosen as the starting model. Thus $(HPO_4)^{2-}$, $(C_2O_4)^{2-}$ and water were considered to be rigid molecules and a rigid body formalism [35] was used to describe them in the refinements and to limit the number of refinable parameters. It was assumed that the $[(VO)_2(HPO_4)_2(C_2O_4)]^{2-}$ framework is identical in both the compounds whereas the Li ions and water structure had to be different due to the much smaller Li cation and a higher water content of the compound. Only the $[(VO)_2(HPO_4)_2(C_2O_4)]^{2-}$ framework was used in the first refinement cycles. The 6 oxygen positions (corresponding to six water molecules) and 2 Li positions were found from the difference Fourier maps. The stoichiometry of the model corresponded to the formula; $[Li_{1.5}(VO)_2(HPO_4)_2(C_2O_4)]\cdot 6H_2O$, since one lithium (Li1) is on a special position. Therefore one more Li atom was to be found, either as a fully occupied position on an inversion center or as a half-filled general site. The Li atom was tentatively located on a half-filled general site. Since the lithium cation has only two electrons, a half filled Li-site is as difficult to locate by powder diffraction as a hydrogen atom. Consequently, there was some uncertainty with respect to the newly found Li3 position. Therefore, the structure model was geometrically optimized by density functional theory.

The geometrically optimized structure was used as the input for final Rietveld refinements [36]. The following refinement strategy was used: In all refinement cycles the background was fitted with a Chebychev polynomial of order 15, the zero shift was fixed to the value refined from a corundum standard on the same day, specimen displacement and sample absorption were refined. In the first refinement cycle the following sample parameters were refined: Scale factor, lattice parameters, Lorentzian size broadening and Gaussian strain broadening. Then the March-Dollase correction [37] for preferred orientation along (001) and an overall isothermal displacement parameter were released. In the next step, the isothermal parameters were refined per atom type, with a minimum value of 0.1 for each B_{iso}. Subsequently, the vanadium positions were released. Then all hydrogenphosphate and the oxalate molecules were released. This was followed by refining of the positions of water molecules. Subsequently, the CO-, PO- and CC-bonds of the rigid bodies were refined in a constraint manner. In the final refinement cycle, the two Li sites on general positions were also refined. The final refinement (Fig. 3.5) converged with a weighted profile R-value of 6.83 % and a Bragg R-value of 1.47 %.

3.3.5 *Structure Description*

The structural analysis of $[Li_2(VO)_2(HPO_4)_2(C_2O_4)]\cdot 6H_2O$ revealed that the compound crystallizes in triclinic space group $P\bar{1}$ with lattice parameters; a = 6.4133(0) Å, b = 9.2173(1) Å, c = 14.6206(0) Å, α = 95.01(5)°, β = 91.79(6)°, γ = 107.76 (2)°, V = 818.38(0) Å^3 and Z = 2. Each vanadium atom is six coordinated, three are shared with three different hydrogenphosphate (HPO_4) groups having V-O

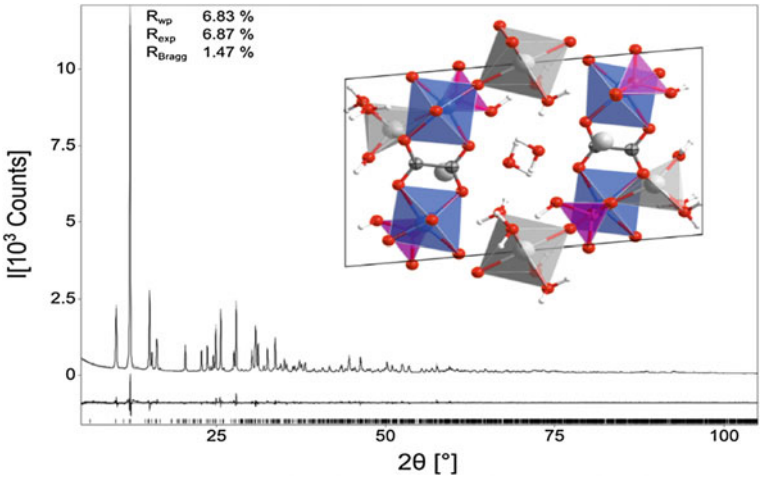

Fig. 3.5 Rietveld refinement of $[Li_2(VO)_2(HPO_4)_2(C_2O_4)]\cdot 6H_2O$. The inset figure shows its crystal structure

bond lengths in the range of 1.956–2.059 Å, two with an oxalate unit ($d_{V\text{-}O}$ = 2.076–2.341 Å) and another to a free oxo ligand with shorter bond length of 1.613–1.619 Å. The distorted octahedral VO_6 units are connected to three different HPO_4 groups by corner sharing, thus forming infinite 1 D chains of ($VOHPO_4$) along the *a*-axis. In these chains, each HPO_4 group in turn is coordinated to three different vanadium atoms with P-O bond length of the range 1.538–1.558 Å and the remaining oxygen atom exists as free OH group. These $VOHPO_4$ chains are interlinked by oxalate ligands in a bis-bidendate fashion, resulting in anionic 2D layers of $[(VO)_2(HPO_4)_2(C_2O_4)]^{2-}$ in the *ab*-plane. Stacking of these layers along the *c*-axis resulted in a layered structure, with Li ions balancing the charge (Fig. 3.6). The Li ions are present in the interlayer space and each lithium sites are environmentally different. The bond valence calculation confirms the oxidation state of vanadium to be +4. Further neutron diffraction studies will be helpful to determine the precise atomic positions of the lithium atoms. Lattice parameters and refinement details of $[Li_2(VO)_2(C_2O_4)(HPO_4)_2]\cdot 6H_2O$ are provided in Table 3.1 and the atomic coordinates are given in Table 3.2.

3.3.6 Galvanostatic Cycling Studies

The as-synthesized hydrated material, $[Li_2(VO)_2(HPO_4)_2(C_2O_4)]\cdot 6H_2O$ was found to contain micron sized particles (Fig. 3.7a). Hence, it was subjected to low energy ball-milling to obtain smaller particles without destroying the crystal structure. The anhydrous phase, $[Li_2(VO)_2(HPO_4)_2(C_2O_4)]$ obtained by dehydration of the hydrated phase, was subjected to galvanostatic charge-discharge cycling in the

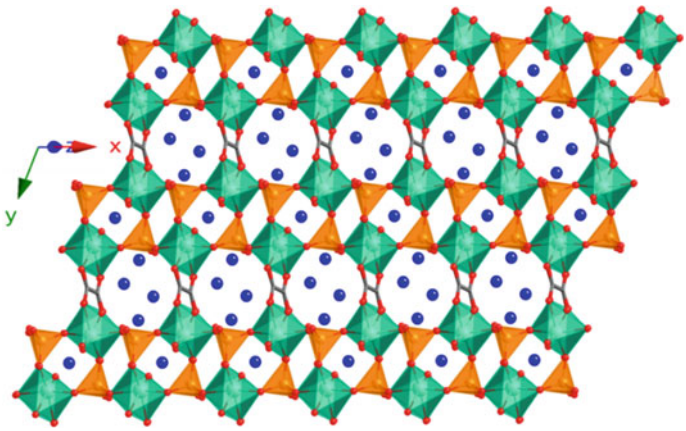

Fig. 3.6 Crystal structure of $Li_2(VO)_2(HPO_4)_2(C_2O_4)\cdot 6H_2O$. Water molecules and hydrogen atoms are removed for clarity. VO_6 octahedra and HPO_4 tetrahedra are shown in green and orange respectively. Lithium atoms and oxygen atoms are shown as *blue* and *red* balls respectively

Table 3.1 Lattice parameters and refinement details of $[Li_2(VO)_2(C_2O_4)(HPO_4)_2]\cdot 6H_2O$

Compound name	Dilithium Bis(vanadylhydrogenphosphate) Oxalate Hexahydrate
Formula sum	$[Li_2(VO)_2(C_2O_4)(HPO_4)_2]\cdot 6H_2O$
Formula weight	535.84 g/mol
Crystal system	Triclinic
Space-group	$P\bar{1}$ (2)
Cell parameters	a = 6.4133(0 Å
	b = 9.2173(1) Å
	c = 14.6206(0) Å
	α = 95.01(5)°
	β = 91.79(6)°
	γ = 107.76 (2)°
Cell volume	818.38(0) $Å^3$
Z	2
Calc. density	2.17 g cm^{-3}
R_{wp}	6.83 %
R_{exp}	6.87 %
R_{Bragg}	1.47 %
Pearson code	aP85
Formula type	NOPQR10…
Wyckoff sequence	i42b

Table 3.2 Atomic Parameters of $Li_2[(VO)_2(C_2O_4)(HPO_4)_2]\cdot 6H_2O$

Atom	Wyck.	S.O.F.	x	y	z	B_{iso} ($Å^2$)
V1	2i	1	0.07627(26)	0.19209(2)	0.28353(36)	1.1141(97)
V2	2i	1	0.42122(77)	0.81421(13)	0.21974(15)	1.1141(97)
Li1	1b	1	0	0	½	0.1[a]
Li2	2i	1	0.10269(77)	0.45563(60)	−0.2792(15)	0.1[a]
Li3	2i	0.5	0.76241(72)	0.2923(49)	0.1337(14)	0.1[a]
C1	2i	1	0.2372(14)	0.4860(4)	0.19774(11)	0.819(81)
C2	2i	1	0.2651(15)	0.52144(53)	0.29829(11)	0.819(81)
O1	2i	1	0.1404(18)	0.35392(47)	0.16573(17)	0.780(10)
O2	2i	1	0.29732(88)	0.59139(27)	0.14909(7)	0.780(10)
O3	2i	1	0.1927(19)	0.41540(68)	0.34547(15)	0.780(10)
O4	2i	1	0.3501(10)	0.65687(49)	0.32664(5)	0.780(10)
P1	2i	1	1.06798(44)	0.15475(49)	−0.18994(9)	1.024(29)
O5	2i	1	1.09422(72)	0.22876(26)	−0.08860(19)	0.780(10)
O6	2i	1	0.89561(47)	0.2054(15)	−0.24308(27)	0.780(10)
O7	2i	1	1.27767(45)	0.21790(14)	−0.2411(16)	0.780(10)
O8	2i	1	1.0010(18)	−0.01996(18)	−0.18735(35)	0.780(10)
H8	2i	1	1.1952(15)	0.20205(33)	−0.04421(25)	0.780(10)
P2	2i	1	−0.42258(11)	0.15759(69)	1.30900(3)	1.024(29)

(continued)

Table 3.2 (continued)

Atom	Wyck.	S.O.F.	x	y	z	B_{iso} (Å^2)
O9	2i	1	−0.21697(88)	0.21296(70)	1.25418(83)	0.780(10)
O10	2i	1	−0.6059(12)	0.2068(10)	1.26306(53)	0.780(10)
O11	2i	1	−0.49440(72)	−0.01548(82)	1.31828(23)	0.780(10)
O12	2i	1	−0.3615(20)	0.24128(12)	1.40795(1)	0.780(10)
H12	2i	1	−0.3760(32)	0.17634(12)	1.46017(8)	0.780(10)
O13	2i	1	0.02647(81)	1.09300(14)	0.3710(27)	0.780(10)
O14	2i	1	0.45208(29)	0.8827(11)	0.12144(57)	0.780(10)
O15	2i	1	0.4209(32)	0.17019(57)	0.06455(32)	0.780(10)
H15A	2i	1	0.3373(32)	0.17088(57)	0.11918(32)	0.780(10)
H15B	2i	1	0.3422(32)	0.20888(57)	0.01910(32)	0.780(10)
O16	2i	1	0.9505(14)	0.21180(14)	−0.43274(25)	0.780(10)
H16A	2i	1	0.8870(14)	0.17169(14)	−0.37677(25)	0.780(10)
H16B	2i	1	0.8623(14)	0.27613(14)	−0.44969(24)	0.780(10)
O17	2i	1	0.8098(25)	0.1293(16)	0.04967(54)	0.780(10)
H17A	2i	1	0.6955(25)	0.0475(16)	0.01353(54)	0.780(10)
H17B	2i	1	0.9170(25)	0.1687(16)	0.00472(53)	0.780(10)
O18	2i	1	1.33701(97)	0.11843(69)	−0.4676(25)	0.780(10)
H18A	2i	1	1.40541(97)	0.20917(69)	−0.42466(25)	0.780(10)
H18B	2i	1	1.35489(97)	0.03471(69)	−0.43484(24)	0.780(10)
O19	2i	1	0.7505(16)	0.4304(14)	0.06532(37)	0.780(10)
H19A	2i	1	0.9065(16)	0.4596(14)	0.05411(37)	0.780(10)
H19B	2i	1	0.6973(16)	0.5005(14)	0.03180(37)	0.780(10)
O20	2i	1	0.72458(90)	0.5247(17)	0.45875(43)	0.780(10)
H20A	2i	1	0.74816(89)	0.5939(17)	0.51526(43)	0.780(10)
H20B	2i	1	0.65277(89)	0.4243(17)	0.47911(43)	0.780(10)

[a]The B_{iso} for Lithium refined to the minimum value allowed in the refinement

voltage window of 2.5–4.5 V *versus* Li/Li^+ using lithium metal as anode. Figure 3.8 shows the voltage *versus* capacity profile of the material for few selected cycles. During the first charge cycle (lithium extraction), voltage increases steeply to ~3.8 V from the open circuit voltage (3.0 V) and then the voltage increases slowly to the cut off voltage of 4.1 V and increases steeply to the cut off voltage of 4.5 V, resulting in a capacity of 75 mAh g^{-1}. When the sample was subjected to lithium re-insertion (discharge), a similar kind of plateau was seen resulting in a discharge capacity of 56 mAh g^{-1}. The sloping plateaus indicate a single phase reaction over the entire lithium extraction/insertion. The subsequent charge-discharge curves showed similar curves indicating a good reversibility of lithium insertion/extraction in the compound. The inset in Fig. 3.8 shows the variation of specific capacity and coulombic efficiency of the material while cycled at 0.1 C current rate. The capacity of the material increases during the initial few cycles and stabilizes after 10 cycles. This increase in capacity might be attributed to the disintegration/breaking of the

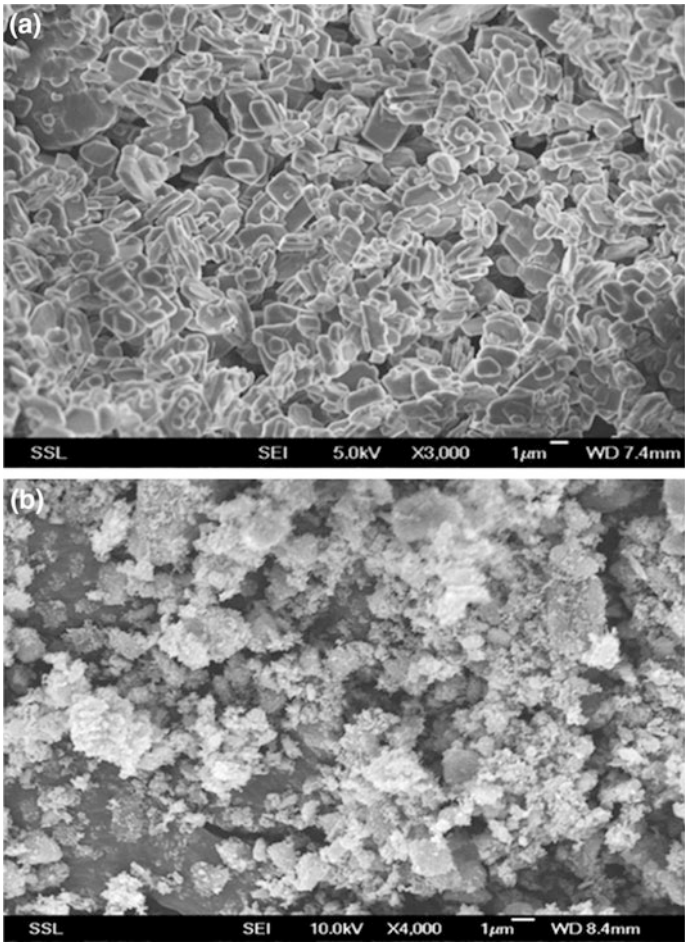

Fig. 3.7 Scanning electron micrographs of **a** as-synthesized and **b** ball-milled $[Li_2(VO)_2(HPO_4)_2(C_2O_4)]\cdot 6H_2O$

particles to smaller size and the consequent ease of lithium diffusion in the electrode [38]. The charge and the discharge capacities obtained at the end of 25 cycles were 83 and 80 mAh g^{-1} respectively which corresponds storage to ~ 1.3 mol of Li per mole of the material. The coulombic efficiency of the material was 97 %. The material exhibits better cycling stability and slightly higher capacity than the previously studies potassium and sodium analogues. $[K_{2.5}(VO)_2(HPO_4)_{1.5}(PO_4)_{0.5}(C_2O_4)]$ showed a capacity of 59 mAh g^{-1} for 60th cycle while the Na analogue provided a capacity of 60 mAh g^{-1} for 25th cycle at 20 mA g^{-1} [26].

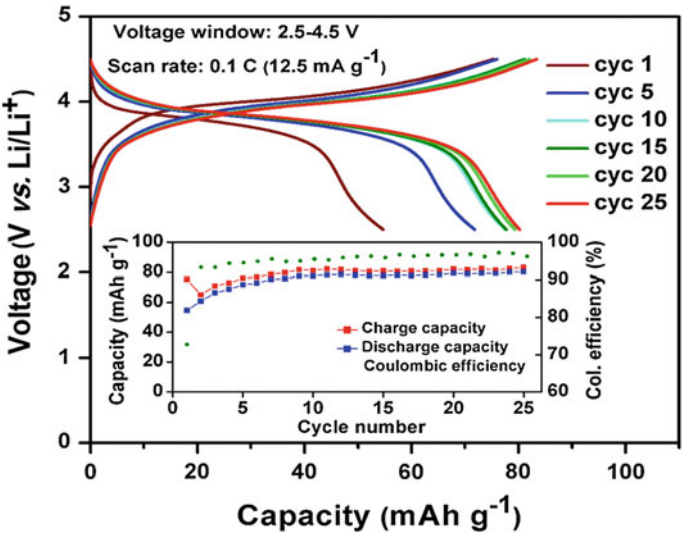

Fig. 3.8 Galvanostatic cycling studies (charge-discharge profiles) of $[Li_2(VO)_2(HPO_4)_2(C_2O_4)]$ at a current density of 12.5 mA g^{-1} (0.1 C), showing voltage versus capacity plots for few selected cycles. The inset figure shows the variation of specific capacity and coulombic efficiency with cycle number

3.3.6.1 Rate Capability

To investigate the rate capability of $[Li_2(VO)_2(HPO_4)_2(C_2O_4)]$, galvanostatic cycling was carried out at different current densities such as 12.5, 25, 62.5, 125, 250 and 500 mA g^{-1} which correspond to 0.1, 0.2, 0.5, 1, 2 and 4 C respectively (1 C represents a current density of 125 mA g^{-1}). When the current density was increased from 12.5 mA g^{-1} to higher, capacity of the material decreased as expected owing to slow diffusion kinetics at higher current rates. The discharge capacities obtained at the end of 20 cycles for the current densities of 25, 62.5, 125, 250 and 500 mA g^{-1} were 72, 64, 58, 52 and 47 mAh g^{-1} (Fig. 3.9). The coulombic efficiency of the material also increases to 98, 99, 99.5, 99.7 and 99.9 % with increase in current rate to 0.2, 0.5, 1, 2 and 4 C respectively. The material also shows good capacity retention at all current rates as shown in Fig. 3.10. By far, this is the best capacity achieved in a MOF and MOPOF cathodes at high current rates.

3.3.7 Cyclic Voltammetry

Cyclic voltammetric studies were carried out with Li metal as counter electrode at a slow scan rate of 58 μV s^{-1}, in the potential window of 2.5–4.5 V for 10 cycles (shown in Fig. 3.11). The first anodic scan started from the open circuit voltage (OCV) of 3.0 V and the voltage was increased slowly to 4.5 V. The anodic peak at

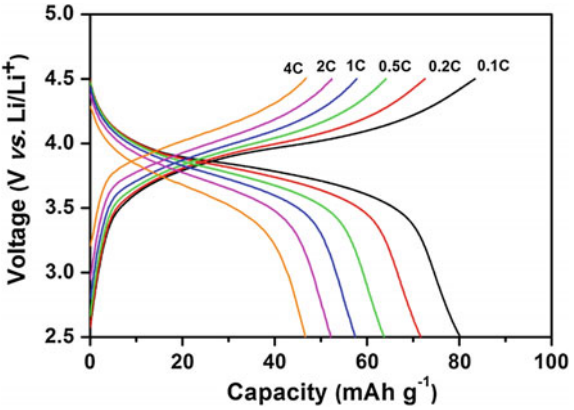

Fig. 3.9 Galvanostatic charge-discharge profiles of $[Li_2(VO)_2(HPO_4)_2(C_2O_4)]$ at different current rates (1 C represents a current density of 125 mA g^{-1})

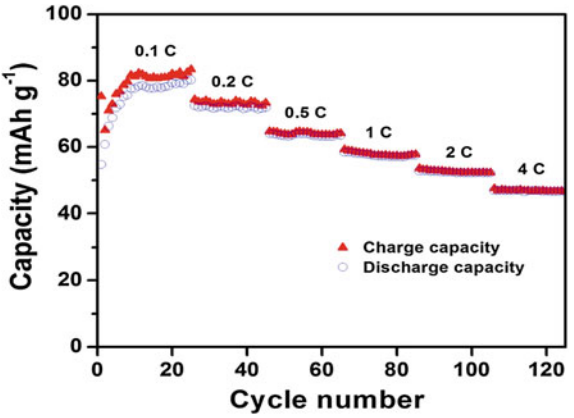

Fig. 3.10 Plot of capacity versus cycle number of $[Li_2(VO)_2(HPO_4)_2(C_2O_4)]$ at various current rates (1 C represents a current density of 125 mA g^{-1})

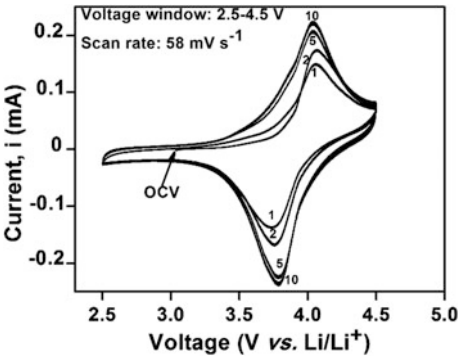

Fig. 3.11 Cyclic voltammograms (CVs) of $[Li_2(VO)_2(HPO_4)_2(C_2O_4)]$ for few selected cycles recorded with a scan rate of 58 μV s^{-1}

4.05 V corresponds to the removal of Li and the simultaneous oxidation of V^{4+} to V^{5+}. During the first cathodic scan to the lower cut-off voltage of 2.5 V, a similar single peak appeared at 3.75 V corresponding to lithium re-insertion and

simultaneous reduction of V^{5+} to V^{4+}. This is in agreement with the redox couple of the sodium and potassium analogues [26] reported earlier and also with the galvanostatic cycling data. The voltammograms of the second and subsequent cycles exhibit similar oxidation and reduction behaviour at almost same voltages indicating the good reversibility of lithium insertion/extraction process in the material. The increasing trend in the capacity during initial few cycles of galvanostatic charge-discharge cycling is also pronounced in the cyclic voltammograms.

3.3.8 Electrochemical Impedance Spectroscopy (EIS)

Reversible lithium insertion in the material was further characterized by EIS studies. Data were collected for the 1st and 6th cycles (both charge and discharge) at various selected voltages. During each voltage increment (charging) and decrement (discharging), the cell was subjected to a current density of 25 mA g^{-1} and was relaxed at the given voltage for 30 min before data collection. The results are plotted as Nyquist plots (Z_{re} *vs.* Z_{im}), where Z_{re} and Z_{im} are respectively the real and imaginary parts of cell impedance (Fig. 3.12). At each voltage, the experimentally observed spectrum was fitted using an equivalent electrical circuit (Fig. 3.12e) and the individual parameters contributing to the total impedance were calculated using Zview software (Table 3.3).

The Nyquist plot for the data collected at open circuit voltage (2.6 V) showed a single semicircle with an overall impedance of $\sim$250 Ω at high to medium frequency range. It may be attributed to the high surface film resistance (R_{sf}) and the associated capacitance (CPE_{sf}). With the onset of lithium extraction, the impedance starts decreasing, and becomes 85–100 Ω in the plateau region. From the fitting of Nyquist plots of first charge cycle at different voltages, the overall observed impedance was found to be the surface film and charge transfer resistances (R_{sf+ct}), though a single semicircle was observed. The electrolyte resistance (R_e) was found to be 3−4 (±0.5) Ω irrespective of the state of discharge/charge of the cell. At 4.5 V, where all the vanadium are converted to V^{5+} state, the impedance slightly increases to 120 Ω. When the cell was subjected to discharge, the impedance was found to be $\sim$120–145 Ω in the plateau region where the lithium insertion is almost complete. Further decrease in the voltage leads to increase in the impedance as shown in Fig. 3.12b.

After few charge-discharge cycles, the impedance was measured again for the 6th cycle (charge and discharge). During the 6th charge cycle an overall impedance of $\sim$100 Ω was observed in the plateau region (3.9–4.3 V) and these values are similar to that of the first charge cycle. This is in agreement with the galvanostatic cycling data for 1st and 6th charge cycles. Similarly, a slight increase in the discharge capacity of 6th cycle compared to 1st cycle as shown in the galvanostatic cycling can be explained by slight decrease in the impedance values during the 6th discharge cycle. Good reversibility in lithium insertion/extraction of the sample can be inferred from the smaller impedance values of the material.

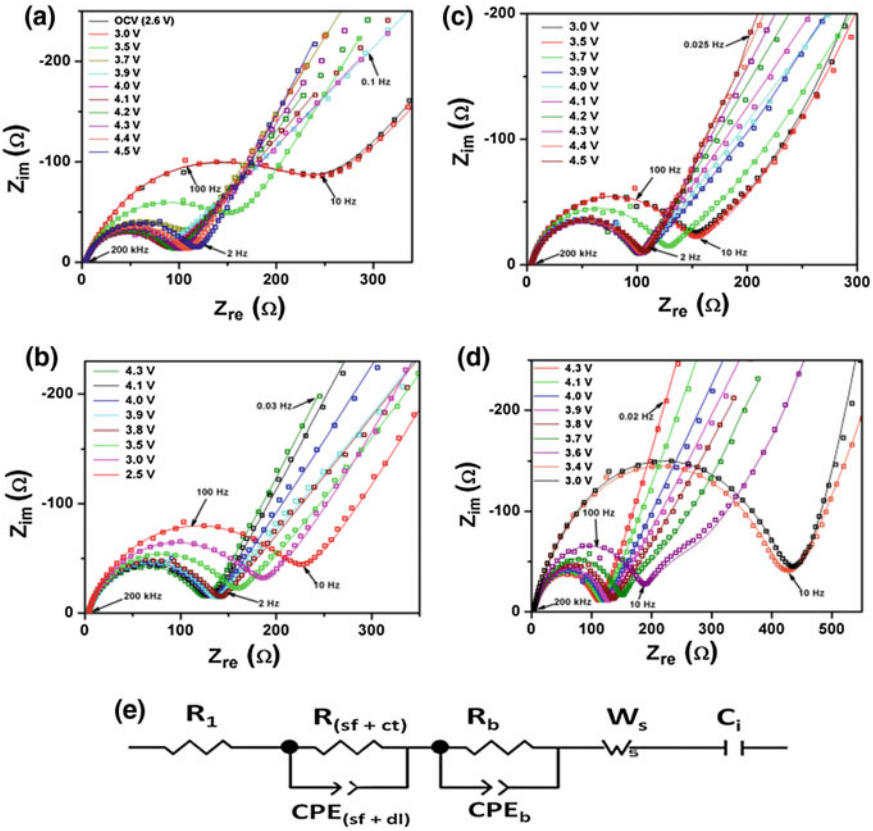

Fig. 3.12 EIS spectra (Nyquist plots) of $[Li_2(VO)_2(HPO_4)_2(C_2O_4)]$ at various voltages during. **a** 1st charge cycle, **b** 1st discharge cycle, **c** 6th charge cycle, **d** 6th discharge cycle and **e** Equivalent circuit used for fitting the experimental Nyquist plots

3.3.9 Ex Situ XRD Studies

Ex situ XRD experiments were carried out to demonstrate the structural stability of the material upon cycling. XRD patterns of the bare electrode and the cycled electrode after 60 cycles (Fig. 3.13) were recorded by fixing the electrode on a glass slide and covering the electrode surface with a kapton film. These XRD patterns prove the retention of the crystal structure of the material even after 60 cycles of lithium insertion/extraction. These preliminary results validate the structural stability of the material upon cycling. Additional information on the crystal structure can be obtained from in situ XRD studies of the cell during electrochemical cycling.

Table 3.3 EIS fitting results of $[Li_2(VO)_2(C_2O_4)(HPO_4)_2]$ at various voltages for 1st and 6th cycles

Voltage (V)	$R_{(sf+ct)}$ (±5 Ω)	$CPE_{(sf+dl)}$ (±3 μF)	α (±0.02)	R_b (±5 Ω)	CPE_b (±3 mF)	C_i (F)
1st charge cycle						
2.6	209	28	0.83	–	–	0.02
3.0	208	27	0.83	–	–	0.07
3.5	144	31	0.80	–	–	3.94
3.7	100	34	0.79	–	–	0.04
3.9	74	32	0.80	–	–	0.22
4.0	81	40	0.76	–	–	1.07
4.1	84	41	0.76	–	–	0.64
4.3	97	41	0.76	–	–	0.58
4.5	112	41	0.76	–	–	0.19
1st discharge cycle						
4.3	123	44	0.75	–	–	0.66
4.1	125	39	0.77	–	–	0.55
4.0	125	31	0.79	–	–	0.75
3.9	124	28	0.81	–	–	2.01
3.7	132	33	0.78	–	–	6.08
3.6	138	35	0.77	–	–	1.03
3.5	145	32	0.79	–	–	0.35
3.4	154	31	0.79	–	–	0.16
3.0	171	31	0.79	–	–	0.05
2.5	212	31	0.78	–	–	0.09
6th charge cycle						
3.0	128	22	0.83	–	–	0.03
3.5	134	23	0.82	–	–	0.06
3.7	114	22	0.82	–	–	0.24
3.9	96	23	0.81	–	–	1.13
4.0	95	25	0.81	–	–	4.22
4.1	94	27	0.80	–	–	1.68
4.3	97	33	0.78	–	–	0.58
4.4	100	34	0.78	–	–	0.27
4.5	101	33	0.78	–	–	0.15
6th discharge cycle						
4.3	108	36	0.77	–	–	0.18
4.1	112	35	0.76	–	–	0.51
4.0	116	34	0.78	–	–	4.04
3.9	119	31	0.79	–	–	2.42
3.8	123	26	0.81	–	–	1.58
3.7	142	27	0.81	29	32	–
3.6	180	28	0.79	71	9	–
3.4	416	32	0.77	–	–	0.20
3.0	425	30	0.77	–	–	0.04

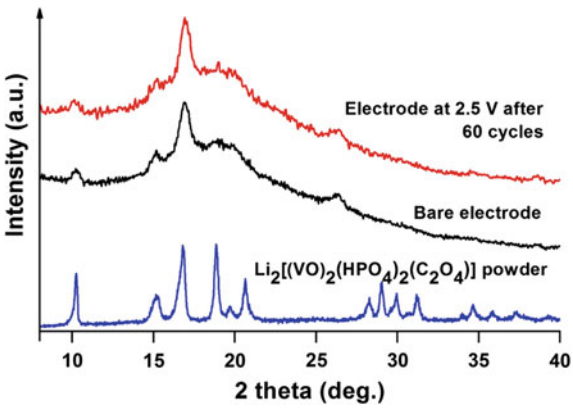

Fig. 3.13 PXRD patterns of bare electrode before cycling and cycled electrode at discharged state (after 60 cycles)

3.4 Conclusions

In summary, a metal organophosphate open framework (MOPOF) material containing extractable lithium was synthesized for the first time and studied as a 4 V cathode material for LIBs. Ab initio structure determination of the compound was carried out from the PXRD data. Electrochemical characterization of $[Li_2(VO)_2(HPO_4)_2(C_2O_4)]$ by galvanostatic cycling, cyclic voltammetry, electrochemical impedance spectroscopy (EIS) and ex situ XRD studies, corroborate the highly reversible lithium insertion/extraction of the compound at $\sim$3.9 V. The material shows a stable reversible capacity of 80 mAh g^{-1} at 0.1 C current rate. In addition, the material exhibits good capacity retention at high current rates. The ability to enhance the energy density of these materials by varying the metal ions, ligands and the cost effective synthetic procedures could lead to significant improvements in battery materials.

References

1. S.-Y. Chung, J.T. Bloking, Y.-M. Chiang, Nat. Mater. **1**, 123–128 (2002)
2. A.K. Padhi, K.S. Nanjundaswamy, J.B. Goodenough, J. Electrochem. Soc. **144**, 1188–1194 (1997)
3. M.K. Devaraju, I. Honma, Adv. Energy Mater. **2**, 284–297 (2012)
4. T.A. Kerr, J. Gaubicher, L.F. Nazar, Electrochem. Solid-State Lett. **3**, 460–462 (2000)
5. K.H. Lii, C.H. Li, C.Y. Cheng, S.L. Wang, J. Solid State Chem. **95**, 352–359 (1991)
6. H. Huang, S.-C. Yin, T. Kerr, N. Taylor, L.F. Nazar, Adv. Mater. (Weinheim, Ger.) **14**, 1525–1528 (2002)
7. X.H. Rui, C. Li, C.H. Chen, Electrochim. Acta **54**, 3374–3380 (2009)
8. H. Karami, F. Taala, J. Power Sources **196**, 6400–6411 (2011)
9. T. Muraliganth, K.R. Stroukoff, A. Manthiram, Chem. Mater. **22**, 5754–5761 (2010)
10. A. Nyten, A. Abouimrane, M. Armand, T. Gustafsson, J.O. Thomas, Electrochem. Commun. **7**, 156–160 (2005)

11. S.J. Kim, J. Suk, Y.J. Yun, H.-K. Jung, S. Choi, Phys. Chem. Chem. Phys. **16**, 2085–2089 (2014)
12. P. Barpanda, M. Ati, B.C. Melot, G. Rousse, J.N. Chotard, M.L. Doublet, M.T. Sougrati, S.A. Corr, J.C. Jumas, J.M. Tarascon, Nat. Mater. **10**, 772–779 (2011)
13. J.M. Clark, C. Eames, M. Reynaud, G. Rousse, J.-N. Chotard, J.-M. Tarascon, M.S. Islam, J. Mater. Chem. A **2**, 7446–7453 (2014)
14. N. Recham, J.N. Chotard, L. Dupont, C. Delacourt, W. Walker, M. Armand, J.M. Tarascon, Nat. Mater. **9**, 68–74 (2010)
15. Y. Janssen, D.S. Middlemiss, S.-H. Bo, C.P. Grey, P.G. Khalifah, J. Am. Chem. Soc. **134**, 12516–12527 (2012)
16. L. Tao, G. Rousse, J.N. Chotard, L. Dupont, S. Bruyere, D. Hanzel, G. Mali, R. Dominko, S. Levasseur, C. Masquelier, J. Mater. Chem. A **2**, 2060–2070 (2014)
17. M. Tamaru, P. Barpanda, Y. Yamada, S.-I. Nishimura, A. Yamada, J. Mater. Chem. **22**, 24526–24529 (2012)
18. S.-I. Nishimura, M. Nakamura, R. Natsui, A. Yamada, J. Am. Chem. Soc. **132**, 13596–13597 (2010)
19. J. Barker, M.Y. Saidi, J.L. Swoyer, J. Electrochem. Soc. **150**, A1394–A1398 (2003)
20. M.V. Reddy, G.V. Subba, Rao and B. V. R. Chowdari. J. Power Sources **195**, 5768–5774 (2010)
21. S.-L. Li, Q. Xu, Energy Environ. Sci. **6**, 1656–1683 (2013)
22. X. Li, F. Cheng, S. Zhang, J. Chen, J. Power Sources **160**, 542–547 (2006)
23. G. Férey, F. Millange, M. Morcrette, C. Serre, M.-L. Doublet, J.-M. Grenèche, J.-M. Tarascon, Angew. Chem. Int. Ed. **46**, 3259–3263 (2007)
24. G. de Combarieu, M. Morcrette, F. Millange, N. Guillou, J. Cabana, C.P. Grey, I. Margiolaki, G. Ferey, J.M. Tarascon, Chem. Mater. **21**, 1602–1611 (2009)
25. K. Saravanan, M. Nagarathinam, P. Balaya, J.J. Vittal, J. Mater. Chem. **20**, 8329–8335 (2010)
26. M. Nagarathinam, K. Saravanan, E.J.H. Phua, M.V. Reddy, B.V.R. Chowdari, J.J. Vittal, Angew. Chem. Int. Ed. **51**, 5866–5870 (2012)
27. J.F. Colin, T. Bataille, S.E. Ashbrook, N. Audebrand, L. Le Pollès, J.Y. Pivan, E. Le Fur, Inorg. Chem. **45**, 6034–6040 (2006)
28. F.R. Kizewski, P. Boyle, D. Hesterberg, J.D. Martin, J. Am. Chem. Soc. **132**, 2301–2308 (2010)
29. C.-Y. Sheu, S.-F. Lee, K.-H. Lii, Inorg. Chem. **45**, 1891–1893 (2006)
30. S. Natarajan, S. Mandal, Angew. Chem. Int. Ed. **47**, 4798–4828 (2008)
31. I.C. Madsen, R.J. Hill, J. Appl. Cryst. **27**, 385–392 (1994)
32. A. Coelho, J. Appl. Cryst. **36**, 86–95 (2003)
33. R.W. Cheary, A. Coelho, J. Appl. Cryst. **25**, 109–121 (1992)
34. R.W. Cheary, A.A. Coelho, J. Appl. Cryst. **31**, 862–868 (1998)
35. C. Scheringer, Acta Crystallogr. **16**, 546–550 (1963)
36. H. Rietveld, J. Appl. Cryst. **2**, 65–71 (1969)
37. W. Dollase, J. Appl. Cryst. **19**, 267–272 (1986)
38. M. Bianchini, J.M. Ateba-Mba, P. Dagault, E. Bogdan, D. Carlier, E. Suard, C. Masquelier, L. Croguennec, J. Mater. Chem. A **2**, 10182–10192 (2014)

Chapter 4
Room Temperature Synthesis of rGO/$[K_2(VO)_2(C_2O_4)(HPO_4)_2]$ for Greener and Cheaper Lithium Ion Batteries

Abstract This chapter deals with the synthesis of a MOPOF material, $[K_2(VO)_2(HPO_4)_2(C_2O_4)]$ and its rGO composites for application as cathode materials for Lithium ion batteries. Synthesis of a hydrated phase, $[K_2(VO)_2(HPO_4)_2(C_2O_4)]\cdot 4.5H_2O$ was achieved at room temperature by a simple magnetic stirring. The rGO composites of the material was prepared by carrying out the reaction in the presence of graphene oxide. During the synthesis, tartaric acid was used as the organic ligand which was found to undergo in situ oxidation to oxalate resulting in formation of oxalatophosphate framework. The anhydrous phase, $[K_2(VO)_2(HPO_4)_2(C_2O_4)]$ and the composite rGO/$[K_2(VO)_2(HPO_4)_2(C_2O_4)]$ were obtained by dehydration of the respective hydrated phases at 120 °C. These phases were investigated as 4 V cathode for Lithium ion batteries. The pristine compound undergoes highly reversible lithium storage with good capacity. However, there was slight capacity fading. The rGO composites (4 and 8 wt% of rGO) exhibit enhanced lithium cycling with excellent capacity retention.

4.1 Introduction

As discussed in the introduction chapter, the cost of cathode material accounts for more than 40 % of the total cost of LIBs [1]. Cost reduction is one of the important issue to achieve better LIB technology for large scale utilization in electric vehicles and for the storage and utilization of renewable energy. The others issues are the operational safety, identification and development of electrode materials with high energy density and finding electrolyte materials that can cater high voltage cathodes [2, 3].

In the previous chapter, investigation of the novel family of cathodes known as MOPOFs has been described. The oxalatophosphate frameworks, $A_2(VO)_2(HPO_4)_2(C_2O_4)$; (A = Li, Na or K) are constructed from transition metal phosphates cross-linked by oxalate ligand. This class of inorganic-organic hybrid framework materials can encapsulate different alkali ions (Li^+, Na^+, K^+ and Cs^+) between the layers made of anionic frameworks [4–8]. These MOPOF materials

A.S. Hameed, *Phosphate Based Cathodes and Reduced Graphene Oxide Composite Anodes for Energy Storage Applications*,
Springer Theses, DOI 10.1007/978-981-10-2302-6_4

have been proved to undergo reversible lithiation at ~4 V with a good theoretical capacity of 108–125 mAh g^{-1}. These MOPOF materials were prepared by hydrothermal reaction at 120 °C followed by dehydration. During the first charge, Na^+ or K^+ is removed from the framework and the discharge cycle comprises the insertion of lithium into the framework [4]. Feasibility of K^+ exchange by Li^+ ions was demonstrated by isolation and characterization of the lithiated species after few charge-discharge cycles. However, the compounds were found to undergo reversible cycling of only ~1.2 Li^+ resulting in a capacity, much lesser than the theoretical capacity. Slight improvement in the capacity was observed for the lithium analogue (Chap. 3) especially at high current rates. To achieve better capacity, electronic conductivity and Li diffusion of the sample need to be improved.

In this study, $[K_2(VO)_2(HPO_4)_2(C_2O_4)]\cdot 4.5H_2O$ was synthesized just at room temperature by simple magnetic stirring. This synthetic procedure has double advantages. Firstly, the hydrothermal synthesis with autoclave limits scaling up of reaction while this reaction procedure can be optimized for large scale synthesis. Secondly, particle size of the material can be smaller than the hydrothermally obtained sample which helps in improved lithium storage. In addition, the rGO composites of the MOPOF material were prepared since the better electronic conductivity of the composites can enhance the lithium storage performance.

4.2 Experimental Section

All the chemicals and solvents used in this study are commercially available and used without further purification.

4.2.1 Preparation of Graphene Oxide

Graphene oxide was prepared in this study according to a previous publication [9, 10]. Graphite powder (2 g) was added carefully to an 80 °C mixture of concentrated H_2SO_4 (3 mL), $K_2S_2O_8$ (1 g), and P_2O_5 (1 g) and stirred for few minutes until a dark blue mixture was obtained. The mixture was allowed to cool to room temperature over a period of 8 h. Later, it was carefully diluted with ~1 L of distilled water. The partially oxidized graphite was filtered and washed with distilled water until the pH of the filtrate became neutral. The product was then dried overnight in air at room temperature. The partially oxidized graphite powder (2 g) was slowly added to 50 mL of cold (0 °C) conc H_2SO_4 and 6 g of $KMnO_4$ was added in small amounts with continuous stirring so that the temperature of the mixture was never allowed to reach 20 °C. After complete addition of $KMnO_4$, the temperature of the mixture was increased to 35 °C and stirred for 2 h. Then 200 mL of distilled water was added carefully. After 15 min of stirring, the reaction was terminated by the addition of ~2 L of distilled water and 5 mL of 35 % H_2O_2. The

colour of the mixture changed to bright yellow. The mixture was filtered and washed with 1:10 HCl solution (500 mL) for the removal of metal ions. The resulting product was washed with water and suspended in distilled water to prepare 0.1 % (w/v) solution. To prepare graphene oxide (GO), the graphite oxide dispersion was exfoliated by sonication on an ultrasonic bath for 30 min. The resulting GO solution was yellowish brown in colour and was stable over a period of few months.

4.2.2 Synthesis of $[K_2(VO)_2(HPO_4)_2(C_2O_4)]$

Synthesis of $[K_2(VO)_2(HPO_4)_2(C_2O_4)]\cdot 4.5H_2O$ was carried out at room temperature by a simple magnetic stirring. In a typical synthesis, an aqueous mixture containing vanadium pentoxide (Alfa Aesar, 98 %), tartaric acid (Merck, 99.5 %) and potassium hydroxide (BDH, 99 %) in a molar ratio of 1:1.4:4 was prepared and stirred until a clear brown solution was obtained. Then, phosphoric acid (20 molar ratio) was slowly added and stirred continuously for 12 h to obtain a bluish green precipitate of $[K_2(VO)_2(HPO_4)_2(C_2O_4)]\cdot 4.5H_2O$. In this reaction, the tartrate ligand was found to undergo in situ decompose to oxalate, resulting in the oxalatophosphate framework. The resultant precipitate was filtered, washed with distilled water and dried in air.

$[K_2(VO)_2(HPO_4)_2(C_2O_4)]\cdot 4.5H_2O$ was also prepared by mechanical grinding. The reactants in the above mentioned ratio were added to an electric mortar grinder (RM 100, Retsch) and ground for 30 min using minimum quantity of water. A similar bluish green precipitate was obtained which was filtered and washed with water.

The compound could also be synthesized by a sonochemical reaction using an ultrasonic bath. Firstly, an aqueous solution containing V_2O_5, H_4tar and KOH in the ratio of 1:1.4:4 was prepared by sonication for few minutes. After a clear solution was obtained, H_3PO_4 was added and sonication of the mixture was continued for another 30 min which resulted in a bluish green precipitate of the desired product.

The anhydrous compound, $[K_2(VO)_2(HPO_4)_2(C_2O_4)]$ was obtained by dehydration of the hydrated phase at $\sim$120 °C in vacuum and used for electrochemical characterization.

4.2.3 Synthesis of rGO/$[K_2(VO)_2(HPO_4)_2(C_2O_4)]$

Synthesis of the rGO composite of the MOPOF material, rGO/$[K_2(VO)_2(HPO_4)_2(C_2O_4)]\cdot 4.5H_2O$ was carried out at room temperature by magnetic stirring. In a typical synthesis, 50 or 100 mL of GO solution (0.1 wt%) was added to a 10 mL aqueous solution containing vanadium pentoxide (Alfa Aesar, 98 %), tartaric acid (Merck, 99.5 %) and potassium hydroxide (BDH, 99 %) in a molar ratio of

1:1.4:8 and stirred for 2 h. To the resulting brown solution, phosphoric acid (20 molar ratio) was added and stirred continuously for 12 h to obtain the greyish precipitate of rGO/$[K_2(VO)_2(HPO_4)_2(C_2O_4)]\cdot 4.5H_2O$. Elemental analysis determined the rGO in the two samples as 4 and 8 %. The resultant precipitate was filtered, washed with distilled water and dried in air. The anhydrous composites obtained by dehydration of the hydrated composites were used for electrochemical testing.

4.2.4 Structural and Electrochemical Characterization

Details of the structural, morphological and electrochemical characterization methods used for the prepared composites are described in Chap. 2.

4.3 Results and Discussion

4.3.1 Structural Analysis

As described in Sect. 4.2.2, synthesis of the MOPOF material, $[K_2(VO)_2(HPO_4)_2(C_2O_4)]\cdot 4.5H_2O$ was carried out at room temperature by three different methods namely, magnetic stirring, mechanical grinding and sonochemical reaction. PXRD patterns of the product obtained by the different reactions are presented in Fig. 4.1. Formation of pure phase of $[K_2(VO)_2(HPO_4)_2(C_2O_4)]\cdot 4.5H_2O$ without any noticeable impurities was evidenced from the PXRD patterns. In our attempt to synthesize the hybrid inorganic-organic framework containing

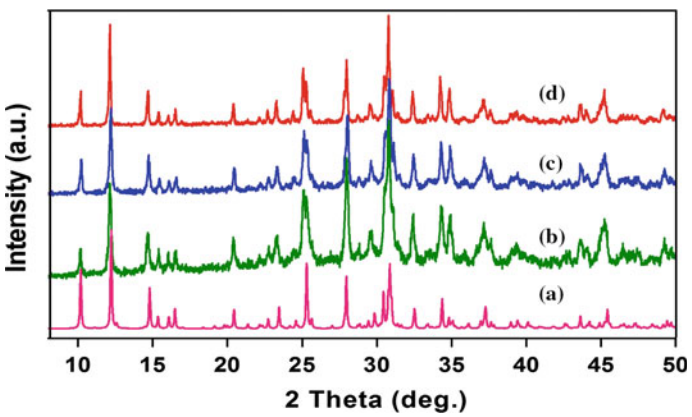

Fig. 4.1 *a* Simulated powder pattern of $[K_2(VO)_2(HPO_4)_2(C_2O_4)]\cdot 4.5H_2O$. PXRD patterns of $[K_2(VO)_2(HPO_4)_2(C_2O_4)]\cdot 4.5H_2O$ prepared by *b* RT stirring, *c* grinding and *d* sonochemical synthesis

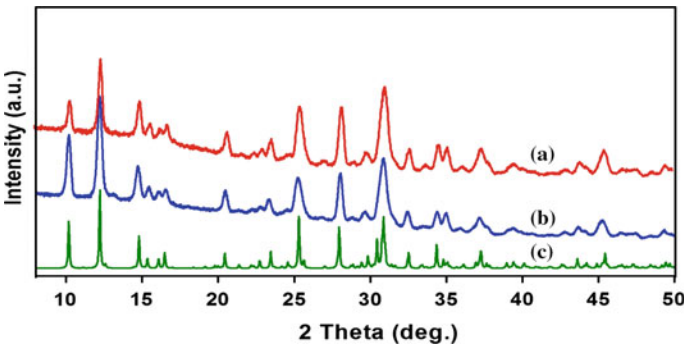

Fig. 4.2 PXRD patterns of *a* rGO/$[K_2(VO)_2(HPO_4)_2(C_2O_4)]\cdot 4.5H_2O$; *b* pristine compound and *c* simulated pattern

tartrate and phosphate ligands, reactions were carried out using tartaric acid as the source for organic part. However, during the reaction, tartrate was found to undergo in situ decomposition to oxalate resulting in the precipitation of oxalatophosphate ramework. In situ decomposition of various organic ligands such as pyridinedicarboxylate [11, 12], croconate [13], orotate [14] and tartrate [15] to oxalate has been reported in the literature which support this observation.

Figure 4.2 shows the PXRD patterns of pristine and rGO composites of $[K_2(VO)_2(HPO_4)_2(C_2O_4)]\cdot 4.5H_2O$. The XRD patterns match well with the simulated pattern of $[K_2(VO)_2(HPO_4)_2(C_2O_4)]\cdot 4.5H_2O$, indicating formation of the rGO composites in pure phase. Rietveld refinement of the pristine sample and the rGO composite are shown in Fig. 4.3a, b respectively. As can be seen the experimental pattern matches well with the calculated pattern.

4.3.2 In Situ PXRD

In situ PXRD of $[K_2(VO)_2(HPO_4)_2(C_2O_4)]\cdot 4.5H_2O$ was carried out to investigate its dehydration behaviour. Figure 4.4 shows the XRD patterns recorded in air at intervals of 5 °C from room temperature to 150 °C. With increase in temperature from RT, the peak intensity at $2\theta = 12.2°$ decreases and at 50 °C new peak start appearing at $2\theta = 13.2°$. This indicates the formation of the dihydrate phase by loss of 2.5 mol of water. At 75 °C, the dihydrate phase is present alone as the pure phase. All the water molecules are completely lost at 90 °C, forming the anhydrous phase as indicated by the disappearance of peak at 13.2° while new peak appear at 14.8°. The XRD pattern remain the same till 150 °C. Thus the anhydrous phase can be obtained above 90 °C.

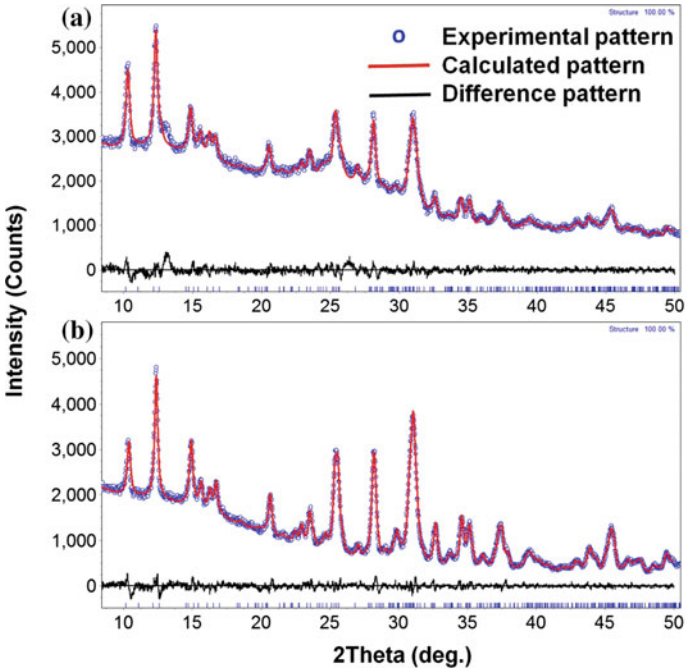

Fig. 4.3 Rietveld refinement of PXRD patterns of **a** pristine $[K_2(VO)_2(HPO_4)_2(C_2O_4)]\cdot 4.5H_2O$ and **b** rGO composite of $[K_2(VO)_2(HPO_4)_2(C_2O_4)]\cdot 4.5H_2O$

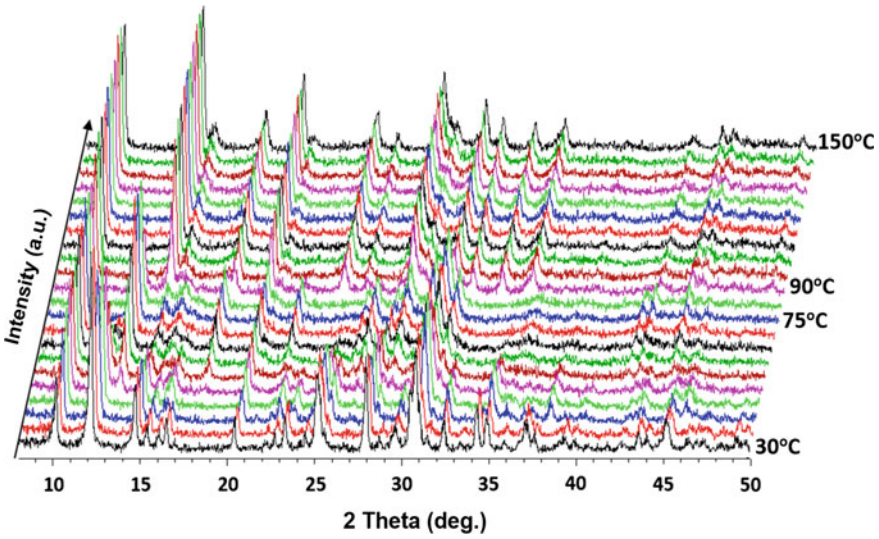

Fig. 4.4 In-situ PXRD patterns of $[K_2(VO)_2(HPO_4)_2(C_2O_4)]\cdot 4.5H_2O$ recorded in air between 30 and 150 °C

4.3.3 TGA

TGA of $[K_2(VO)_2(HPO_4)_2(C_2O_4)]\cdot 4.5H_2O$ (Fig. 4.5) was carried out between RT and 900 °C. It shows two continuous weight loss steps between before 100 °C, which correspond to the removal of water molecules. In the first weight loss step, 2.5 H_2O molecules (8 %) are lost while the second weight loss of ~7 % corresponds to removal of other two molecules of water. (Observed, 14.6 %, Calculated, 14.2 %.) This can be interpreted as the formation of dihydrate phase and the anhydrous phase during first and second weight loss steps respectively. This is in agreement with the in situ XRD results. The weight loss between ~300 and 450 °C can be interpreted as the loss of oxalate ligand and hydrogen atoms from HPO_4 units (Observed, 16.1 %, Calculated, 15.3 %). From the TGA and in situ XRD results, the ideal temperature for dehydration of $[K_2(VO)_2(HPO_4)_2(C_2O_4)]\cdot 4.5H_2O$ was found to be ~120–200 °C.

4.3.4 Raman Spectroscopy

Raman spectroscopy of the rGO/$[K_2(VO)_2(HPO_4)_2(C_2O_4)]\cdot 4.5H_2O$ was carried out to analyse the presence of rGO in the composites. Figure 4.6 shows the Raman spectra of bare GO sample and rGO composites of $[K_2(VO)_2(HPO_4)_2(C_2O_4)]\cdot 4.5H_2O$ containing 4 and 8 % rGO. Bare GO (Fig. 4.6a) shows Raman bands at 1600 and 1350 cm^{-1} which are described as G and D bands respectively. The D band is attributed to the defects and disordered atomic arrangement caused by sp^3-carbon atom while the plane vibration of the sp^2-carbon atom in the two dimensional lattice gives rise to the G band. The I_D/I_G ratio of Graphene oxide is lower,

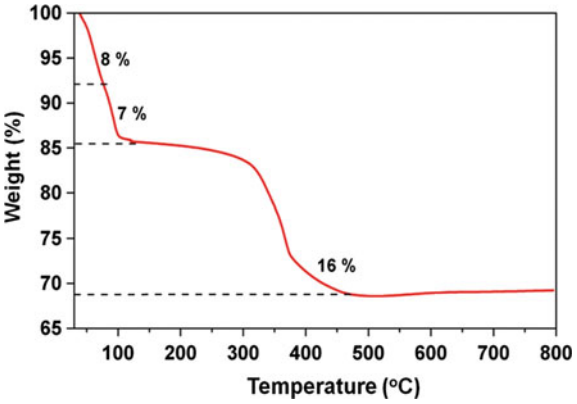

Fig. 4.5 TGA of $[K_2(VO)_2(HPO_4)_2(C_2O_4)]\cdot 4.5H_2O$ in N_2 flow at a heating rate of 5 °C min^{-1}

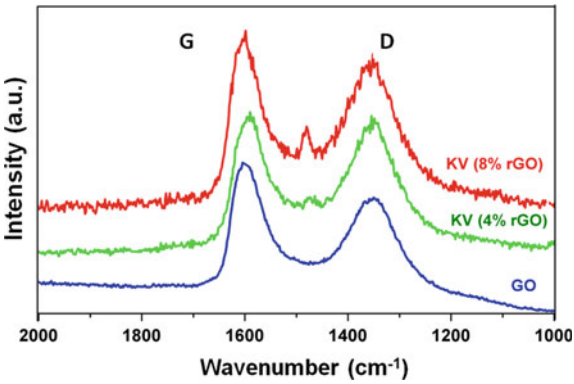

Fig. 4.6 Raman spectra of GO; KV (4 % rGO) and KV (8 % rGO)

while the reduction of GO results in higher I_D/I_G ratio. In the case of the rGO/$[K_2(VO)_2(HPO_4)_2(C_2O_4)]\cdot 4.5H_2O$ composites, the I_D/I_G ratio are higher than the bare GO indicating the reduction of graphene oxide. The composite with 4 % rGO shows I_D/I_G ratio of close to unity, indicating better reduction of GO in the sample.

4.3.5 Morphology

The morphology and particle size of the prepared composites were investigated with SEM and TEM. Figure 4.7 shows the SEM images of bare sample and rGO composites. As the compound exhibits a layered structure, it crystallizes in the form of plates. The bare sample has particle size of ~1 μm (Fig. 4.7a) while the rGO composites displayed decreased particle size. When the reaction time was limited to 12 h, nanoplates of size ~100–200 nm was formed which are wrapped by rGO layers (Fig. 4.7 d and f). This is supported by the TEM images (Fig. 4.8a, b) which clearly indicates the presence of nanoparticles of $[K_2(VO)_2(HPO_4)_2(C_2O_4)]\cdot 4.5H_2O$ wrapped by rGO layers. The increased rGO content helps in holding the nanoparticles together. With increase in the reaction time to 48 h, particle size increases to ~0.5–2 μm as evident from the SEM image (Fig. 4.7b) and the TEM images (Fig. 4.8c, d). The presence of rGO can assist in improving the electronic conductivity of the sample and hence better lithium storage.

The porosity and Brunauer-Emmett-Teller (BET) specific surface area of rGO composites of $[K_2(VO)_2(HPO_4)_2(C_2O_4)]\cdot 4.5H_2O$ containing 4 and 8 % of rGO were investigated using N_2 adsorption-desorption isotherms (Fig. 4.9). The samples with 4 and 8 % rGO possess considerably good BET surface area of 6.7 and 7.9 $m^2\ g^{-1}$. This can be attributed to the rGO and nanosized particles. The pore diameter of the two samples were 12.5 and 11.3 nm respectively.

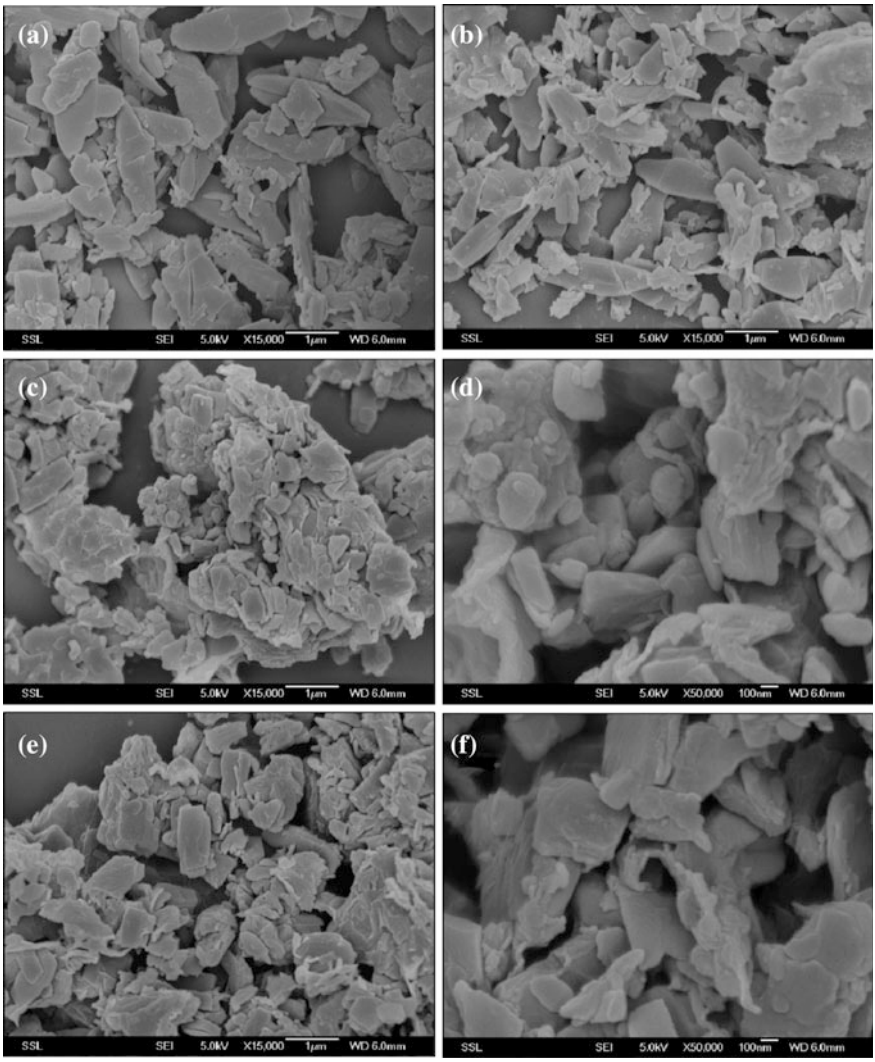

Fig. 4.7 SEM images of **a** bare $[K_2(VO)_2(HPO_4)_2(C_2O_4)]\cdot 4.5H_2O$; **b** rGO/$[K_2(VO)_2(HPO_4)_2(C_2O_4)]\cdot 4.5H_2O$ containing 4 % rGO prepared in 48 h; **c** and **d** rGO composite (4 % rGO) prepared in 12 h and **e** and **f** rGO composite (8 % rGO) prepared in 12 h

4.3.6 Galvanostatic Cycling

Galvanostatic cycling studies of bare $[K_2(VO)_2(HPO_4)_2(C_2O_4)]$ and the rGO composites were carried out in the voltage window of 2.5–4.5 V *versus* Li/Li^+ using lithium metal as the counter electrode. Preliminary battery testing of the bare sample prepared by RT stirring, mechanical grinding and sonochemical reaction

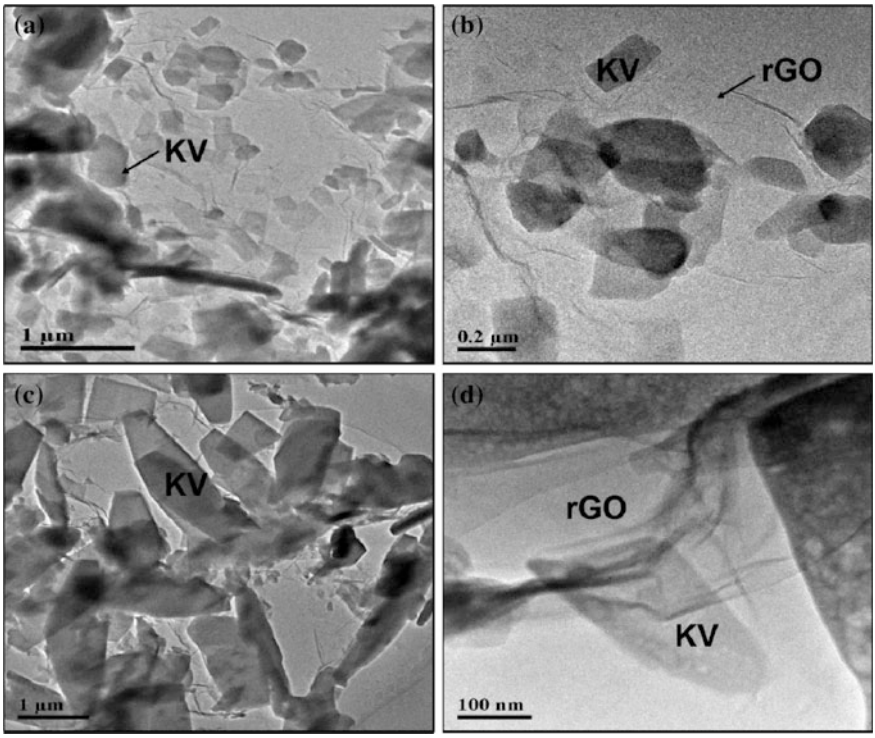

Fig. 4.8 TEM images of rGO/$[K_2(VO)_2(HPO_4)_2(C_2O_4)]\cdot 4.5H_2O$ containing 4 % rGO prepared in 12 h (**a** and **b**), prepared in 48 h (**c** and **d**)

was carried out to find the optimum condition. The RT stirred sample provided the best result than the other two samples. Hence, the rGO/$[K_2(VO)_2(HPO_4)_2(C_2O_4)]$ composites were prepared by magnetic stirring at room temperature.

Figure 4.10 shows the galvanostatic cycling results of the bare sample obtained by RT stirring. A constant current density of 11 mA g^{-1} was applied which corresponds to a current rate of 0.1 C. During the first charge cycle K^+ ions are extracted from the framework resulting in a flat plateau at 4.1 V. This indicates a bi-phasic reaction which results in a capacity of 122 mAh g^{-1}. When the sample was subjected to discharge, Li^+ ions are inserted into the framework in preference to K^+ ions as proved by ex situ EDX studies in the previous study. The sloping plateau of the discharge indicates a single phase behaviour constituting of a solid solution, $[Li_x(VO)_2(HPO_4)_2(C_2O_4)]$. During the second and subsequent cycles, lithium extraction (discharge) and lithium re-insertion (discharge) exhibits a similar kind of plateau showing good reversibility of lithium cycling in the sample. However, a slight decrease in the capacity of the sample was observed upon cycling as shown in Fig. 4.12. The capacity decreases from 100 to 87 mAh g^{-1} at the end of 30 cycles.

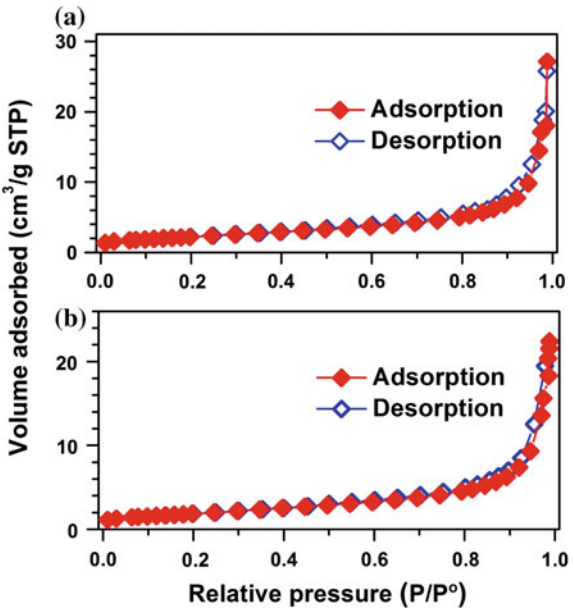

Fig. 4.9 N_2 adsorption-desorption isotherms of rGO composites of $[K_2(VO)_2(HPO_4)_2(C_2O_4)]$ containing **a** 8 % rGO and **b** 4 % rGO

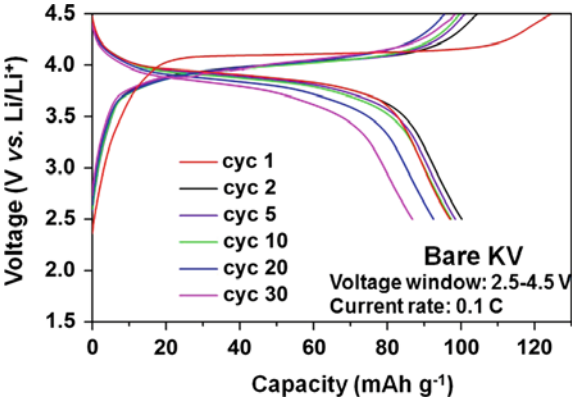

Fig. 4.10 Galvanostatic cycling studies of $[K_2(VO)_2(HPO_4)_2(C_2O_4)]$ in the voltage range, 2.5–4.5 V at a current density of 11 mA g^{-1} (0.1 C), showing voltage *versus* capacity profiles for few selected cycles

The lithium storage in the sample was found to be better than the $[K_{2.5}(VO)_2(HPO_4)_2(C_2O_4)]$ sample reported previously. This can be explained as the decrease in particle size of the sample prepared by magnetic stirring compared to the hydrothermally obtained big particles of few hundred microns. Though the decreased particle size may help in improved lithium diffusion, the electronic conductivity was still poor leading to capacity fading. Hence, rGO composites of the MOPOF material were prepared and investigated.

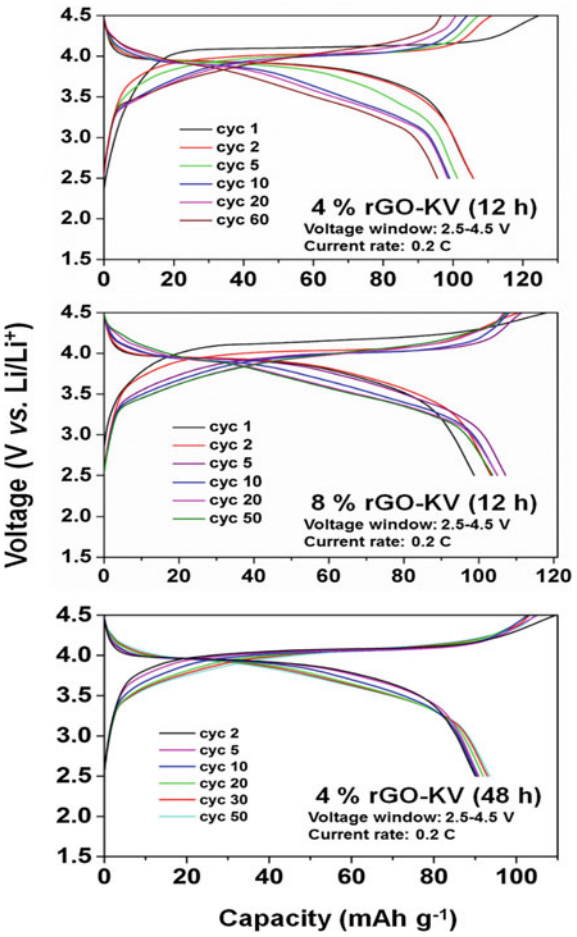

Fig. 4.11 Galvanostatic cycling studies of different rGO/$[K_2(VO)_2(HPO_4)_2(C_2O_4)]$ composites in the voltage range, 2.5–4.5 V at a current density of 20 mA g^{-1} (0.19 C), showing voltage *versus* capacity profiles

Figure 4.11 shows the voltage *vs.* capacity profile of rGO/$[K_2(VO)_2(HPO_4)_2(C_2O_4)]$ for few selected cycles. The weight of the MOPOF material alone was considered for capacity calculation. Similar to the bare sample, rGO composites show initial flat plateau indicating the removal of K^+ ions by a bi-phasic reaction. In the first discharge cycle and subsequent charge/discharge cycles, Li ions are preferably inserted/extracted. The capacity was improved for the rGO composites than the bare sample. However, slight drop in the voltage was observed with increase in cycle number. With increase in the rGO content to 8 % from 4 %, the capacity retention was improved as shown in Fig. 4.12. When the reaction time was increased from 12 to 48 h, the particle size increases as shown in Fig. 4.8, which resulted in decreased capacity and poor coulombic efficiency. However, the voltage drop was found to be avoided. Hence, further optimization of rGo content and the reaction time may be beneficial.

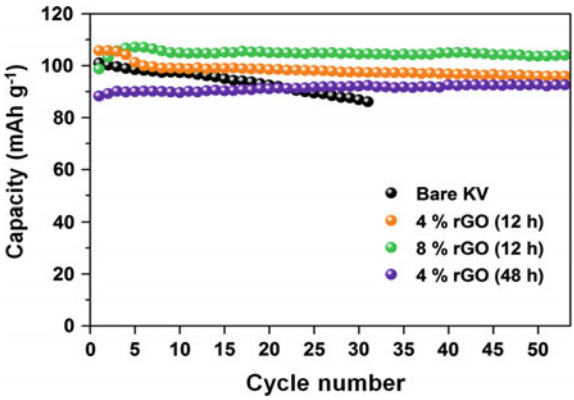

Fig. 4.12 Capacity (discharge) versus cycle number plots of bare $[K_2(VO)_2(HPO_4)_2(C_2O_4)]$ and different rGO/$[K_2(VO)_2(HPO_4)_2(C_2O_4)]$ composites

4.4 Conclusions

In summary, the MOPOF material, $[K_2(VO)_2(HPO_4)_2(C_2O_4)]\cdot 4.5H_2O$ and its rGO composites were successfully obtained at room temperature by magnetic stirring. Tartaric acid used as the organic ligand was found to undergo in situ decomposition to oxalate resulting in the oxalatophosphate framework. Thus the oxalatophosphate compound was achieved at room temperature. The anhydrous phases obtained by dehydration at 120 °C were investigated as cathode materials for Lithium ion batteries. The bare $[K_2(VO)_2(HPO_4)_2(C_2O_4)]$ sample exhibits better capacity than the previous report. However, it undergoes slight capacity fading upon cycling. The rGO/$[K_2(VO)_2(HPO_4)_2(C_2O_4)]$ composites exhibits enhanced lithium cycling than the pristine sample and possess excellent capacity retention throughout the cycling with minimal capacity fading.

References

1. R.J. Brodd, C. Helou, J. Power Sources **231**, 293–300 (2013)
2. J.B. Goodenough, Y. Kim, Chem. Mater. **22**, 587–603 (2010)
3. B. Scrosati, J. Garche, J. Power Sources **195**, 2419–2430 (2010)
4. M. Nagarathinam, K. Saravanan, E.J.H. Phua, M.V. Reddy, B.V.R. Chowdari, J.J. Vittal, Angew. Chem. Int. Ed. **51**, 5866–5870 (2012)
5. J.F. Colin, T. Bataille, S.E. Ashbrook, N. Audebrand, L. Le Polles, J.Y. Pivan, E. Le Fur, Inorg. Chem. **45**, 6034–6040 (2006)
6. S.F. Lee, T.C. Tsai, G.S. Chang, C.Y. Sheu, K.H. Lii, J. Appl. Phys. **101**, 09E107/101–109E107/103 (2007)
7. C.-Y. Sheu, S.-F. Lee, K.-H. Lii, Inorg. Chem. **45**, 1891–1893 (2006)
8. X. Yang, J. Li, Y. Hou, S. Shi, Y. Shan, Inorg. Chim. Acta **361**, 1510–1514 (2008)

9. W.S. Hummers Jr., R.E. Offeman, J. Am. Chem. Soc. **80**, 1339 (1958)
10. N.I. Kovtyukhova, P.J. Ollivier, B.R. Martin, T.E. Mallouk, S.A. Chizhik, E.V. Buzaneva, A.D. Gorchinskiy, Chem. Mater. **11**, 771–778 (1999)
11. D. Min, S.W. Lee, Inorg. Chem. Commun. **5**, 978–983 (2002)
12. X.-W. Wang, X. Li, J.-Z. Chen, G. Zheng, H.-L. Hong, Eur. J. Inorg. Chem. 98–105 (2008)
13. D. Deguenon, G. Bernardinelli, J.P. Tuchagues, P. Castan, Inorg. Chem. **29**, 3031–3037 (1990)
14. X. Li, R. Cao, D. Sun, Q. Shi, W. Bi, M. Hong, Inorg. Chem. Commun. **6**, 815–818 (2003)
15. Y.-K. Lv, Y.-L. Feng, J.-W. Cheng, Inorg. Chem. Commun. **15**, 130–135 (2012)

Chapter 5
Single Source Precursor Route to Carbon Coated $Li_3V_2(PO_4)_3$ for Cathode and Anode Applications in Lithium Ion Batteries

Abstract This chapter deals with the synthesis of monoclinic $Li_3V_2(PO_4)_3$ using the MOPOF material, $[Li_2(VO)_2(HPO_4)_2(C_2O_4)]\cdot 6H_2O$ as a single source precursor. Thermal decomposition of the oxalatophosphate precursor at 800 °C in argon atmosphere resulted in a $Li_3V_2(PO_4)_3$–V_2O_3 composite. Carbon coating of the particles were carried out by addition of sucrose to the precursor prior to thermal decomposition, to achieve better electronic conductivity. The carbon coated sample exhibits a large BET surface area of 75 $m^2\ g^{-1}$ while the pristine sample has a lesser surface area of 5.4 $m^2\ g^{-1}$. In the voltage range of 2.5–4.3 V, carbon coated sample shows a reversible capacity of 132 mAh g^{-1} at 0.1 C current rate with good capacity retention. In addition, it shows good rate capability with 56 mAh g^{-1} obtained at a high current rate of 20 C. In comparison, the pristine sample shows inferior electrochemical performance with capacity fading. The carbon coated sample was also investigated as an anode material. It exhibits a good reversible capacity of 125 mAh g^{-1} when cycled in the voltage range of 1–3 V at a current density of 50 mA g^{-1} (0.4 C).

5.1 Introduction

Single Source Precursor (SSP) approach can be defined as a synthetic procedure in which the final product was obtained from a single molecule by a single step decomposition. All the elements that are required in the target compound are incorporated in the precursor such as an organometallic compound or a metal complex with the desired stoichiometry. Solution phase or solid state decomposition the precursor yields the desired product in a single step, upon removal of the unwanted organic molecules. Some of the major advantages of this method [1] over other synthetic procedures are:

- Precise stoichiometry of active elements in the desired product
- Lower defect concentrations
- Easier formation of thin films by chemical vapour deposition (CVD) as conditions of flow and temperature can be simpler

A.S. Hameed, *Phosphate Based Cathodes and Reduced Graphene Oxide Composite Anodes for Energy Storage Applications*,
Springer Theses, DOI 10.1007/978-981-10-2302-6_5

- Single source precursors are often air-stable, non-toxic and easy to handle
- Synthesis of crystalline nanomaterials with minimal impurity incorporation
- Low-temperature required for decomposition.

Single-source precursors have been widely used in the synthesis of different class of nanomaterials such as metal oxides [2], metal sulphides [3–5], metal selenides [6–8], etc. Lithium containing cathode materials such as $LiCoO_2$ [9, 10], $LiNiO_2$ [10], $LiMn_2O_4$ [11], and $LiFePO_4$ [12] have been synthesized previously by single source precursor route. In this work, $Li_3V_2(PO_4)_3$ has been synthesized employing the MOPOF precursor, $Li_2(VO)_2(HPO_4)_2(C_2O_4)\cdot 6H_2O$.

$Li_3V_2(PO_4)_3$ is one of the prospective cathode material for Lithium ion batteries [13]. This polyanionic phosphate has high structural stability and good theoretical capacity of 197 mAh g^{-1}, comparably higher than the well-studied olivine structured phosphate, $LiFePO_4$ (170 mAh g^{-1}) [14, 15]. The average working potential of $Li_3V_2(PO_4)_3$ is also higher than $LiFePO_4$ and hence it has higher energy density than the latter. In addition, it has better ionic conductivity because of three dimensional Li^+ ion migration (Fig. 5.1) in the material [16]. Despite having such advantages, separated VO_6 octahedra in this compound make the electronic conductivity very low which affects the electrochemical lithium storage in this material. Improvement in the electrochemical properties could be achieved by decrement in particle size via suitable synthetic route [17], doping with other atoms [18] or coating the surface of the particles with an electronic conductor [19–22]. Carbon coating has been found to the effective and cheaper way of improving the electronic conductivity [19, 20]. In $Li_3V_2(PO_4)_3$ only two Li ions can be reversibly extracted when cycled in the voltage window of 3.0–4.3 V, which gives a theoretical capacity of 133 mAh g^{-1} [23, 24], while the extraction of all the three Li ions by charging to 4.7 V can give rise to a large capacity of 197 mAh g^{-1} [24].

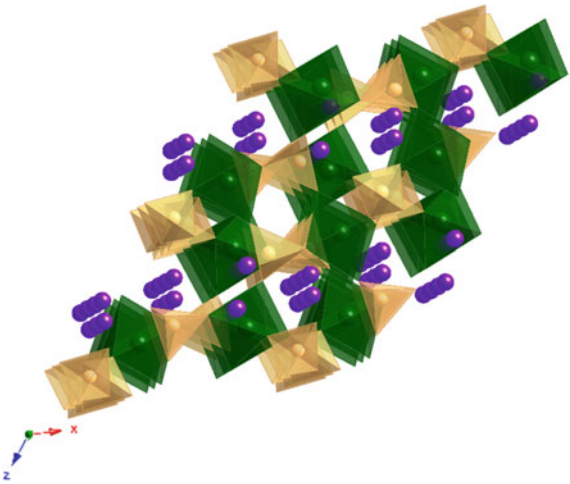

Fig. 5.1 Crystal structure of monoclinic $Li_3V_2(PO_4)_3$ viewed along *b*-axis (*Green*—VO_6 octahedra, *pale yellow*—PO_4 tetrahedra and *purple*—Li ions)

$Li_3V_2(PO_4)_3$ has been synthesized by various techniques such as solid state reaction [25], carbothermal reduction [26], sol-gel route [27, 28] and hydrothermal/solvothermal synthesis [21, 29]. In this study, $Li_3V_2(PO_4)_3$–V_2O_3 composite was synthesized by single-source precursor (SSP) route from $[Li_2(VO)_2(HPO_4)_2(C_2O_4)]\cdot 6H_2O$ by thermal decomposition in argon atmosphere at 800 °C. Carbon coating of the composite was also achieved by grinding the precursor with sucrose and subsequent decomposition. Reversible lithium intercalation of the composite was studied at different voltage ranges using galvanostatic charge-discharge, cyclic voltammetry and EIS studies.

5.2 Experimental Section

All the chemicals and solvents used in this study are commercially available and used without further purification.

5.2.1 Synthesis of $[Li_2(VO)_2(HPO_4)_2(C_2O_4)]\cdot 6H_2O$

The single source precursor, $[Li_2(VO)_2(HPO_4)_2(C_2O_4)]\cdot 6H_2O$ was synthesized by hydrothermal route according to the procedure described in Sect. 3.2.1.

5.2.2 Synthesis of $Li_3V_2(PO_4)_3$

$Li_3V_2(PO_4)_3$ was prepared by thermal decomposition of the precursor $[Li_2(VO)_2(HPO_4)_2(C_2O_4)]\cdot 6H_2O$ at 800 °C in a tube furnace for 4 h under argon atmosphere as described in Eq. 5.1. The excess vanadium in the precursor compound has been converted of V_2O_3. Thus the decomposition resulted in $Li_3V_2(PO_4)_3$–V_2O_3 composite material. Carbon coating of the particles was also achieved by grinding the precursor with sucrose before subjected to thermal decomposition. The pristine and the carbon coated $Li_3V_2(PO_4)_3$–V_2O_3 composites will be referred to as LVPV and c-LVPV respectively from here on.

$$3\left[Li_2(VO)_2(HPO_4)_2(C_2O_4)\right]\cdot 6H_2O \rightarrow 2Li_3V_2(PO_4)_3 + V_2O_3 + 6CO_2 + 9H_2O \tag{5.1}$$

5.2.3 Structural and Electrochemical Characterization

The LVPV and c-LVPV composites synthesized in this study were characterized by PXRD, Rietveld refinement, BET surface area, galvanostatic cycling, cyclic

voltammetry and EIS studies. Details of these characterization techniques have been described previously in Chap. 2.

5.3 Results and Discussion

5.3.1 *Structure Analysis*

TGA of the precursor compound is shown in Fig. 5.2. The compound loses water between room temperature and 210 °C while the removal of organic moieties are completed before 600 °C. When the decomposition was carried out at 600 °C, it resulted in an amorphous phase. To facilitate the complete formation of $Li_3V_2(PO_4)_3$ phase and to enhance the crystallinity of the product, the precursor was annealed at a higher temperature of 800 °C. Flowing argon atmosphere was employed throughout the synthesis to help the reduction of V^{4+} to V^{3+}. PXRD pattern of the pristine LVPV composite obtained at 800 °C is shown in Fig. 5.3a, which indicates the formation of monclinic $Li_3V_2(PO_4)_3$ phase. The peaks can be well assigned to the monoclinic space group $P2_1/n$ (JCPDS: 01-072-7074). However, few peaks were found to have higher intensity than the standard pattern, which infers the the presence of a minor phase. Careful examination of the pattern revealed the formation of V_2O_3 (JCPDS: 00-001-1293) as minor phase (indicated by blue lines in Fig. 5.3a).

The percentage of V_2O_3 in the final product was calculated from the difference in the molar ratio of Li and V in the precursor and pure $Li_3V_2(PO_4)_3$. The precursor has 1:1 molar ratio of Li and V while pure $Li_3V_2(PO_4)_3$ contain Li and V in a molar ratio of 1:0.67. This suggests that the decomposition product should contain 84.6 wt% $Li_3V_2(PO_4)_3$ and 15.4 wt% V_2O_3. Quantitative Rietveld refinement of the XRD pattern of LVPV was carried out using TOPAS software (version 3). Refinement results (shown in Fig. 5.3b) indicate that LVPV contains 84.2 % of $Li_3V_2(PO_4)_3$ and 15.8 % of V_2O_3 which is close to the calculated values. The lattice parameters

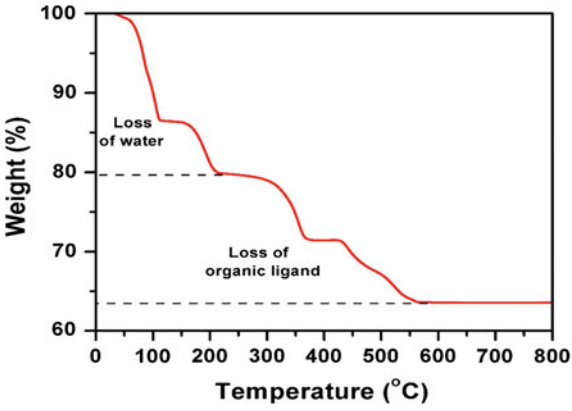

Fig. 5.2 TGA $[Li_2(VO)_2(HPO_4)_2(C_2O_4)]\cdot 6H_2O$ in N_2 atmosphere at a heating rate of 5 °C min^{-1}

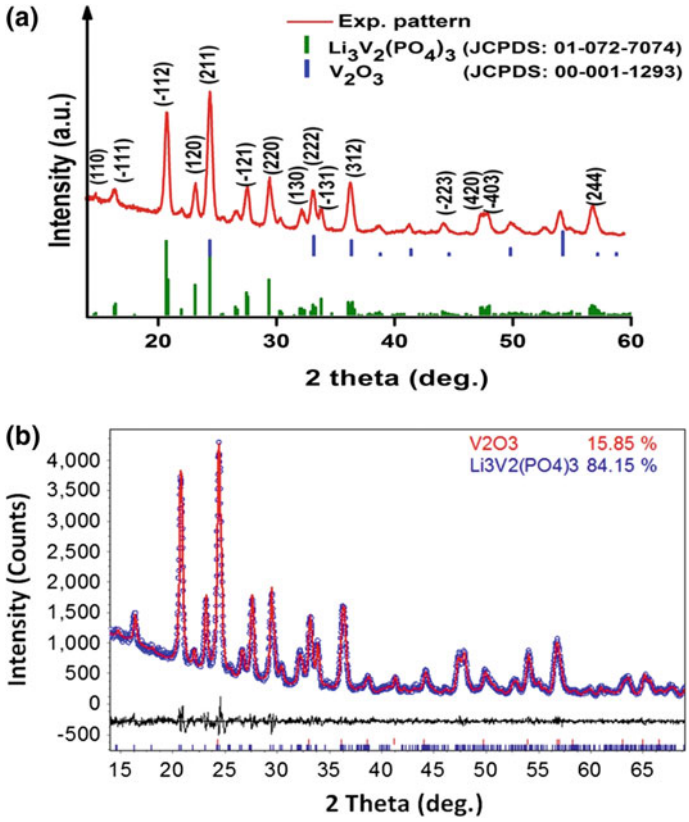

Fig. 5.3 **a** Powder X-ray diffraction pattern of LVPV and **b** Quantitative Rietveld refinement of LVPV showing its composition as 84.2 % $Li_3V_2(PO_4)_3$ and 15.8 % V_2O_3

of $Li_3V_2(PO_4)_3$ phase (space group: $P2_1/n$) are: a = 8.6197(6) Å, b = 8.5988(2) Å, c = 12.0683(2) Å and β = 90.55(2)°. The lattice parameters of V_2O_3 phase (space group: $R3c$) are: a = 4.9658(3) and c = 13.9774(1) Å. The calculated lattice parameters of $Li_3V_2(PO_4)_3$ are close to literature reports [24].

5.3.2 *Morphology*

SEM images of the single source precursor, LVPV and c-LVPV are shown in Fig. 5.4. The precursor compound has a layered structure and hence it prefers to form plate like morphology. The particle size of the SSP was found to be in the range of few microns (Fig. 5.4a). Upon annealing, water molecules are lost, oxalate group decomposed as CO_2 which results in the breaking down of the plates into smaller particles of size, few hundred nanometres as evident from the SEM

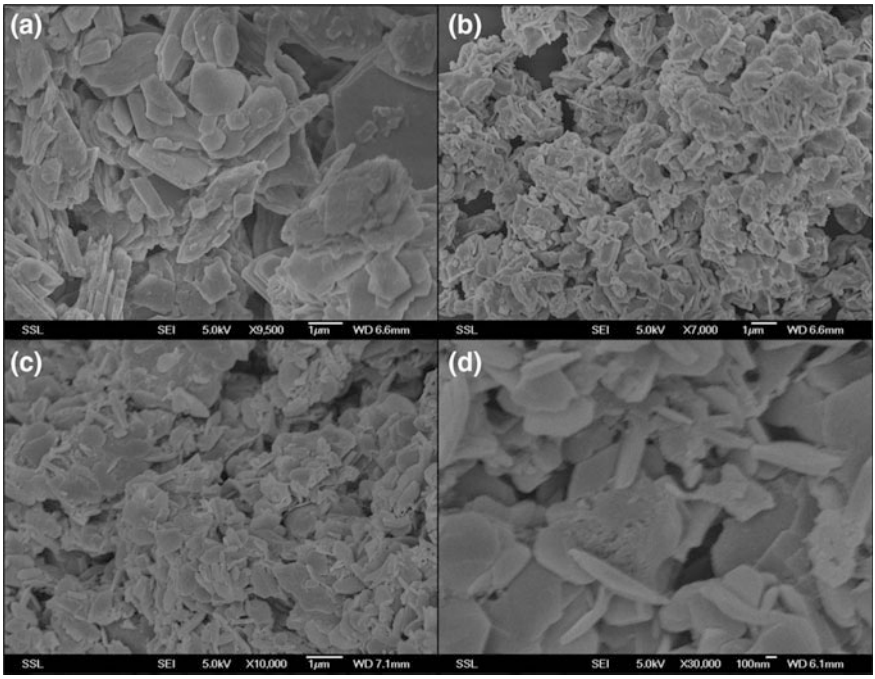

Fig. 5.4 SEM images of **a** $[Li_2(VO)_2(HPO_4)_2(C_2O_4)]\cdot 6H_2O$, **b** LVPV, **c** c-LVPV at lower magnification and **d** c-LVPV at higher magnification

micrographs (Fig. 5.4b–d). It can be noticed that the particles are fused together in the absence of carbon additive (Fig. 5.4b), while addition of sucrose to the precursor resulted in more separated particles which has high porosity (Fig. 5.4c–d).

To study the porosity of the annealed samples, specific surface area and pore size of LVPV and c-LVPV were investigated from N_2 adsorption–desorption isotherms. Figure 5.5 shows that both the compounds exhibit type IV isotherm. This is characteristic of mesoporous materials with high energy of adsorption. The pristine sample, LVPV obtained from the as-synthesized precursor has a small surface area of 5.4 $m^2\ g^{-1}$. The pore diameter and pore volume of the sample were found to be 16.7 nm and 0.023 $cm^3\ g^{-1}$ respectively. In comparison, c-LVPV has a larger specific surface area of 75 $m^2\ g^{-1}$ with pore diameter and pore volume of 4.5 nm and 0.082 $cm^3\ g^{-1}$ respectively. This increment in the surface area of carbon coated sample can be attributed to the pores created by decomposition of sucrose molecules during annealing. This large surface area of c-LVPV could be advantageous for a better electrochemical performance, especially at higher current rates. Surface area of 16.8 and 8.9 $m^2\ g^{-1}$ were reported for $G/Li_3V_2(PO_4)_3$ and $c/Li_3V_2(PO_4)_3$ composites [30], while sol-gel derived $Li_3V_2(PO_4)_3$ with higher surface areas of 75 and 255 $m^2\ g^{-1}$ were reported when cyclodextrin and sucrose respectively were used as the carbon source [31, 32].

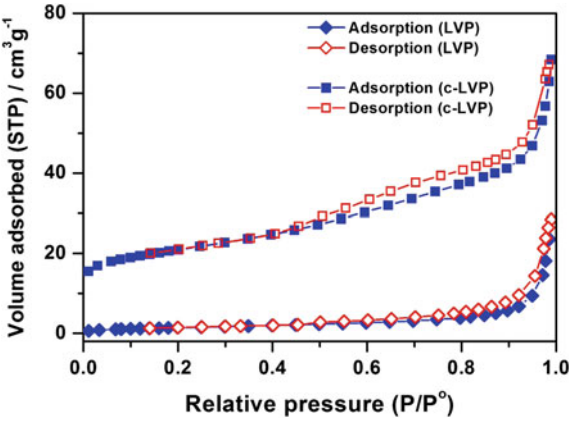

Fig. 5.5 Nitrogen adsorption-desorption isotherms of LVPV and c-LVPV

5.3.3 Galvanostatic Cycling Studies

5.3.3.1 Voltage Range: 2.5–4.3 V

The electrodes made of LVPV and c-LVPV were subjected to galvanostatic charge-discharge cycling using lithium metal as counter electrode in the voltage window of 2.5–4.3 V versus Li/Li^+ at a current density of 13 mA g^{-1} (0.1 C current rate). Selected charge–discharge cycles of c-LVPV are shown in Fig. 5.6a. In this voltage window, reversible lithium intercalation occurs in the compound according to Eqs. 5.2–5.4 [24]. During the oxidation (lithium extraction) process, two flat plateaus were observed at 3.59 and 3.67 V for the removal of first Li^+ ion. The third plateau observed at 4.07 V corresponds to the removal of second lithium resulting in the formation of $LiV_2(PO_4)_3$, where the vanadium is V^{4+} state. The discharge cycle shows similar bi-phasic reactions with flat plateaus observed at 4.05, 3.65 and 3.57 V. Small polarization values of 0.02 V was observed for the three plateaus and was consistent throughout the cycling. This indicates better reversibility of the redox system. Subsequent cycles show overlapping plateaus which suggests excellent cyclability. The discharge capacity obtained at the end of 30 cycles was 132 mAh g^{-1} which is close to the theoretical capacity. For capacity calculation, only the weight of $Li_3V_2(PO_4)_3$ present in the electrode were considered. On the other hand, pristine LVPV encountered capacity fading during cycling with a discharge capacity of 107 mAh g^{-1} obtained at the end of 30 cycles. Comparison of capacity versus cycle number of LVPV and c-LVPV is shown in Fig. 5.6b. This increment in capacity by carbon coating can be attributed to the enhanced electronic conductivity of the composite. Improvement in the capacity of $Li_3V_2(PO_4)_3$ due to better electronic conductivity on carbon coating have been reported in literature [16, 27, 35]. The presence of V_2O_3 does not interfere in the lithium storage of $Li_3V_2(PO_4)_3$. However, its presence can lead to better electronic conductivity of the composite as it is a good conductor.

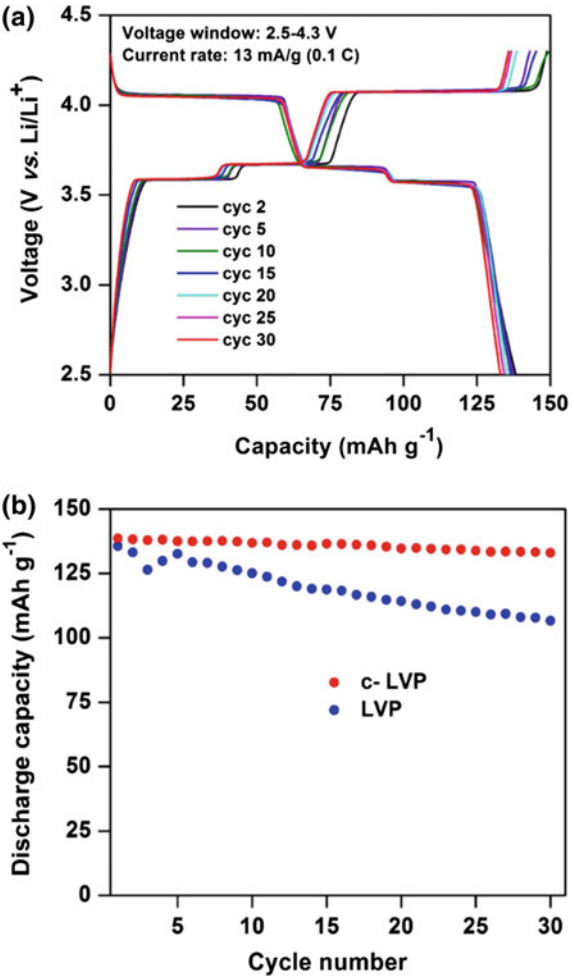

Fig. 5.6 **a** Galvanostatic charge–discharge cycles of c-LVPV in the voltage window of 2.5–4.3 V at a current rate of 13 mA g^{-1} and **b** Comparison of capacity versus cycle number plots of LVPV and c-LVPV

$$Li_3V_2(PO_4)_3 \leftrightarrow Li_{2.5}V_2(PO_4)_3 + 0.5\ Li^+ + 0.5\ e^- \quad (5.2)$$

$$Li_{2.5}V_2(PO_4)_3 \leftrightarrow Li_2V_2(PO_4)_3 + 0.5\ Li^+ + 0.5\ e^- \quad (5.3)$$

$$Li_2V_2(PO_4)_3 \leftrightarrow LiV_2(PO_4)_3 + Li^+ + e^- \quad (5.4)$$

$$LiV_2(PO_4)_3 \leftrightarrow V_2(PO_4)_3 + Li^+ + e^- \quad (5.5)$$

5.3.3.2 Rate Capability

Rate capability of c-LVPV was studied at different current densities of 66, 133, 400, 660 1330 and 2660 mA g^{-1} which corresponds to 0.5, 1, 3, 5, 10 and 20 C current rates respectively (where 1 C represents 133 mA g^{-1}). The discharge profiles of c-LVPV at these current rates are displayed in Fig. 5.7a. As expected, there is a decrease in the capacity with increasing current rates due to poor Li diffusion kinetics at high current rates and there is an increase in the polarization. The discharge capacity obtained at the current rates of 0.5, 1, 3, 5, 10 and 20 C are 133, 133, 129, 119, 97 and 56 (±3) mAh g^{-1} respectively. In addition, the sample retained a capacity of 131 mAh g^{-1} when the current rate was decreased from 20 C to 0.5 C. The capacity versus cycle number plot of c-LVPV at different current rates is shown in Fig. 5.7b which reveals good cycling stabilities of the material at all the current rates up to 20 C. The intrinsic poor electronic conductivity of LVPV hinders the reversible lithium storage in $Li_3V_2(PO_4)_3$ at high current rates resulting in poor rate capability [19, 20]. Therefore, carbon coating of $Li_3V_2(PO_4)_3$ has been reported as the way to enhance the electronic conductivity for achieving good rate capability [17, 24, 36, 37]. The c-LVPV particles prepared in the current study have good carbon coating and hence they have good electronic conductivity resulting in good

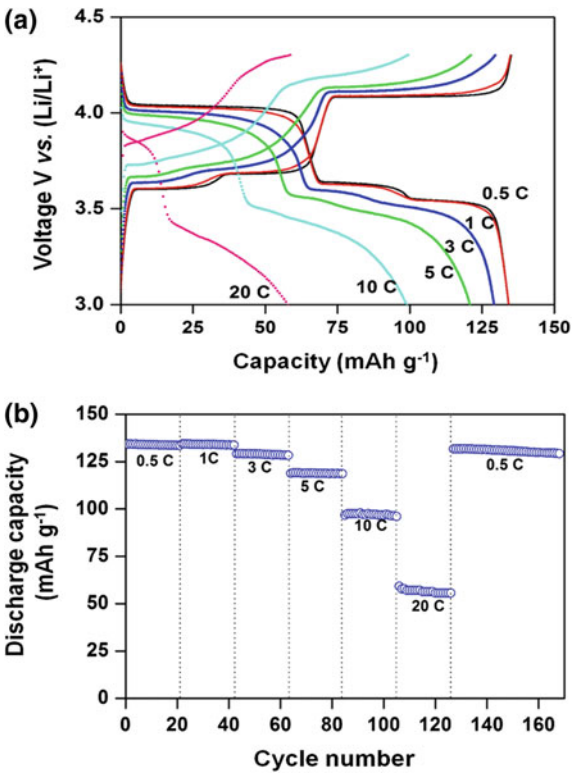

Fig. 5.7 **a** Galvanostatic charge-discharge cycles of c-LVPV in the voltage window of 2.5–4.3 V at different current rates and **b** Capacity versus cycle number plots of c-LVPV at different current rates (1 C represents a current density of 133 mA g^{-1})

rate capability. However, the relatively big particle size of c-LVPV limits its lithium diffusion at very high current rates. At 20 C, capacity of only 56 mAh g^{-1} was obtained.

5.3.3.3 Voltage Range: 2.5–4.7 V

Galvanostatic cycling of c-LVPV was also carried out in the voltage window of 2.5–4.7 V versus Li/Li^+ at a current rate of 20 mA g^{-1} (0.1 C). When charged to 4.7 V, all three Li ions can be extracted from $Li_3V_2(PO_4)_3$. Figure 5.8a shows the charge-discharge curves for few selected cycles. During the first charge cycle, flat plateaus were observed for the extraction of two Li^+ ions from $Li_3V_2(PO_4)_3$ according to Eqs. 5.2–5.4 as discussed earlier. The third Li^+ ion extraction and the corresponding oxidation of half of the vanadium happens at 4.55 V, resulting in $V_2(PO_4)_3$ according to Eq. 5.5. In this phase vanadium exists in mixed V^{4+}/V^{5+} state. The four plateaus observed in the charge cycle at 3.61, 3.70, 4.11 and 4.55 V correspond to a sequence of four phase transitions between the phases of

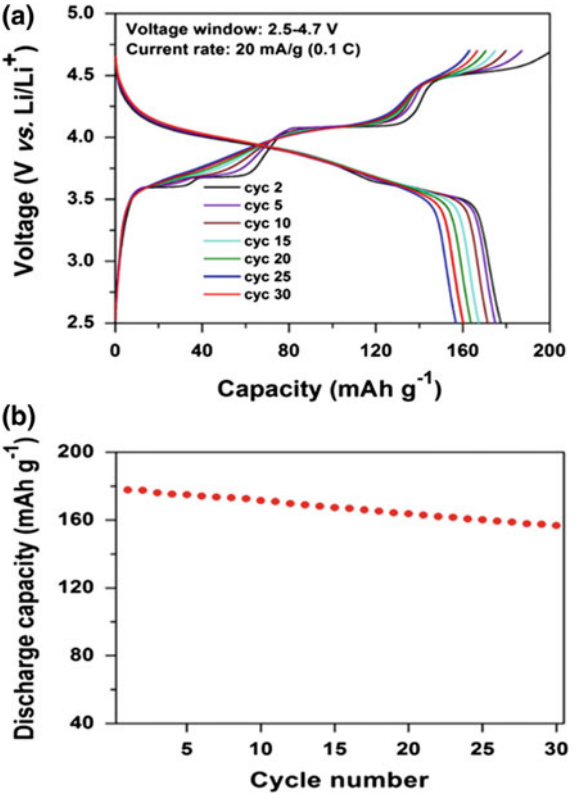

Fig. 5.8 **a** Galvanostatic charge–discharge cycles of c-LVPV in the voltage window of 2.5–4.7 V at a current rate of 20 mA g^{-1} and **b** Capacity versus cycle number plots of c-LVPV in the voltage window of 2.5–4.7 V

$Li_xV_2(PO_4)_3$ where x = 3.0, 2.5, 2.0, 1.0 and 0. A capacity of 198 mAh g^{-1} was obtained for the first charge cycle (Theoretical capacity is 197 mAh g^{-1}). During the first discharge cycle, a sloping curve was observed resulting in a capacity of 178 mAh g^{-1}. Upon cycling, the flat plateaus observed in the first charge cycle becomes slopy and the capacity gradually decreased to 156 mAh g^{-1} after 30 cycles. The capacity versus cycle number plot is shown in Fig. 5.8b. Contrary to the highly reversible lithium cycling observed when only two Li^+ ions are extracted, the complete removal of three Li^+ ions leads to capacity fading. The third Li extraction at 4.55 V is energetically unfavorable and possess large overvoltage. Similar capacity fading were observed for 3 Li extraction in $Li_3V_2(PO_4)_3$ by Rui et al. [20], and Liu et al. [38].

5.3.3.4 Voltage Range: 1.0–3.0 V

Recently, few reports on the anodic studies of $Li_3V_2(PO_4)_3$ have appeared in the literature. It can behave as an anode material due to lithium insertion into the framework, forming $Li_5V_2(PO_4)_3$ at lower voltages [39–41]. In our work, the synthesized c-LVPV composite was also investigated as an anode material in the voltage range of 1.0–3.0 V. Figure 5.9 shows the galvanostatic charge-discharge profiles of the material at a current rate of 50 mA g^{-1} ($\sim$0.4 C) for selected cycles. Four plateaus can be observed in the charge and discharge curves. During lithium insertion or discharge cycle, the first Li^+ ion is inserted in two steps at 1.96 and 1.86 V via two bi-phasic reactions forming $Li_{3.5}V_2(PO_4)_3$ and $Li_4V_2(PO_4)_3$. The plateaus observed at 1.73 and 1.66 V corresponds to the addition of next lithium ion, via two phase reactions forming $Li_{4.5}V_2(PO_4)_3$ and $Li_5V_2(PO_4)_3$. In the charge cycle, similar plateaus were observed for the lithium extraction in four steps at 1.71, 1.77, 1.90 and 2.02 V with four phase transitions between the phases of

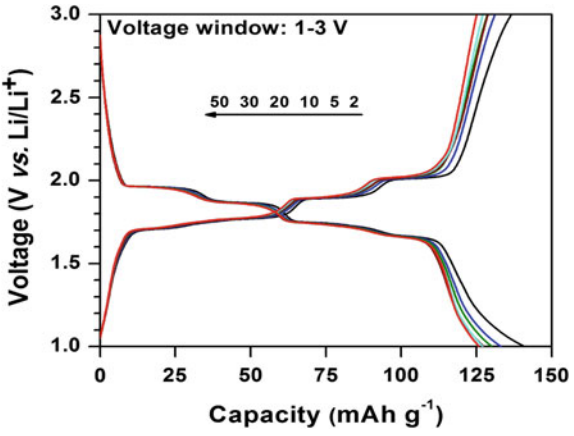

Fig. 5.9 Galvanostatic charge–discharge cycles of c-LVPV in the voltage window of 1.0–3.0 V at a current rate of 50 mA g^{-1}

$Li_xV_2(PO_4)_3$ where x = 3.0, 3.5, 4.0, 4.5 and 5.0. These redox potentials are close to the values reported by Rui et al. [40]. The possible redox reactions occurring in this voltage range can be summarized in Eqs. 5.6–5.9. The cycling results demonstrate that $2Li^+$ ions can be reversibly inserted between ~1.5 and 2.0 V in a very efficient manner. A stable capacity of 126 mAh g^{-1} was obtained at 50 mA g^{-1} (0.4 C rate) which is ~95 % of the theoretical capacity (133 mAh g^{-1}). The obtained capacity in this study is higher than the previous reports [39–41]. This is attributed to the better conductivity of c-LVPV particles.

$$Li_3V_2(PO_4)_3 + 0.5\ Li^+ + 0.5\ e^- \leftrightarrow Li_{3.5}V_2(PO_4)_3 \tag{5.6}$$

$$Li_{3.5}V_2(PO_4)_3 + 0.5\ Li^+ + 0.5\ e^- \leftrightarrow Li_4V_2(PO_4)_3 \tag{5.7}$$

$$Li_4V_2(PO_4)_3 + 0.5\ Li^+ + 0.5\ e^- \leftrightarrow Li_{4.5}V_2(PO_4)_3 \tag{5.8}$$

$$Li_{4.5}V_2(PO_4)_3 + 0.5\ Li^+ + 0.5\ e^- \leftrightarrow Li_5V_2(PO_4)_3 \tag{5.9}$$

5.3.3.5 Voltage Range: 1.5–4.3 V

To demonstrate the structural stability of the material, simultaneous extraction and insertion of four Li ions were carried out in the voltage range of 1.5–4.3 V at a current rate of 50 mA g^{-1}. In the first charge cycle, two Li ions are extracted from the material to form the $LiV_2(PO_4)_3$ phase as described earlier. In the first discharge cycle, two Li ions are inserted in the 4.1–3.5 V range as described in Sect. 5.3.3.1 and two more Li^+ ions are inserted in the range of 2.0–1.7 V as described in Sect. 5.3.3.3 to form the divalent vanadium containing framework, $Li_5V_2(PO_4)_3$. Figure 5.10 shows the discharge curves for selected cycles. As can be inferred from the figure, the redox reaction happens in highly reversible manner resulting in a stable capacity of 240 mAh g^{-1}.

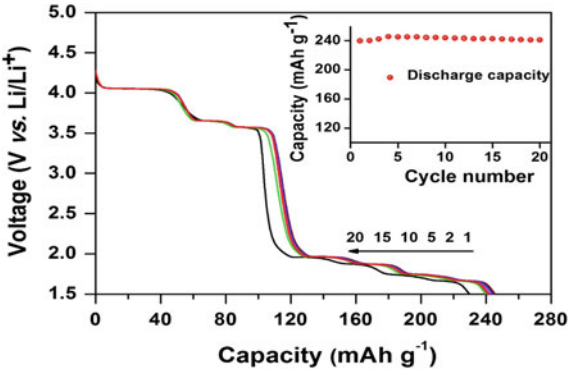

Fig. 5.10 Galvanostatic cycling of c-LVPV in the voltage window of 1.5–4.3 V at a current density of 50 mA g^{-1} (For clarity, only the discharge cycles are shown). The inset graph shows the plot of discharge capacity versus cycle number

5.3.4 Cyclic Voltammetry

Cyclic voltammetric studies of c-LVPV were carried out at room temperature with Li metal as counter electrode. CV curves of the composite was recorded in different voltage ranges like 2.5–4.3, 2.5–4.7 and 1.3–4.3 V versus Li/Li^+ at a scan rate of 0.058 mV s^{-1} The CV curves in the potential window of 2.5–4.3 V versus Li/Li^+ is shown in Fig. 5.11a. In this potential window, only two of the three Li ions can be inserted/extracted reversibly. During the anodic scan (charging), a pair of sharp oxidation peaks were observed at 3.60 and 3.69 V. This corresponds to the removal of first lithium from $Li_3V_2(PO_4)_3$ via two bi-phasic reactions [33]. At 3.60 V, 0.5 mol of Li^+ ion was extracted forming a stable phase of $Li_{2.5}V_2(PO_4)_3$ and the removal of another 0.5 mol of Li^+ results in the $Li_2V_2(PO_4)_3$ phase at 3.69 V. The third sharp peak at 4.10 V corresponds to the removal of second lithium from the material, leading to $LiV_2(PO_4)_3$. In the cathodic scan (discharge), similar peaks were observed at 4.04, 3.64 and 3.56 V revealing the insertion of 2 mol of Li^+ into $LiV_2(PO_4)_3$ and the corresponding reduction of vanadium from V^{4+} to V^{3+}. The redox potentials observed in the CV measurements are close to reported values [34]. The high reversibility of the redox reaction can be confirmed by the overlapping CV curves and also the similar redox potentials observed in the subsequent cycles. There are no additional peaks from V_2O_3 indicating that it is electrochemically inactive in this potential window.

Cyclic voltammograms of c-LVPV was also recorded in the voltage window of 2.5–4.7 V versus Li/Li^+ (Fig. 5.11b), where all the three Li ions can be reversibly extracted from $Li_3V_2(PO_4)_3$. During the first anodic scan, sharp peaks were observed at 3.60, 3.69 and 4.10 V corresponding to the extraction of first two Li ions. A broad peak was observed at 4.55 V corresponding to third Li^+ ion extraction. In the cathodic scan, broad peaks were observed for the removal of all 3 Li^+ ions which is distinct from cycling in the 2.5–4.3 V range. During the subsequent cycles, the peaks became broader for both anodic and cathodic scans, indicating the destruction of crystal structure and the deterioration of electrochemical performance of the material upon complete extraction of all the three Li ions.

To demonstrate the structural stability of the framework, the material was subjected to cyclic voltammetric studies in the voltage range of 1.3–4.3 V versus Li. In this potential window, four Li ions can be reversibly inserted and extracted. During the first oxidation scan to the cut-off voltage of 4.3 V, two Li^+ ions are removed to form $LiV_2(PO_4)_3$. In the first reduction scan, two Li ions are inserted at 4.05, 3.64 and 3.56 V to form back $Li_3V_2(PO_4)_3$. Continuing lithium insertion into the compound gave rise to peaks at 1.91, 1.84, 1.71 and 1.65 V which correspond to insertion of 2 mol of Li into $Li_3V_2(PO_4)_3$ forming $Li_5V_2(PO_4)_3$. The vanadium atoms at this stage are reduced to V^{2+}. Oxidation peaks in the next anodic scan appeared at 1.73, 1.79, 1.91 and 2.03 V corresponding to removal of two Li ions, forming $Li_3V_2(PO_4)_3$. The reversibility in extraction of 4 Li^+ ions can be inferred by the overlapping CV curves in Fig. 5.11c.

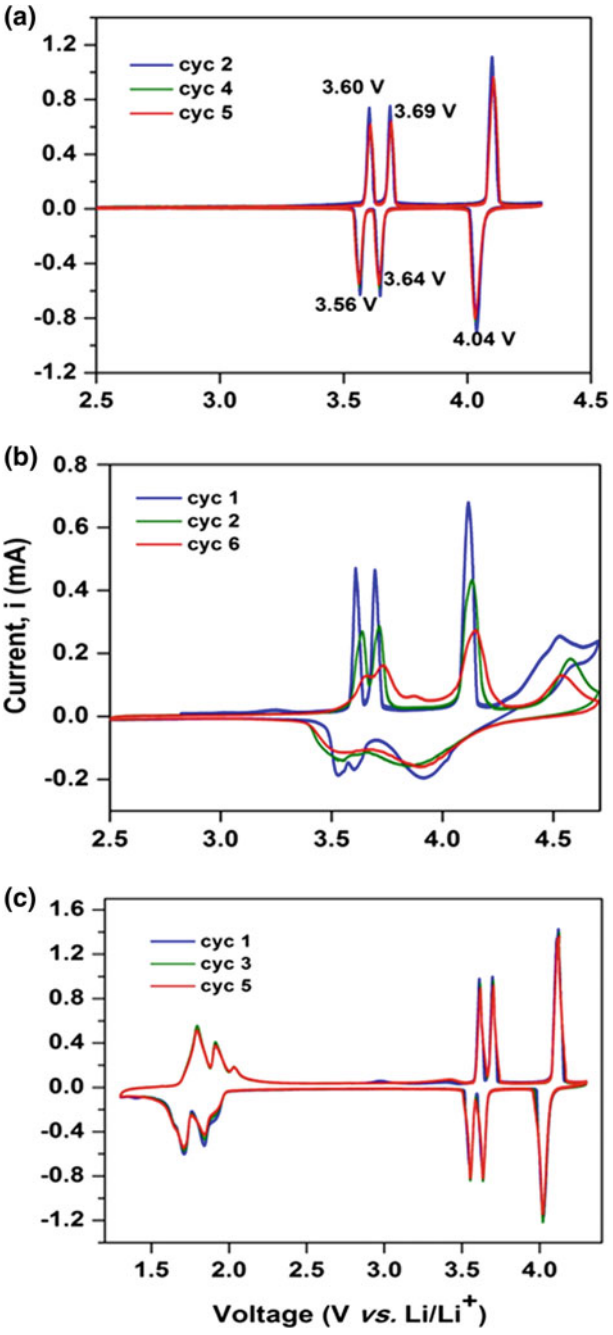

Fig. 5.11 Cyclic voltammogramms (CV) of c-LVPV in the voltage window of **a** 2.5–4.3 V, **b** 2.5–4.7 V and **c** 1.3–4.3 V at a scan rate of 0.058 mV s^{-1}

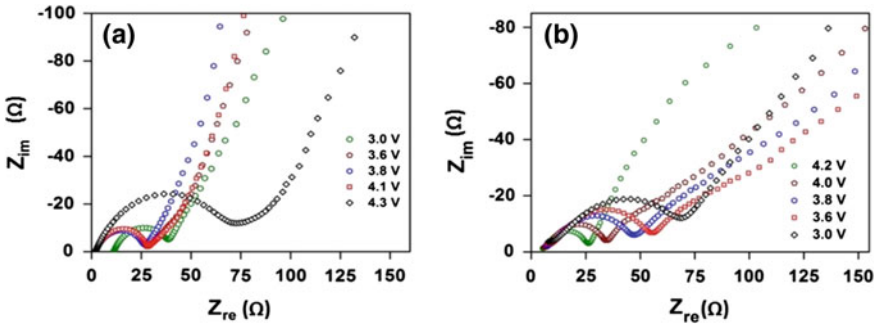

Fig. 5.12 Nyquist plots of c-LVPV at various voltages during **a** 1st charge and **b** 1st discharge cycle

5.3.5 Electrochemical Impedance Spectroscopy

EIS studies were carried out for c-LVPV with lithium metal as counter electrode. Measurements were carried out at various voltages between 2.5 and 4.3 V versus Li for the 1st charge and discharge cycle in the frequency range of 180 kHz to 0.001 Hz. During each increment (charging) or decrement (discharge) of voltage, the cell was relaxed at the particular voltage for 30 min before data collection. The results are presented as Nyquist plots (Z_{re} vs. Z_{im}), where Z_{re} and Z_{im} are respectively the real and imaginary parts of cell impedance (Fig. 5.12). The semi-circle at high to medium frequency denotes the charge transfer resistance (R_{ct}) and the corresponding double-layer capacitance (C_{dl}). At OCV, the electrolyte resistance was found to be 12 Ω and the overall resistance was 40 Ω (intersection of the semi-circle on the X-axis). On the onset of lithium extraction (charging), the impedance decreases to 27–28 Ω which was consistent till the Li ions are completely extracted. However, the resistance increase to 73 Ω at 4.3 V (Fig. 5.12a). Impedance values during the discharge cycle are slightly higher (25–55 Ω) in the lithium insertion range as shown in Fig. 5.12b. The curves indicate clearly the low charge transfer resistance due to nice electrode kinetics. The impedance of c-$Li_3V_2(PO_4)_3$ prepared in the current study are lesser owing to its good conductivity produced by the combined effect of carbon coating and the presence of a good conductor, V_2O_3 in the composite.

5.4 Conclusions

Single source precursor approach was used in the synthesis of $Li_3V_2(PO_4)_3$–V_2O_3 composite material from a MOPOF material, $Li_2(VO)_2(HPO_4)_2(C_2O_4)\cdot 6H_2O$. The presence of V_2O_3 and its percentage were confirmed from XRD and quantitative Rietveld refinement. Carbon coating of the composite was also achieved by sucrose

addition to the precursor prior to decomposition. The carbon coated sample shows good electrochemical performance and stable capacity up to 20 C current rate in the potential window of 3.0–4.3 V. The good electrochemical property of c-$Li_3V_2(PO_4)_3$ arises from the combined effect of conducting carbon and the presence of a good conductor, V_2O_3 in the composite. In contrary, the pristine LVPV shows poor electrochemical stability. When the sample was subjected to potential window of 2.5–4.7 V, three Li ions can be inserted/extracted reversibly. However, capacity fading was observed during cycling. The compound was also studied as anode in the potential window of 1–3 V. Good capacity of 126 mAh g^{-1} and good cycling stability of the material in the low potential window indicates its feasibility as a good anode material. The low impedance of the sample infers good conductivity due to carbon coating.

References

1. N.O. Boadi, M.A. Malik, P. O'Brien, J.A.M. Awudza, Dalton Trans. **41**, 10497–10506 (2012)
2. S. Daniele, R. Papiernik, L.G. Hubert-Pfalzgraf, S. Jagner, M. Håkansson, Inorg. Chem. **34**, 628–632 (1995)
3. J. Sun, W.E. Buhro, Angew. Chem. Int. Ed. **47**, 3215–3218 (2008)
4. S.L. Cumberland, K.M. Hanif, A. Javier, G.A. Khitrov, G.F. Strouse, S.M. Woessner, C.S. Yun, Chem. Mater. **14**, 1576–1584 (2002)
5. P.S. Nair, T. Radhakrishnan, N. Revaprasadu, G. Kolawole, P. O'Brien, J. Mater. Chem. **12**, 2722–2725 (2002)
6. J.J. Vittal, M.T. Ng, Acc. Chem. Res. **39**, 869–877 (2006)
7. M.A. Malik, P. O'Brien, N. Revaprasadu, Adv. Mater. **11**, 1441–1444 (1999)
8. S.L. Castro, S.G. Bailey, R.P. Raffaelle, K.K. Banger, A.F. Hepp, Chem. Mater. **15**, 3142–3147 (2003)
9. T.J. Boyle, M.A. Rodriguez, D. Ingersoll, T.J. Headley, S.D. Bunge, D.M. Pedrotty, S.M. De'Angeli, S.C. Vick, H. Fan, Chem. Mater. **15**, 3903–3912 (2003)
10. S.L. Tey, M.V. Reddy, G.V. Subba Rao, B.V.R. Chowdari, J. Yi, J. Ding, J.J. Vittal, Chem. Mater. **18**, 1587–1594 (2006)
11. A. Navulla, L. Huynh, Z. Wei, A.S. Filatov, E.V. Dikarev, J. Am. Chem. Soc. **134**, 5762–5765 (2012)
12. M.R. Hill, G.J. Wilson, L. Bourgeois, A.G. Pandolfo, Energy Environ. Sci. **4**, 965–972 (2011)
13. M.Y. Saidi, J. Barker, H. Huang, J.L. Swoyer, G. Adamson, Electrochem. Solid-State Lett. **5**, A149–A151 (2002)
14. S.-Y. Chung, J.T. Bloking, Y.-M. Chiang, Nat. Mater. **1**, 123–128 (2002)
15. A.K. Padhi, K.S. Nanjundaswamy, J.B. Goodenough, J. Electrochem. Soc. **144**, 1188–1194 (1997)
16. X.H. Rui, N. Ding, J. Liu, C. Li, C.H. Chen, Electrochim. Acta **55**, 2384–2390 (2010)
17. A. Pan, J. Liu, J.G. Zhang, W. Xu, G. Cao, Z. Nie, B.W. Arey, S. Liang, Electrochem. Commun. **12**, 1674–1677 (2010)
18. M. Ren, Z. Zhou, Y. Li, X.P. Gao, J. Yan, J. Power Sources **162**, 1357–1362 (2006)
19. M.M. Ren, Z. Zhou, X.P. Gao, W.X. Peng, J.P. Wei, J. Phys. Chem. C **112**, 5689–5693 (2008)
20. X.H. Rui, C. Li, C.H. Chen, Electrochim. Acta **54**, 3374–3380 (2009)
21. B. Pei, Z. Jiang, W. Zhang, Z. Yang, A. Manthiram, J. Power Sources **239**, 475–482 (2013)
22. J. Zhu, R. Yang, K. Wu, Ionics **19**, 577–580 (2013)

23. D. Morgan, G. Ceder, M.Y. Saïdi, J. Barker, J. Swoyer, H. Huang, G. Adamson, Chem. Mater. **14**, 4684–4693 (2002)
24. H. Huang, S.C. Yin, T. Kerr, N. Taylor, L.F. Nazar, Adv. Mater. **14**, 1525–1528 (2002)
25. P. Fu, Y. Zhao, Y. Dong, X. An, G. Shen, J. Power Sources **162**, 651–657 (2006)
26. J. Barker, M.Y. Saidi, J.L. Swoyer, J. Electrochem. Soc. **150**, A684–A688 (2003)
27. Y. Li, Z. Zhou, X. Gao, J. Yan, Electrochim. Acta **52**, 4922–4926 (2007)
28. Y. Li, Z. Zhou, M. Ren, X. Gao, J. Yan, Electrochim. Acta **51**, 6498–6502 (2006)
29. F. Teng, Z.H. Hu, X.H. Ma, L.C. Zhang, C.X. Ding, Y. Yu, C.H. Chen, Electrochim. Acta **91**, 43–49 (2013)
30. H. Liu, G. Yang, X. Zhang, P. Gao, L. Wang, J. Fang, J. Pinto, X. Jiang, J. Mater. Chem. **22**, 11039–11047 (2012)
31. J. Fan, X.C. Deng, S.Y. Li, G.X. Li, Z.H. Mao, Rus. J. Electrochem. **47**, 1399–1403 (2011)
32. L. Wang, C. Du, Z. Tang, X. Zhang, Q. Xu, Electrochim. Acta **98**, 218–224 (2013)
33. M. Morcrette, J.B. Leriche, S. Patoux, C. Wurm, C. Masquelier, Electrochem. Solid-State Lett. **6**, A80–A84 (2003)
34. M.Y. Saïdi, J. Barker, H. Huang, J.L. Swoyer, G. Adamson, J. Power Sources **119–121**, 266–272 (2003)
35. T. Jiang, W. Pan, J. Wang, X. Bie, F. Du, Y. Wei, C. Wang, G. Chen, Electrochim. Acta **55**, 3864–3869 (2010)
36. J. Kang, V. Mathew, J. Gim, S. Kim, J. Song, W.B. Im, J. Han, J.Y. Lee, J. Kim, Sci. Rep. **4** (2014)
37. V. Mani, K. Nathiya, N. Kalaiselvi, RSC Adv. **4**, 17091–17096 (2014)
38. Q. Liu, F. Yang, S. Wang, L. Feng, W. Zhang, H. Wei, Electrochim. Acta **111**, 903–908 (2013)
39. W.F. Mao, H.Q. Tang, Z.Y. Tang, J. Yan, Q. Xu, ECS Electrochem. Lett. **2**, A69–A71 (2013)
40. X.H. Rui, N. Yesibolati, C.H. Chen, J. Power Sources **196**, 2279–2282 (2011)
41. N. Böckenfeld, A. Balducci, J. Power Sources **235**, 265–273 (2013)

Chapter 6
Synthesis and Electrochemical Studies of a Metastable, Layered Phosphate α_I-$LiVOPO_4$

Abstract In this chapter, synthesis of a metastable phosphate material, α_I-$LiVOPO_4$ via dehydration of a hydrothermally prepared precursor, $LiVOPO_4{\cdot}2H_2O$ have been presented. Single crystal X-ray diffraction analysis ascertained the formation of $LiVOPO_4{\cdot}2H_2O$ in the orthorhombic space group, *Cmca* with the lattice parameters; a = 8.9454(7) Å, b = 9.0406(7) Å and c = 12.7373(10) Å. We have also investigated the crystal structure transformation of orthorhombic $LiVOPO_4{\cdot}2H_2O$ to tetragonal α_I-$LiVOPO_4$ accompanying the solid-state dehydration. A probable mechanism for the phase transformation was proposed with the help of crystal structures of the two phases. Electrochemical studies on this rarely studied tetragonal phase was carried out using cyclic voltammetry and galvanostatic cycling studies which revealed its excellent lithium cycling at 4 V and a capacity of 103 mAh g^{-1} was obtained at a current rate of 0.1 C.

6.1 Introduction

High cost, toxicity and safety issues of the commercial cathode material, $LiCoO_2$ had alarmed the need for a potential replacement. In the past two decades, extensive research has been carried out on the olivine structured cathode materials $LiMPO_4$ (M = Fe, Mn, Ni or Co) [1–6]. Among these materials, $LiFePO_4$ has been considered to be the most promising material to replace $LiCoO_2$ because of low cost, environmental friendliness, very flat potentials during charge–discharge processes and high theoretical capacity of 170 mAh g^{-1}. In addition, the phosphates are safer cathodes as they do not encounter the problem of oxygen evolution which is commonly observed in the oxide cathodes. Despite having these advantages, poor electronic and ionic conductivities of $LiFePO_4$ along with its low operating voltage of 3.4 V has restrained its large scale application in commercial LIBs.

In this context, the higher redox potential ($\sim$4 V) of $LiVOPO_4$ combined with a good theoretical capacity of 166 mAh g^{-1} makes its energy density ($\sim$660 Wh kg^{-1}) higher than that of $LiFePO_4$ ($\sim$578 Wh kg^{-1}) and projects to be a promising high voltage cathode material for LIBs. $LiVOPO_4$ is known to exist in

A.S. Hameed, *Phosphate Based Cathodes and Reduced Graphene Oxide Composite Anodes for Energy Storage Applications*,
Springer Theses, DOI 10.1007/978-981-10-2302-6_6

three different crystal systems, namely, α-, β- and α_I-phases. Lavrov et al. reported the first synthesis of α-$LiVOPO_4$ which crystallizes in the triclinic space group, $P\bar{1}$ [7]. The structure can be described as chains of corner-sharing VO_6 octahedra along the *b*-axis which are inter-connected in three dimension by tetrahedral $(PO_4)^{3-}$ units by corner sharing. It has two crystallographically distinct five-coordinate Li ions (Fig. 6.1a). Single crystals of the orthorhombic β-$LiVOPO_4$ was obtained by Lii et al. by hydrothermal synthesis in a sealed quartz tube at 450 °C [8]. This phase is characterized by a framework consisting of infinite chains of corner-shared VO_6 octahedra having alternate short and long V–O bonds parallel to the *a*-axis. These chains are cross-linked by corner-shared PO_4 tetrahedra while the Li atom has six close oxygen neighbors (Fig. 6.1b). The third phase named as α_I-$LiVOPO_4$ is a metastable phase observed by Dupre et al. when two different phases of $VOPO_4$ was

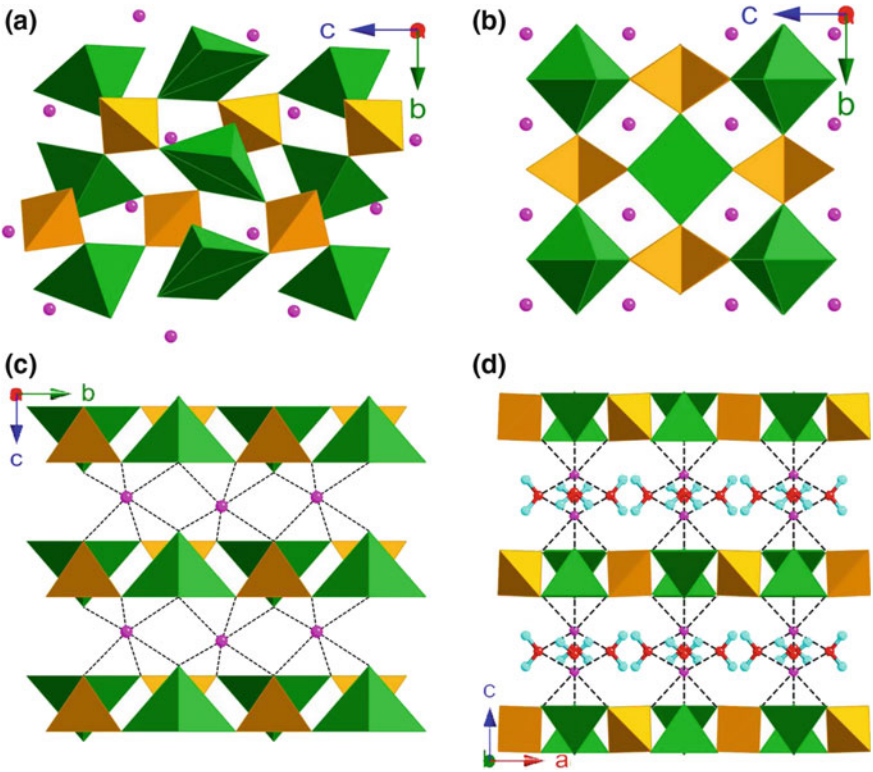

Fig. 6.1 Crystal structures of **a** α-$LiVOPO_4$, **b** β-$LiVOPO_4$, **c** α_I-$LiVOPO_4$ viewed along *a*-axis and **d** $LiVOPO_4{\cdot}2H_2O$ viewed along *b*-axis. Green and orange polyhedra represent VO_5 and PO_4 units respectively. Pink balls represent Li while blue and red colored balls respectively represent H and O atoms

lithiated chemically and electrochemically. This phase is known to crystallize in the tetragonal space group *P*4/nmm. This phase is characterized by a layered structure in which corner sharing of VO_5 units with four different $(PO_4)^{3-}$ tetrahedra resulting in $VOPO_4$ layers. These layers are stacked along *c*-axis by Li ions which are present in the interlayer space exhibiting an octahedral geometry (Fig. 6.1c).

Electrochemical studies of $LiVOPO_4$ has been focused mainly on the orthorhombic and the triclinic phases. Gaubicher et al. demonstrated the first lithium storage in β-$VOPO_4$ which forms an isostructural phase, β-$LiVOPO_4$ upon lithium intercalation [9]. It was found that only $\sim$0.55 mol of Li intercalates per mole of $VOPO_4$, leading to a capacity of 90 mAh g^{-1} at 0.02 C current rate with a constant working voltage of 3.95 V. Later, Kerr et al. reported another 4 V cathode material ε-$VOPO_4$ which leads to the formation of α-$LiVOPO_4$ phase after the first reduction process [10]. In α-$LiVOPO_4$, the Li ions are loosely bound in five-coordinate sites allowing a facile Li^+ ion conduction. A capacity of over 100 mAh g^{-1} at a cycling rate of 0.1 C was obtained. As the lithiated phase, $LiVOPO_4$ can exhibit better electrochemical lithium reversibility than $VOPO_4$, it was prepared by various methods like carbothermal reduction, impregnation method, hydrothermal and microwave sintering [11–19]. Though these materials showed slightly better performance, they were not impressive. Recently, enhancement in the capacity was observed for α and β-$LiVOPO_4$ phases obtained with good carbon coating due to enhancement in the electronic conductivity [20, 21]. However, it has still been a challenge to attain the theoretical capacity and to achieve better rate performance for both the systems.

The sole report in the literature for the electrochemical lithium storage of tetragonal α_I-$LiVOPO_4$ phase was by Dupre et al. [22] This α_I-$LiVOPO_4$ phase was observed during lithium insertion in two phases of $VOPO_4$ namely α_I- and α_{II}-$VOPO_4$ [23]. Theoretical studies on this phase has shown the possibility of a 2D lithium ion migration and expected to exhibit a better lithium storage performance than the α and β phases. However, a detailed electrochemical study of this phase is still lacking.

In this chapter, we report the first direct synthesis of tetragonal α_I-$LiVOPO_4$ by an easier and cost-effective route. The isolation of pure α_I-phase has been carried out by dehydration of the hydrated precursor $LiVOPO_4{\cdot}2H_2O$ which was obtained by a hydrothermal reaction at 120 °C. Electrochemical properties of the material was investigated by cyclic voltammetry and galvanostatic cycling studies which indicate the highly reversible lithium storage in the material at 4 V.

6.2 Experimental Section

All the chemicals and solvents used in this study are commercially available and used without further purification.

6.2.1 Synthesis of $LiVOPO_4{\cdot}2H_2O$

$LiVOPO_4{\cdot}2H_2O$ was synthesized by hydrothermal method at 120 °C. In a typical synthesis, vanadium pentoxide (1 mmol, 0.182 g, Aldrich, purity 98 %), oxalic acid dihydrate (1.4 mmol, 0.176 g, Merck, purity 99.5 %) and $LiPO_3$ (2 mmol, 0.172 g, Johnson Matthey, purity 97 %) was added to 10 mL of deionised water and sonicated for 30 min to get a homogenous mixture. The solution was sealed tightly in a Teflon-lined stainless steel autoclave with a fill factor of ~40 %. The mixture was heated under autogenous pressure for 48 h at 120 °C, followed by slow cooling to room temperature. In this reaction, oxalic acid acts as a reducing agent for the reduction of V^{5+} to V^{4+}. Upon cooling, bluish-green platy single crystals of $LiVOPO_4{\cdot}2H_2O$ were obtained. Yield: 0.34 g (84 %). Anal. Calcd for H_4LiO_7PV: H, 1.97; Li, 3.39; P, 15.12; V, 24.86. Found: H, 1.80; Li, 3.06; P, 15.50; V, 24.01. A selected single crystal was utilized for structural analysis by single crystal X-ray diffraction technique. The compound was washed thoroughly with deionised water, dried under vacuum and used for further studies.

6.2.2 Synthesis of α_I-$LiVOPO_4$

The hydrothermally prepared $LiVOPO_4{\cdot}2H_2O$ was dehydrated to obtain the tetragonal α_I-$LiVOPO_4$ phase. For this purpose, the hydrated precursor was kept in a round-bottom flask and heated on a heating mantle at 300 °C under vacuum for 2 h and cooled to room temperature under argon atmosphere. The single crystals became opaque on the removal of water and turned to dark green from bluish green. The obtained α_I-$LiVOPO_4$ powder was utilized for the electrochemical studies.

6.2.3 Structural and Electrochemical Characterization

6.2.3.1 Crystal Structure Determination

The structure of $LiVOPO_4{\cdot}2H_2O$ was determined by single-crystal X-ray diffraction. A platy crystal of dimensions 0.40 × 0.36 × 0.16 mm^3 was selected under an optical microscope and the data were collected on a Bruker AXS SMART CCD diffractometer. The detailed crystallographic data are summarized in Table 6.1. Unit cell dimensions were obtained by least-squares refinements, and the structure was solved by direct methods. The program *SMART* [24] was used for collecting frames of data, indexing reflections and determining lattice parameters and *SAINT* [24] for integration of intensity of reflections and scaling; *SADABS* [25] was used for empirical absorption correction and *SHELX TL* [26] was used for space-group determination, structure solution and least-squares refinements on F^2.

Table 6.1 Crystallographic data and structure refinement details of $LiVOPO_4{\cdot}2H_2O$

Formula	H_4LiO_7PV
Formula weight	204.88
T (K)	223(2)
Crystal system	Orthorhombic
Space group	*Cmca*
Unit cell dimensions (Å)	a = 8.9454(7)
	b = 9.0406(7)
	c = 12.747(1)
V ($Å^3$)	1030.9(1)
Z	8
Density (calculated, g cm^{-3})	2.640
μ (mm^{-1})	2.206
Crystal size (mm^3)	0.40 × 0.36 × 0.16
Theta range	3.20 to 27.48°
Reflections collected	3374
Independent reflections	633 [R(int) = 0.023]
Absorption correction	Semi-empirical from equivalents
Max. and min. transmission	0.7192 and 0.4724
Refinement method	Full-matrix least-squares on F^2
Data/restraints/parameters	633/0/61
Goodness of fit on F^2	1.175
Final R indices [I > 2sigma(I)]	R_1 = 0.025, wR_2 = 0.0679
R indices (all data)	R_1 = 0.0252, wR_2 = 0.0681
Largest diff. peak and hole	0.261 and −0.718 e $Å^{-3}$

The α_I-$LiVOPO_4$ synthesized in this study were characterized by PXRD, Rietveld refinement, temperature dependent XRD, SEM, TGA, cyclic voltammetry and galvanostatic cycling studies. Details of these characterization techniques have been described previously in Chap. 2.

6.3 Results and Discussion

6.3.1 Structure Analysis

Single crystal X-ray diffraction analysis of the precursor, $LiVOPO_4{\cdot}2H_2O$ revealed that the compound crystallizes in the orthorhombic crystal system (*Cmca* space group). The lattice parameters are found to be a = 8.9454(7) Å, b = 9.0406(7) Å and c = 12.7373(10) Å. The asymmetric unit is made up of half of the formula unit. Each vanadium atom is connected to four different phosphate units by corner sharing and a V = O oxygen atom, forming a distorted VO_5 square pyramidal

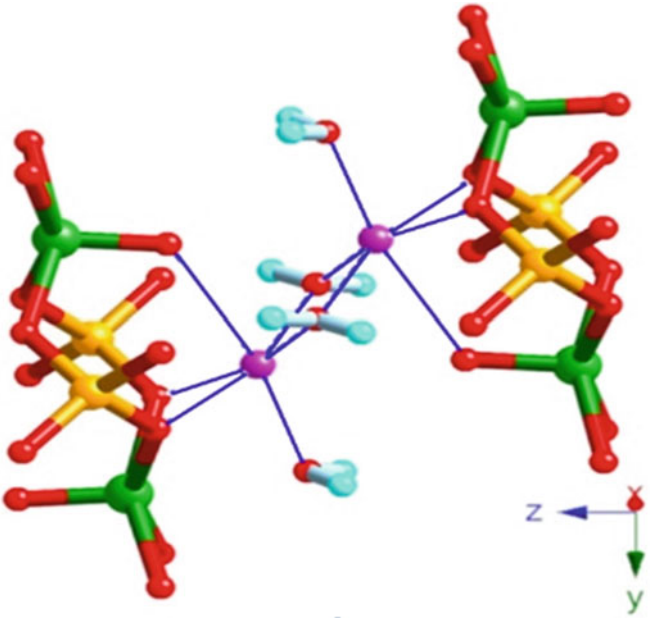

Fig. 6.2 Crystal structure of $LiVOPO_4{\cdot}2H_2O$ showing the environment of lithium. V, P, O, H and Li atoms are shown in *green*, *orange*, *red*, *blue* and *purple* respectively

geometry. The four equatorial V–O bonds have an average bond length of 2.002 Å which is well within the reported values, while the apical oxo group has a shorter bond length of 1.587(2) Å. The tetrahedral phosphate groups have an average P–O bond length of 1.539 Å. Corner sharing of these VO_5 and PO_4 polyhedra results in the formation of anionic vanadylphosphate layers, $[VOPO_4]_\infty$ along the *ab*-plane as shown in Fig. 6.1d. The negative charges of the layers are neutralized by Li ions which are present in between the layers. The two adjacent $[VOPO_4]$ layers are bridged by $[(H_2O)Li(\mu\text{-}OH_2)_2Li(OH_2)]$ moieties. Each lithium ion forms an octahedral geometry by coordinating to three oxygen atoms from vanadyl phosphate layer and three water molecules of which two are bridged aqua ligands and one terminal aqua ligand as shown in Fig. 6.2. It may be noted that the apical V = O oxygen atom (O2) is also bonded to the lithium ion. These $VOPO_4$ layers are stacked along the *c*-axis in ABAB fashion as shown in Fig. 6.3. The atomic coordinates of $LiVOPO_4{\cdot}2H_2O$ are given in Table 6.2.

6.3.2 TGA and PXRD

TGA of $LiVOPO_4{\cdot}2H_2O$ shows a single weight loss of 17.8 % (Fig. 6.4) in the range of 100–250 °C, corresponding to the removal of two molecules of water (Observed,

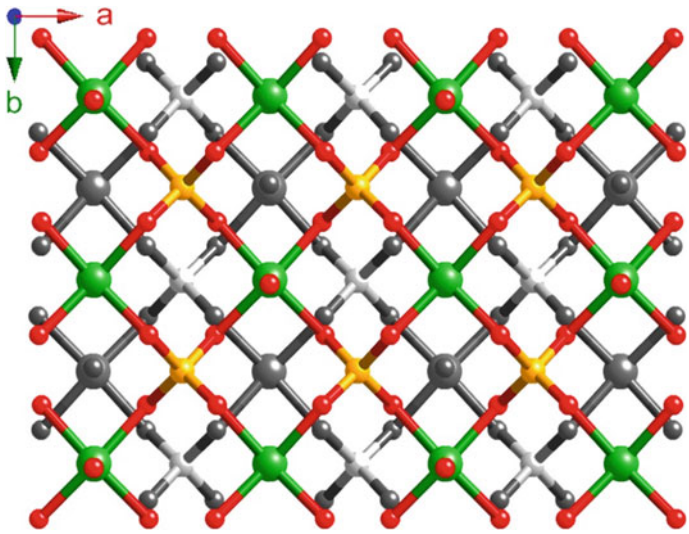

Fig. 6.3 Crystal structure of $LiVOPO_4{\cdot}2H_2O$ showing the ABAB type packing of $VOPO_4$ layers along *c*-axis. Layer A is shown in colour while layer B is shown in grayscale or vice versa. Li ions and water are removed for clarity. V, P, O atoms are shown as *green*, *orange* and *red* balls respectively

Table 6.2 Atomic coordinates and equivalent isotropic displacement parameters ($Å^2$) of $LiVOPO_4{\cdot}2H_2O$

Atom	x	y	z	B_{iso} ($Å^2$)
V1	0.5	0.6234(1)	0.7906(1)	0.005(1)
Li1	0.5	0.8776(5)	0.9344(4)	0.018(1)
P1	0.25	0.8761(1)	0.75	0.004(1)
O1	0.6567(1)	0.4727(1)	0.8257(1)	0.008(1)
O2	0.5	0.6125(2)	0.6664(2)	0.012(1)
O3	0.3507(1)	0.7822(1)	0.8209(1)	0.008(1)
O1w	0.3359(2)	1.0	1.0	0.013(1)
O2w	0.5	0.6676(2)	0.9989(2)	0.014(1)

17.8 %, Calculated, 17.6 %). The high temperature required for dehydration supports the existence of strong coordination of the water molecules to lithium.

PXRD pattern of the synthesized bulk sample is shown in Fig. 6.5. As can be seen from the Rietveld refinement, the bulk powder matches very well with the single crystal structure and no other impurities were observed. However, the intensity of (110) peak is comparably very high due to preferred orientation of the crystals at plates along *ab*-plane. In situ PXRD patterns were recorded in vacuum between RT and 500 °C (Fig. 6.6) to study the dehydration of $LiVOPO_4{\cdot}2H_2O$. As inferred from these patterns, at 80 °C the structure of $LiVOPO_4{\cdot}2H_2O$ is almost

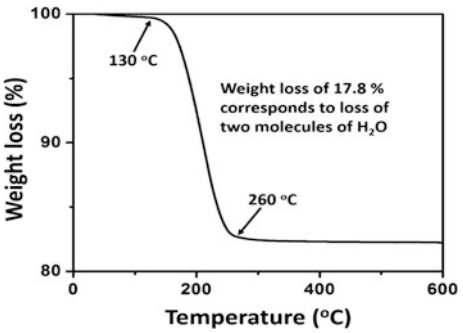

Fig. 6.4 TGA of $LiVOPO_4{\cdot}2H_2O$ recorded in air at a rate of 5 °C min^{-1}

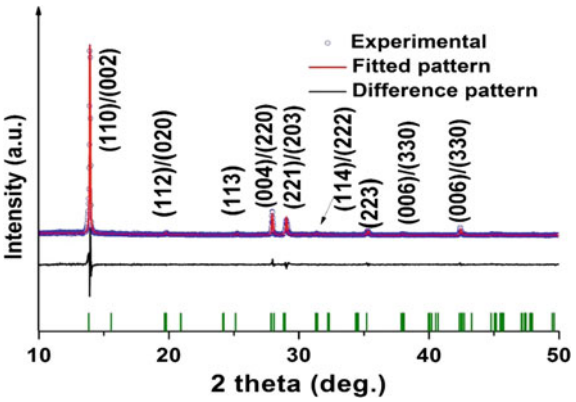

Fig. 6.5 Rietveld refinement of $LiVOPO_4{\cdot}2H_2O$

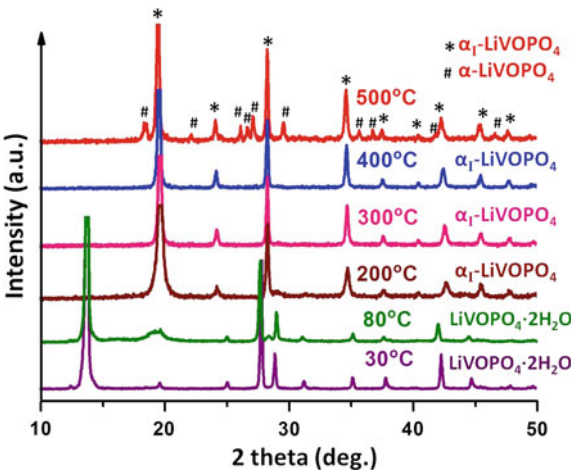

Fig. 6.6 In-situ PXRD patterns of $LiVOPO_4{\cdot}2H_2O$ between RT and 500 °C

retained while new peaks begin to appear on the onset of dehydration. At 200 °C, the original peaks disappear completely and a new set of peaks which matches exactly with that of α_I-$LiVOPO_4$ appears as the main phase. PXRD patterns at 300 and 400 °C revealed the presence of α_I-$LiVOPO_4$ as the single phase without any other impurity phases. The peaks matches well with that of α_I-$LiVOPO_4$ obtained by Dupre et al., via lithiation of $VOPO_4$ [23]. The lattice parameters of α_I-$LiVOPO_4$ at different temperatures were calculated by Reitveld refinement of the respective PXRD patterns which are tabulated in Table 6.3. The results show that the lattice parameters are close to that of α_I-$LiVOPO_4$ obtained by lithiation of α_I- and α_{II}-$VOPO_4$. Upon further increase in temperature, there is a phase transformation from α_I-$LiVOPO_4$ to α-$LiVOPO_4$. The PXRD pattern collected at 500 °C shows a mixture of α-$LiVOPO_4$ and α_I-$LiVOPO_4$.

As inferred from the in situ XRD patterns the α_I-phase exists as pure phase between ~200 and 400 °C. In our attempts to obatin the α_I-phase by complete dehydration of the dihydrate phase at 300 °C in air. However, PXRD pattern of the dehydration product possessed additional peaks along with that of the α_I-phase (Fig. 6.7). TGA of the powder indicated ~3 % weight loss inferring the re-absorption of water by the sample. To eliminate this possibility, dehydration of the precursor was carried out in vacuum for 2 h followed by cooling to room temperature in argon atmosphere. This resulted in the pure α_I-$LiVOPO_4$ phase as confirmed from Fig. 6.7a.

Table 6.3 Comparison of lattice parameters of α_I-$LiVOPO_4$ at different temperatures, obtained from the Rietveld refinement

Temperature	*a* (Å)	*c* (Å)	*V* (Å^3)
200 °C	6.2821	4.5087	177.94
300 °C	6.2863	4.4965	177.69
400 °C	6.2953	4.5092	178.70
Lithiation of α_I-$VOPO_4$ (Dupre et al. [23])	6.2910(1)	4.4452(1)	175.92(1)

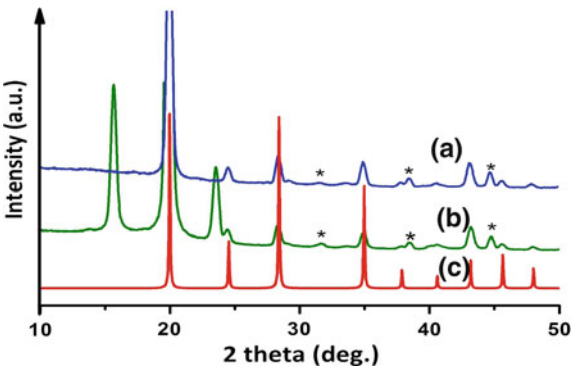

Fig. 6.7 PXRD pattern of the dehydration product of $LiVOPO_4 \cdot 2H_2O$ in **a** argon and **b** air (Peaks from the sample holder are shown in *asterisk*). **c** Simulated pattern of α_I-$LiVOPO_4$

6.3.3 Structural Transformation Mechanism

The dehydration reaction of $LiVOPO_4{\cdot}2H_2O$ to α_I-$LiVOPO_4$ involves crystal structure transformation from orthorhombic to tetragonal system. To understand the structural transformation accompanying this dehydration reaction, crystal structures of these two compounds need careful examination which indicates that 2-D $VOPO_4$ layers in both structures are identical. In both phases, $VOPO_4$ layers are made of corner shared VO_5 and PO_4 polyhedra which are oriented along *ab*-plane (Fig. 6.1c, d).

The basic difference in their structure arises from stacking of these $VOPO_4$ layers along the *c*-axis. In $LiVOPO_4{\cdot}2H_2O$, the layers are stacked along the *c*-axis by Li ions present in between the layers. Each lithium ion is coordinated to two phosphate groups and a vanadate oxygen and three water molecules (Fig. 6.2). In α_I-$LiVOPO_4$, the $VOPO_4$ layers are arranged along *c*-axis by symmetrical bridging of the layers by Li^+ ions present in the interlayer space. Li^+ ions in this phase are coordinated to two phosphate groups and a vanadate oxygen from both layers forming an octahedral geometry (Fig. 6.8) [23]. Another striking difference between the two structures arise from the stacking of the $VOPO_4$ layers. In $LiVOPO_4{\cdot}2H_2O$, the $VOPO_4$ layers are stacked one above the other in ABAB manner while α_I-$LiVOPO_4$ is characterized by parallel stacking (AAA) of the layers. Hence, removal of the aqua ligands from $LiVOPO_4{\cdot}2H_2O$ results in three-coordinated Li-ions which would trigger a spontaneous molecular movement in which the alternate $VOPO_4$ layers slide along the *ab*-plane to facilitate the establishment of LiO_6 octahedra resulting in the α_I-$LiVOPO_4$ phase. A probable mechanism for the structural transformation of $LiVOPO_4{\cdot}2H_2O$ to α_I-$LiVOPO_4$ is narrated in Fig. 6.9.

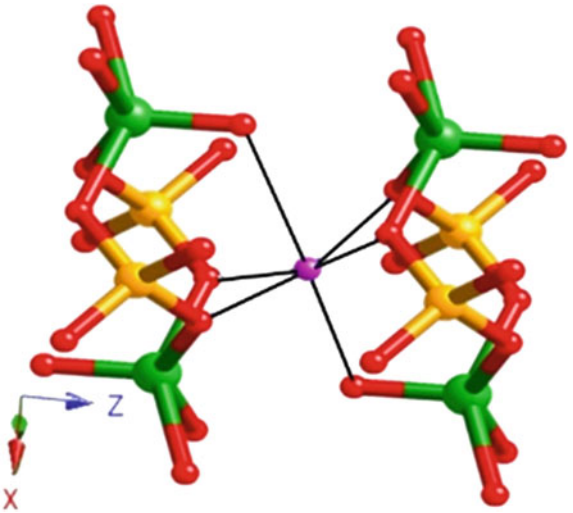

Fig. 6.8 Crystal structure of α_I-$LiVOPO_4$ showing the environment of Li. V, P, O and Li atoms are shown as *green*, *orange*, *red* and *purple* balls

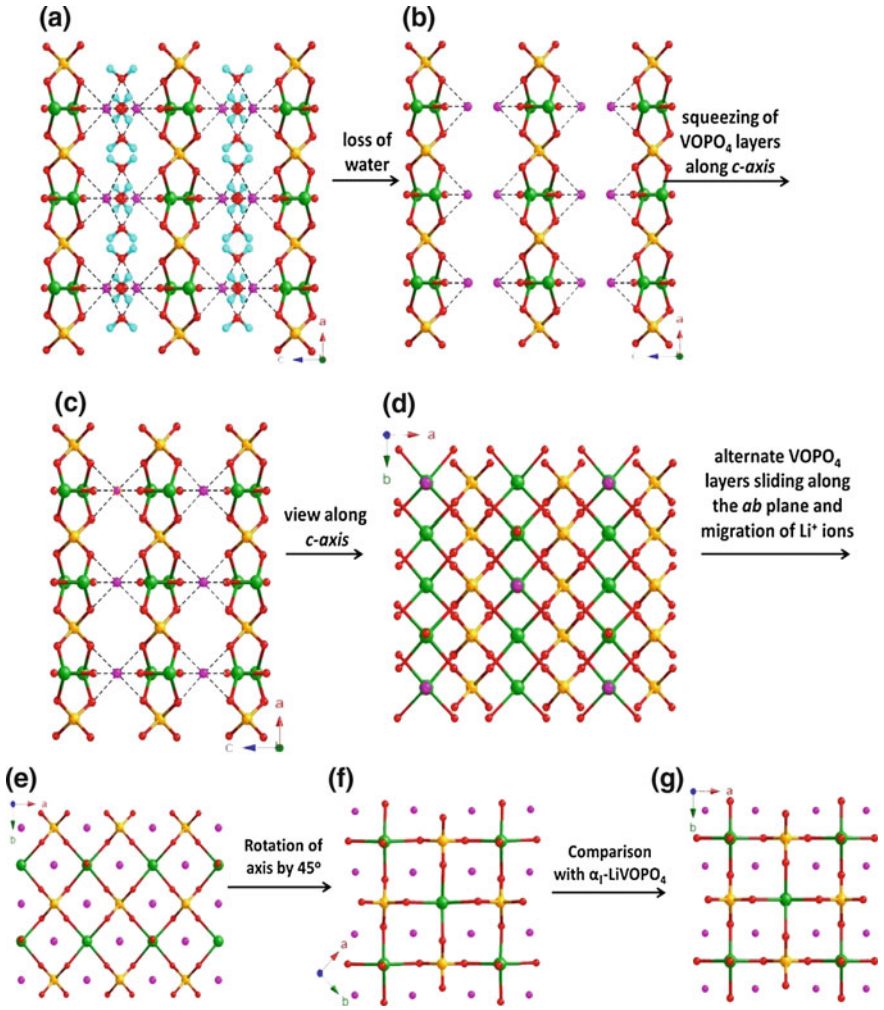

Fig. 6.9 Proposed mechanism for the structural transformation of $LiVOPO_4{\cdot}2H_2O$ to α_I-$LiVOPO_4$: **a** $LiVOPO_4{\cdot}2H_2O$ viewed along *b*-axis, **b**, **c** both removal of water bonded to the Li ions and movements of $VOPO_4$ layers occur simultaneously. The Li ions are aligned one behind another in **c**; **d** viewed along *c*-axis, **e** viewed along *c*-axis, $VOPO_4$ layers are aligned in parallel, **f** rotation by 45° along *c*-axis and **g** α_I-$LiVOPO_4$ viewed along *c*-axis

6.3.4 Galvanostatic Cycling

To investigate the electrochemical properties of the material, as-synthesized $LiVOPO_4{\cdot}2H_2O$ was ball-milled for 2 h in an agate vial of volume 5 mL (ball: sample weight ratio of 2:1) as the precursor mainly contained single crystals of size 200–500 μm. As a result of mild milling, particle size decreases to of few hundred

nanometers. It was then subjected to dehydration to the obtain α_I-phase as described in the experimental section. PXRD pattern of α_I-$LiVOPO_4$ obtained from the ball-milled precursor reveals the phase purity and the SEM micrographs reveal the formation of α_I-$LiVOPO_4$ nanoplates with thickness of few hundred nanometers.

Electrodes prepared from this sample as discussed in Chap. 2 were subjected to galvanostatic charge-discharge cycling in the voltage window of 2.5–4.5 V versus Li/Li^+ at a current density of 16 mA g^{-1} (0.1 C). During the first charge cycle (Lithium de-intercalation or oxidation), voltage increases sharply to ~4 V from the open circuit voltage (~2.8 V), followed by a long plateau at ~4.05 V (Fig. 6.10) and then increases steeply to the cut-off voltage of 4.5 V. This results in a capacity of 141 mAh g^{-1} which is just 25 mAh g^{-1} short of its theoretical capacity (166 mAh g^{-1}). During the first discharge cycle, lithium intercalation follows a similar behaviour with a plateau at ~3.9 V and a discharge capacity of 103 mAh g^{-1} was obtained. An irreversible capacity loss of 38 mAh g^{-1} was observed during the first cycle. The small voltage difference of ~0.15 V between the charge and discharge reveals a small polarization, indicating a reasonably good conductivity of the sample. Subsequent charge and discharge cycles show similar plateau and a charge capacity of 113 (±3) mAh g^{-1} was obtained at the end of 30 cycles. The discharge capacity was almost retained after 30 cycles with a coulombic efficiency of 91 %. The reason for higher charge capacity than the discharge capacity may be attributed to the cathode electrolyte interface. The plot of capacity versus cycle number is shown in Fig. 6.11. The α_I-$LiVOPO_4$ phase synthesized by this procedure shows better electrochemical performance than the one reported by Dupre et al. which was synthesized by lithiation of $VOPO_4$ [22]. The obtained reversible capacity of the material is comparable with the other phases of $LiVOPO_4$ (α- and β-$LiVOPO_4$) containing similar sized particles [12–18]. Enhancement in the capacity was observed for α- and β-$LiVOPO_4$ phases with good carbon coating due to enhancement in electronic conductivity [20, 21]. Many cathode and anode materials such as $LiFePO_4$, $Li_3V_2(PO_4)_3$, Fe_2O_3, etc., were found to exhibit better lithium cycling when the material was prepared in the form of nanoparticles [27–32]. So, we believe that the electrochemical performance of α_I-$LiVOPO_4$ can

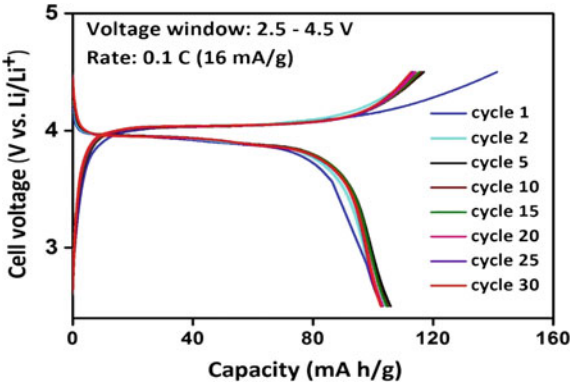

Fig. 6.10 Galvanostatic charge-discharge cycling of α_I-$LiVOPO_4$ at a current rate of 0.1 C in the potential window of 2.5–4.5 V

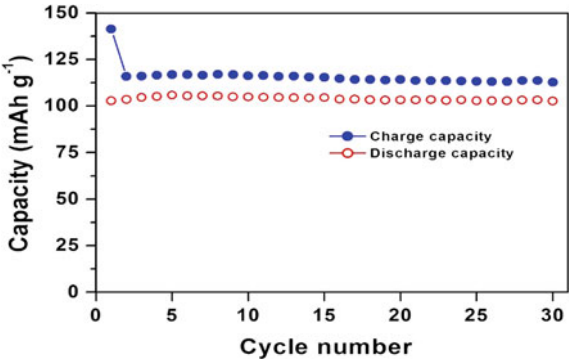

Fig. 6.11 Plot of capacity versus cycle number of α_I-$LiVOPO_4$ at a current rate of 0.1 C in the potential window of 2.5–4.5 V

be further improved upon decreasing the particle size to nano-scale along with good carbon coating by suitable chemical synthesis.

6.3.4.1 Rate Capability Studies

Further investigation on the electrochemical properties of the material was carried out by examining the rate capability. The material was subjected to galvanostatic cycling at different current densities like 16, 33, 83, 166, 332, 500 mA g^{-1} which correspond to the current rates of 0.1, 0.2, 0.5, 1, 2 and 3 C respectively (1 C represents a current density of 166 mA g^{-1}). Figure 6.12 shows the plot of reversible capacity versus cycle number at different current rates. The discharge capacities obtained for the different current rates are 103, 93, 73, 57, 37 and 25 (±3) mAh g^{-1}, respectively. Even though the material exhibits good reversible lithium intercalation with excellent capacity retention, the rate capability of the material decrease on increasing current rate from 0.1 to 3 C. This is due to the sluggish lithium diffusion kinetics at high current rates due to big particle size and poor electronic conductivity. However, the coulombic efficiency which was lesser

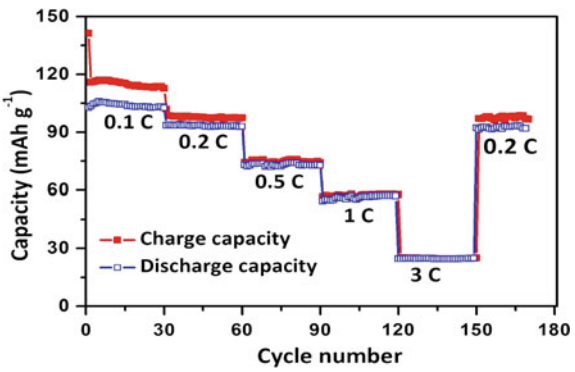

Fig. 6.12 Rate capability of α_I-$LiVOPO_4$ at different current rates in the potential window of 2.5–4.5 V

at lower current rate was found to be better at higher current rates. The coulombic efficiency increases from 91 to 99.6 % when current rate was increased from 0.1 to 3 C. However, as expected there was an increase of polarization on moving to higher current rates which may be due to increase in the electrode resistance. The material also recovered its capacity of 92 mAh g^{-1} when the current rate was decreased back to 0.2 C from 3 C.

6.3.4.2 Long Term Cycling

Capacity retention of the material upon long term cycling is also important for a good cathode material. In order to investigate the long term cycling performance of α_I-$LiVOPO_4$, it was subjected to galvanostatic cycling at a current rate of 0.5 C which corresponds to a current density of 80 mA g^{-1}. As inferred from Fig. 6.13, the material exhibits excellent capacity retention as there was a very minimal capacity decay. A capacity of 69 mAh g^{-1} was obtained at the end of 200th cycle.

6.3.5 Cyclic Voltammetry

Cyclic voltammograms (CV) of α_I-$LiVOPO_4$ (Fig. 6.14) was recorded in the potential range of 2.5–4.5 V versus Li/Li^+ at room temperature using lithium metal as anode with a scan rate of 0.058 mV s^{-1}. The CV curves show a single peak in the anodic (Li-extraction) scan at 4.17 V indicating a single electron transfer which corresponds to the oxidation of V^{4+} to V^{5+}. The cathodic scan (Li-insertion) is characterized by a reduction peak at 3.75 V. The redox reaction involving V^{4+}/V^{5+} redox couple during the lithium extraction/insertion is shown in Eq. 6.1. This redox potential is in agreement with the galvanostatic charge-discharge cycling and also with other reported V^{4+}/V^{5+} systems [12, 14]. The overlapping curves for different cycles infer excellent reversibility of lithium cycling in the material.

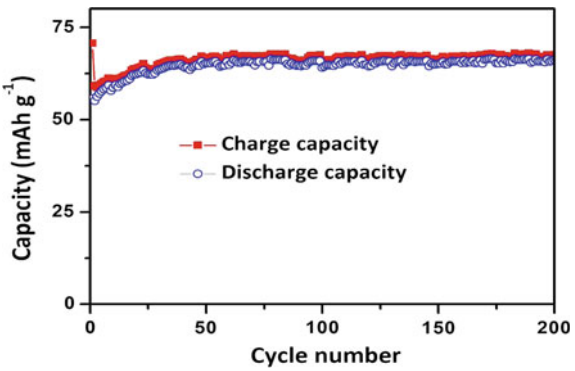

Fig. 6.13 Long term cycling of α_I-$LiVOPO_4$ at a current rate of 0.5 C in the potential window of 2.5–4.5 V

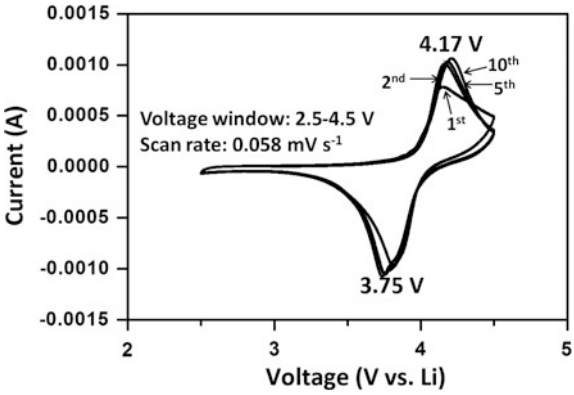

Fig. 6.14 Cyclic voltammograms of α_I-$LiVOPO_4$ at a scan rate of 0.058 mV s^{-1} in the potential window of 2.5–4.5 V

$$LiVOPO_4 \leftrightarrow VOPO_4 + Li^+ + e^- \tag{6.1}$$

6.4 Conclusions

In summary, the metastable α_I-$LiVOPO_4$ phase was synthesized by a direct chemical synthesis for the first time via dehydration of the hydrothermally synthesized phase, $LiVOPO_4{\cdot}2H_2O$. A probable mechanism for structural transformation of the hydrated phase into the α_I-phase was also proposed. The electrochemical investigation of α_I-$LiVOPO_4$ revealed its good lithium storage performance. Further improvement in the lithium storage of the material may be attained by nano-scale synthesis.

References

1. S.-Y. Chung, J.T. Bloking, Y.-M. Chiang, Nat. Mater. **1**, 123–128 (2002)
2. A.K. Padhi, K.S. Nanjundaswamy, J.B. Goodenough, J. Electrochem. Soc. **144**, 1188–1194 (1997)
3. M.K. Devaraju, I. Honma, Adv. Energy Mater. **2**, 284–297 (2012)
4. K. Amine, H. Yasuda, M. Yamachi, Electrochem. Solid-State Lett. **3**, 178–179 (2000)
5. L. Dimesso, D. Becker, C. Spanheimer, W. Jaegermann, J. Solid State Electrochem. **16**, 3791–3798 (2012)
6. C.A.J. Fisher, V.M. Hart, Prieto and M. S. Islam. Chem. Mater. **20**, 5907–5915 (2008)
7. A.V. Lavrov, V.P. Nikolaev, G.G. Sadikov, M.A. Porai-Koshits, Dokl. Akad. Nauk SSSR **266**, 343–346 (1982)
8. K.H. Lii, C.H. Li, C.Y. Cheng, S.L. Wang, J. Solid State Chem. **95**, 352–359 (1991)
9. J. Gaubicher, T.L. Mercier, Y. Chabre, J. Angenault, M. Quarton, J. Electrochem. Soc. **146**, 4375–4379 (1999)
10. T.A. Kerr, J. Gaubicher, L.F. Nazar, Electrochem. Solid-State Lett. **3**, 460–462 (2000)

11. L. Wang, L. Yang, L. Gong, X. Jiang, K. Yuan, Z. Hu, Electrochim. Acta **56**, 6906–6911 (2011)
12. K. Saravanan, H.S. Lee, M. Kuezma, J.J. Vittal, P. Balaya, J. Mater. Chem. **21**, 10042–10050 (2011)
13. C.J. Allen, Q. Jia, C.N. Chinnasamy, S. Mukerjee, K.M. Abraham, J. Electrochem. Soc. **158**, A1250–A1259 (2011)
14. M.M. Ren, Z. Zhou, L.W. Su, X.P. Gao, J. Power Sources **189**, 786–789 (2009)
15. M.M. Ren, Z. Zhou, X.P. Gao, L. Liu, W.X. Peng, J. Phys. Chem. C **112**, 13043–13046 (2008)
16. J. Barker, M.Y. Saidi, J.L. Swoyer, J. Electrochem. Soc. **151**, A796–A800 (2004)
17. B.M. Azmi, H.S. Munirah, T. Ishihara, Y. Takita, Ionics **11**, 402–405 (2005)
18. B.M. Azmi, T. Ishihara, H. Nishiguchi, Y. Takita, J. Power Sources **146**, 525–528 (2005)
19. M. Bianchini, J.M. Ateba-Mba, P. Dagault, E. Bogdan, D. Carlier, E. Suard, C. Masquelier, L. Croguennec, J. Mater. Chem. A **2**, 10182–10192 (2014)
20. A. Tang, J. Shen, Y. Hu, G. Xu, D. He, Q. Yi, R. Peng, J. Electrochem. Soc. **161**, A10–A13 (2014)
21. B.J. Paul, V. Mathew, G.X. Do, J.-W. Kang, J. Gim, A.K. Rai, N.K. Singh, J. Song, J. Kim, E.C.S. Electrochem, Lett. **1**, A63–A65 (2012)
22. N. Dupre, J. Gaubicher, J. Angenault, G. Wallez, M. Quarton, J. Power Sources **97–98**, 532–534 (2001)
23. N. Dupre, G. Wallez, J. Gaubicher, M. Quarton, J. Solid State Chem. **177**, 2896–2902 (2004)
24. *SMART and SAINT Software Reference Manuals Version 5.0 2000* (Bruker Analytical X-ray Systems, Inc., Madison)
25. G.M. Sheldrick, *SADABS, A Software for Empirical Absorptions Correction, Version 2.03 2001 (University of Göttingen, Göttingen)*
26. *SHELXTL Reference Manual, Version 6.1 2000 (Bruker Analytical X-ray Systems, Inc., Madison)*
27. C. Delmas, M. Maccario, L. Croguennec, F. Le Cras, F. Weill, Nat. Mater. **7**, 665–671 (2008)
28. H. Huang, S.C. Yin, L.F. Nazar, Electrochem. Solid-State Lett. **4**, A170–A172 (2001)
29. M.M. Ren, Z. Zhou, X.P. Gao, W.X. Peng, J.P. Wei, J. Phys. Chem. C **112**, 5689–5693 (2008)
30. L. Wang, L.-C. Zhang, I. Lieberwirth, H.-W. Xu, C.-H. Chen, Electrochem. Commun. **12**, 52–55 (2010)
31. D. Larcher, C. Masquelier, D. Bonnin, Y. Chabre, V. Masson, J.B. Leriche, J.M. Tarascon, J. Electrochem. Soc. **150**, A133–A139 (2003)
32. M.V. Reddy, T. Yu, C.-H. Sow, Z.X. Shen, C.T. Lim, G.V.S. Rao, B.V.R. Chowdari, Adv. Funct. Mater. **17**, 2792–2799 (2007)

Chapter 7
Single Source Precursor Route to rGO/Sb_2S_3 Nanocomposites for Lithium Ion Battery Anodes

Abstract In this chapter, the synthesis of Sb_2S_3 and rGO/Sb_2S_3 composites for Lithium ion battery applications have been reported. The stibnite phase was obtained employing single source precursor approach. A metal complex, $Sb(SCOPh)_3$ was prepared at room temperature by the reaction of sodium thiobenzoate with $SbCl_3$. Annealing of the precursor at 400 °C in Ar leads to the stibnite phase of Sb_2S_3. To improve the battery performance, rGO composite of Sb_2S_3 were also prepared by annealing the rGO/$Sb(SCOPh)_3$ mixtures obtained by different techniques. Electrochemical performance of the prepared composites were investigated using galvanostatic cycling, cyclic voltammetry and ex situ XRD studies. The pristine sample shows very poor lithium cycling while the rGO composites demonstrate better lithium storage. The rGO/Sb_2S_3 obtained by microwave irradiation of rGO/$Sb(SCOPh)_3$ followed by annealing at 400 °C shows good capacity retention.

7.1 Introduction

Graphite is the commonly used anode material in commercial Lithium ion batteries owing to its abundance, low cost, good cycle life and environmental friendliness [1, 2]. However, it has low specific capacity of 372 mAh g^{-1}. In addition, graphite poses safety concerns when charged at faster rates as Li metal deposition on the graphite anode results in dendrite formation [3]. This leads to the rupture of micro-porous separator, resulting in short-circuiting of LIBs. This illustrates the demand for alternate safer anode materials which should also possess better theoretical capacity compared to graphite [4]. Various binary and ternary metal oxides like TiO_2 [5–7], SnO_2 [8, 9], Fe_2O_3 [10–12], MoOx [13, 14], MFe_2O_4 (M = Ni, Co, Mn, Zn) [15–20], etc., especially in the form of nanoparticles have been investigated extensively for anode applications. These oxides possess various advantages such as very high capacity, good volumetric energy density, easy availability, good cycleability, and environmental benignity.

A.S. Hameed, *Phosphate Based Cathodes and Reduced Graphene Oxide Composite Anodes for Energy Storage Applications*,
Springer Theses, DOI 10.1007/978-981-10-2302-6_7

Sulphide based materials such as CuS [21, 22], NiS [23], SnS_2 [24, 25], MoS_2 [26, 27] Sb_2S_3 [28, 29], etc., have also received considerable attention for anode applications. Lithium storage properties of various sulphide based electrode materials have been compared with other anodes like oxides, nitrides and phosphides by Cabana et al. [30]. Similar to the oxides, these sulphides undergo lithium cycling via conversion reaction leading to large capacity [31]. However, the cycling stability of these materials has been poor which illustrates the need for more research. Of these sulphides, Sb_2S_3 is an interesting anode material as they can undergo lithium storage via conversion reaction as well as alloying/de-alloying mechanism resulting in a very high capacity of 946 mAh g^{-1}. Sb_2S_3 reacts with 6 mol of Li by conversion reaction resulting in the formation of Li_2S and Sb which accounts for a theoretical capacity of 473 mAh g^{-1}. The Sb nanoparticles undergo further lithium storage via reversible alloying and de-alloying reaction with 3 mol of Li forming Li_3Sb alloy which gives rise to additional capacity of 473 mAh g^{-1}. Thus each mole of Sb_2S_3 consumes 12 mol of Li resulting in a combined theoretical capacity of 946 mAh g^{-1}.

Zhou et al. prepared hierarchical Sb_2S_3/C composites containing nanorods by solvothermal method. A high reversible capacity of 1084 mAh g^{-1} at a current density of 100 mA g^{-1} and superior rate capability was observed [32]. Prikhodchenko et al. [33] prepared rGO supported antimony sulfide by sulfurization of peroxoantimonate coated GO which showed enhancement in the electrochemical performance owing to the presence of graphene. Yi et al. [34] achieved good cycling stability in bulk Sb_2S_3 using a polyimide binder which provides good mechanical stability and FEC additive in the electrolyte. A charge capacity of $\sim$800 mAh g^{-1} with stable cycle stability was achieved.

In this project, Sb_2S_3 was synthesized employing a single source precursor approach. This method is widely used to prepare different class of materials such as metal oxides [35], metal sulphides [36–38], metal selenides [39–41], etc. Antimony thiobenzoate complex, $Sb(SCOPh)_3$ prepared by the reaction of $SbCl_3$ with sodium thiobenzoate was used as the precursor. Single step solid state decomposition of the precursor at 400 °C in argon atmosphere resulted in the formation of stibnite phase. The pristine sample shows inferior lithium storage. To achieve better cycling stability, rGO composites of Sb_2S_3 were also synthesized by annealing the rGO/$Sb(SCOPh)_3$ mixtures prepared by different methods.

7.2 Experimental Section

All the chemicals and solvents used in this study are commercially available and used without further purification.

7.2.1 Synthesis of $Sb(SCOPh)_3$

The single-source precursor, $Sb(SCOPh)_3$ was prepared by a simple precipitation method [42]. Typically, 340 mg of NaOH (8.5 mmol) was dissolved in 20 mL MeOH followed by addition of 1 mL (8.5 mmol) of thiobenzoic acid under argon atmosphere. The mixture was stirred for 10 min which resulted in an orange coloured solution of sodium thiobenzoate (as per Eq. 7.1). Subsequent addition of 654 mg (2.9 mmol) of $SbCl_3$ in Ar atmosphere generated a cream coloured precipitate of $Sb(SCOPh)_3$ (as per Eq. 7.2) which was further stirred for 30 more minutes at room temperature. The precipitate was filtered under vacuum, washed with MeOH and air-dried. Yield: 1.5 g (~100 %). The resulted $Sb(SCOPh)_3$ was used for the synthesis of Sb_2S_3 without further purification.

$$3\,PhCOSH + 3\,NaOH \rightarrow 3\,Na(SCOPh) + 3\,H_2O \tag{7.1}$$

$$3\,Na(SCOPh) + SbCl_3 \rightarrow Sb(SCOPh)_3 + 3\,NaCl \tag{7.2}$$

7.2.2 Synthesis of Sb_2S_3

Sb_2S_3 was prepared from the thiobenzoate precursor by solid state decomposition under argon atmosphere. Around 1 g of the precursor was kept in an alumina boat and heated at 400 °C under continuous argon flow for 6 h to obtain a black crystalline powder of Sb_2S_3.

7.2.3 Synthesis of rGO/Sb_2S_3

The synthesis of GO solution has been detailed in Sect. 4.2.1. To prepare the rGO/Sb_2S_3 composite, 1 g of the precursor was added to 50 mL of GO solution (~0.1 wt%) and diluted to 200 mL and stirred until a homogeneous mixture was obtained. The grey coloured mixture was evaporated at 60 °C on a hot plate with continuous stirring. The $GO/Sb(SCOPh)_3$ mixture was annealed at 400 °C under argon flow for 6 h to obtain a fine powder of rGO/Sb_2S_3.

The rGO/Sb_2S_3 composite was also made by sonication or microwave irradiation of $GO/Sb(SCOPh)_3$ mixture followed by annealing at 400 °C under Ar. Sonication of $GO/Sb(SCOPh)_3$ mixture at 50 °C or microwave irradiation for 10 min resulted in a black precipitate of $rGO/Sb(SCOPh)_3$. The black colour indicates the reduction of graphene oxide. It was then filtered under vacuum and air-dried. Subsequent annealing of the mixture at 400 °C in argon resulted in rGO/Sb_2S_3 composites.

7.2.4 Structural and Electrochemical Characterization

The Sb_2S_3 and rGO/Sb_2S_3 composites synthesized in this study were characterized by PXRD, SEM, TEM, TGA, cyclic voltammetry and galvanostatic cycling studies. Details of these characterization techniques have been described previously in Chap. 2.

7.3 Results and Discussion

7.3.1 TGA and PXRD

Thermogravimetric analysis of the single source precursor and its GO composite was carried out to understand their decomposition behaviour. Figure 7.1 shows the TGA curves recorded in nitrogen atmosphere between RT and 900 °C. Both the pristine precursor and its GO composite show a weight loss of ~60 % between 200 and 260 °C, which is associated with the removal of organic ligand, resulting in the formation of Sb_2S_3. Above 550 °C, the antimony sulphide is removed completely as there was no residue after heating to 900 °C. Therefore, the annealing of the precursor was performed at 400 °C in argon atmosphere to obtain the stibnite phase.

The phase and purity of the pristine and rGO composites of Sb_2S_3 were examined by Powder X-ray diffraction (PXRD). The PXRD patterns shown in Fig. 7.2b–e reveal the formation of pristine Sb_2S_3 and rGO/Sb_2S_3 composites in the orthorhombic space group, *P*bnm. The peaks were found to match well with the standard pattern of Sb_2S_3 (JCPDS: 42–1393). However, the elemental analysis of the samples carried out by CHNS and ICP analysis revealed that the amount of sulphur in the final product is higher than expected (1:3 molar ratio of Sb:S). This suggests that the final product consists of stibnite Sb_2S_3 and additional sulphur.

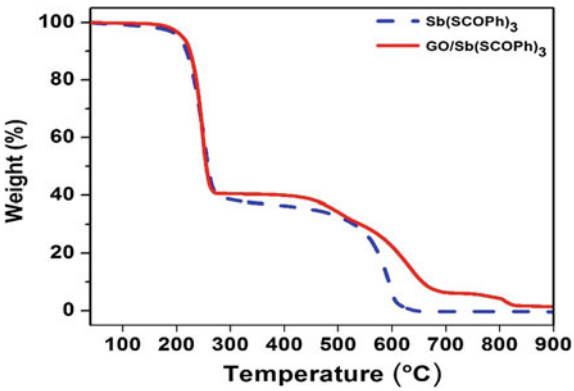

Fig. 7.1 TGA of Sb $(SCOPh)_3$ and rGO/Sb $(SCOPh)_3$ in nitrogen atmosphere at a heating rate of 10 °C min^{-1}

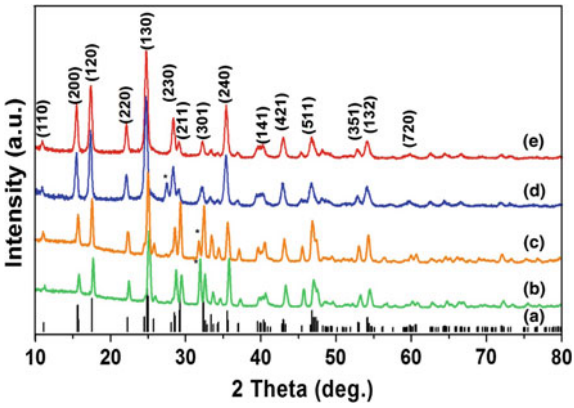

Fig. 7.2 Powder X-ray diffraction pattern of *a* JCPDS standard of Sb_2S_3, *b* p-Sb_2S_3; *c* rGO/Sb_2S_3 (stir), *d* rGO/Sb_2S_3 (sono) and *e* rGO/Sb_2S_3 (MW). The peaks shown in *asterisk* correspond to sulphur

Some impurity peaks indicated by asterisk in the XRD patterns are found to match with diffraction peaks of sulphur. The strong and sharp peaks indicate the good crystallinity of the composites.

7.3.2 Raman Spectroscopy

Raman spectroscopy helps in the characterization of graphene related materials. Figure 7.3 shows the Raman spectra of pristine and rGO composites of Sb_2S_3 synthesized at different conditions. Bare GO (Fig. 7.3a) shows Raman bands at 1600 and 1350 cm^{-1} which are described as G and D bands respectively. The D band corresponds to the defects and disordered atomic arrangement caused by the sp^3-carbon atom while the plane vibration of the sp^2-carbon atom in the two dimensional lattice gives rise to the G band. The I_D/I_G ratio of Graphene oxide is lower, while its reduction to rGO makes the ratio higher. In the case of different rGO/Sb_2S_3 composites, the I_D/I_G ratio are higher than the bare GO indicating the

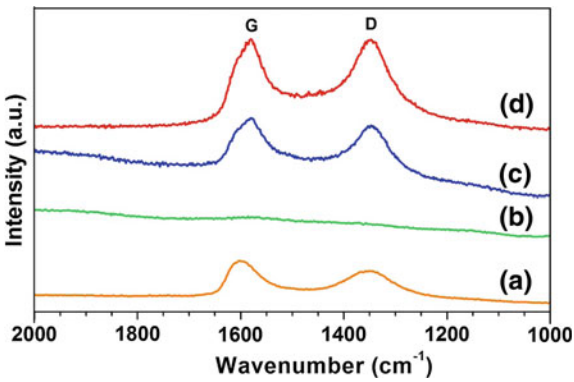

Fig. 7.3 Raman spectra of *a* bare GO; *b* p-Sb_2S_3; *c* rGO/Sb_2S_3 (stir); *d* rGO/Sb_2S_3 (sono) and *e* rGO/Sb_2S_3 (MW)

reduction of graphene oxide. The composites obtained by sonication and microwave irradiation assisted annealing has the I_D/I_G ratio of ~1. The wavelength of the G band in the composites also shifts to ~1580 cm^{-1} indicating the incorporation of Sb_2S_3 particles into the rGO layers. In comparison, the pristine sample does not show any characteristic band in this region.

7.3.3 Morphology

Morphology and particle size of p-Sb_2S_3 and rGO/Sb_2S_3 composites prepared in this study were investigated using SEM and TEM. As evidenced from the SEM image (Fig. 7.4a) annealing of the precursor alone resulted in micron sized rods of size up to 10 μm. When the precursor was mixed with GO by stirring, it gave rise to rGO/Sb_2S_3 after annealing. As can be seen from Fig. 7.4b, the sample contains mixture of rGO/Sb_2S_3 composites and big particles of bare Sb_2S_3. This indicates the inefficient mixing of GO and the precursor. When the GO and precursor mixture were subjected to sonication or microwave irradiation before annealing, it resulted in homogeneous rGO/Sb_2S_3 as seen from Fig. 7.4c, d. They form a uniform network of rGO with Sb_2S_3 particles trapped in between the layers. The particle size of Sb_2S_3 in these composites were found to be ~20–50 nm.

The porosity and BET surface area of the pristine and rGO composites of Sb_2S_3 synthesized at different conditions were investigated using N_2 adsorption-desorption isotherms (Fig. 7.5). The p-Sb_2S_3 exhibits a poor BET surface area of 0.6 m^2 g^{-1} owing to the large crystallite size of ~10 μm as indicated by the SEM image. The rGO composites show a better surface area thanks to the large surface provided by rGO sheets and smaller particle size of Sb_2S_3. The rGO composite obtained by stirring shows mixture of individual Sb_2S_3 and the rGO composite and has higher porosity than the pristine sample. The rGO composites obtained by sonication and microwave irradiation has high surface area of 27 and 30 m^2 g^{-1}. The high surface area can be attributed to the homogeneity of the composites with nanoparticle of small size resulted from uniform mixing of the precursor and GO before annealing. The BET surface area, pore size and pore volume of the different samples are compared in Table 7.1.

7.3.4 Galvanostatic Cycling

Electrochemical properties of p-Sb_2S_3 and rGO/Sb_2S_3 synthesized at different conditions were investigated using galvanostatic cycling studies. The cells were subjected to charge-discharge cycling using Li as anode. A constant current density of 100 mA g^{-1} was used which is ~0.1 C current rate as its theoretical capacity is 946 mAh g^{-1}. The charge-discharge profiles of p-Sb_2S_3, rGO/Sb_2S_3 (stir),

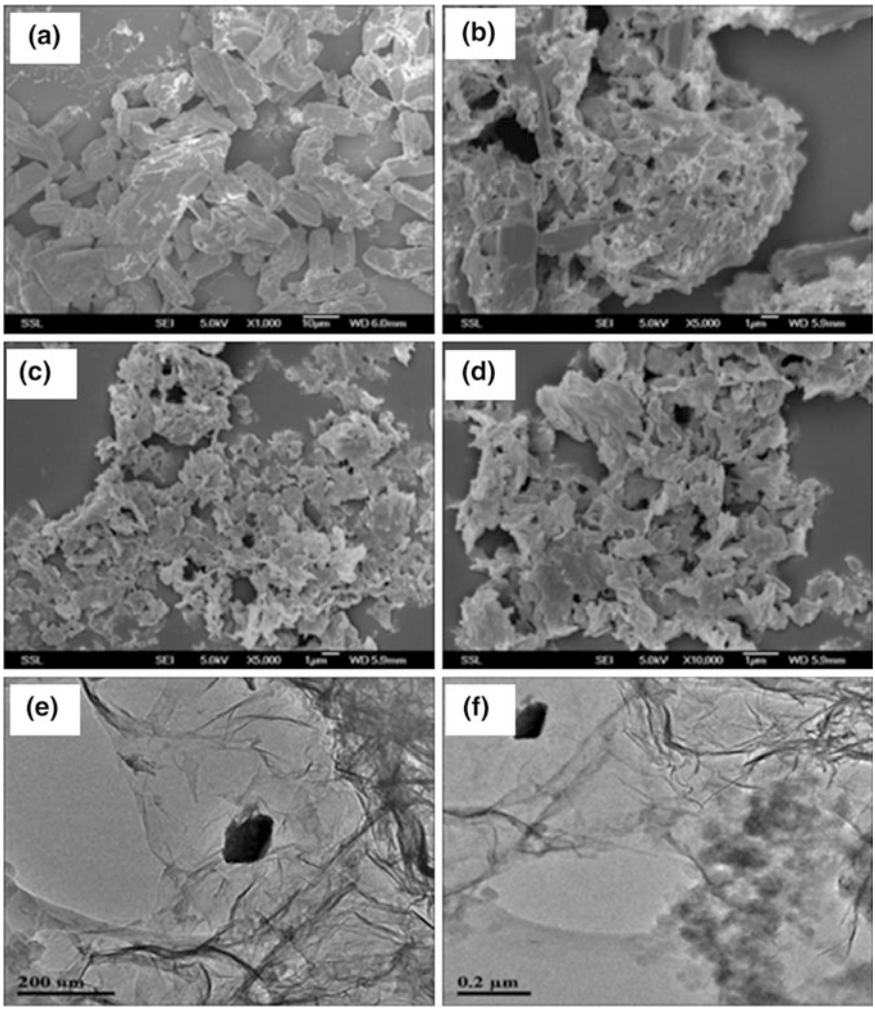

Fig. 7.4 SEM micrographs of **a** p-Sb_2S_3; **b** rGO/Sb_2S_3 (stir); **c** rGO/Sb_2S_3 (sono); **d** rGO/Sb_2S_3 (MW) and **e** and **f** TEM images of rGO/Sb_2S_3 (MW)

rGO/Sb_2S_3 (sono) and rGO/Sb_2S_3 (MW) for selected cycles are shown in Fig. 7.6a–d respectively.

7.3.4.1 Pristine Sb_2S_3

The pristine sample (p-Sb_2S_3) was subjected to discharge from the open circuit voltage (OCV) of ~2.8 V to insert lithium (Fig. 7.6a). It undergoes lithiation via two distinct mechanisms namely, conversion reaction and alloying reaction as

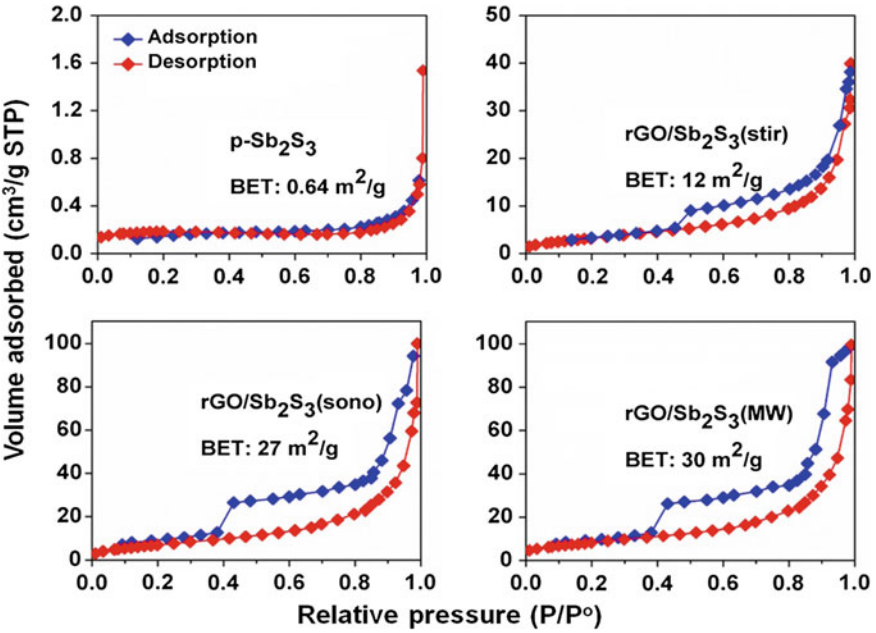

Fig. 7.5 Nitrogen adsorption-desorption isotherms of p-Sb_2S_3 and rGO/Sb_2S_3 composites

Table 7.1 BET surface area, pore size and pore volume of rGO/Sb_2S_3 composites obtained at different conditions

Sample	BET surface area (m^2 g^{-1})	Pore diameter (nm)	Pore volume (cm^3 g^{-1})
p-Sb_2S_3	0.6	4.82	0.0008
rGO/Sb_2S_3 (stir)	12.2	13.76	0.04
rGO/Sb_2S_3 (sono)	26.8	13.72	0.09
rGO/Sb_2S_3 (MW)	30.1	13.26	0.10

indicated by two different plateaus. The plateau at 1.6 V is due to the conversion reaction as indicated by Eq. 7.3, which results in the formation of Sb nanoparticles embedded in a matrix of Li_2S. During this process, 6 mol of lithium are consumed which corresponds to a theoretical capacity of 473 mAh g^{-1}. The excess sulphur present in the sample did not undergo any electrochemical reaction as no plateau was observed in the discharge curve at 2 V, which is characteristic voltage for conversion of sulphur to Li_2S. Further decrease in the potential of the cell leads to another plateau at ~0.9 V which is ascribed to the consumption of additional 6 mol of Lithium via alloying reaction. This generates the Li_3Sb alloy as indicated by Eq. 7.4. This process results in an additional capacity (theoretical) of 473 mAh g^{-1} taking the total capacity to 946 mAh g^{-1}. The overall initial discharge capacity obtained for p-Sb_2S_3 was 1386 mAh g^{-1}. The origin of the additional capacity,

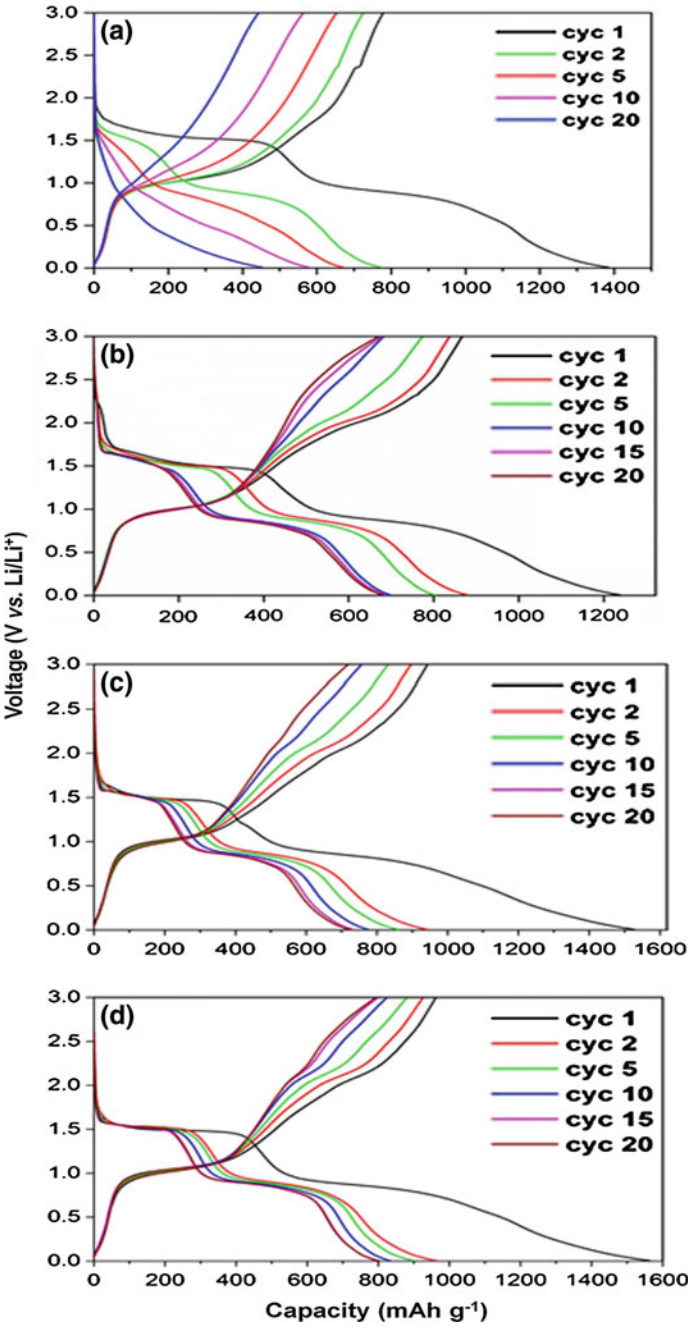

Fig. 7.6 Galvanostatic cycling of **a** p-Sb_2S_3; **b** rGO/Sb_2S_3 (stir); **c** rGO/Sb_2S_3 (sono); and **d** rGO/Sb_2S_3 (MW)

beyond the plateau region can be ascribed to the formation of solid electrolyte interface (SEI). The SEI results from the reaction of Li with the organic solvents present in the liquid electrolyte. This phenomenon is commonly observed in many oxide and sulphide based anode materials like Fe_2O_3, $ZnFe_2O_4$, CuS, etc.

$$Sb_2S_3 + 6\,Li \leftrightarrow 2\,Sb + 3\,Li_2S \tag{7.3}$$

$$2\,Sb + 6\,Li \leftrightarrow 2\,Li_3Sb \tag{7.4}$$

During the first charge process, the voltage of the cell increased rapidly to 0.9 V, followed by a plateau at ~1 V, which contributes a capacity of around 450 mAh g^{-1}. At this voltage, the de-alloying reaction of Li_3Sb occurs, forming back Sb nanoparticles. With further increase in the voltage the Sb nanoparticles should react with Li_2S by conversion reaction to form back Sb_2S_3 and Li. However, in this sample only a small plateau was observed at 1.7 V followed by a sloping potential to the cut off range of 3.0 V. This indicates that the conversion of Sb to Sb_2S_3 is not highly feasible in the sample, limiting the first charge capacity to only 778 mAh g^{-1} compared to its theoretical capacity of 946 mAh g^{-1}. This can be explained as the poor contact between Sb particles and Li_2S matrix which makes them unavailable for the conversion reaction.

The second and subsequent cycles follow the same mechanism as the first cycle resulting in reversible lithium storage. The second discharge cycle is characterized by a smaller plateau at 1.6 V compared to the first discharge, which contributes a capacity of only ~190 mAh g^{-1}. This can be explained as decreased availability of Sb_2S_3 due to the incomplete conversion reaction occurred during the first charge cycle. However, there was no observable decrease in the capacity from alloying reaction. The overall discharge capacity for the 2nd cycle was found to be 775 mAh g^{-1}. During subsequent cycles, the capacity decreases further as can be seen from Fig. 7.6a. The variation of capacity with cycle number for p-Sb_2S_3 is shown in Fig. 7.7. At the end of 40 cycles, the charge and discharge capacities obtained were only 348 and 344 mAh g^{-1} respectively. The huge capacity fading of p-Sb_2S_3 can be attributed to the big particle size and large volume change during the alloying

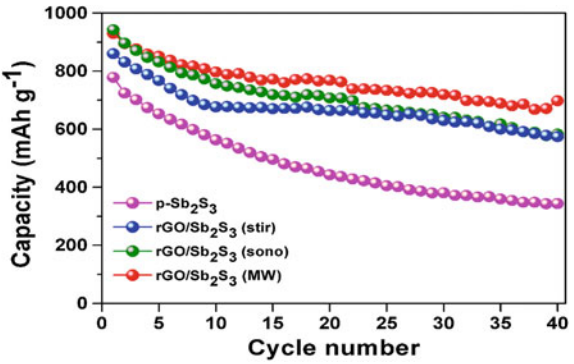

Fig. 7.7 Capacity (charge) versus cycle number plots of p-Sb_2S_3 and rGO/Sb_2S_3

de-alloying reactions which results in the localization of particles. Due to this Li_2S and Sb particles are separated from each other and are not in contact to undergo the conversion reaction.

7.3.4.2 rGO/Sb_2S_3

Figure 7.6b shows the charge-discharge profiles of rGO/Sb_2S_3 obtained by stirring the GO/$Sb(SCOPh)_3$ mixture at 60 °C, followed by annealing at 400 °C. The first discharge cycle was also similar to that of the pristine sample, with two plateaus at 1.6 and 0.9 V with an overall capacity of 1230 mAh g^{-1}. During the first charge cycle the plateau at ~1 V was similar to p-Sb_2S_3. However, the second plateau at ~2 V becomes well defined compared to the pristine sample indicating that the conversion reaction is better. This accounts for a charge capacity of 860 mAh g^{-1}. During the second and subsequent cycles, the plateau at ~1 V for both the charge and discharge cycles remain intact, indicating the excellent reversibility of the alloying/de-alloying reaction of the material. However, the plateau at ~1.6 V becomes shorter with increasing cycle number. This can be explained as the decreasing tendency of the reaction between Sb and Li_2S converting back to the Sb_2S_3 via conversion reaction. At the end of 40 cycles, the charge and discharge capacities obtained were 588 and 574 mAh g^{-1} respectively. The better capacity retention of the rGO composite can be attributed to increase in conductivity of the sample. In addition, the presence of rGO layers can accommodate the volume change occurring during the alloying/de-alloying reaction providing a better contact between the particles compared to the pristine sample. However, prolonged lithium cycling breaks the Sb_2S_3 particles and into smaller Sb and Li_2S particles which are separated from each other resulting in poor contact between them. This hinders the probability of conversion reaction and hence the capacity from this mechanism decreases over prolonged cycling.

The charge-discharge profiles of rGO/Sb_2S_3 obtained by sonication and microwave irradiation of the GO/$Sb(SCOPh)_3$ mixture, followed by annealing at 400 °C are shown in Fig. 7.6c, d respectively. The charge-discharge profiles were similar to the pristine sample. However, the capacity was found to be better which is partly due to smaller particle size of Sb_2S_3 and due to the increased surface area. The rGO/Sb_2S_3 obtained by sonication exhibits charge and discharge capacities of 584 and 589 mAh g^{-1} respectively at the end of 40 cycles. The sample obtained via microwave irradiation followed by annealing shows the best capacity retention of all the samples. The charge and discharge capacities obtained for the 40th cycle were 685 and 698 mAh g^{-1} respectively.

All the rGO/Sb_2S_3 composites show high capacity fading during the initial 10 cycles which is due to the "formation" or "conditioning" of the electrode, referred to as electrochemical grinding effect. This disintegrates the Li_2S matrix and Sb

Table 7.2 Charge and discharge capacities of p-Sb_2S_3 and rGO/Sb_2S_3 composites obtained at different conditions for the 1st, 2nd and 40th cycles

Compound	Discharge capacity (mAh g^{-1})			Charge capacity (mAh g^{-1})		
	1st cycle	2nd cycle	40th cycle	1st cycle	2nd cycle	40th cycle
p-Sb_2S_3	1386	775	348	778	724	344
rGO/Sb_2S_3 (stir)	1230	874	588	860	831	574
rGO/Sb_2S_3 (sono)	1528	942	589	943	896	584
rGO/Sb_2S_3 (MW)	1511	930	698	920	895	685

nanoparticles. The capacity then gets stabilized for ~10–15 cycles. After ~25 cycles, the capacity was found to decrease again slowly which is attributed to the large volume change occurring in the electrode during the alloying/de-alloying reaction (Table 7.2).

7.3.5 Cyclic Voltammetry

Cyclic voltammetry (CV) gives information about the redox potentials of electrochemical reactions occurring in the electrodes. Figure 7.8 shows the cyclic voltammograms of p-Sb_2S_3 and the different rGO/Sb_2S_3 composites. The CV curves were recored at room temperature using Li metal as the counter electrode in the potential window of 0.005–3 V at a constant scan rate of 58 μV s^{-1}. During the first cathodic scan, voltage of the cell decreased from the open circuit voltage of ~3 V to the cut off voltage of 0.005 V. Two reduction peaks appear at 1.39 and 0.78 V for the pristine sample while the rGO composites show the reduction peaks at ~1.2 and ~0.7 V. The peak at 1.2–1.4 V is attributed to the lithiation of Sb_2S_3 via conversion reaction, leading to formation of Sb nanoparticles embedded in Li_2S matrix as per Eq. 7.3. The next peak at ~0.7 V is due to the alloying reaction of Sb. Each mole of Sb reacts with 3 mol of Li forming Li_3Sb alloy as indicated by the Eq. 7.4. During the first anodic scan (charge cycle), de-alloying reaction happens first forming Sb and Li_2S at 1.05–1.13 V which react together upon further lithium extraction to form back Sb_2S_3. The peak for the conversion reaction was very broad and appear at ~2.1 V for all the samples. In the pristine stibnite phase this peak is very small and disappears after few scans indicating that the reaction stops after few cycles. However, the rGO composites shows a substantial peak at 2.1 V even after few cycles indicating that the conversion reaction is more feasible in the rGO composites than the pristine sample. The overlapping peak for the alloying/de-alloying reaction indicates the excellent reversibility of lithium cycling by this mechanism. During the cathodic scans, the peak for the conversion reaction decreases with cycling for the rGO/Sb_2S_3 synthesized by stirring, while the rGO/Sb_2S_3 composites prepared by sonication or microwave irradiation showed better reversibility in lithium cycling due to improved homogeneity of the sample.

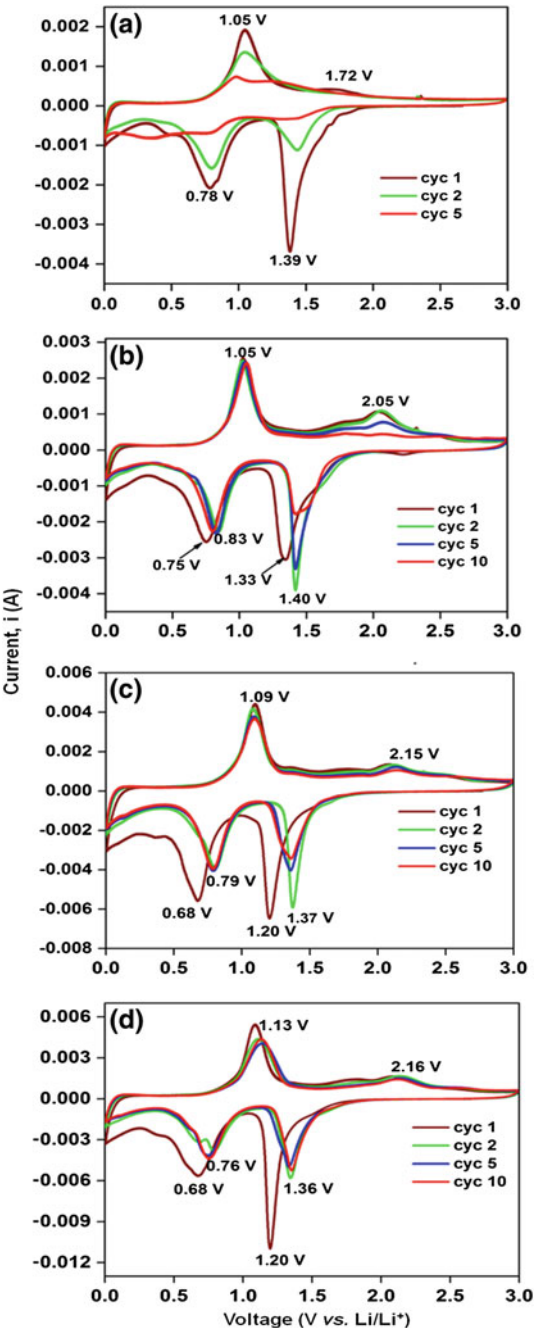

Fig. 7.8 Cyclic voltammograms (CV) of **a** pristine Sb_2S_3; **b** rGO/Sb_2S_3 (stir); **c** rGO/Sb_2S_3 (sono); and **d** rGO/Sb_2S_3 (MW)

7.4 Conclusions

Single source precursor approach was employed for the successful synthesis of rGO/Sb_2S_3 composites by annealing the GO/$Sb(SCOPh)_3$ at 400 °C in argon atmosphere. The pristine stibnite sample shows inferior electrochemical performance while the rGO composites show better lithium storage properties. The rGO/Sb_2S_3 obtained via microwave irradiation followed by annealing shows the best capacity retention with a reversible capacity of 698 mAh g^{-1} after 40 cycles. The capacity fading may be improved by solution phase decomposition of the precursor to obtain much smaller particles which can improve the electrochemical performance.

References

1. J.O. Besenhard, Carbon **14**, 111–115 (1976)
2. J.O. Besenhard, H.P. Fritz, J. Electroanal. Chem. Interfacial Electrochem. **53**, 329–333 (1974)
3. D. Aurbach, E. Zinigrad, Y. Cohen, H. Teller, Solid State Ionics **148**, 405–416 (2002)
4. J. Liu, X.-W. Liu, Adv. Mater. **24**, 4097–4111 (2012)
5. A.R. Armstrong, G. Armstrong, J. Canales, P.G. Bruce, Angew. Chem. Int. Ed. **43**, 2286–2288 (2004)
6. X. Jiang, X. Yang, Y. Zhu, H. Jiang, Y. Yao, P. Zhao, C. Li, J. Mater. Chem. A **2**, 11124–11133 (2014)
7. W. Li, Z. Wu, J. Wang, A.A. Elzatahry, D. Zhao, Chem. Mater. **26**, 287–298 (2014)
8. X.W. Lou, Y. Wang, C. Yuan, J.Y. Lee, L.A. Archer, Adv. Mater. **18**, 2325–2329 (2006)
9. S.-M. Paek, E. Yoo, I. Honma, Nano Lett. **9**, 72–75 (2009)
10. M.V. Reddy, T. Yu, C.-H. Sow, Z.X. Shen, C.T. Lim, G.V.S. Rao, B.V.R. Chowdari, Adv. Funct. Mater. **17**, 2792–2799 (2007)
11. X. Zhu, Y. Zhu, S. Murali, M.D. Stoller, R.S. Ruoff, ACS Nano **5**, 3333–3338 (2011)
12. L. Zhang, H.B. Wu, X.W. Lou, Adv. Energy Mater. **4**, 1300958/1300951–1300958/1300911 (2014)
13. S.-H. Lee, Y.-H. Kim, R. Deshpande, P.A. Parilla, E. Whitney, D.T. Gillaspie, K.M. Jones, A.H. Mahan, S. Zhang, A.C. Dillon, Adv. Mater. **20**, 3627–3632 (2008)
14. L. Mai, B. Hu, W. Chen, Y. Qi, C. Lao, R. Yang, Y. Dai, Z.L. Wang, Adv. Mater. **19**, 3712–3716 (2007)
15. A.S. Hameed, H. Bahiraei, M.V. Reddy, M.Z. Shoushtari, J.J. Vittal, C.K. Ong, B.V.R. Chowdari, A.C.S. Appl, Mater. Interfaces **6**, 10744–10753 (2014)
16. Y. Sharma, N. Sharma, G.V.S. Rao, B.V.R. Chowdari, Electrochim. Acta **53**, 2380–2385 (2008)
17. H. Tang, P. Gao, A. Xing, S. Tian, Z. Bao, RSC Adv. **4**, 28421–28425 (2014)
18. C.T. Cherian, J. Sundaramurthy, M.V. Reddy, P. Suresh Kumar, K. Mani, D. Pliszka, C.H. Sow, S. Ramakrishna, B.V.R. Chowdari, ACS Appl. Mater. Interfaces **5**, 9957–9963 (2013)
19. P. Lavela, J.L. Tirado, J. Power Sources **172**, 379–387 (2007)
20. N. Wang, H. Xu, L. Chen, X. Gu, J. Yang, Y. Qian, J. Power Sources **247**, 163–169 (2014)
21. B. Jache, B. Mogwitz, F. Klein, P. Adelhelm, J. Power Sources **247**, 703–711 (2014)
22. J.S. Chung, H.J. Sohn, J. Power Sources **108**, 226–231 (2002)
23. Z. Wang, X. Li, Y. Yang, Y. Cui, H. Pan, Z. Wang, B. Chen, G. Qian, J. Mater. Chem. A **2**, 7912–7916 (2014)

24. D. Kong, H. He, Q. Song, B. Wang, Q.-H. Yang, L. Zhi, RSC Adv. **4**, 23372–23376 (2014)
25. J.-W. Seo, J.-T. Jang, S.-W. Park, C. Kim, B. Park, J. Cheon, Adv. Mater. **20**, 4269–4273 (2008)
26. K. Chang, W. Chen, ACS Nano **5**, 4720–4728 (2011)
27. Z. Wan, J. Shao, J. Yun, H. Zheng, T. Gao, M. Shen, Q. Qu, H. Zheng, Small, Ahead of Print (2014)
28. J. Ma, X. Duan, J. Lian, T. Kim, P. Peng, X. Liu, Z. Liu, H. Li, W. Zheng, Chem.-Eur. J. **16**, 13210–13217 (2010)
29. C. Yan, G. Chen, D. Chen, J. Pei, J. Sun, H. Xu, Y. Zhang, Z. Qiu, CrystEngComm, Ahead of Print (2014)
30. J. Cabana, L. Monconduit, D. Larcher, M.R. Palacín, Adv. Mater. **22**, E170–E192 (2010)
31. M.V. Reddy, G.V. Subba Rao, B.V.R. Chowdari, Chem. Rev. **113**, 5364–5457 (2013)
32. X. Zhou, L. Bai, J. Yan, S. He, Z. Lei, Electrochim. Acta **108**, 17–21 (2013)
33. P.V. Prikhodchenko, J. Gun, S. Sladkevich, A.A. Mikhaylov, O. Lev, Y.Y. Tay, S.K. Batabyal, D.Y.W. Yu, Chem. Mater. **24**, 4750–4757 (2012)
34. X. Yi, X. Wang, B. Ju, H. Shu, W. Wen, R. Yu, D. Wang, X. Yang, Electrochim. Acta **134**, 143–149 (2014)
35. S. Daniele, R. Papiernik, L.G. Hubert-Pfalzgraf, S. Jagner, M. Håkansson, Inorg. Chem. **34**, 628–632 (1995)
36. J. Sun, W.E. Buhro, Angew. Chem. Int. Ed. **47**, 3215–3218 (2008)
37. S.L. Cumberland, K.M. Hanif, A. Javier, G.A. Khitrov, G.F. Strouse, S.M. Woessner, C.S. Yun, Chem. Mater. **14**, 1576–1584 (2002)
38. P.S. Nair, T. Radhakrishnan, N. Revaprasadu, G. Kolawole, P. O'Brien, J. Mater. Chem. **12**, 2722–2725 (2002)
39. J.J. Vittal, T.N. Meng, Acc. Chem. Res. **39**, 869–877 (2006)
40. M.A. Malik, P. O'Brien, N. Revaprasadu, Adv. Mater. **11**, 1441–1444 (1999)
41. S.L. Castro, S.G. Bailey, R.P. Raffaelle, K.K. Banger, A.F. Hepp, Chem. Mater. **15**, 3142–3147 (2003)
42. J.L.T. Chen, V. Nalla, G. Kannaiyan, V. Mamidala, W. Ji, J.J. Vittal, New J. Chem. **38**, 985–992 (2014)

Chapter 8
Graphene Wrapped Fe_3O_4 Nanoparticles as Stable and High Performance Anodes for Lithium Ion Batteries

Abstract This chapter deals with the investigation of lithium storage in rGO/Fe_3O_4 nanocomposites prepared by a simple precipitation method followed by annealing at different temperatures and environments such as 80 °C in air, 600 °C in Ar, 700 °C in Ar and 700 °C in Ar–H_2. The sample obtained at 80 °C exhibit a high surface area of 30 m^2 g^{-1}. Electrochemcial properties of the different rGO wrapped magnetite nanoparticles were investigated by cyclic voltammetry and galvanostatic cycling and EIS studies. They exhibit stable and high capacity and minimal capacity fading. In addition, they exhibit good rate capability. The rGO/Fe_3O_4 composite obtained at 700 °C in Ar–H_2 exhibits the best rate capability with a high reversible capacity of 480 mAh g^{-1} at a high current density of 3000 mA g^{-1}.

8.1 Introduction

In the recent years, various iron based oxides such as Fe_2O_3 [1–3], Fe_3O_4 [4–6], MFe_2O_4 (M = Ni, Co, Mn, Zn) [7–12], etc., have attracted huge interest as anode materials for Lithium ion batteries as a replacement for commercial graphite. Lithium storage occurs in these oxides via conversion (redox) mechanism in which the oxides reversibly react with lithium forming Li_2O along with metal nanoparticles [13]. These Fe based oxides have great advantages as anode materials due to their high reversible capacities, environmental benignity, low cost and abundance [2]. However, their commercialization has been hindered by their poor Lithium cycling, high operating potentials and large polarization due to the poor lithiation/de-lithiation kinetics which need to be addressed for utilization of these oxides as commercial anodes.

Magnetite phase (Fe_3O_4) is one of the attractive anodes and it exhibits a normal spinel structure in which the divalent and trivalent ions occupy the tetrahedral and octahedral sites respectively. It undergoes reversible lithium storage via a conversion reaction described by the Eq. 8.1. It has a theoretical capacity of 926 mAh g^{-1}, assuming 8 mol of Li uptake/extraction per mole of Fe_3O_4.

A.S. Hameed, *Phosphate Based Cathodes and Reduced Graphene Oxide Composite Anodes for Energy Storage Applications*,
Springer Theses, DOI 10.1007/978-981-10-2302-6_8

$$Fe_3O_4 + 8\,Li \leftrightarrow 3\,Fe + 4\,Li_2O \tag{8.1}$$

Lithium storage properties of the iron oxide α-Fe_2O_3 has been reported to improve when they are prepared in the form of nanoparticles, owing to the good Li transport as well as they ease the strain of the conversion reaction [14]. This motivated the study of Fe_3O_4 nanoparticles prepared by various synthetic routes like solvothermal [15, 16], hydrothermal [17, 18], carbothermal reduction [19], sol gel [20], electrospinning [21], etc., for anode application in LIBs. In addition, different strategies were used to improve the electronic conductivity of the material which include carbon coating [22, 23] and compositing with CNT [24, 25] and graphene [6, 18].

Fe_3O_4 can also be prepared by a simple and well-known precipitation method. Upon addition of NH_4OH to an aqueous solution containing ferrous ions, it results in immediate precipitation of $Fe(OH)_2$ as per Eq. 8.2. The ferrous hydroxide can be oxidized under anaerobic conditions to form magnetite, releasing hydrogen which is described by the Schikorr reaction (Eq. 8.3) [26]. The high thermodynamic stability of magnetite acts as driving force for the conversion of $Fe(OH)_2$ into Fe_3O_4.

$$FeSO_4 + 2\,NH_4OH \rightarrow Fe(OH)_2 + (NH_4)_2SO_4 \tag{8.2}$$

$$3\,Fe(OH)_2 \rightarrow Fe_3O_4 + H_2 + 2\,H_2O \tag{8.3}$$

In this study, graphene wrapped magnetite nanoparticles were obtained via precipitation of GO/$FeSO_4$ solution by addition of NH_4OH. The resulted precipitate of rGO/$Fe(OH)_2$ was heated at different conditions to obtain the rGO/Fe_3O_4 nanocomposites. Electrochemical investigation of these composites has affirmed stable and very high reversible capacity of the composites with good rate capability.

8.2 Experimental Section

All the chemicals and solvents used in this study are commercially available and used without further purification.

8.2.1 Synthesis of Graphene Oxide

The synthesis of graphene oxide has been detailed previously in the Sect. 4.2.1.

8.2.2 Synthesis of rGO/Fe_3O_4

The rGO/Fe_3O_4 nanocomposites were obtained by a simple precipitation method followed by heat treatment. In a typical reaction, ~1.4 g (5 mmol) of $FeSO_4 \cdot 7H_2O$ was added to ~100 mL of deionized water and ~25 mL of graphene oxide (GO) solution (0.1 wt%) was added and stirred for 12 h to obtain a homogeneous solution. Then, ammonium hydroxide was added slowly until the pH becomes 7 which resulted in the formation of a black colloidal solution. This indicated the precipitation of ferrous ions in the form of GO/$Fe(OH)_2$. The colloidal precipitate was then collected by centrifugation at 6000 rpm. It was then freeze dried for 12 h for complete removal of water which also averts the aggregation of particles in comparison to normal drying. The rGO/magnetite nanocomposites which were obtained as a porous material was annealed at different temperatures and environments such as (a) 80 °C in air, (b) 600 °C in Ar, (c) 700 °C in Ar and (d) 700 °C in Ar–H_2. The as-synthesized rGO/Fe_3O_4 composites at 80 °C was brown coloured while other samples were black in colour.

8.2.3 Structural and Electrochemical Characterization

The rGO/Fe_3O_4 nanocomposites synthesized in this study were characterized by PXRD, Rietveld refinement, Raman spectroscopy, SEM, TEM, cyclic voltammetry, galvanostatic cycling and EIS studies. Details of these characterization techniques have been described previously in Chap. 2.

8.3 Results and Discussion

8.3.1 Structural Analysis

During the synthesis, addition of NH_4OH to GO/$FeSO_4$ solution gave out a black precipitate was obtained which was amorphous in nature. Hence it was heated at different conditions to obtain rGO/Fe_3O_4 nanocomposites as mentioned in the synthesis. Powder X-ray diffraction pattern of the different rGO/Fe_3O_4 composites are shown in Fig. 8.1. The diffraction patterns of all the samples match well with the JCPDS standard pattern (#75-0033) and can be indexed to the cubic space group *F*d3m. Absence of any impurity peaks like Fe_2O_3 and FeO indicates the phase purity of the prepared composites. In addition, reduction of graphene oxide to rGO is affirmed by the absence of GO peaks in the XRD patterns. The sample annealed at 80 °C shows slightly broadened peaks compared to sample annealed at high temperatures. This indicates the increase in crystallinity and particle size of the rGO/Fe_3O_4 composites with increase in the annealing temperature. Fe_3O_4 exhibits a

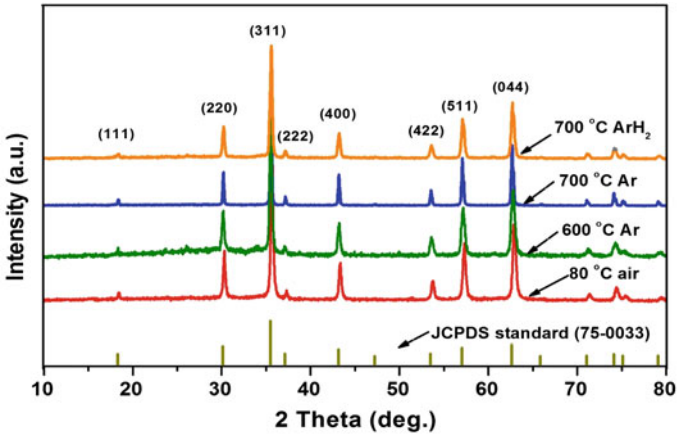

Fig. 8.1 PXRD patterns of rGO/Fe_3O_4 synthesized at different conditions

normal spinel structure containing iron in $Fe^{2+/3+}$ state. The divalent Fe^{2+} ions (r_i = 0.74 Å) and the trivalent Fe^{3+} ions (r_i = 0.69 Å) occupy the tetrahedral and octahedral sites respectively. The lattice parameter of the different composites were obtained from Rietveld refinement of the respective PXRD pattern using TOPAS software. Figure 8.2 shows the Rietveld refinement of rGO/Fe_3O_4 obtained at 80 °C. The experimental pattern matches well with the calculated pattern as evidenced from the figure. The lattice parameter of rGO/Fe_3O_4 obtained at 80 °C in air, 600 °C in Ar, 700 °C in Ar and 700 °C in Ar–H_2 are calculated to be 8.3665(1), 8.3700(4), 8.3947(9) and 8.3824(6) Å respectively which are close the reported lattice parameter of Fe_3O_4 [27]. The percentage of rGO in the samples have been confirmed by CHNS analysis. The sample obtained at 80 and 600 °C has ∼4 % while the samples annealed at 700 °C has ∼3 % graphene as the carbon is partially burnt at high temperature.

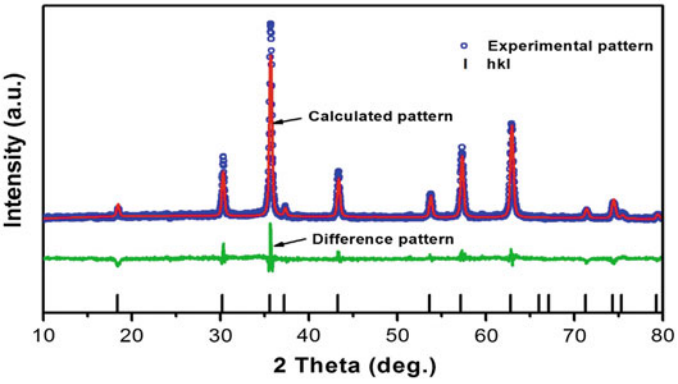

Fig. 8.2 Rietveld refinement of rGO/Fe_3O_4 (80 °C in air)

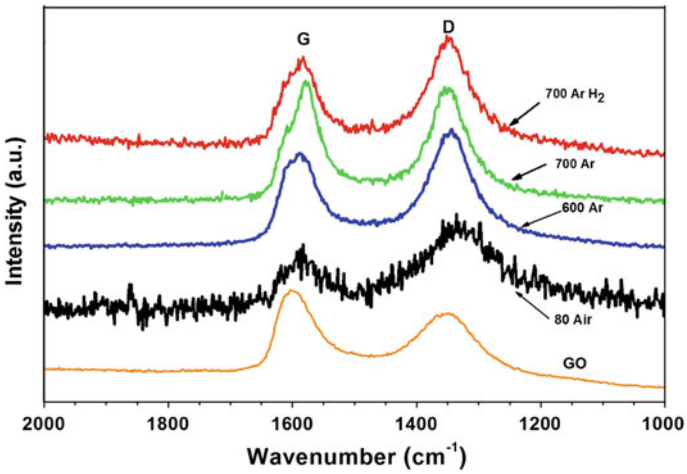

Fig. 8.3 Raman spectra rGO/Fe_3O_4 synthesized at different conditions

8.3.2 Raman Spectroscopy

Figure 8.3 shows the Raman spectra of all rGO/Fe_3O_4 nanocomposites at room temperature in the range of 2000–1000 cm^{-1}. Bare GO exhibits bands at 1600 and 1350 cm^{-1} which are described as G and D bands respectively. The D band corresponds to the defects and disordered atomic arrangement caused by the sp^3-carbon atom while the plane vibration of the sp^2-carbon atoms in the two dimensional lattice give rise to the G band. Graphene oxide is characterized by a higher intensity G band and a smaller intensity D band. Upon reduction of graphene oxide to rGO, the intensity ratio of the D band to the G band (I_D/I_G) increases. In the case of different rGO/Fe_3O_4 composites the characteristic G and D bands appear at $\sim$1580 and $\sim$1350 cm^{-1} respectively. The I_D/I_G ratio of the composites are greater than 1 expect the sample annealed at 700 °C in Ar which shows a ratio slightly lesser than 1. This higher I_D/I_G ratio of the rGO/Fe_3O_4 composites indicates the in situ reduction of graphene oxide. The G band of the composites shifts by $\sim$20 cm^{-1} which indicates the incorporation of Fe_3O_4 nanoparticles into the rGO layers.

8.3.3 Morphology

Morphology of rGO/Fe_3O_4 nanocomposites and their particle size were probed with the help of SEM (Fig. 8.4) and TEM (Fig. 8.5). The sample obtained at 80 °C (Fig. 8.4b) consists of nanoparticles of size $\sim$50 nm and are wrapped by rGO layers which are visible from the TEM image (Fig. 8.5a). The presence of rGO

along with the Fe_3O_4 nanoparticles has better electronic conductivity than bare Fe_3O_4. When the sample was annealed at 600 °C, the particles aggregate (Fig. 8.4d) with the individual particles having size of ~100 nm. When the annealing temperature was increased further to 700 °C in Ar atmosphere, the particles fuse together resulting in remarkable increase in the particle size to ~200–500 nm. Part of rGO is lost at 700 °C which also plays a role in the fusion of particles. When annealed at 700 °C in Ar–H_2 the increase in particle size was slightly decreased.

The porosity and Brunauer-Emmett-Teller (BET) specific surface area of the different rGO/Fe_3O_4 nanocomposites were investigated using N_2 adsorption-desorption isotherms (Fig. 8.6). Though the rGO/Fe_3O_4 (80 °C) composite has rGO content of only 4 %, it shows a high BET surface area of 30 $m^2\ g^{-1}$ which can be attributed to the smaller particle size of Fe_3O_4. High temperature annealed samples have lower surface area due to increased particle size and slightly decreased amount of rGO. The BET surface area of the different rGO/Fe_3O_4 nanocomposites along with their pore size and pore volume are compared in Table 8.1.

8.3.4 Galvanostatic Cycling

Galvanostatic cycling studies of the different rGO/Fe_3O_4 nanocomposites were carried out in the potential window, 0.005–3.0 V versus Li/Li^+ to investigate the Li-storage and cyclability of the composites. A constant current density of 60 mA g^{-1} was used for the testing at room temperature. The charge-discharge profiles of the composites for few selected cycles are shown in Fig. 8.7a–d.

The first discharge curve of all the rGO/Fe_3O_4 composites are distinct from other cycles indicating that the lithium storage mechanism of the initial discharge is different from the rest. The first discharge curve starts at OCV of ~2.9 V with a steep decrease in the voltage to 1.6 V. It is followed by two plateaus at ~1.6 and ~1.0 V which are due to the Li-intercalation into Fe_3O_4 forming a lithium intercalated phase, $Li_xFe_3O_4$ ($x \approx 2$) as shown in Eq. 8.4 [28]. During this reaction, the two Fe^{3+} ions in Fe_3O_4 are converted to Fe^{2+}. This plateau was observed in all the composites other than the sample annealed at 700 °C in Ar. With further decrease in the voltage, the intercalated phase undergoes lithiation indicated by a large plateau at ~0.85 V. During this process, irreversible destruction of the crystal structure with reduction of all Fe^{2+} ions to Fe metal nanoparticles embedded in an amorphous Li_2O matrix [28]. During this 6 more moles of Li are consumed as per Eq. 8.5, thus 8 mol of Li are utilized per mole of Fe_3O_4, which corresponds to a theoretical capacity of 926 mAh g^{-1}. However, the first discharge capacities observed for rGO/Fe_3O_4 obtained at 80 °C (air), 600 °C (Ar), 700 °C (Ar) and 700 °C (Ar–H_2) were 1855, 1716, 1406 and 1554 mAh g^{-1} respectively. The additional capacity can be interpreted as the formation of solid electrolyte interface (SEI) by the reaction of lithium with the solvents of the electrolyte [22, 29]. In

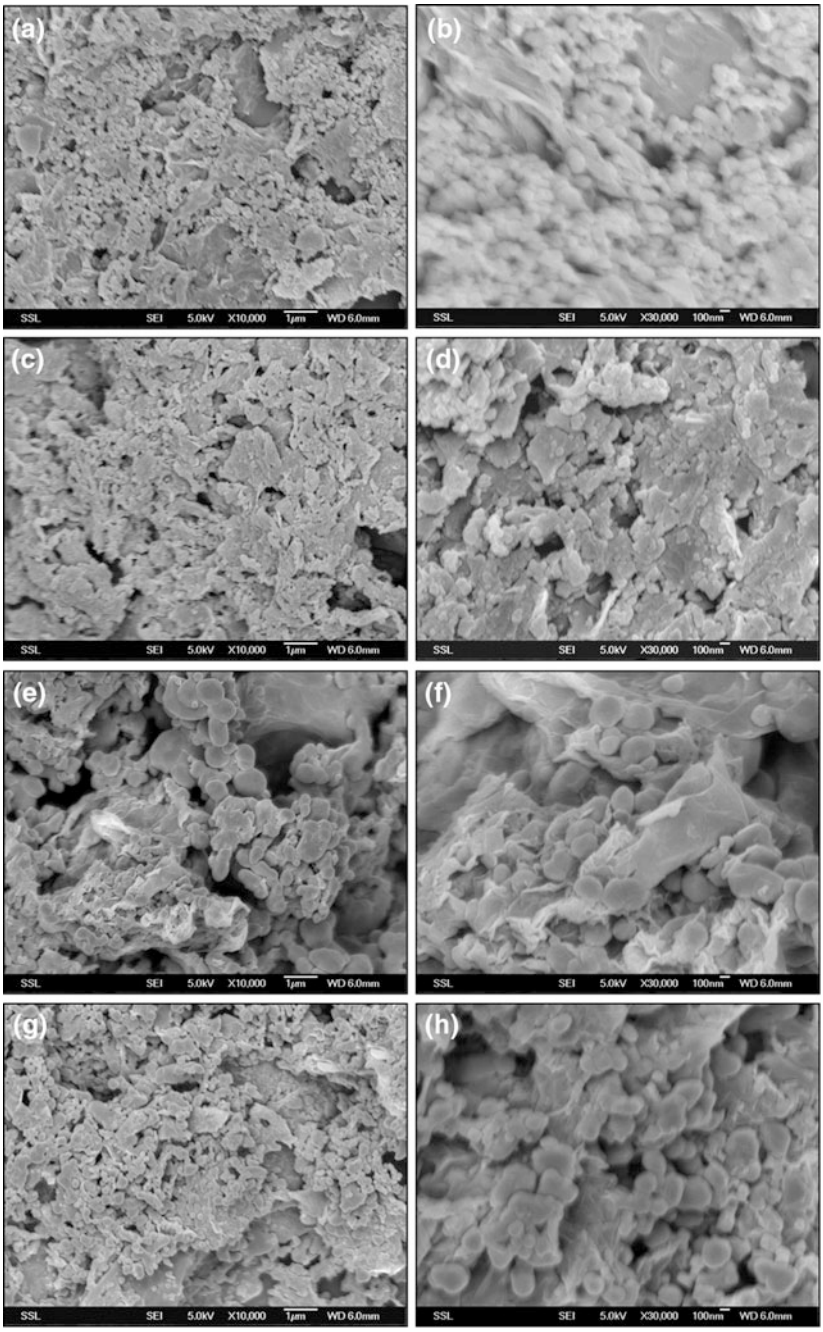

Fig. 8.4 Scanning electron micrographs of rGO/Fe_3O_4 nanocomposites annealed at: **a** and **b** 80 °C in air; **c** and **d** 600 °C in Ar; **e** and **f** 700 °C in Ar and **g** and **h** 700 °C in Ar–H_2

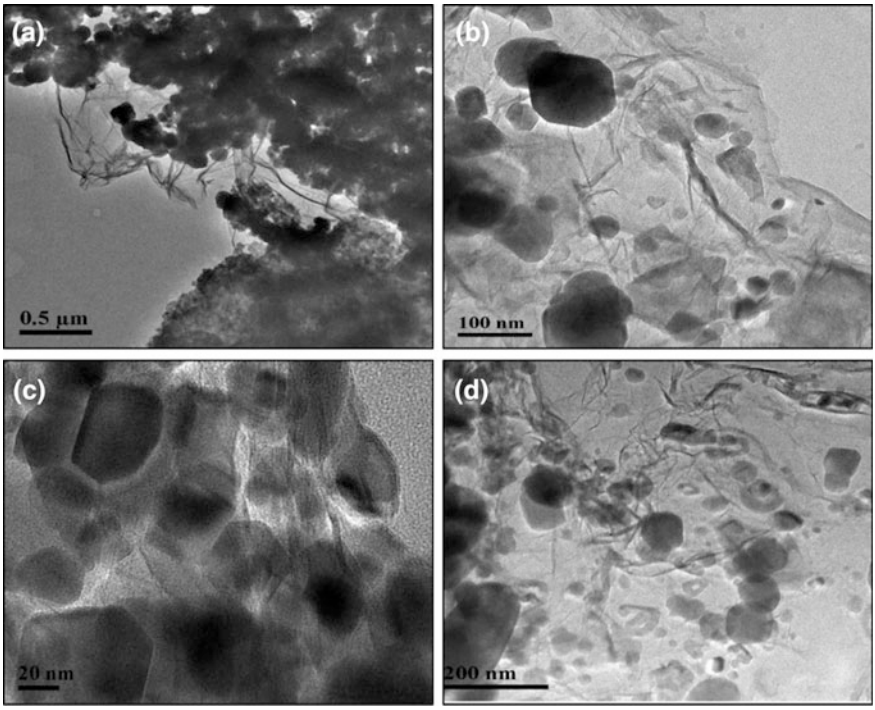

Fig. 8.5 Transmission electron micrographs of rGO/Fe_3O_4 nanocomposites annealed at different conditions: **a** 80 °C in air; **b** and **c** 600 °C in Ar; **d** 700 °C in Ar–H_2

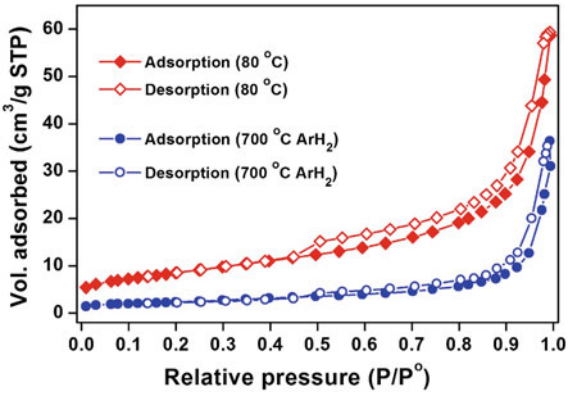

Fig. 8.6 N_2 adsorption-desorption isotherms of different rGO/Fe_3O_4 nanocomposites annealed at 80 °C in air and 700 °C in Ar–H_2

addition, rGO present in the samples (3–4 %) also contributes to lithium storage and SEI formation [30].

During the first charge cycle, Lithium is extracted from the material at ~1.4–2.0 V as indicated by a slopping plateau. The Li_2O and Fe nanoparticles formed

Table 8.1 Lattice parameter, (*a*), BET surface area, pore size and pore volume of rGO/Fe_3O_4 nanocomposites obtained at different conditions

Sample	Lattice parameter *a* (Å)	BET surface area ($m^2\ g^{-1}$)	Pore diameter (nm)	Pore volume ($cm^3\ g^{-1}$)
rGO/Fe_3O_4 80 °C in air	8.3665(1)	30.4	9.0	0.069
rGO/Fe_3O_4 600 °C in Ar	8.3700(4)	19.2	13.0	0.060
rGO/Fe_3O_4 700 °C in Ar	8.3947(9)	3.2	18.7	0.015
rGO/Fe_3O_4 700 °C in Ar–H_2	8.3824(6)	8.2	16.3	0.033

during the initial discharge cycle react with each other to form iron oxide according to Eq. 8.6. The first charge capacities obtained for rGO/Fe_3O_4 synthesized at 80 °C in air, 600 °C in Ar, 700 °C in Ar and 700 °C in Ar–H_2 were 1254, 1082, 853 and 1001 mAh g^{-1} respectively. The second discharge curve in all the samples are different from the first discharge cycle. The second and subsequent cycles rely on the reversible conversion of iron oxide to Fe nanoparticles embedded in Li_2O matrix. The voltage of the discharge plateau also shifts to ~1.0 V compared to 0.85 V observed for the first cycle.

$$Fe_3O_4 + x\ Li^+ + x\ e^- \rightarrow Li_xFe_3O_4 \tag{8.4}$$

$$Li_xFe_3O_4 + (8 - x)\,Li^+ + (8 - x)\,e^- \rightarrow 3\,Fe + 4\,Li_2O \tag{8.5}$$

$$3\,Fe + 4\,Li_2O \leftrightarrow Fe_3O_4 + 8\,Li^+ + 8\,e^- \tag{8.6}$$

The conversion reaction happening in the rGO/Fe_3O_4 anodes is found to be highly reversible as inferred from the overlapping charge-discharge curves of the different cycles (Fig. 8.7). The variation of charge and discharge capacities with cycle number of the different composites and their corresponding coulombic efficiencies are shown in Fig. 8.8. The sample obtained at 80 °C shows the highest charge capacity of 1254 mAh g^{-1} for the first cycle which can be attributed to smaller particle size and high surface area. However, the cycling stability was slightly poor resulting in a capacity of 1046 mAh g^{-1} at the end of 40 cycles which is still higher than the theoretical capacity. Upon increase in the annealing temperature, the particle size of Fe_3O_4 increases and hence the surface area decreases dramatically. The sample obtained at 600 °C in Ar shows a slightly lesser capacity 1082 mAh g^{-1} for the first cycle. However, it exhibits better cycling stability with a capacity of 1062 mAh g^{-1} obtained at the end of 40 cycles. With further increase in annealing temperature to 700 °C, the capacity decreases further due to slightly decreased graphene content and increased particle size. The charge capacity

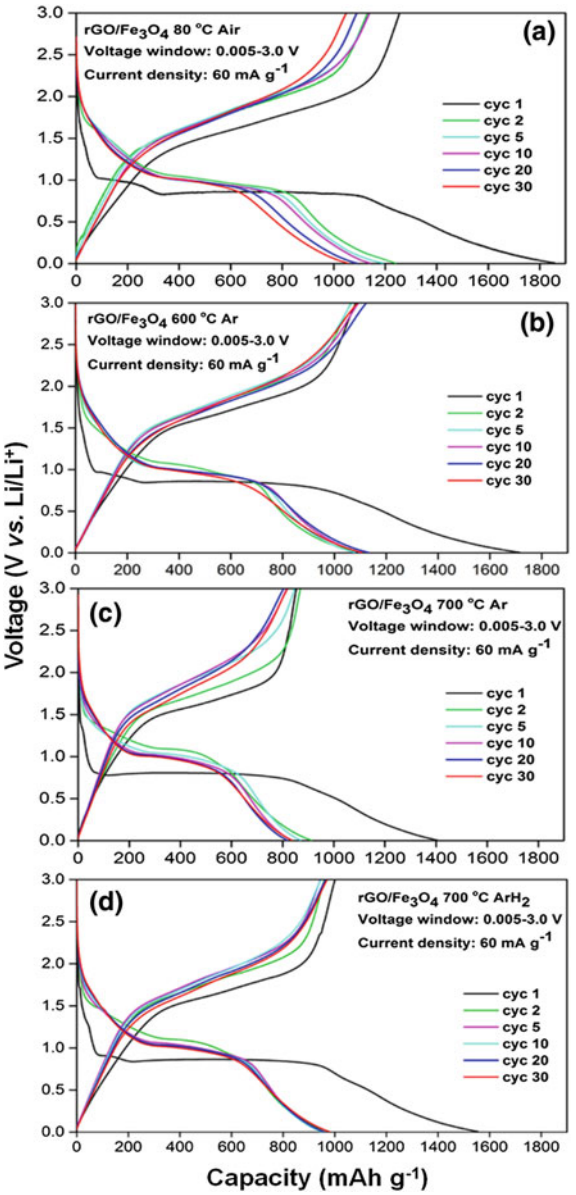

Fig. 8.7 Galvanostatic cycling studies showing charge-discharge profiles of rGO/Fe_3O_4 synthesized at: **a** 80 °C in air; **b** 600 °C in Ar; **c** 700 °C in Ar and **d** 700 °C in Ar–H_2

obtained for the samples annealed at 700 °C in Ar and Ar–H_2 environment were 853 and 1001 mAh g^{-1}. However, capacity retention of these samples were found to be excellent with reversible capacity of 854 and 972 mAh g^{-1} obtained after 40 cycles. In addition, all the composites possess high coulombic efficiency of ~99 %. The details of the charge and discharge capacities of the individual samples for the 1st, 2nd and 40th cycles are listed in Table 8.2. Though the reversible capacities

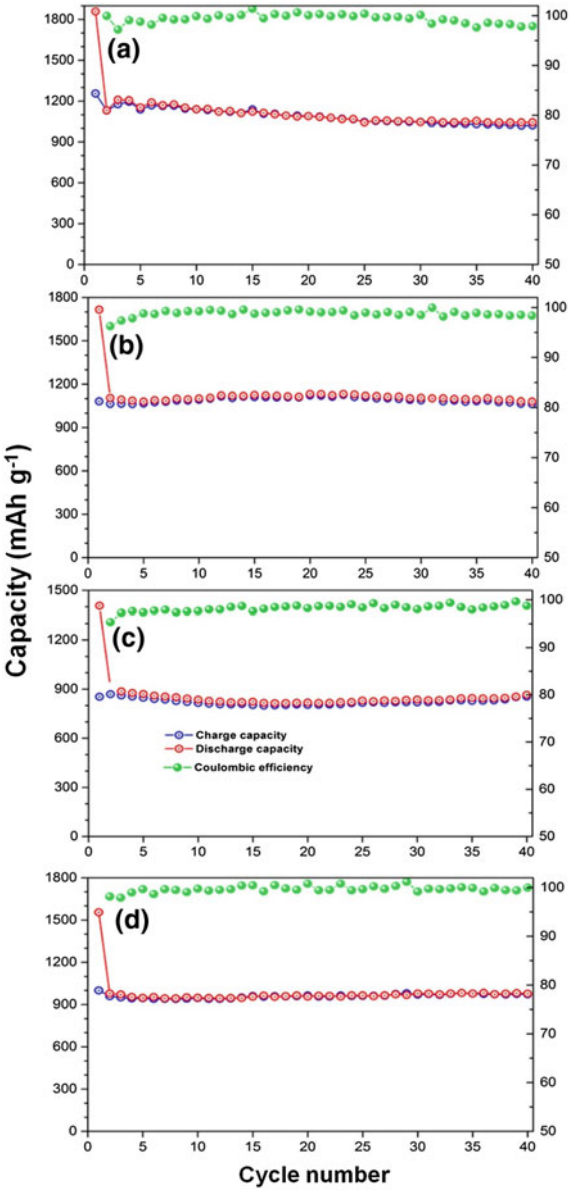

Fig. 8.8 Capacity versus cycle number plots of rGO/Fe_3O_4 synthesized at: **a** 80 °C in air; **b** 600 °C in Ar; **c** 700 °C in Ar and **d** 700 °C in Ar–H_2

obtained for these composites are quite high and stable, high polarization of ~0.6 V is observed which is characteristic of these oxides. Though many reports on rGO/Fe_3O_4 appear in the literature, the graphene/rGO content in the samples were very high leading to good capacity [6, 31–33]. Better electrochemical performance were achieved for the samples studied here with only 3–4 % of rGO.

Table 8.2 Charge and discharge capacities of rGO/Fe_3O_4 nanocomposites synthesized at different conditions

Compound	Discharge capacity (mAh g^{-1})			Charge capacity (mAh g^{-1})		
	1st cycle	2nd cycle	40th cycle	1st cycle	2nd cycle	40th cycle
rGO/Fe_3O_4 80 °C in air	1855	1236	1047	1254	1127	1046
rGO/Fe_3O_4 600 °C in Ar	1716	1105	1080	1082	1063	1062
rGO/Fe_3O_4 700 °C in Ar	1406	911	865	853	869	854
rGO/Fe_3O_4 700 °C in Ar–H_2	1554	978	977	1001	960	972

8.3.4.1 Rate Capability Studies

High rate capability is an important characteristic of a good electrode material. Rate capability studies help in understanding the material's ability to store lithium at different current rates. A material with a good capacity at high current rates is very useful as it can be charged and discharged in a short time. All the different rGO/Fe_3O_4 composites were subjected to galvanostatic charge-discharge cycling at different current densities of 500, 1000, 2000 and 3000 mA g^{-1} which corresponds to current rates of ~0.5, 1.1, 2.2 and 3.2 C respectively (1 C represents a current density of 928 mA g^{-1}). As expected, the capacity of the composites decreases when the current density was increased from 60 mA g^{-1} to higher current densities. Figure 8.9 shows the capacity versus cycle number plots at different current rates for the rGO/Fe_3O_4 composites synthesized at different conditions. The sample obtained at 600 °C in Ar shows the best performance at 500 and 1000 mA g^{-1}. However, at higher rates, the reversible capacity obtained was poor. The sample annealed at 700 °C in Ar–H_2 shows the best capacity at high current rates. This can be attributed to the better reduction of rGO in reducing Ar–H_2 environment. When the current was decreased from 3000 to 60 mA g^{-1}, the capacity obtained was found to be higher than the original capacity obtained at 60 mA g^{-1}. This increase in capacity can be attributed to the increase in the activity of graphene upon cycling, as evidenced by the large capacity obtained after the plateau region (Fig. 8.10).

8.3.5 Cyclic Voltammetry

Cyclic voltammetry (CV) is a complementary technique to galvanostatic cycling which gives information about the redox potentials of electrochemical reactions occurring in the electrodes. Figure 8.11 shows the cyclic voltammograms of the

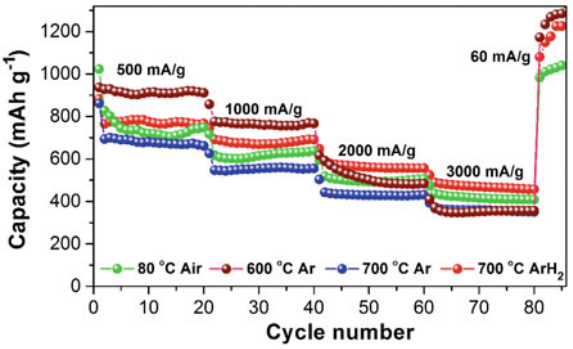

Fig. 8.9 Rate capability of rGO/Fe_3O_4 synthesized at different conditions

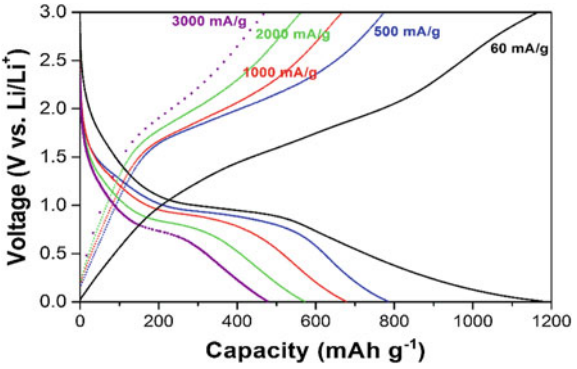

Fig. 8.10 Charge-discharge profiles at different current rates for rGO/Fe_3O_4 obtained at 700 °C in Ar–H_2

different rGO/Fe_3O_4 composites for selected cycles. The experiments were carried out at room temperature using Li metal as the counter electrode in the potential window of 0.005–3 V at a constant scan rate of 58 μV s^{-1}. All the four samples shows similar CV curves and their first cycle exhibits substantial difference with the subsequent cycles. During the first cathodic scan (reduction or Li-insertion), two small peaks at ~1.4 and ~0.8 V were observed which are due to the formation of a lithium intercalated compound $Li_xFe_3O_4$ from the magnetite phase (Fe_3O_4) as per Eq. 8.4. In the case of sample annealed at 700 °C in Ar, the peak at 0.8 V did not appear, similar to the galvanostatic cycling results. Upon further discharge to the cut-off voltage of 0.005 V, a sharp peak appears at ~0.5–0.6 V, which corresponds to crystal structure destruction of Fe_3O_4 forming Fe nanoparticles embedded in Li_2O matrix. This peak was not seen in the subsequent cycles, indicating the irreversible nature of the first discharge cycle (Eq. 8.5). The first anodic scan shows two overlapped peaks at ~1.7 V which correspond to the oxidation of Fe to form Fe_3O_4 (Eq. 8.6). In the subsequent cycles, a single broad peak was observed at 0.7–0.8 V for the different composites during cathodic scans and 2.0 V during the anodic scans. Similar redox potentials have been reported for magnetite anode materials [34]. The overlapping CV curves also indicate excellent reversibility of lithium cycling in the material.

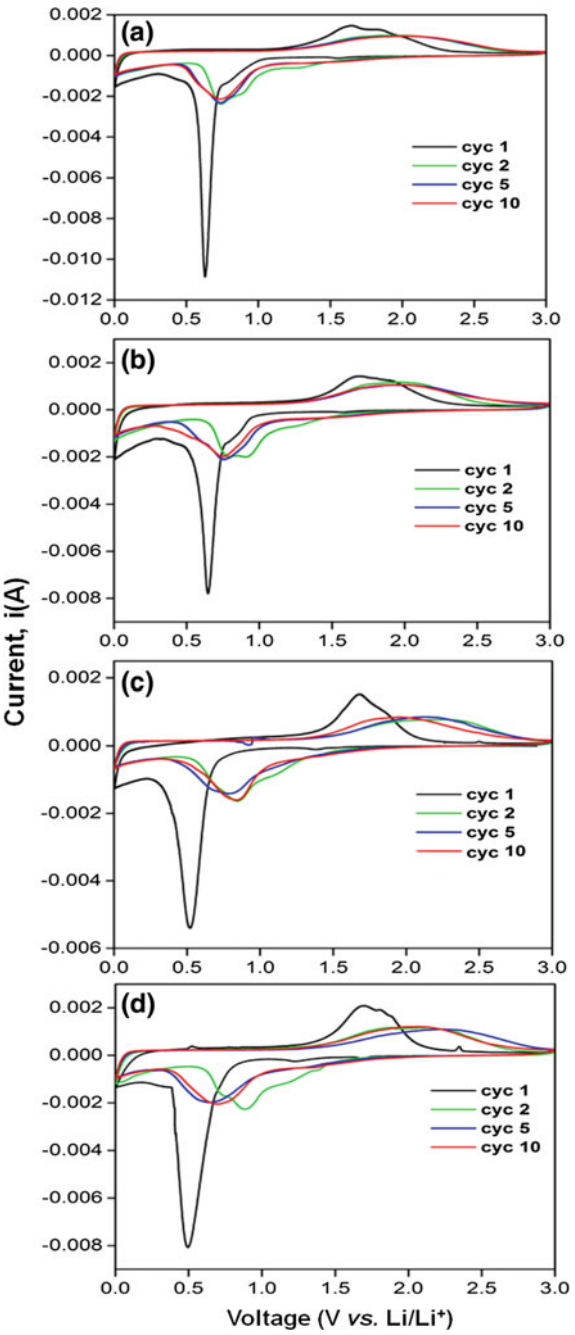

Fig. 8.11 Cyclic voltammograms (CV) of rGO/Fe_3O_4 synthesized at: **a** 80 °C in air; **b** 600 °C in Ar; **c** 700 °C in Ar and **d** 700 °C in Ar–H_2

8.3.6 ElS Studies

ElS is an important technique used to analyse electrode kinetics. The impedance measurements were carried out for the different rGO/Fe_3O_4 nanocomposites for the 1st and 40th cycles at selected voltages. During each voltage increment (charging) and decrement (discharging), the cell was subjected to a current density of $\sim$200 mA g^{-1} and was relaxed at the given voltage for 2 h before data collection. The results are plotted as Nyquist plots (Z_{re} vs. Z_{im}), where Z_{re} and Z_{im} are respectively the real and imaginary parts of cell impedance.

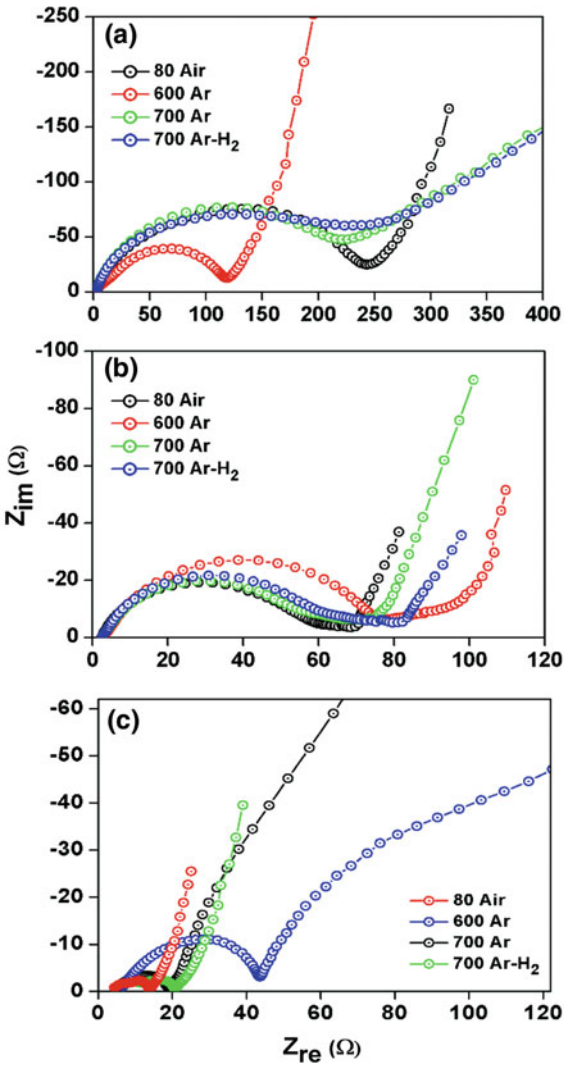

Fig. 8.12 Nyquist plots of the different rGO/Fe_3O_4 composites at: **a** OCV; **b** fully discharged state (1st cycle) and **c** fully discharged state (40th cycle)

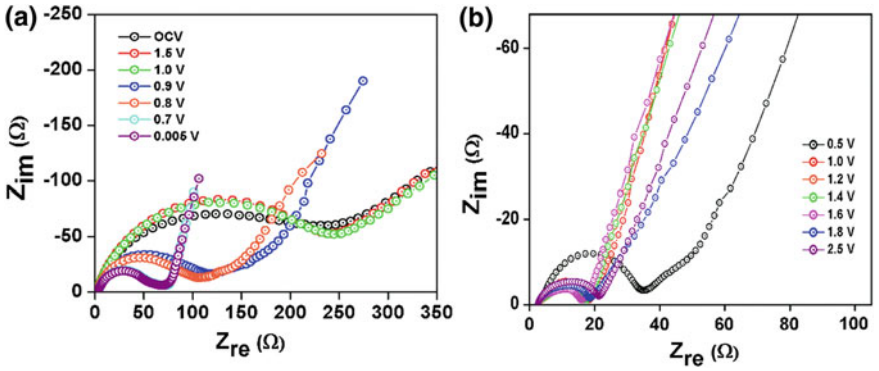

Fig. 8.13 Nyquist plots of rGO/Fe_3O_4 (700 °C Ar–H_2) at different voltages for **a** 1st discharge and **b** 1st charge cycle

Figure 8.12a shows the Nyquist plots obtained at open circuit voltage for all the composites. They showed a single semicircle with an overall impedance of ~220–250 Ω except for the 80 °C sample which shows only 120 Ω. This is attributed to the high surface film resistance and charge transfer resistance (R_{sf} + R_{ct}) and the associated capacitances (CPE_{sf} and CPE_{dl}) though a single semicircle was observed. With the onset of lithium insertion the impedance decreases and becomes ~60–80 Ω at the fully discharged state (0.005 V).

Detailed EIS measurements were carried out for the rGO/Fe_3O_4 composite prepared at 700 °C in Ar–H_2. EIS data were collected for the sample at different voltages for the 1st charge and discharge cycle as shown in Fig. 8.13. During the discharge cycle, as mentioned above the impedance decreases once the lithiation starts and reaches ~60 Ω at the fully discharged state. During the charge cycle, the impedance was very low (15–20 Ω) in the plateau region indicating good conductivity of the sample.

The composites were also subjected to 40 charge-discharge cycles and the EIS data were recorded at the discharged state (Fig. 8.12c). As can be seen the impedance was very low ~20 Ω for all the samples except the sample annealed at 600 °C in Ar. This can explain the good cycling stability of the composites. The fast capacity fading of the sample prepared at 600 °C in Ar can be explained by their high impedance compared to other samples.

8.4 Conclusions

In summary, rGO wrapped magnetite nanoparticles were obtained by a simple precipitation reaction followed by heating at 80 °C in air. The sample has high surface area of 30 m^2 g^{-1} and exhibits high reversible capacity of over 1200 mAh g^{-1} at a current density of 60 mA g^{-1}. However, the capacity retention

was slightly poor. Annealing the composites at higher temperatures leads to increased particle size and decreased surface area. However, these composites exhibits very good lithium cycling properties and minimal capacity fading. The sample annealed at 700 °C in Ar–H_2 atmosphere exhibits the best rate capability with a capacity of $\sim$480 mAh g^{-1} at a high current rate of 3.2 C (3000 mA g^{-1}).

References

1. M.V. Reddy, T. Yu, C.-H. Sow, Z.X. Shen, C.T. Lim, G.V.S. Rao, B.V.R. Chowdari, Adv. Funct. Mater. **17**, 2792–2799 (2007)
2. L. Zhang, H.B. Wu, X.W. Lou, Adv. Energy Mater. **4**, 1300958 (2014)
3. X. Zhu, Y. Zhu, S. Murali, M.D. Stoller, R.S. Ruoff, ACS Nano **5**, 3333–3338 (2011)
4. S.-D. Seo, D.-H. Lee, H.-W. Shim, S. Lee, D.-W. Kim, J. Am. Ceram. Soc. **97**, 1413–1420 (2014)
5. P.L. Taberna, S. Mitra, P. Poizot, P. Simon, J.M. Tarascon, Nat. Mater. **5**, 567–573 (2006)
6. G. Zhou, D.-W. Wang, F. Li, L. Zhang, N. Li, Z.-S. Wu, L. Wen, G.Q. Lu, H.-M. Cheng, Chem. Mater. **22**, 5306–5313 (2010)
7. A.S. Hameed, H. Bahiraei, M.V. Reddy, M.Z. Shoushtari, J.J. Vittal, C.K. Ong, B.V.R. Chowdari, A.C.S. Appl, Mater. Interfaces **6**, 10744–10753 (2014)
8. Y. Sharma, N. Sharma, G.V.S. Rao, B.V.R. Chowdari, Electrochim. Acta **53**, 2380–2385 (2008)
9. H. Tang, P. Gao, A. Xing, S. Tian, Z. Bao, RSC Adv. **4**, 28421–28425 (2014)
10. C.T. Cherian, J. Sundaramurthy, M.V. Reddy, P. Suresh Kumar, K. Mani, D. Pliszka, C.H. Sow, S. Ramakrishna, B.V.R. Chowdari, *ACS Appl. Mater. Interfaces* **5**, 9957–9963 (2013)
11. P. Lavela, J.L. Tirado, J. Power Sources **172**, 379–387 (2007)
12. N. Wang, H. Xu, L. Chen, X. Gu, J. Yang, Y. Qian, J. Power Sources **247**, 163–169 (2014)
13. M.V. Reddy, G.V. Subba Rao, B.V.R. Chowdari, *Chem. Rev.* **113**, 5364–5457 (2013)
14. F. Jiao, J. Bao, P.G. Bruce, Electrochem. Solid-State Lett. **10**, A264–A266 (2007)
15. Y. Chen, B. Song, X. Tang, L. Lu, J. Xue, J. Mater. Chem. **22**, 17656–17662 (2012)
16. C. Wang, G. Shao, Z. Ma, S. Liu, W. Song, J. Song, Electrochim. Acta **130**, 679–688 (2014)
17. C. Ban, Z. Wu, D.T. Gillaspie, L. Chen, Y. Yan, J.L. Blackburn, A.C. Dillon, Adv. Mater. **22**, E145–E149 (2010)
18. J.-Z. Wang, C. Zhong, D. Wexler, N.H. Idris, Z.-X. Wang, L.-Q. Chen, H.-K. Liu, Chem. Eur. J. **17**, 661–667 (2011)
19. P. Wang, M. Gao, H. Pan, J. Zhang, C. Liang, J. Wang, P. Zhou, Y. Liu, J. Power Sources **239**, 466–474 (2013)
20. P. Lv, H. Zhao, Z. Zeng, J. Wang, T. Zhang, X. Li, J. Power Sources **259**, 92–97 (2014)
21. L. Lang, Z. Xu, A.C.S. Appl, Mater. Interfaces **5**, 1698–1703 (2013)
22. W.-M. Zhang, X.-L. Wu, J.-S. Hu, Y.-G. Guo, L.-J. Wan, Adv. Funct. Mater. **18**, 3941–3946 (2008)
23. T. Zhu, J.S. Chen, X.W. Lou, J. Phys. Chem. C **115**, 9814–9820 (2011)
24. J. Cheng, B. Wang, C.-M. Park, Y. Wu, H. Huang, F. Nie, Chem. Eur. J. **19**, 9866–9874 (2013)
25. Y. Wu, Y. Wei, J. Wang, K. Jiang, S. Fan, Nano Lett. **13**, 818–823 (2013)
26. M. Ma, Y. Zhang, Z. Guo, N. Gu, Nanoscale Res. Lett. **8**, 16 (2013)
27. B. Bateer, C. Tian, Y. Qu, S. Du, T. Tan, R. Wang, G. Tian, H. Fu, CrystEngComm **15**, 3366–3371 (2013)
28. S. Bhuvaneswari, P.M. Pratheeksha, S. Anandan, D. Rangappa, R. Gopalan, T.N. Rao, Phys. Chem. Chem. Phys. **16**, 5284–5294 (2014)

29. C.T. Cherian, J. Sundaramurthy, M. Kalaivani, P. Ragupathy, P.S. Kumar, V. Thavasi, M.V. Reddy, C.H. Sow, S.G. Mhaisalkar, S. Ramakrishna, B.V.R. Chowdari, J. Mater. Chem. **22**, 12198–12204 (2012)
30. E. Yoo, J. Kim, E. Hosono, H.-S. Zhou, T. Kudo, I. Honma, Nano Lett. **8**, 2277–2282 (2008)
31. P. Lian, X. Zhu, H. Xiang, Z. Li, W. Yang, H. Wang, Electrochim. Acta **56**, 834–840 (2010)
32. S. Tao, W. Yue, M. Zhong, Z. Chen, Y. Ren, A.C.S. Appl, Mater. Interfaces **6**, 6332–6339 (2014)
33. J. Zhao, B. Yang, Z. Zheng, J. Yang, Z. Yang, P. Zhang, W. Ren, X. Yan, A.C.S. Appl, Mater. Interfaces **6**, 9890–9896 (2014)
34. Z. Xiao, Y. Xia, Z. Ren, Z. Liu, G. Xu, C. Chao, X. Li, G. Shen, G. Han, J. Mater. Chem. **22**, 20566–20573 (2012)